2018-07-13

Versatile High Performance Photomechanical Actuators Based on Two-dimensional Nanomaterials

Vahid Rahneshin
vrahneshin@wpi.edu

VERSATILE HIGH PERFORMANCE PHOTOMECHANICAL ACTUATORS BASED ON TWO-DIMENSIONAL NANOMATERIALS

By

Vahid Rahneshin

A Dissertation

Submitted to the Faculty of the

WORCESTER POLYTECHNIC INSTITUTE

In partial fulfillment of the requirements for the

Degree of Doctor of Philosophy

in

Mechanical Engineering

April 2018

APPROVED:

_____

Professor Balaji Panchapakesan, Advisor

_____

Professor Nikhil Karanjgaokar, Committee Member

_____

Professor Christopher R. Lambert, Committee Member

_____

Professor Cagdas Denizel Onal, Committee Member

_____

Professor Mark W. Richman, Graduate Committee Representative

ABSTRACT
VERSATILE HIGH PERFORMANCE PHOTOMECHANICAL ACTUATORS
BASED ON TWO-DIMENSIONAL NANOMATERIALS

Vahid Rahneshin

Worcester Polytechnic Institute (WPI)
April 2018

The ability to convert photons into mechanical motion is of significant importance for many energy conversion and reconfigurable technologies. Establishing an optical-mechanical interface has been attempted since 1881; nevertheless, only few materials exist that can convert photons of different wavelengths into mechanical motion that is large enough for practical import. Recently, various nanomaterials including nanoparticles, nanowires, carbon nanotubes, and graphene have been used as photo-thermal agents in different polymer systems and triggered using near infrared (NIR) light for photo-thermal actuation. In general, most photomechanical actuators based on *sp* bonded carbon namely nanotube and graphene are triggered mainly using near infra-red light and they do not exhibit wavelength selectivity.

Layered transition metal dichalcogenides (TMDs) provide intriguing opportunities to develop low cost, light and wavelength tunable stimuli responsive systems that are not possible with their conventional macroscopic counterparts. Compared to graphene, which is just a layer of carbon atoms and has no bandgap, TMDs are stacks of triple layers with transition metal layer between two chalcogen layers and they also possess an intrinsic bandgap. While the atoms within the layers are

chemically bonded using covalent bonds, the triple layers can be mechanically/chemically exfoliated due to weak van der Waals bonding between the layers. Due to the large optical absorption in these materials, they are already being exploited for photocatalytic, photoluminescence, photo-transistors, and solar cell applications. The large breaking strength together with large band gap and strong light-matter interaction in these materials have resulted in plethora of investigation on electronic, optical and magnetic properties of such layered ultra-thin semiconductors.

This dissertation will go in depth in the synthesis, characterization, development, and application of two-dimensional (2D) nanomaterials, with an emphasis on TMDs and molybdenum disulfide (MoS_2), when used as photo-thermal agents in photoactuation technologies. It will present a new class of photo-thermal actuators based on TMDs and hyperelastic elastomers with large opto-mechanical energy conversion, and investigate the layer-dependent optoelectronics and light-matter interaction in these nanomaterials and nanocomposites. Different attributes of semiconductive nanoparticles will be studied through different applications, and the possibility of globally/locally engineering the bandgap of such nanomaterials, along with its consequent effect on optomechanical properties of photo thermal actuators will be investigated. Using liquid phase exfoliation in deionized water, inks based on 2D-materials will be developed, and inkjet printing of 2D materials will be utilized as an efficient method for fast fabrication of functional devices based on nanomaterials, such as paper-graphene-based photo actuators. The scalability, simplicity, biocompatibility, and fast fabrication characteristics of the inkjet printing of 2D materials along with its

applicability to a variety of substrates such as plastics and papers can potentially be implemented to fabricate high-performance devices with countless applications in soft robotics, wearable technologies, flexible electronics and optoelectronics, bio-sensing, photovoltaics, artificial skins/muscles, transparent displays and photo-detectors.

ACKNOWLEDGMENTS

It has been a great pleasure and an extraordinary opportunity to study at Worcester Polytechnic Institute (WPI) during the past few years. Many people have provided assistance and support throughout my graduate studies at WPI, including my family, friends, labmates, professors, and colleagues. Special thanks to my parents, for encouraging me in all of my pursuits and inspiring me to follow my dreams. I would like to express my special appreciation to my advisor, Professor Balaji Panchapakesan, a gifted scholar and tremendous mentor, for his contagious enthusiasm as well as his advice and support throughout my dissertation studies. I would also like to thank my committee members, Professor Christopher R. Lambert, Professor Cagdas Denizel Onal, Professor Nikhil Karanjgaokar, and Professor Mark W. Richman, for their supports, comments, and encouragements. I like to thank my colleagues, friends, and individuals for their help, support, or scientific discussions during my Ph.D. studies, including Dr. Jacek B. Jasinski, Dr. Dominika A. Ziolkowska, Dr. Farhad Khosravi, Dr. James Loomis, Dr. Geoffrey Tompsett, Prof. Maria Chierichetti, Prof. John Hall, Prof. Nima Rahbar, and Mr. Sia Najafi. I would also like to express my appreciation to Professor Jamal Yagoobi for his continuous support and priceless advices throughout my studies in the department of mechanical engineering at Worcester Polytechnic Institute.

TABLE OF CONTENTS

LIST OF FIGURES

LIST OF TABLES

ABBREVIATIONS

PDMS	polydimethyl siloxane
NP	nanoparticle
GNP	graphene nanoplatelet
CNT	carbon nanotubes
SWNT	single wall carbon nanotubes
MWNT	multi-walled carbon nanotubes
FET	field effect transistor
LBL	layer-by-layer
SM	shear mixing
EM	evaporative mixing
PS1	1-pyrenesulfunic acid sodium salt
PL	photoluminescence
UV	ultraviolet
PA	photo actuation
IR	infrared
NIR	near infrared
VIS	visible
DMF	dimethylformamide
NMP	n-methyl-2-pyrrolidone
IPA	isopropyl alcohol
LPE	liquid phase exfoliation
TMD	transition metal dichalcogenides
TMDC	transition metal dichalcogenides
2D	two-dimensional
2DM	two-dimensional material
SEM	scanning electron microscope
AFM	atomic force microscopy

TEM	transition electron microscopy
HRTEM	high resolution transition electron micrograph
FFT	fast Fourier transform
LCE	liquid crystal elastomer
DMA	dynamic mechanical analyzer
DSC	differential scanning calorimeter
PVDF	polyvinyledene difluride
MOMS	micro-opto-mechanical systems
MEMS	micro-electro-mechanical system
NEMS	nano-electro-mechanical system
CMOS	complementary metal oxide semiconductor
RE	Reynolds number
WE	Weber number
OH	Ohnesorge number
PZT	lead zirconate titanate

CHAPTER 1
INTRODUCTION

The ability to convert photons into mechanical motion is of significant importance for many energy conversion technologies. Establishing an optical-mechanical interface has been attempted since 1881 when Alexander Graham Bell used the optoacoustic effect (photophone) to produce sound in a gas with chopped beam of sun light [1]. Nevertheless, only few materials exist that can convert photons of different wavelengths into mechanical motion that is large enough for practical import. Azobenzene liquid crystal elastomers were one of the first materials to exhibit such photomechanical effects [2]. However, their application required two different light sources for reversible thermal switching (420 nm and 365 nm) between an extended *trans* and a shorter *cis* configuration [3]. Examples of other materials that can directly convert light of different wavelengths into mechanical motion include range of organic photochromic compounds [4, 5], lead-lanthanum-zirconate-titanate (PLZT) ceramics [6], carbon nanotube polymer composites with selective chirality distributions [7] and more recently gold nanoparticle-polymer composites [8, 9]. Photomechanical actuators, motors, and micro-walking devices based on these materials have also been developed in recent years [4-8].

Photo-thermal actuation is the conversion of light into thermal and consequently mechanical work, and is an important concept in energy conversion and reconfigurable technologies. Advantages of such photo-thermal mechanisms for transducers include remote energy transfer, remote controllability, control of actuation using number of

photons (intensity) and photon energies (wavelength), fast actuation (milliseconds), low signal to noise ratio, high stored elastic strain energy densities with hyperelastic elastomers and scalability at different length scales using batch fabrication and high-volume semiconductor manufacturing. Recently, various nanomaterials including nanoparticles, nanowires, carbon nanotubes, and graphene have been used as photo-thermal agents by being mixed into different polymers from hyperelastic rubbers [10, 11], shape memory polymers [12] and liquid crystal elastomers [8, 9, 13], and triggered using near infra-red (NIR) light for photo-thermal actuation. In hyperelastic elastomers, based on the pre-strains, the samples when heated, can either expand, exhibit zero stress or contract in volume and can enable high photo-thermal strain energy densities [10, 11]. Large pre-strains result in large volume contraction on photo-thermal heating due to entropic elasticity. The mechanism in these nanocomposites is non-radiative decay of photons resulting in localized thermal effect [10, 12, 14-16]. In general, most photomechanical actuators based on *sp* bonded carbon namely nanotube and graphene [10, 12, 14-16] are triggered mainly using near infra-red light and they do not exhibit wavelength selectivity.

While the field is growing rapidly with many applications reported from cantilever based photomechanical actuators [17], photo-mechanical micro-grippers with milli-second time constants [18], photo-thermal micro-pillar actuators [8], micro-mirrors with large rotational angles [19], nanopositioners [20], plastic motors [7, 21], and polymer based actuators [7-9, 17-19, 21, 22], there is still need for a material design that is simple, versatile, reversible, wavelength selective, scalable and

encompasses large optical to mechanical stress response that is based on their unique structure-based tunability in optical absorption at different wavelengths. Nanocomposites based on transition metal dichalcogenides (TMDs) may offer a new material design and approach for chromatic photomechanical actuation with large stress release owing to the van Hove singularities in the joint density of states in the visible region of the electromagnetic spectrum that could be useful in designing future wavelength selective reconfigurable technologies [23].

Layered transition metal dichalcogenides provide intriguing opportunities to develop low cost, light and wavelength tunable stimuli responsive systems that are not possible with their conventional macroscopic counterparts. Compared to graphene, which is just a layer of carbon atoms and has no bandgap, TMDs are stacks of triple layers with transition metal layer between two chalcogen layers and they also possess an intrinsic bandgap. While the atoms within the layers are chemically bonded using covalent bonds, the triple layers can be mechanically/chemically exfoliated due to weak van der Waals bonding between the layers. Due to the large optical absorption ($\sim 10^7 m^{-1}$ [23]) in these materials, they are already being exploited for photocatalytic [24], photoluminescence [25], photo-transistors [26] and solar cell [27] applications. Bulk form of Molybdenum Disulfide (MoS_2), one family member of TMDs, has an indirect band gap of ~1.29 eV [28]. With decreasing thickness, the past experiments have revealed a progressive confinement-induced shift in the indirect gap from the bulk value of 1.29 eV up to 1.90 eV [28]. The in-plane structure of MoS_2 is determined by strong covalent bonds resulting from the overlap between the *4d* and *3p* electron

orbitals of Mo and S atoms, respectively [29]. The elastic modulus and the breaking strength of an ideal defect-free single-layer MoS_2 is expected to be $E^{2D}/9$, where E^{2D} is the in-plane stiffness as per the theory of rupture and flow in solids [29, 30]. The in-plane stiffness of monolayer MoS_2 is reported as 180 ± 60 Nm^{-1} corresponding to an effective Young's modulus of 270 ± 100 GPa, which is comparable to that of steel [29]. Breaking occurs at an effective strain between 6 and 11% with the average breaking strength of 23 GPa [29]. The ultra-high strength is generated from the *p* orbitals of the chalcogen atoms which generate the σ bonds [23]. The large breaking strength (potentially capable of withstanding 25% strains) [31] together with large band gap and strong light-matter interaction in these materials has resulted in plethora of investigation on electronic, optical and magnetic properties of such layered ultra-thin semiconductors [31-37]. Moreover, two-dimensional (2D) nanomaterials based on transition metal dichalcogenides encompass large optical absorption (107 m-1) [22, 23] and strain engineering of such TMDs incorporated into hyperelastic matrix presents new opportunities in photo-thermal transducers.

Strain engineering, i.e., the change in the electronic properties using mechanical deformation is an important concept in condensed matter physics and material science that is being exploited in 2D materials due to their ultra-large mechanical strength (capable of withstanding 10-20% strains) and possessing a bandgap [31, 36, 38-41]. Strain engineering in 2D layered materials brings potential benefits such as those explored in graphene including; strain induced bandgap opening [42], strain enhanced electron-phonon coupling [43, 44], non-uniform strain induced pseudo-magnetic field

[45] and even strain engineered self-assembly of hydrogen on graphene surfaces [46]. In TMDs, The large breaking strength makes strain engineering an interesting prospect, as the bandgaps are highly sensitive to external strains. In Bulk form of MoS_2 with an indirect band gap of ~1.29 eV, strain engineering has no effect and does not produce any significant chromatic mechanical response. On the other hand, single layer MoS_2 has a band gap of ~1.9 eV [28]; bi-layer has a bandgap of 1.5-1.6 eV [36] and strain engineering can modulate electronic and optoelectronic properties. In few layer 2H-MoS_2, the bandgap goes from direct-to-indirect at >1 % strains [36] and undergoes semiconductor-to-metal transition at 10-15% strains [32]. Several techniques are realized for strain engineering of 2D layered materials including bending/elongating a flexible substrate [36], piezoelectric compression [47], exploiting thermal expansion mismatch [48], creating artificial atoms through indentation/capillary forces [49], and controlled wrinkling [31]. However, large area photo-thermal devices based on these mentioned techniques of strain engineering of 2D layered TMDs are yet to be explored with hyperelastic materials.

The goals of this dissertation are as follows: (1) develop a new class of photo-thermal actuators based on TMDs and hyperelastic elastomers with large opto-mechanical energy conversion; (2) investigate the most efficient fabrication methods for TMD-based nanocomposite which results in the maximum energy conversion efficiency; (3) investigate the layer-dependent optical and electronic properties of MoS_2 nanoparticles and their effects in layer-by-layer elastomer based nanocomposites; (4) investigate the possibility of globally/locally bandgap engineering of such TMDs and

its effect on optomechanical properties of photo thermal actuators; (5) develop mathematical models for analogy between opto-thermal and purely-thermal actuations and locally induced strains in van der Waals packed films of nanoparticles; (6) develop rapid prototyping (inkjet printing) of electronic and optoelectronic devices based on 2D materials on different substrates; (7) demonstrate a new class of photo-thermal hygroscopic actuators with large mechanical energy release. To this end, this dissertation is organized into the following chapters:

- Chapter 2 gives an overview into the discovery of 2D materials and TMDs. Different properties of TMDs including crystal structure, electronic structure and bandgap, vibrational and optical properties, exfoliation techniques, and strain engineering are discussed in detail. The state of the art on the application of 2D materials, with a specific focus on TMDs, in different fields such as electronics, optoelectronics, sensors, and actuators are discussed. Finally, an important application of 2D layered materials, i.e. the application in photo-actuation technologies, are reviewed and discussed.

- Chapter 3 details the first study on the importance of different fabrication methods on the yielded optomechanical properties of nanocomposites based on TMDs (MoS_2) and poly (dimethyl) siloxane (PDMS). In this chapter, it is shown that to achieve the best light to mechanical energy transduction in such nanocomposites not only depends on the type of nanoparticle used in them, but also on various factors such as fabrication methods and/or cross-linking ratio of the host polymer matrix. Either of these factors, individually or in

combination with others, play an important role in the final properties of nanocomposites and can be manipulated to achieve totally different and new behaviors.

- Chapter 4 presents an interesting observation; a reversible and chromatic mechanical response observed in MoS_2 based nanocmposites when illuminated by different photon wavelengths. This chromatic mechanical response originates from the d orbitals and is related to the strength of the direct exciton resonance A and B of the few layer TMDs affecting optical absorption and subsequent mechanical response of the nanocomposite, which is not available in nanocomposites based on *sp* bonded graphene and carbon nanotubes, as well as those based on metallic nanoparticles.

- Chapter 5 presents a new effect, as we call it *the coupled straintronic-photothermic effect*, in TMD-based actuators. The coupled straintronic-photothermic effect is an intimate coupling between the bandgap of the 2D layered semiconductor under localized strains, optical absorption and the photo-thermal effect resulting in a large chromatic mechanical response in TMD-nanocomposites. Under the irradiation of visible light (405 nm to 808 nm), such locally strained atomic thin films based on 2H-MoS_2 embedded in an elastomer matrix exhibits a large amplitude of photo-thermal actuation compared to their unstrained counterparts. This chapter demonstrates a new mechanism in TMD-based photo actuators that would be useful for developing broad range of transducers.

- Chapter 6 provide some mathematical models related to photo-induced and heat-induced actuations in polymer based nanocomposites. An analogy between photo- and thermal- actuations are presented and the corresponding temperature profiles in the two mechanisms are compared. Then a new analytical strain model for loosely van der Waals packed films of nanoparticles are presented to estimate the strain gradient in each of individual nanoparticles.

- Chapter 7 presents a fast fabrication method, i.e. inkjet printing, of 2D materials using a material printer. Inks based on 2D materials and TMDs are developed and used to print patterns on different surfaces, such as flexible and transparent substrates. Using this fabrication technology, hygroscopic photo thermal actuators based on 2D materials are presented for the first time, with a large mechanical energy release. These actuators benefits from a fast, simple, inexpensive and yet highly efficient design and fabrication method.

- Finally, Chapter 8 concludes this dissertation and provides directions for future studies on photo-thermal actuators based on 2D materials and TMDs.

CHAPTER 2
BACKGROUND

2.1. 2D MATERIALS

2.1.1. GRAPHENE AND DISCOVERY OF 2D CRYSTALS

Graphene is the name introduced for a mono layer of carbon atoms sitting in a two-dimensional flat honeycomb structure [50]. For more than 70 years, it was presumed not to exist in a free state as it forms thermodynamically unstable structures due to thermal fluctuations. Consequently, it had been viewed by researchers as a theoretical material existing only as an integral part of its three-dimensional structure: graphite [50]. This presumption, first made by Landau and Peierls [51, 52] in the late 30s and supported by other scientists as well [53], came to an end when Andre Geim and Konstantin Novoselov published their findings in their Nobel-prize winning paper entitled *"electric field effect in atomically thin carbon films"* in 2004. This was a revolutionary discovery, as it opened up numerous opportunities with applications in various fields.

2D materials, such as graphene, are a building block for materials of all other dimensionalities, where the same chemical compound can display drastically different characteristics depending on whether it is arranged in a zero-dimensional (0D), one-dimensional (1D), two-dimensional (2D), or three-dimensional (3D) structure [50, 54]. Graphene, for instance, can be wrapped into 0D buckyballs (C_{60} fullerene), rolled into 1D carbon nanotubes, or stacked into 3D graphite [50]. The failure to identify such 2D crystals in the years prior to discovery of graphene arises from several facts: first,

because monolayers are in great minority among accompanying thicker flakes, it was tremendously difficult to find them [54]. Second, 2D materials show no clear signature in transmission electron microscopy unlike other nanomaterials such as carbon nanotubes [54-57]. Third, single atomic layers of materials are totally transparent to visible light, and as a result, cannot be seen under conventional optical microscopes on many substrates such as glass or silicon. Fourth, AFM as the only definitive method to identify single crystals, has a low speed and throughput, and in practice it had been impossible to find cleaved 2D crystals by randomly scanning surfaces using AFM [54]. Fifth and most importantly, as mentioned before, it was presumed that 2D materials could not exist and form stable structures. Novoselov and Geim later associated their success in finding such 2D crystals to the tentative identification of these materials under an optical microscope when they were placed on top of a silicon dioxide wafer (SiO_2) [54].

The discovery of such materials was a breakthrough, especially for the semiconductive industry, as it was believed to near its performance limits with the conventional silicon-based technology: it was difficult to further improve the technology with conventional semiconductive materials, by scaling down in size, consuming less energy, and yet performing faster with higher frequencies [58-60]. Monolayers of 2D crystals were promising materials to this end. Graphene, for instance, exhibits typical values of carrier mobility between 2,000 and 5,000 cm^2/Vs [54]. For other 2D materials such as $NbSe_2$ and MoS_2, electron mobilities between 0.5 and 3 cm^2/Vs were initially reported [54], which later improved to values as high as

200 cm^2/Vs for MoS_2 [61]. Detailed studies on these types of materials and their conductivities as a function of temperature and *Vg* discovered that materials such as 2D-MoS_2 was a heavily doped semiconductor with an activation gap of ≥ 0.6 eV [54].

2.1.2. PROPERTIES OF GRAPHENE

Graphene, as the most researched 2D material, has shown many stimulating properties during the past decade. Many researchers have focused on exploring its unusual properties, including high thermal conductivity [62], mechanical strength [63], quantum Hall effect [64], electrical conductivity [65], modulus of elasticity [66], and nanocomposites applicability [67]. It has also offered extraordinary opto-mechanical properties, which are very useful in remote actuation systems and photo-activated technologies [11, 68-70]. Despite all the great properties and propitious opportunities of graphene especially for electron-device community, in 2010, however, Frank Schwierz showed that a main obstacle in developments of such devices is the lack of an intrinsic bandgap in its structure [71]. It was concluded that, contrary to what was collectively believed, the excellent mobility of graphene may not be its most compelling feature, when viewed from a device standpoint. The lack of such intrinsic bandgap implies that although the high mobilities offered by graphene can increase the speed of post-silicon electronic devices, they come at the expense of a lower *on-off* ratio in these devices, which in turn eliminates one of the main advantages of CMOS configuration, i.e. its low power consumption [71].

Figure 1- Graphite and Molybdenite, as displayed at Harvard Museum of Natural History, Cambridge, MA.

2.2.TRANSISTION METAL DICHALCOGENIDES AND MOS_2

2.2.1. CRYSTAL STRUCTURE AND PROPERTIES

Stimulated by the discovery of two-dimensional crystals, Transition metal dichalcogenides (TMDs) have become important materials for next generation electronics, photonics and opto-electronics [54]. Compared to graphene, which is just a layer of carbon atoms and has no bandgap, TMDs are a class of layered material with X-M-X layer structure where a chalcogen atom (S, Se, or Te) is placed in two planes separated by a transition metal atom (group IV, V, or VI), and possessing an intrinsic bandgap (Figure 2a) [72]. While there exist strong covalent bonds in each layer of TMDs, the weak out of plane van der Waals bonds make it possible to exfoliate atomically thin layers of these new class of materials using various exfoliation methods

[54, 73-76]. Figure 2b depicts the crystal structure of monolayer MoS_2 [77]. The blue sphere represents Molybdenum (Mo) and the golden sphere Sulphur (S) in the structure. The top view of the MoS_2 lattice suggests a honeycomb structure for connections between atoms. The calculated unit cell parameter for MoS_2 is reported as a=3.12 Å with a vertical separation between Sulphur layers of 3.11 Å [77]. Figure 2c depicts different polytypes associated with TMDs, which differ based on stacking order and metal atom coordination [72]. The chalcogen atom is shown in yellow and the transition metal in gray. Three different polytypes 2H, 3R, and 1T are associated with TMDs with *c* being the stacking index indicating the number of layers in each stacking order. For different TMDs, the lattice constant ranges from 3.1 to 3.7 Å and the interlayer spacing is ~6.5 Å [72]. Table 1 has listed different TMDs with their associated electronic properties [72]. Due to the large optical absorption (~$107m^{-1}$ [23]) in these materials, they are already being exploited for photocatalytic [24], photoluminescence [25], photo-transistors [26] and solar cell [27] applications.

As a good example of TMDs, molybdenum disulfide (MoS_2) has attracted plethora of research due to its superior properties, owing to the existence of an intrinsic and tunable bandgap in its electronic structure [60, 78-83]. MoS_2 is an inorganic compound with a silvery black appearance which is available as the mineral molybdenite, the principal ore for molybdenum [84]. Molybdenum disulfide looks very similar to graphite in appearance (Figure 1), and due to its low-friction properties, it has been commonly used as a solid lubricant [85-87].

Similar to other members of TMD family, MoS_2 nanoparticles are stacks of weakly bonded layers held together with van der Waals forces. Mo and S atoms in each of these layers are bonded by strong covalent bonds, resulting from the overlap between the *4d* and *3p* electron orbitals of Mo and S, in a hexagonal structure [29]. Unlike Graphene, the existence of an intrinsic bandgap in MoS_2 brings in interesting properties, such as large on-off ratio while keeping an acceptable electron mobility, all of which necessary for any potential replacement of silicon industry in electronic or optoelectrronic devices as well as energy harvesting in near future [60]. While bulk MoS_2 has an indirect optical bandgap of about 1.29 eV, the bandgap changes to a direct band with a value of 1.9 eV when the number of layers is reduced to one [28]. The elastic modulus and the breaking strength of an ideal defect-free single-layer MoS_2 is expected to be $E^{2D}/9$, where E^{2D} is the in-plane stiffness as per the theory of rupture and flow in solids [29, 30]. The ultra-high strength is generated from the *p* orbitals of the chalcogen atoms, which generate the σ bonds [23]. The large breaking strength [31] together with large band gap and strong light-matter interaction in these materials has resulted in plethora of investigation on electronic, optical and magnetic properties of such layered ultra-thin semiconductors [31-37], with applications in various areas such as phototransistors [79, 80], biosensors [88], solar cells [27], piezoelectric energy harvesters [89] and actuators [22, 90].

Table 1- Summary of TMDs and associated properties [72]

	Electronic characteristics		
	$-S_2$	$-Se_2$	$-Te_2$
Nb	Metal Superconducting CDW* [92]	Metal Superconducting CDW [92, 93]	Metal [91]
Ta	Metal Superconducting CDW [92, 93]	Metal Superconducting CDW [92, 93]	Metal [91]
Mo	Semiconducting 1L: 1.8 eV Bulk: 1.2 eV [82, 94]	Semiconducting 1L: 1.5 eV Bulk: 1.1 eV [94, 95]	Semiconducting 1L: 1.1 eV Bulk: 1.0 eV [95, 96]
W	Semiconducting 1L: 2.1 eV 1L: 1.9 eV Bulk: 1.4 eV [94, 95, 97]	Semiconducting 1L: 1.7 eV Bulk: 1.2 eV [91, 94]	Semiconducting 1L: 1.1 eV [91]

* Charge density wave

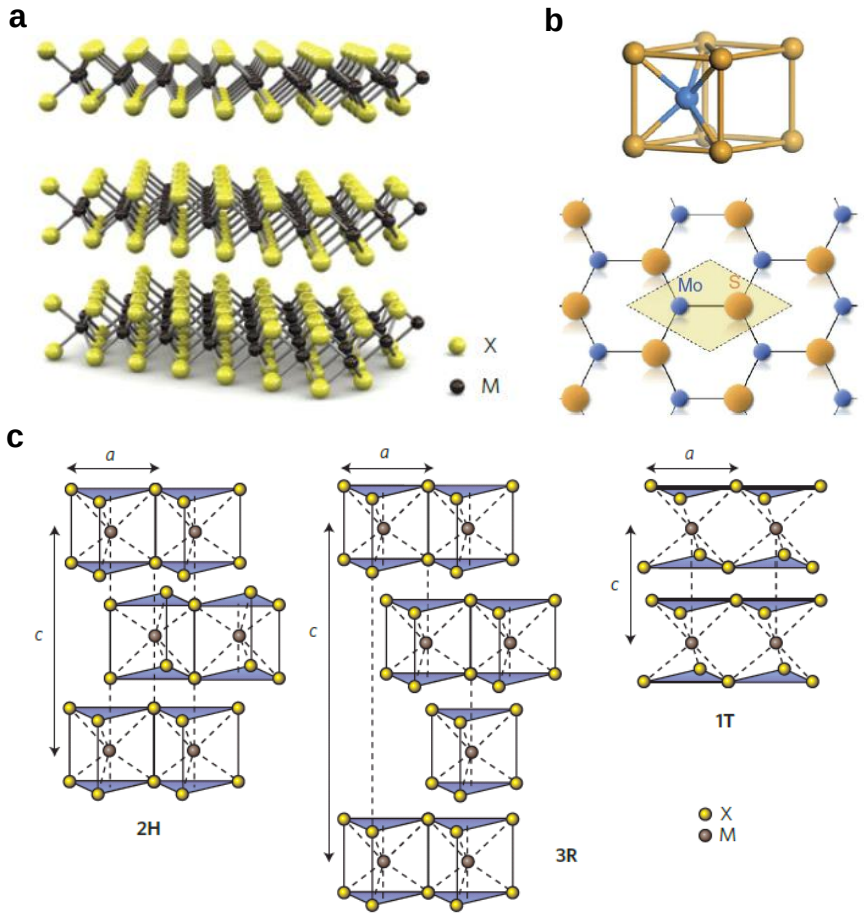

Figure 2- Structure of TMDs: (a) Schematic of MX_2 structure of TMDs with transition metal atoms in black and chalcogen atoms in yellow [60]. (b) Coordination environement MoS_2; Mo atoms are shown in blue and sulphur atoms in gold. Top view of the structure suggests a honeycomb lattice. The unit cell parameter is a=3.12Å and vertical separation between sulphur layers is 3.11Å [77]. (c) Schematic of different polytypes 2H, 3R, and 1T in TMDs. 2H is identified by hexagonal symmetry, two layers per repeat unit, and trigonal prismatic coordination; 3R has rhombohedral symmetry, three layer per repeat unit, and trigonal prismatic coordination; 1T has tetragonal symmetry with octahedral coordination and one layer per repeat [72]. a indicated the lattice constant (3.1Å to 3.7Å for different TMDs), and c the number of layers in each stacking order [72, 91].

2.2.2. ELECTRONIC STRUCTURE AND BANDGAP

In TMDs, as listed in Table 1, the compounds based on Mo and W metals give semiconducting properties, whereas their Ta and Nb counterparts give metallic and superconducting behavior [97-99]. The band structure for bulk and single layer MoS_2 is shown in Figure 3a [97]. The indirect bandgap at Γ point for bulk MoS_2 gradually changes to a direct bandgap for monolayers, which is believed to be due to the quantum confinement and hybridization change between p_z and *d* orbitals of S and Mo atoms [82, 83, 97]. As a result of this transition, the photoluminescence quantum yield displays a dramatic enhancement in going from the indirect bandgap in dark MoS_2 crystals to a direct gap in bright monolayer flakes (Figure 3b) [82, 83]. The photoluminescence in bulk MoS_2, which is an indirect bandgap material, is a weak phonon-assisted process with negligible quantum yield. On the other hand, a significant and bright photoluminescence is observed in few-layer MoS_2 samples, with a 10^4-fold enhancement of luminescence quantum yield for monolayers [82]. Monolayer MoS_2 is the first effective emitter of light with an atomically thin dimension [82].

It is expected that with decreasing the number of layers, all TMDs show a similar transition from indirect bandgap in bulk form to direct bandgap in monolayers [72]. The comparable value of bandgap energy in bulk or monolayers of TMDs to that of silicon (~1.1 eV) makes them appropriate substitutes for silicon in digital electronic and optoelectronic industries [71].

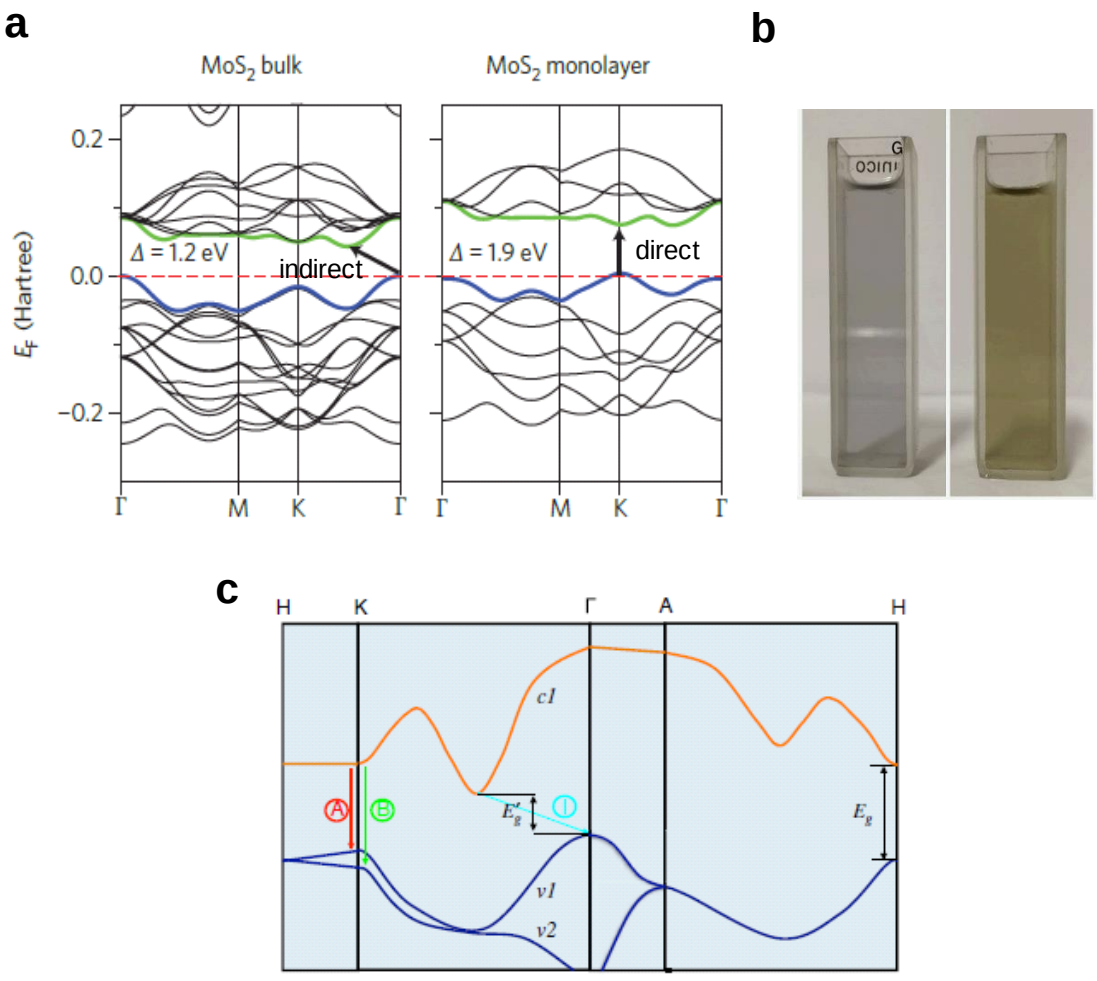

Figure 3- Electronic properties of TMDs: (a) Band structure for monolayer and bulk MoS_2 as calculated by density functional theory (DFT); red dashed line indicates the fermi level, blue line the top of valence band, and green line the bottom of conduction band. The arrows show the indirect and direct transitions in bulk and single-layer MoS_2 [72, 97]. (b) Optical photographs of bulk (in grey) and monolayer (in dark green) MoS_2 nanoparticles dispersed in solvent [22]. (c) Simplified band structure of bulk MoS_2; *c1* indicates the lowest conduction band, *v1* and *v2* the highest split valence bands. "I" is the indirect gap transition in bulk particles, and A and B indicate direct bandgap transitions in monolayer particles. E_g is the direct bandgap energy for monolayer and E'_g the indirect bandgap energy in bulk [82].

2.2.3. VIBRATIONAL AND OPTICAL PROPERTIES

The change from an indirect bandgap in bulk form to a direct bandgap in monolayers in TMDs has definite influences on their vibrational and optical properties, and the consequent influence can be observed in their photoconductivity, photoluminescence, absorbance spectra (UV-VIS spectroscopy), and Raman shifts [72]. As was discussed earlier, an increase of 10^4 fold in the photoluminescence quantum yield was observed as a result of this transition in MoS_2 flakes [82].

For mechanically exfoliated MoS_2 flakes on a Si/SiO_2 wafer, Splendiani *et al.* have shown that MoS_2 photoluminescence increases with decreasing layer thickness (Figure 4a) [83]. The silicon wafer is covered with 280 nm SiO_2 (Figure 4b). While bulk MoS_2 shows negligible photoluminescence, a strong photoluminescence emerges in monolayer regions, which is an indication of the indirect to direct band transition in the d-electron system of MoS_2 crystals. These results show that d-electron materials such as layered MoS_2 can bring about new opportunities to engineer their electronic structure at the nanoscale [83].

For chemically exfoliated MoS_2 flakes and the resulted thin film of nanoparticles by vacuum filtration method, Eda *et al.* studied the absorbance spectra as well as the photoluminescence (Figure 4c and d) [100]. The dominant peak in the photoluminescence spectra of monolayer is a single peak observed around 1.9 eV, which is associated to direct-gap luminescence [82]. However, in few layers other peaks in the photoluminescence are observed suggesting the direct-gap hot luminescence (peaks A and B) or indirect-gap luminescence (peak I), as depicted in

Figure 4e. Excitonic peaks A and B corresponds to direct-gap transitions between the maxima of split valence bands and the conduction bands at the K-point of the Brillouin zone (Figure 3c) [82].

The vibrational properties of MoS_2 atoms in its unit cell have been investigated in many studies in recent years [78, 101-104]. Figure 5a shows the atomic vibrations of different Raman modes of MoS_2 crystal. In MoS_2, the main Raman peaks corresponds to the in plane E^1_2g and the out of plane A_{1g} phonon modes. Based on the number of layers of MoS_2, the Raman spectra displays slight variations; with decreasing the number of layers from bulk to a single atomic layer, the A_{1g} mode near 406 cm^{-1} wavenumber decreases, and at the same time, the E^1_2g mode near 382 cm^{-1} increases (Figure 5b). In addition, the difference between frequencies of E^1_2g and A_{1g} decreases as the number of layers decreases (Figure 5c). These Raman shifts roots in the influence of adjacent layers on vibrational properties of atoms and the increase of long-range Coulomb interactions [72, 105]. These observations can be used as powerful criteria for identifying the number of layers based on Raman measurements [104].

2.2.4. STRAIN ENGINEERING

Strain engineering, i.e., the change in electronic properties using mechanical deformation is an important concept in condensed matter physics and material science that is being exploited in 2D materials, especially TMDs, due to their ultra-large mechanical strength (capable of withstanding 10-20% strains) and possessing an intrinsic bandgap [31, 36, 38-41, 106-108]. Strain engineering in 2D layered materials

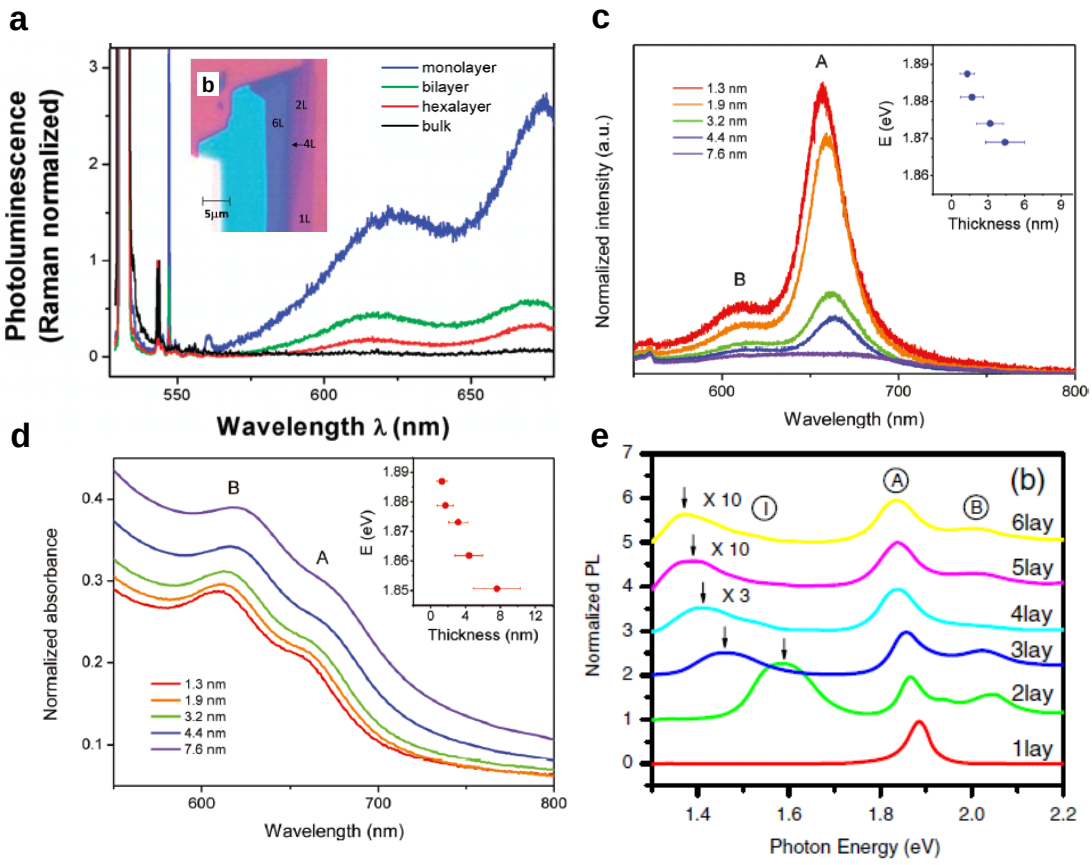

Figure 4- (a) Photoluminescence in monolayer, bilayer, hexalayer, and bulk MoS_2 normalized by Raman intensity showing a dramatic increase of luminescence when number of layers is decreased to one [25]. Inset (b) shows optical microscopy image of mechanically exfoliated MoS_2 flakes on a Si/SiO_2 substrate; flakes with different number of layers appears with different colors [25]. (c) Thickness dependent photoluminescence in thin films of chemically exfoliated MoS_2 nanoflakes. Inset shows the energy of A exciton peak versus thickness of thin film [100]. (d) UV-VIS spectroscopy of the same films of (c); inset shows the energy of A exciton peak versus thickness of the film as calculated based on UV-VIS measurements [100]. (e) Normalized PL spectra by intensity of exciton A for 1-6 layers versus photon energy [82].

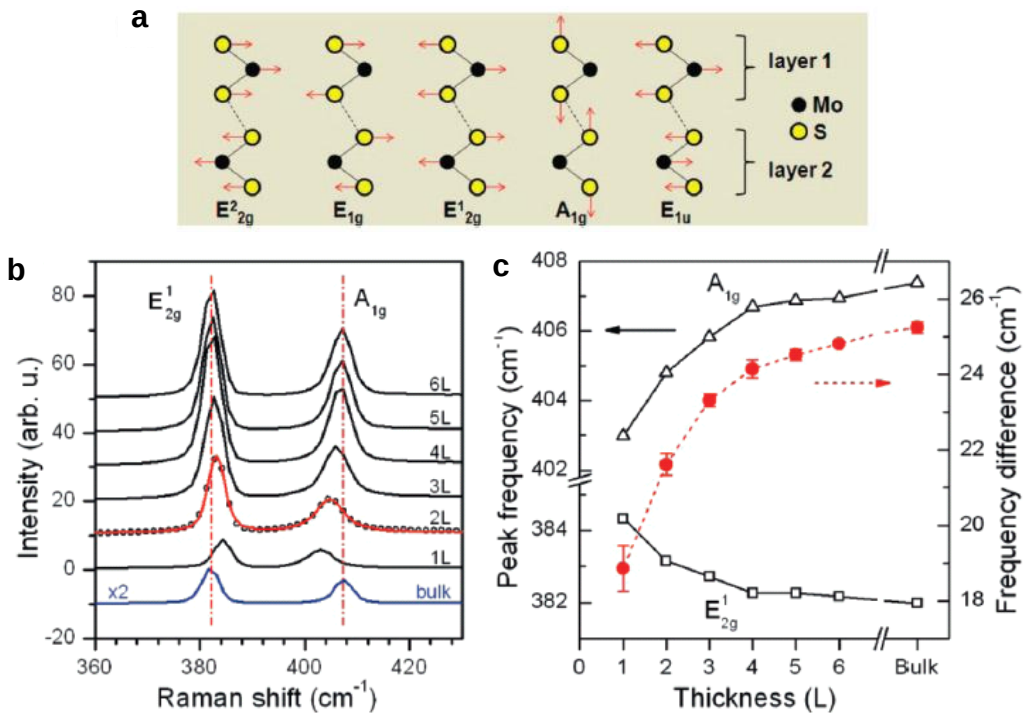

Figure 5- Vibrational properties of MoS_2: (a) Atomic vibrations of different Raman modes (E^2_{2g}, E_{1g}, E^1_{2g}, A_{1g}) and IR mode (E_{1u}) [78]. (b) Raman spectroscopy of mono- and few-layers and bulk MoS_2, and indication of Raman shifts in E^1_{2g} and A_{1g} modes with decreasing the number of layers [78]. (c) Frequencies of E^1_{2g} and A_{1g} modes and their difference versus number of layers [78].

brings potential benefits such as those explored in graphene including; strain induced bandgap opening [42], strain enhanced electron-phonon coupling [43, 44], non-uniform strain induced pseudo-magnetic field [45] and even strain engineered self-assembly of hydrogen on graphene surfaces [46]. Owing to an intrinsic bandgap, electronic properties of TMDs are highly sensitive to external strains applied to the material's atomic structure. The opto-electro-mechanical behavior of TMDs can be engineered

with an external and controllable applied strain and the resulting change in the bandgap structure of the material [31, 36, 38-41, 106-108]. Several techniques have been realized for strain engineering of TMDs, including bending/elongating a flexible substrate [36], piezoelectric compression [47], exploiting thermal expansion mismatch [48], creating artificial atoms through indentation/capillary forces [49], and controlled wrinkling [31].

For MoS_2 nanosheets consisting of 3-5 atomic layers and being obtained by mechanical exfoliation techniques, Castellanos-Gomez *et al.* showed that a strain-induced reduction of the direct bandgap and funneling of photogenerated excitons occurs when large localized strain is applied to these nanosheets [31]. The maximum uniaxial strain on top of wrinkles was estimated based on the geometry of each individual wrinkle as $\varepsilon \sim \pi^2 h\delta/(1-\sigma^2)\lambda^2$, where σ is the Poisson's ratio of the material, h is the thickness of the flake, δ the height and λ the width of the wrinkle [31, 109]. The localized strains of up to 2.5% was applied through controlled delamination from an elastomeric substrate. From photoluminescence measurements, a maximum direct bandgap reduction of 5% or 90 meV energy reduction was associated to this level of external strain applied to the material lattice (Figure 6a). Raman measurements revealed that both E^1_{2g} and A_{1g} modes shifted toward lower wavenumbers; however, the change in A_{1g} was small compared to the large blue shift in E^1_{2g} mode (Figure 6b) [31]. A Raman shift of -1.7 cm^{-1} per percentage strain was found for E^1_{2g} mode in MoS_2 [31, 108]. Figure 6c and d shows the change in direct bandgap energy (A exciton) and Raman shift of E^1_{2g} mode as a function of applied strain to the MoS_2 lattice. The ability

of strain engineering in such layered materials and generating confinement potential for exciton drifting using external strains opens up new possibilities to design and control the electronic and optoelectronic properties of atomically thin TMDs with applications in photovoltaics, quantum optics, and 2D optoelectronic devices [31].

2.2.5. SYNTHESIS & EXFOLIATION TECHNIQUES

2D materials are stacks of weakly van der Walls bonded layers. This weak interaction along the thickness of these materials makes it possible to be exfoliated and reduced to single- and few- layers with satisfactory control of layers number. Generally, the exfoliation/synthesis of 2D materials into single/few layers can be categorized into three categories: physical exfoliation, chemical exfoliation, and chemical synthesis. In the following, these exfoliation techniques are going to be described briefly.

2.2.5.1.Physical Exfoliation

The principle in physical exfoliation methods is using a force in order to separate layers of 2D materials. This includes mechanical exfoliation method (i.e. scotch tape) [110], shear force exfoliation, plasma assisted exfoliation, and liquid phase exfoliation (LPE). In mechanical exfoliation, single layers of 2D material is obtained by simple scotch tape method introduced first by Novoselov and Geim. Large and high quality single crystal of 2D material can be exfoliated using this method; however, the method drawback is a very limited yield, make it impossible to use for real applications. Plasma thinning of MoS_2 was studied by Liu et al, where they use Ar^+

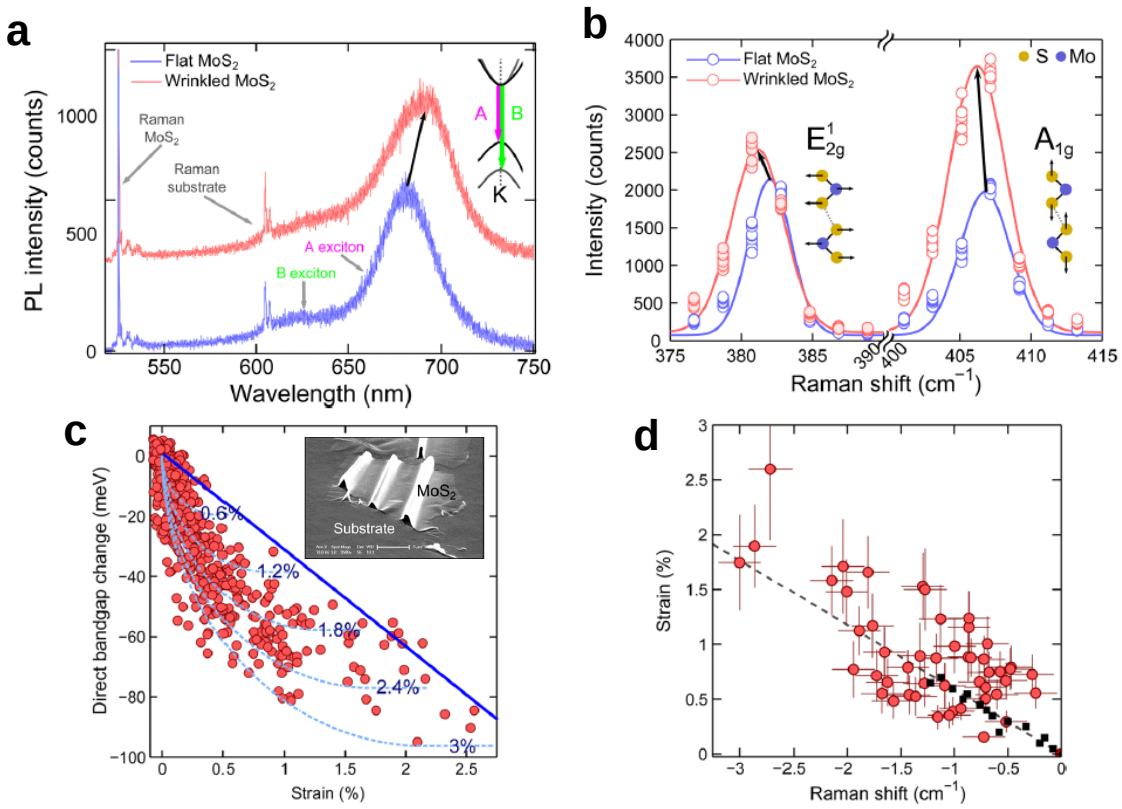

Figure 6- Strain engineering in MoS_2 nanoflakes: (a) Photoluminescence spectra for a flat nanoflake versus a wrinkled nanoflake, showing a red shift when the flakes are wrinkled. A and B exciton peaks have been identified in the PL signal [31]. (b) Raman spectra for a 4-layer mechanically exfoliated nanoflake in flat and wrinkled structures; both E^1_{2g} and A_{1g} modes show shifts toward lower Raman frequencies with the higher shift observed in E^1_{2g} mode [31]. (c) Change in the direct bandgap energy of MoS_2 as a function of applied strain. Red points are experimental data obtained from the change in A exciton in the photoluminescence measurements. Solid line shows the calculated bandgap change versus strain based on tight-binding (TB) model. Inset is SEM of a wrinkled 4-layer MoS_2 flake [31]. (d) The shift in E^1_{2g} Raman mode as a function of applied strain, suggesting a linear relationship with -1.7 cm^{-1} Raman shift per % strain [31].

plasma to strip away multi layer mechanically exfoliated MoS_2 flakes on a SiO2/Si substrate [111].

Liquid phase exfoliation is a method presented firsts by Coleman [73]. LPE is capable of producing large scale high quality mono layers of 2D materials, making it a promising method for practical applications of 2D materials in large scale. In contrast to mechanical exfoliation or plasma assisted exfoliation, the nano flakes yielding by LPE are relatively small particles in the range of 50-200 nm.

2.2.5.2.Chemical Exfoliation

Chemical exfoliation of 2D materials is a relatively old method of exfoliation compared to mechanical or LPE exfoliation methods. Single layer of MoS_2, as an example, was exfoliated by Joensen in 1986 [112]. Chemical methods such as lithium intercalation are based on reaction of atoms of a third material such as lithium with a solvent and exfoliation of 2D materials layers due to this reaction, which happens for trapped atoms of lithium in between 2D material layers. For instance, MoS_2 is soaked in an n-butyl lithium solution in hexane for a period of time. This process results in intercalating MoS_2 by lithium [113]. Immersing the intercalated MoS_2 in a solvent such as water results in formation of copious hydrogen gas between the layers of MoS_2, and separation of layers because of this gas expansion [112]. Chemical exfoliation methods, however, are believed to result in creation of defects in the material lattice, which can adversely affect optical or electronic properties of these materials.

Table 2- Comparison of different synthesis methods of 2DMs nanosheets [114]

Method	Lateral size	Advantage	Disadvantage	Reference
Mechanical exfoliation	up to several micrometer	Mild condition	Low yield, not scalable	[54, 115-118]
Shear exfoliation	~40-220 nm	High yield, easy processing	Large distribution of size and thickness	[73, 90, 119]
Chemical exfoliation	300 nm to sevral microns	High yiled of monolayers	Toxic process, expensive reagents, introduction of defects	[112, 120]
Liquid phase exfoliation	A few hundrads of nanometer	large quantities, high quality, easy processing	Difficult control of size and thickness	[73, 74, 121-126]
Chemical vapor deposition (CVD)	Large area (wafer size)		Ultra high vacuum, high temperature, limited substrates	[75, 127-129]

2.2.5.3.Chemical Synthesis

In contrast to exfoliation methods, which are considered top-down methods, there are bottom-up methods to create single layers of 2D materials. Some of chemical synthesis methods include hydrothermal synthesis [130-133] and chemical vapor deposition (CVD) [75, 134]. In chemical deposition methods, a precursor such as MoO_2, MoO_3, or Mo is deposited on top of a substrate such as SiO_2 or Si, and exposed to sulfur vapor for the sulfurization process [134]. The reaction chamber is heated to a

high temperature, for instance 650°C, which results in reduction of a precursor such as MoO_3 to form volatile suboxide MoO_{3-x} [135]. The suboxide compounds later reacts with sulfur vapor to create MoS_2 film on the substrate [75]. In these methods, the growth of 2D material is usually very sensitive to the substrate treatment prior to the growth [75].

2.3.ELECTRONICS, OPTOELECTRONICS, AND ENERGY CONVERSION TECHNOLOGIES

2.3.1. TRANSISTORS

One of the main applications of semiconducting materials is their use in electronic devices as transistors. The current state of art, for instance, for processors in electronic devices are based on silicon based metal oxide semiconductor field effect transistors (MOSFET). MOSFET transistors suffer from fundamental limits such as statistical and quantum effects and difficulty with heat dissipation when it comes to scaling down these transistors [72]. Although Field Effect Transistors (FET) based on 2D materials such as graphene showed exceptional high carrier mobility [71, 136-138], they lack a high on/off ratio due to extra high conductivity of graphene, which limits their use in low power consumption electronics. The need is a new material with sizable bandgap, high electron mobility, and scalability to small dimensions.

Transistors based on TMDs have unique opportunities to address these problems [60, 139]. FET transistors are made of a semiconducting channel, which is

connected to the source and drain electrodes. The electrical current flowing in the transistor is controlled by the gate electrode, which is separated by a dielectric material from semiconducting channel [140]. One of the first works on TMDs as FET transistors was done by Podzorov *et al.* in 2004, where an on/off ratio of 10^4 and a high electron mobility comparable to silicon FETs were reported [141]. The first MoS_2 top-gate FET transistor was introduced by Radisavljevic *et al.* in 2011 [60]. Their work presents a carrier mobility of greater than 200 $cm^2\ V^{-1}\ s^{-1}$ in room temperature, similar to that of graphene nanoribbons, and demonstrates transistors with room-temperature on/off ratio of 1×10^8 and ultralow standby power consumption. FET transistors based on thin films of MoS_2 obtained from liquid phase exfoliation has been also reported and showed similar electrical performance, which opens up new possibilities for two-dimensional, flexible, and transparent electronic applications [123]. The quantum transport simulations carried out by Yoon *et al.* to project the ultimate performance limits of MoS_2 transistors, suggested that although electron mobility of TMDs transistors may not be able to compete to conventional group III-V semiconductors, but its electrical properties has made it an attractive semi conductive material for low power electronics because of their large bandgap, excellent electrostatic integrity, and high Earth abundance [142]. Also due to large mechanical strength of MoS_2 (30 times stronger than steel) as well as its capacity to deform to a high strain value of 11% before breaking [29], it is a promising candidate with application in flexible electronics, thanks to being one of the strongest semi-conductive materials. The hybrid application of MoS_2 with other members of 2D materials family such as graphene and boron nitride

(BN) makes it possible for rapid fabrication of all-2D flexible and wearable electronics. This can result in stacking of different 2D materials in vertical heterostructures to make hybrid devices with unconventional operating principles and promising to the future of this field [72, 143].

2.3.2. OPTOELECTRONICS

Nanomaterials have been widely studied for the use in optoelectronics in the recent years [144-146]. The band structure of a semiconductor material such as that of TMDs determine their ability to interact with light. For instance, in direct band gap semiconductors, the incident photons with an energy higher than the bandgap of the material can readily be absorbed or emitted. Indirect bandgap materials, on the other hand, an additional phonon is needed to overcome the momentum difference between bands, and as a result, the indirect bandgap semiconductors are less efficient than their direct bandgap counterparts [72]. Owing to an intrinsic direct bandgap and being atomically thin and processable, single layer TMDs have great prospective qualities for applications in flexible and transparent optoelectronics such as transparent displays, wearable electronics, solar cells, optical switches, and photodetectors [80, 147-149].

Thin films of TMDs such as MoS_2 or WS_2 are photosensitive [150], and can be used as phototransistors, photodetectors, or heterojunction solar cells. Yin *et al.* have demonstrated a single-layer MoS_2 photo-transistor and investigated its light-induced electric properties [80]. They have shown that the photocurrent generation solely depends on the illuminating optical power at a constant drain or gate voltage. Photocurrent generation and annihilation can be switched completely within 50 ms and

exhibits stable characteristic. Yin *et al.* showed that single layer MoS_2 phototransistors give a better photo responsivity than graphene-based devices. The unique characteristics of MoS_2 based photo-transistors including incident light control, prompt photo-switching, and good photo responsivity opens up opportunities for low-cost electronic devices with applications in switches, memories, signal amplifiers, and light sensors [80].

As a direct gap semiconductor due to quantum mechanical confinement, monolayer MoS_2 is used as an ultra-sensitive photodetector, where the direct bandgap allows for high optical absorption and efficient electron–hole pair generation under photon excitation [118]. A maximum external photoresponsivity of 880 AW^{-1} at a wavelength of 561 nm was shown, with a photo response in the range of 400–680 nm. This makes MoS_2 photodetectors surpass their graphene counterparts by a factor of $\sim 10^6$ [118]. Monolayer MoS_2 showed a ~9,000-fold higher photoresponsivity compared to multilayer devices due to direct and indirect nature of bandgaps in monolayer and multilayers, respectively [151]. Photoresponsivity has been shown to be dependent on the illumination wavelength; a negligible photoresponsivity was observed for wavelengths above 680 nm, which corresponds to a photon energy of ~1.8 eV which is about the value of direct bandgap in monolayer MoS_2 [118]. Increasing the photon energy, i.e. decreasing the excitation wavelength, results in the excitation of electrons from the valence to the conduction band of MoS_2 and photocurrent generation [118]. Heterojunction solar cells made of MoS_2/TiO_2 nanocomposites with 3-hexylthiophene (P3HT) active layers was demonstrated with a 1.3% photo conversion efficiency [147].

Other optoelectronic applications of WS_2 and MoS_2 includes their use in electrochemical solar cells [149], as well as in polymer LEDs [152, 153].

2.3.3. SENSORS

The working principle for many electronic sensors is the change in the electrical properties of the constituent material due to interaction with an external stimulus. For bulk materials, this usually happens in the form of a change in resistance or capacitance of the sensing element [154]. Due to a big surface to volume ratio, the electrical properties in 2D materials are considerably perturbed even with a small adsorption, making them suitable choices for gas, chemical, or biomolecules sensing [154]. This fact has been utilized as a working principle in many 2D-material based sensors [155].

Semiconducting TMDs have been recently used for gas and chemical sensing based on a change in their resistance [156-159]. Li *et al.* has fabricated MoS_2 FETs based on mechanical exfoliation, and used them for sensing NO gas at room temperature [160]. A sensing capability down to a concentration of 0.8 ppm was reported for two-, three-, and four-layer MoS_2 devices. In another study, the sensing behavior of atomically thin-layered MoS_2 transistors was investigated [161]. Although single-layers of TMDs have been the focus of plethora of research recently, they may not be the ideal case for sensing applications compared to their multi-layer counterparts. Late *et al.* studied MoS_2 FETs ranging from single to multiple layers to find out the best choice for gas sensing applications (NO_2, NH_3). Their findings show that compared to single layer MoS_2 transistors, their few layer counterparts exhibit excellent sensitivity, recovery, and they show better gate-bias manipulation by

humidity or green light [161]. The application of TMDs as chemical sensors have been also investigated recently [162]. Perkins *et al.* showed that single layer MoS_2 is an effective chemical sensor and displays highly selective reactivity to a range of analytes such as trimethylamine (TEA), acetone, and nitrotoluene. MoS_2 sensors was shown to exhibit a much higher selectivity compared to their carbon nanotube counterparts [162].

In addition to resistance-based sensing devices, single layer MoS_2 has been also used for O_2 and H_2O molecule sensing based on modulation of the light emission (photoluminescence). Physi-sorbed molecules of O_2 or H_2O depletes an n-type semiconductor such as MoS_2 or $MoSe_2$ and leads to significant enhancement in photoluminescence, which can be used as a sensing principle [163]. Furthermore, semiconducting TMDs have been also used in other applications such as strain sensing, due to their ultrasensitive band structure to external strains [47], and DNA and small biomolecules sensing [164, 165].

2.4.PHOTO-ACTUATION TECHNOLOGIES

Actuators are mechanical devices that convert different types of energy to a mechanical action. This mechanical action can be in the form of mechanical displacement (strain) or mechanical force (stress). In the past decades, several different actuation mechanisms exploiting different principles have been introduced. Mechanical, electrostatic, magnetic, acoustic, biological, chemical, piezoelectric,

thermal, fluidic, and optical principles have been utilized to convert an input energy source into the mechanical actuation [166-171].

As a relatively new actuation technology, optical (or photo-) actuators are those converting the photon energy to mechanical motion. In general, all optically driven actuators fall into two main categories in term of energy conversion mechanism: direct and indirect methods [172]. While in direct mechanism the optical energy is converted to the mechanical action without any intermediary medium, the indirect-type actuators benefits from a secondary effect of light, such as photon-induced heat, electrical current, or conductivity changes, as the principal mechanism of energy conversion. An example of direct methods is the photo actuation of a silicon micro cantilever as a result of electrostatic forces [172]. Although direct conversion methods are usually faster than indirect ones, they suffer from generating small amount of mechanical forces. The indirect-type actuators, on the other hand, benefit from simpler designs and they generate higher actuation power, which are especially advantageous for macro scale applications of nanotechnology [166].

Compared to traditional forms of actuation, optical actuation technologies have several advantages including remote actuation, remote controllability, electro-mechanical decoupling, no need to electrical circuits reducing problems such as resistive heat dissipation, electrical current loss or electromagnetic interference, scalability to small sizes, and harsh environment applicability. Optical actuators can have numerous applications in technologies such as solar energy convertors in

planetary explorers, optical micro- and nano-positioners, solar tracking actuators in spacecrafts, microrobots, micro-optomechanical systems, and photophones [166].

2.4.1. PHOTO-RESPONSIVE MATERIALS

Photo-responsive materials are those that can convert light to mechanical energy. Due to their promising prospects in micro-, macro-, and nano-technologies, they have been the focus of plethora of research in the past few decades. Examples of materials that can directly convert light of different wavelengths into mechanical motion include range of organic photochromic compounds [4, 5], lead-lanthanum-zirconate-titanate (PLZT) ceramics [6], carbon nanotube polymer composites with selective chirality distributions [7], and more recently gold nanoparticle-polymer composites [8, 9]. Photomechanical actuators, motors, and micro-walking devices based on these materials have been also developed [4-8]. The field of photo-responsive materials are fast growing and expanding; nevertheless, in the following sections some important categories of these materials are being reviewed.

2.4.2. PHOTO-INDUCED SHAPE CHANGING POLYMERS (SCP)

These polymers change shapes upon irradiation of a light source. The shape change in these polymers are usually reversible once the light source is removed. One of the advantages of photo induced SCP compared to their thermally induced counterparts is the ability to revert to the original shape without being affected by the environmental temperature fluctuations, which is specifically an important issue for biomedical implants [166]. A photosensitive functional group or filler must be present

in SCP to make them photo responsive materials [173]. Two of the most commonly used photosensitive functional groups are photoisomerizable azobenzenes and photoreactive cinnamates [173]. Figure 7 shows these two functional groups. Azobenzene is a functional group consisting of two phenyl rings linked by a double bond. In azoebenzene, two different states, namely *cis* and *trans*, can be achieved based on the wavelength of irradiation light. A UV light in the range of 330-380 nm tends to a *cis* structure, while for irradiations with wavelengths greater than 420 nm, the molecule switches to the *trans* isomer [5, 173-175]. In photoreactive groups such as cinnamates in cinnamic acid (CA), the double bond dimerizes with the neighboring molecules when illuminated with UV light of greater than 260 nm wavelength, to form a cyclobutane ring. The formation of these rings is reversible, and can revert to the original structure when illuminated with a light of lower than 260 nm wavelength [176, 177]. These functional groups can be linked to macromolecules in elastomers to cause large actuation upon irradiation with a light source [166]. The speed of shape changing in these polymers are a function of several factors including the intensity, wavelength, and irradiation time of the input source [166].

2.4.3. LIQUID CRYSTAL ELASTOMERS

Liquid crystal elastomers (LCEs) are among shape changing materials that can change their shape upon an external energy source such as light. The shape changing behavior in LCEs is due to their elastic properties as a polymer, along with the ordering of mesogenic liquid crystalline moieties [166]. Classic liquid crystals are fluids of relatively stiff rod molecules with random orientational order. As the isotropic

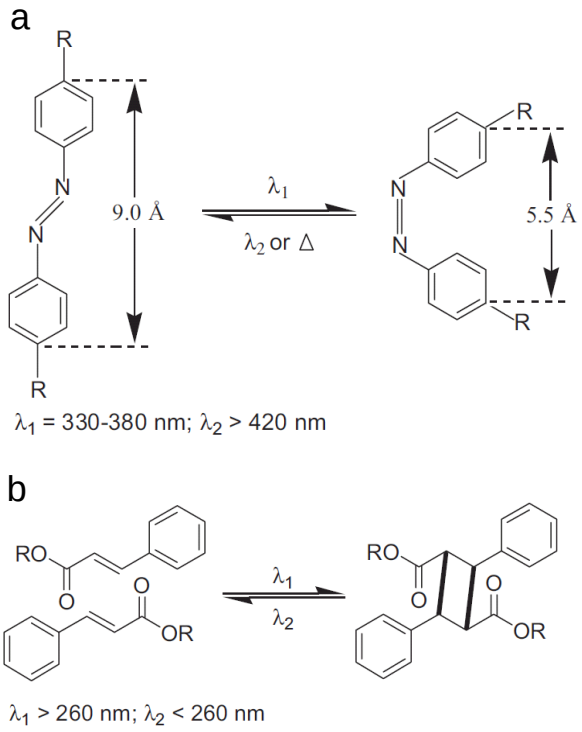

Figure 7- Schematic of photo-induced isomerizations and reactions: (a) *Trans-cis* photo-isomerization in azobenzene. (b) photodimerization of a cinnamic acid group [173]

polymers become nematic, the average molecular shape changes [178]. Nematic elastomers are able to change their shapes to large values, up to 400%, in a narrow range around their nematic-isotropic transition temperature [179].

There have been many experimental studies on the opto-mechanical properties of LCEs. Yamada *et al.* has shown a plastic motor driven by light with the use of liquid crystal elastomers and incorporation of photochromic molecules such as azobenzene [21]. Van Oosten *et al.* uses liquid crystal elastomers to make photo-actuators that bend

toward a light source [180]. Hugel *et al.* have shown a light-powered molecular machine which is able to expand or contract individual polymers and delivering mechanical force [3]. In another work, inkjet printing was utilized to fabricate all-polymer micro devices based on self-organizing liquid crystals. The self-assembly properties of LCEs allow for creation of large strain gradients, which can mimic the motion of natural cilia. These actuators have the applications in lab-on-a-chip devices and can create flow and mixing in wet environments [181].

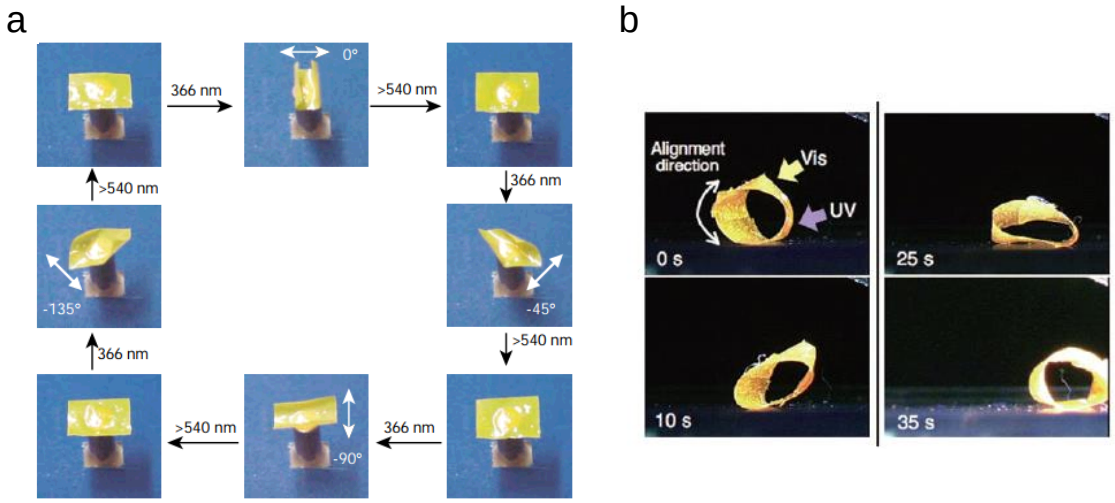

Figure 8- (a) A single film (4.5mm×3mm×7μm) of liquid crystal network containing azobenzene chromophore reversibly bends in different directions in response to a linearly polarized light of different angles at 366 nm wavelength (white arrows); illumination by a wavelength longer than 540 nm will result in flattening of the film. The temperature of the film is controlled at 85°C by a hot plate. The bending and unbending times are in the range of 10 seconds [5]. (b) Photo-driven motion of a ring of LCE film; simultaneous irradiation by UV light (366 nm) of 200 $mWcm^{-2}$ and visible light (>500 nm) of 120 $mWcm^{-2}$ results in the rolling motion. Size of the ring: 18

mm×3 mm×20 μm with 6 mm in diameter. From the photographs, a movement of ~6-10 mm is estimated in 35 seconds [21]

2.4.4. MOLECULAR PHOTO-MOTORS AND PHOTO-SWITCHES

Nanomotors are molecular-scale motors that can perform mechanical work [182]. Although a variety of energy sources have been used to trigger these molecular-scale motors, photon-driven motors seem to be more promising in the nanoscale, and specially for bio applications [166]. Eelkema *et al.* developed a light-driven molecular motor which can rotates microscale objects as big as 10,000 times the size of the motor itself. The molecular motor consists of a right-handed helical structure and an stereogenic center that determines the direction of rotation, and a carbon-carbon bond in the structure which works as the motor axle (Figure 9) [182]. Li *et al.* developed a single DNA molecule nanomotor, which is a 17mer DNA oligonucleotide, and is able to switch between two conformations by changing the DNA hybridization. This nanomotor can perform an extending-shrinking motion [183]. These types of nanomotors, consisting of protein molecules, exist in large quantity in living systems [183]. Another DNA-based nanomotor was developed by Kang *et al.*, where a DNA hairpin-structured molecule along with azobenzene moiety served as a nanomotor. This single molecule motor displayed 40-50% open-close conversion efficiency upon irradiation of UV/Visible light [184].

Molecular photo-switches are another category of molecular photo actuators in which photons trigger a molecule to switch between different states and exhibit

different molecular properties including colors, absorption, emission, or refractive index [166]. Al-Atar *et al.* presented a photo-controlled molecular switch which regulates paralysis in living organisms. In this photo switch, the photon-induced reactions of a photoresponsive material, i.e. dithienylethene, when specific wavelength of light is applied result in a specific structure of the molecule, which in turns causes the paralysis of the living tissue [185]. Such photo switches are of great importance in biochemistry, medicine, and drug delivery, and make it possible to regulate photochemical reactions using a single light source [185-187].

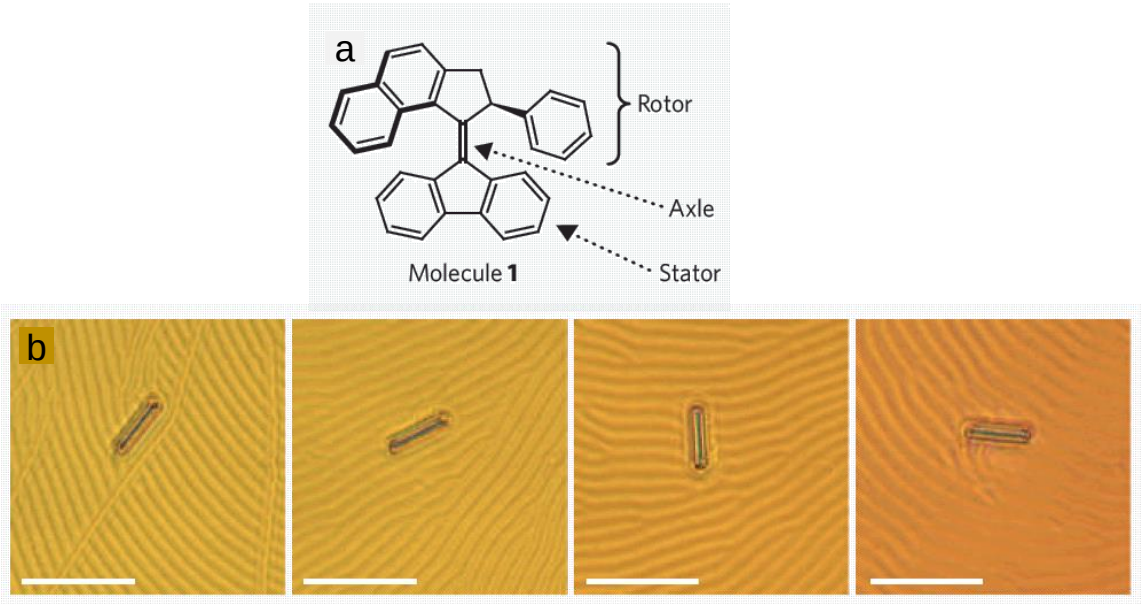

Figure 9- A light-driven molecular motor: (a) Molecular structure of the motor. Bonds in bold are out of the page. (b) A glass rod rotating on the liquid crystal film doped with molecule 1 when irradiated with ultraviolet light. Snapshots show 15-s intervals. Scale bars are 50 μm [182].

2.4.5. PHOTOSTRICTIVE MATERIALS

Photostrictive materials are those who generate mechanical strains upon irradiation of light. The light-to-mechanical energy conversion in photostrictive materials is due to the collective effects of converse-piezoelectric along with photovoltaic [6, 188]. In such materials, while electric voltage is generated upon absorption of photons by means of photovoltaic effect, this photo-generated voltage in turn transduces to expansion or contraction due to the converse piezoelectricity. The photestrictive effect has been observed in many ferroelectric materials. As a standard to quantify the performance of such materials, the product of photovoltage (E_{ph}) and piezoelectric constant (d_{33}) is usually used [6, 166]. As an example of phtostrictive materials, (Pb, La)(Zr, Ti) O_3 (PLZT) ceramics doped with WO_3 show large photo strains under illumination of near ultraviolet light [6]. An optical bimorph-type actuator made from PLZT ceramics was developed to generate several hundred micron displacement upon illumination of a 365 nm light source [189]. PLZT ceramics have been also applied for applications such as photo-driven relays and micro walking machines [190].

2.4.6. PHOTO-INDUCED SURFACE CHARGE CARRIER ACTUATORS

The photogeneration of free charge carriers in the surface of a semiconductive material such as silicon bring about mechanical actuation. Silicon microcantilevers have been used to generate stresses upon irradiation by a λ=780 nm laser diode [191]. The photo generated stress has been shown to be four times larger compared to the stress resulting from thermal excitation. Since the electron and holes charge carriers can

be generated in very short times, this photo-generated actuation is much faster than its thermal counterpart [191]. A similar phenomenon was observed for another semiconductive material, i.e. Cadmium Sulfide (CdS), when the thin wafers were clamped at one end and illuminated with white light [192]. It was found that when the CdS wafers were excited to their fundamental frequencies using optical choppers, the amplitude of vibration was a function of incident light wavelength [192]. Other thin crystals of semiconductive materials such as GaAs have followed a similar photomechanical effect, where their normal mode of vibration was found to depend on the surface preparation as well [193, 194]. The higher efficiency of photo activation of such cantilevers compared to the thermal activation makes them a powerful optical drive for resonant sensors [194].

2.4.7. PHOTO-THERMAL ACTUATION IN CARBON-BASED NANOCOMPOSITES

Photothermal actuators made of a host polymer and carbon-based nanofillers have been reported in recent years. Carbon-based materials such as graphene and carbon nanotubes (CNT) are attractive materials due to their excellent mechanical properties, which can improve the mechanical properties of the host polymer when used as nanofillers. As an example, single wall carbon nanotubes (SWNT)/nafion nanocomposites have been shown superior performance as actuators compared to metal-doped nafion films [195]. In polymer nanocomposites, their unique combination of properties establishes new opportunities for a new class of stimuli-responsive materials which are not otherwise offered in one individual constituent [12]. Koerner *et*

al. have demonstrated that by uniformly dispersing CNT in thermoplastic elastomers, nanocomposites with up to 50% higher stress recovery storage, compared to the pristine polymer host, can be achieved [12]. This improvement was attributed to the increase of rubbery modulus and shape fixity of nanocompiste by anisotropic nanotubes. The non-radiative decay of absorbed photons by CNT fillers results in a temperature rise, which in turn remotely triggers the stored strain energy by melting strain-induced polymer crystallites [12]. Over the past decade, the trend in polymer nanocomposite actuator technology has shifted from its original "improvement" approach toward a more stimulating one, which is the study of new functionalities based on the introduction of exotic nanofillers to a polymer host [196, 197]. As a good example, the combination of CNT exotic properties with rubber elasticity in polymer nanocomposites has shown a continuous and reversible response of large magnitude, which is not achievable with any other material [196, 198-200].

Optically-driven devices based on carbon nanotubes/polymer composites have been abundantly addressed in the literature [18, 19, 201-203]. A micro-opto-mechanical system based on CNT and SU8 was developed using standard microfabrication techniques, achieving a displacement of 24 μm under infrared illumination of 240 μW [18]. Lu *et al.* showed manipulation of small polystyrene microspheres using these CNT/SU8 micro grippers. As another application of CNT-based actuators in macro scale, millimeter-scale nanotube grippers made from single wall carbon nanotubes showed manipulation of small objects [201]. The photomechanical responses in CNT-

based photo actuators were shown to dependent on the alignment of carbon nanotubes in the composite [204].

As another carbon-based material, the incredible physical properties of graphene makes it an exciting material for photo actuation when present in polymer nanocomposites. Different properties of graphene such as thermal conductivity [62], mechanical strength [63], quantum Hall effect [64], and photocurrent [205] have been addressed in the literature. The application of graphene as light-driven actuators was introduced by Loomis *et al.*, where graphene nanoplatelets (GNP) were acting as transducing agents in a polymer matrix [69]. The GNP/PDMS composites showed higher actuation stresses compared to their previous CNT-based counterparts [69]. These samples were prepared by stir mixing of graphene nanoplatelet powder in the polymer host for different weight percentages [69]. In graphene-based actuators, it has been shown that as the number of layers decreases, the energy conversion efficiency increases [11, 70]. As photothermal nanopositioners, graphene nanoplatelets were used in a two-axis submicron-resolution stage with 120 nm resolution, and a maximum actuator efficiency of ~0.03% [68]. Graphene bending photo actuators have also been presented, where a double layer structure made from pristine and GNP reinforced Polydimethylsiloxane constructs a bending mechanism due to the mismatch between thermal expansions of the two layers [206]. These soft and lightweight actuators can be beneficial in applications such as soft robotics, active optics, drug delivery, sports equipment, aircraft composites, and medical implants [68, 206].

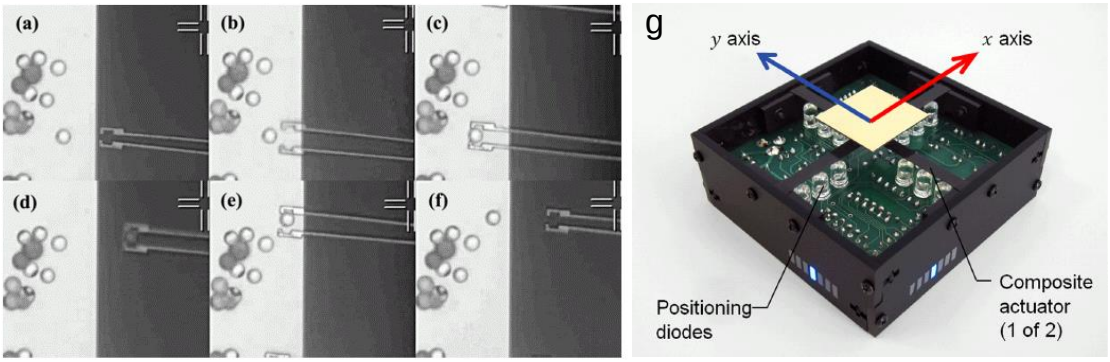

Figure 10- (a-f) A CNT-SU8 MOMS micro gripper manipulating a micro-polystyrene sphere of 16µm diameter [201]. (g) A photo-thermal nanopositioner, made of GNP/PDMS composite actuators, capable of moving in x and y direction [68].

In general, most photomechanical actuators based on *sp* bonded carbon namely nanotube/graphene [10, 12, 14-16] are triggered mainly using near infra-red light and they do not exhibit wavelength selectivity. The mechanism in these nanocomposites is non-radiative decay of photons resulting in localized thermal effect [10, 12, 14-16].

While this field is growing rapidly with many applications reported from cantilever based photomechanical actuators [17], photo-mechanical micro-grippers with milli-second time constants [18], photo-thermal micro-pillar actuators [8], micro-mirrors with large rotational angles [19], nanopositioners [20], and plastic motors [7, 21], there is still need for a material design that is simple, versatile, reversible, wavelength selective, scalable and encompasses large optical to mechanical stress response that is based on their unique structure based tunability in optical absorption at different wavelengths. Nanocomposites based on TMDs may offer a new material

design and approach for chromatic photomechanical actuation with large stress release owing to the van Hove singularities in the joint density of states in the visible region of the electromagnetic spectrum that could be useful in designing future wavelength selective reconfigurable technologies [23]. In this dissertation, several novel light driven actuators based on TMDs are discussed. The use of TMDs in soft actuators is a rather new filed in this area and will introduce intriguing opportunities to develop low cost, light and wavelength tunable stimuli responsive systems that are not possible with their conventional counterparts.

Table 3- A review of different types of actuators [207]

Actuation Technology	Type of Stimulus	Strain (%)	Stress (MPa)	Working Frequency (Hz)	Advantages	Disadvantages	References
Piezoelectric - ceramics (PZT)	Piezoelectric	0.2	110	Fast (kHz)	Fast response High generative force Wide bandwidth	High electric field Low strain Brittle	[208]
Piezoelectric - polymer (PVDF)	Piezoelectric	0.1	4.8	Fast (kHz)	Fast response Flexible Wide bandwidth	Low mechanical output High electric field	[208]
Electrostrictive polymer P(VDF-TrFE)	Electrostrictive	4.3	43	Fast (kHz)	Fast response flexible High stress generation	Operates above Curie temp High electric field	[209] [210]
Dielectric elastomer (Acrylic with pre-strain)	Electrostrictive	215	2.4	Fast (kHz)	Very large stroke Light weight Low cost Stability	Defect sensitive Poor mechanics (viscoelastic) Leakage current	[211]
Shape memory alloy (Ti-Ni)	Phase transformation	5	200	Slow	High work density	Slow Low efficiency	[208] [212]
Natural muscle (human skeletal)	Biochemical	40	0.35	Moderate	High stroke Self-healing	Limited stress generation	[210] [213]
Carbon nanotubes (CNTs)	Thermal expansion	1.5	16	Slow	High stroke High stress	High operating temperature Passive cooling	[214]

Nylon (6,6)	Thermal expansion	10	22	Moderate (5Hz)	High stroke	Need external unit for heating/cooling	[215]
Conjugated polymer (PEE-PPy)	Solvent sorption	-	27	Moderate (0.3 Hz)	High stroke	Require ambient water gradient	[216]
Conductive polymers (PPy)	Electrochemical	7	5	Low (0.01 Hz)	Biocompatible Soft Low potential	Low mechanical strength	[217]
CNT yarns	Electrochemical	0.8 (Torsional) 0.12 (Preload)	- Preload 50	Moderate (0.1-0.5 Hz)	High stroke Withstand high loading	Useful for rotating systems Creep	[218] [219]
CNT/PAni	Electrochemical	0.85 0.7 (Preload)	- Preload 25	Low (0.0035 Hz)	Withstand high loading High work per cycle	Slow response (High frequency is not reported)	[220]
Graphene	Electrochemical	0.85	6.1	Low (0.002 Hz)	Large curvature change	Slow response (Strain is 0.35 at 0.02 Hz)	[221]
Nanoporous metals (Au-Pt)	Electrochemical	3.9	-	Very low (0.00025 Hz)	High elastic energy density	Slow response Expensive Microscale	[222]
Transition metal oxides (V_2O_5)	Electrochemical	0.21	5.9	Low (0.005 Hz)	Redox active Abundant	Slow response Require orientation	[223]

HOPG (Highly oriented pyrolytic graphite)	Electrochemical	6.7 1.3 1	10 100 5	Very low (0.00001 Hz) (0.01 Hz)	High energy density	Very slow response Safety issues due to Li	[224] [225]
MoS_2	Electrochemical	0.8 0.5	17 11	0.0042 Hz 0.125 Hz	High displacement High generated force Low potential	Tendency to delaminate under high load	[207]
SWCNT acrylic	Photothermal	0.01-0.3 (Bending: 4.3 mm)	0.9	-	No need to complicated electrical connections No need to high electric fields No need to electrolyte	No wavelength selectivity NIR region	[202]
GNP elastomer	Photothermal	2-5 (5wt%; 40% pre-strain)	0.0012 (0.1wt%; 0% pre-strain)	-	Reversible expansion/contraction Good at NIR region Higher actuation compared to CNT	No wavelength selectivity NIR region	[69]

LBL MoS_2 elastomer (PDMS)	Photothermal	0.3-1.5 (0.1wt%; at 0% and 60% pre-strains)	0.0055-0.025 (for 0.1wt%; at 0% and 60% pre-strains)	-	Low cost Highly stretchable Can be tailored to applications Stable Robust Wavelength selective Higher generated stress compared to CNT and GNP High stroke (compared to CNT and GNP) Applicability to various environments	Low actuation at NIR regions	This dissertation [22]
2L bandgap-engineered MoS_2 elastomer	Photothermal	0.07 (35 nm film; 0% pre-strains) (Bending: 1mm)	0.0007 (35 nm film; 0% pre-strains)	30 Hz	Low cost Highly stretchable Wavelength selective Moderate frequency response Improved actuation at NIR (2 times improvement compared to LBL)	Access to nanometer (<100 nm) scale for thin film	This dissertation [226]
Graphene/paper	Photothermal/ hygroscopic (Thermal/ hygroscopic)	0.16 (Bending: 33 mm)	8.0	25 Hz	Simple design Foldability Cost effective High generated force High mechanical deformation	Lower relaxation speed due to natural moisture sorption	This dissertation

CHAPTER 3
PHOTOMECHANICAL ACTUATION OF BULK-MOS_2/POLYMER NANOCOMPOSITES

3.1. INTRODUCTION

Following the discovery of graphene, transition metal dichalcogenides have become important materials for next generation electronics and opto-electronics owing to the existence of an intrinsic bandgap in their structure. Due to their excellent mechanical and optical properties, the application of this new class of 2D materials into composites has been a growing filed in the past decade. Utilizing the excellent behavior of TMDs and integrating them on a base host polymer matrix, novel functionalities can be achieved, which is not available in individual constituents. In this chapter, we present a study on the importance of different fabrication methods on the yielded optomechanical properties of nanocomposites based on MoS_2 nanoparticles and Polydimethylsiloxane (PDMS). Such nanocomposites have been widely used and proved to be quite useful in remote actuation applications in the past. Understanding the proper fabrication method of such nanocomposites is essential for translating the novel optoelectronic and electronic properties of TMDs into real applications, making it possible to achieve real-world devices which are reliable, scalable and controllable.

3.2. BACKGROUND

Utilizing the excellent behavior of TMDs and integrating them on a base host matrix, novel functionalities can be achieved, which is not available in individual constituents [22]. A plethora of research has focused on the integration of nanoparticles

into polymer host matrices in the past [227-231]. Various methods of integration of nanoparticles into the host matrix, such as random distribution (0-3 type nanocmposite) or layer-by-layer method (2-2 laminated type), have been used and reported by researchers in recent years [197]. Nevertheless, understanding the right combination of nanoparticles and base matrix and the proper fabrication method to synergistically achieve a superior behavior still remains a challenge.

As a good example of TMDs, molybdenum disulfide (MoS_2) has attracted plethora of research due to its superior properties, owing to the existence of an intrinsic bandgap in its electronic structure [60, 78-83]. MoS_2 nanoparticles are stacks of weakly bonded layers held together with van der Waals forces. This fact has led to numerous research focusing on TMDs, especially MoS_2, in recent years, with applications in various areas such as photo transistors, biosensors, piezoelectric energy harvesters and actuators [22, 80, 88-90]. In this chapter, we present a study on the importance of different fabrication methods on the yielded optomechanical properties of nanocomposites based on MoS_2 and Polydimethylsiloxane (PDMS). Such nanocomposites have been widely used and proved to be quite useful in remote actuation applications in the past [11, 69, 70, 196, 203]. In case of TMD based nanocomposites and their responsivity to photons, layer-by-layer and shear mixing processes have been reported in the literature [22, 90]. Yet, we show in this chapter that the right decision of choosing a method over the other not only depends on the type of nanoparticle used, but also on various factors such as fabrication methods and/or cross-linking ratio of the host polymer matrix. Either of these factors, individually or in

combination with others, play an important role in the final properties of nanocomposites.

In the following, we show that at lower cross-linking ratios of polymer matrix, layer-by-layer method gives the best results of photon-to-mechanical energy transduction, while when higher cross-linking ratios are achieved, shear and evaporative mixing offers higher optical to mechanical energy transduction compared to their layer-by-layer counterparts. In addition, in EM and SM fabrication methods, the peak photo-actuation stress is increased and shifted toward higher weight percentages as higher cross-linking ratio is used. The results of this chapter propose that energy transduction in MoS_2 nanocomposite actuators are not only a function of weight percentage or exfoliation level of nanoparticles as reported earlier in [90] and [22], but also functions of fabrication method and cross-linking ratio of the base polymer.

3.3. RESULTS

Crystal and layer structures of MoS_2 are shown in Figure 11. MoS_2 is a semiconducting material in the category of Transition Metal Dichalcogenides, in which each Mo atom is located at the center of a trigonal prism created by six S atoms. Each single layer of MoS_2 is separated from other layers by a distance of ~0.65 nm [60]. High-resolution transition electron microscopy (TEM) images suggests a hexagonal structure for MoS_2 nanoparticles (Figure 11c).

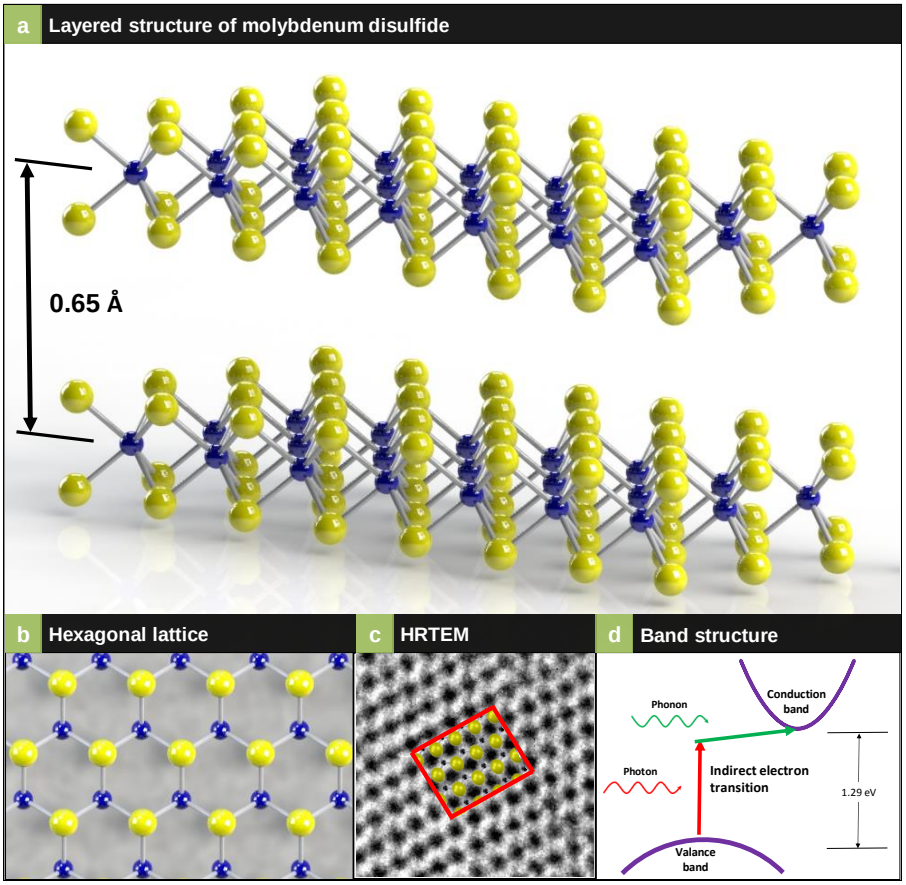

Figure 11- (a) 2D layered structure of Molybdenum disulfide, (b) hexagonal lattice as viewed from the top, (c) High resolution TEM image, and (d) band structure of few-layer nanoparticles

Figure 12 shows the material characterization for MoS_2 nanoparticles used in this chapter. Scanning Electron Microscopy (SEM) images of MoS_2 nanoparticles are depicted in Figure 12b. Ultrafine MoS_2 powder was purchased from Graphene Supermarket. These nanoparticles have an average particle size of ~90 nm and a near spherical morphology per manufacturer. Depending on the fabrication method, these nanoparticles have been directly added to a PDMS host matrix without any further

exfoliation (shear mixed samples), or have been lightly exfoliated in ethanol for 6 hours (layer-by-layer and evaporative mixed samples). The MoS_2-ethanol solutions with different concentrations as used in evaporative mixing samples, and the deposited thin film of MoS_2 nanoparticles on an alumina filter membrane as used in layer-by-layer fabrication method are depicted in Figure 12a. Lambert-Beer plot and optical absorbance for different solutions used in this paper are plotted in Figure 12c and d. Raman spectroscopy of MoS_2/PDMS nanocomposites is shown in Figure 12e and is compared to a pristine PDMS sample.

Figure 13a shows the fabrication steps for three different fabrication methods, namely layer-by-layer (LBL), evaporative mixing (EM), and shear mixing (SM) methods. In LBL fabrication method, nanocomposites are made from three separate layers of pristine PDMS and MoS_2, as shown in Figure 14a. A thin film of MoS_2 nanoparticles have been made using a standard vacuum filtration process and been transferred to a cross-linked layer of PDMS. Another layer of PDMS is then spun coated on top of the MoS_2 thin film. In EM and SM fabrication methods, nanoparticles are directly mixed with the host polymer (PDMS base) and after achieving a uniform mixture, the cross-linker is added to it. The samples are then spun coated on a glass slide and cured at oven at 120℃ for 20 mins, followed by an additional 12-hour curing in room temperature.

Figure 13b schematically shows the cross-linking of polymer in the presence of MoS_2 nanoparticles, with the reaction being shown in Figure 13c [232]. In lower

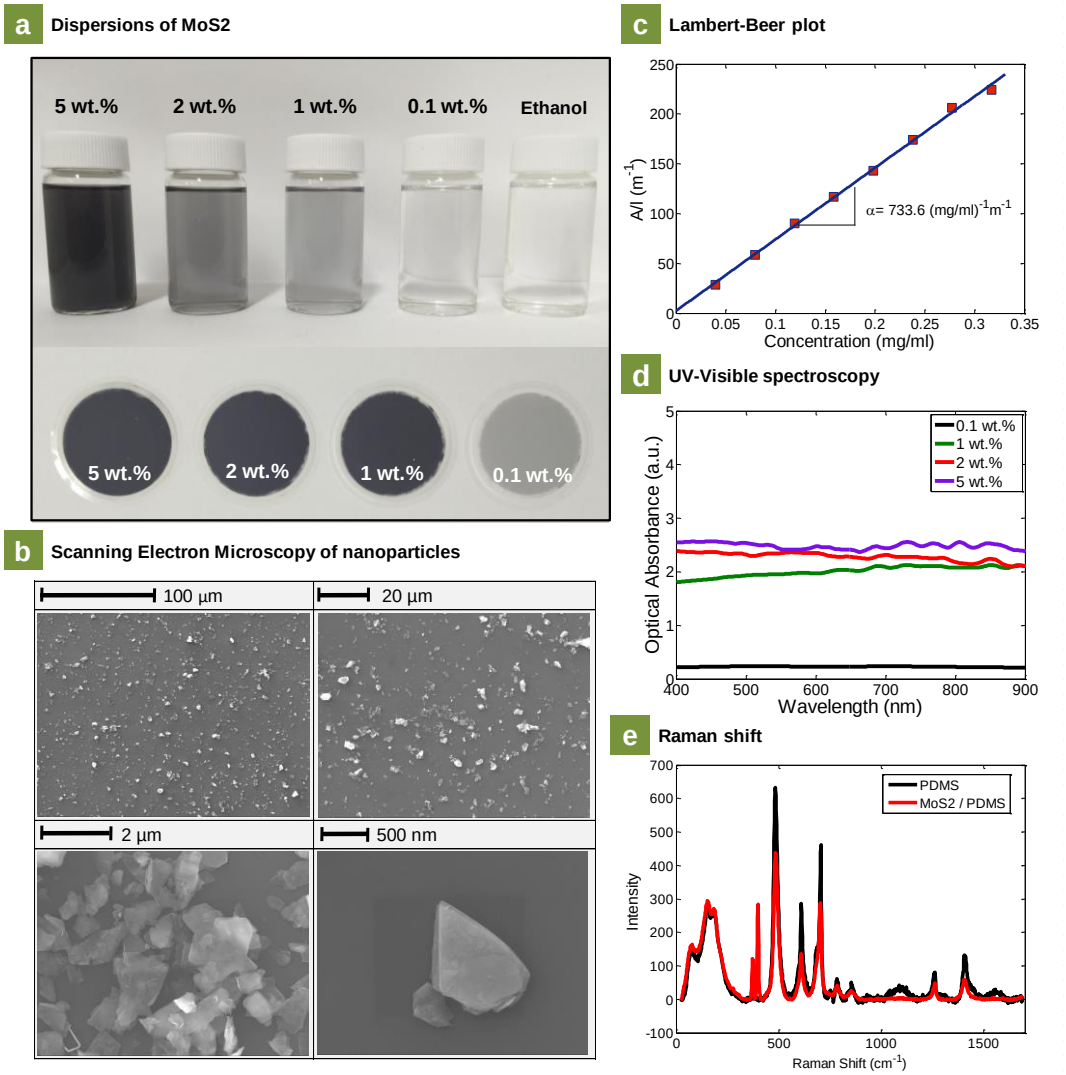

Figure 12- Material characterization: (a) MoS_2 solutions in Ethanol with different concentrations, and the deposited thin film of nanoparticles on filter membranes (b) SEM of individual nanoparticles (c) Lambert-Beer plot for MoS_2 solutions at different concentrations (d) UV-Visible spectroscopy of different MoS_2 solutions (e) Raman shifts for MoS_2/PDMS nanocomposites

concentrations of MoS_2 nanoparticles, the cross linking process is mainly favorable. As the MoS_2 concentration in the polymer base is increased, there is higher chance of MoS_2 nanoparticles piling up and blocking the crosslinking process. This will result in a lower degree of effective crosslinking, which in turn appears as a decrease in the mechanical properties of the composite, such as its modulus of elasticity. While the addition of other nanoparticles such as GNP and MWCNT were shown to improve the mechanical properties of the composite (Figure 16), the adverse effect of MoS_2 addition to host PDMS is believed to be due to its higher tendency to aggregation when mixed in a polymer host [87]. These findings are also in line with previous research [233]. We observed that in case of MoS_2 nanocomposites based on uniformly dispersed nanoparticles in the host polymer matrix, there exist two regimes in the photo-actuation results; an increasing photo-actuation regime with increase in MoS_2 additives, and a decreasing regime after a specific threshold is reached. The unfavorable effect of nanoparticle addition to the polymer host can be remedied by increasing the cross linking ratio of polymer matrix, i.e. increasing the chance of successful cross linking reactions. This is schematically depicted in Figure 13b, where part (1) is pure PDMS with well cross-linked polymer molecules. When PDMS is mixed with low concentrations of MoS_2 nanoparticles, the reactions are still mostly favorable and almost all polymer molecules are cross-linked properly (2). When medium concentration of MoS_2 additives are reached, there are both cross-linked and not cross-linked regions in the polymer matrix, with the reactions being a mixture of favorable

and unfavorable, as depicted in part (3). Higher concentration of MoS_2 will lead to many non-crosslinked polymer regions/holes (4).

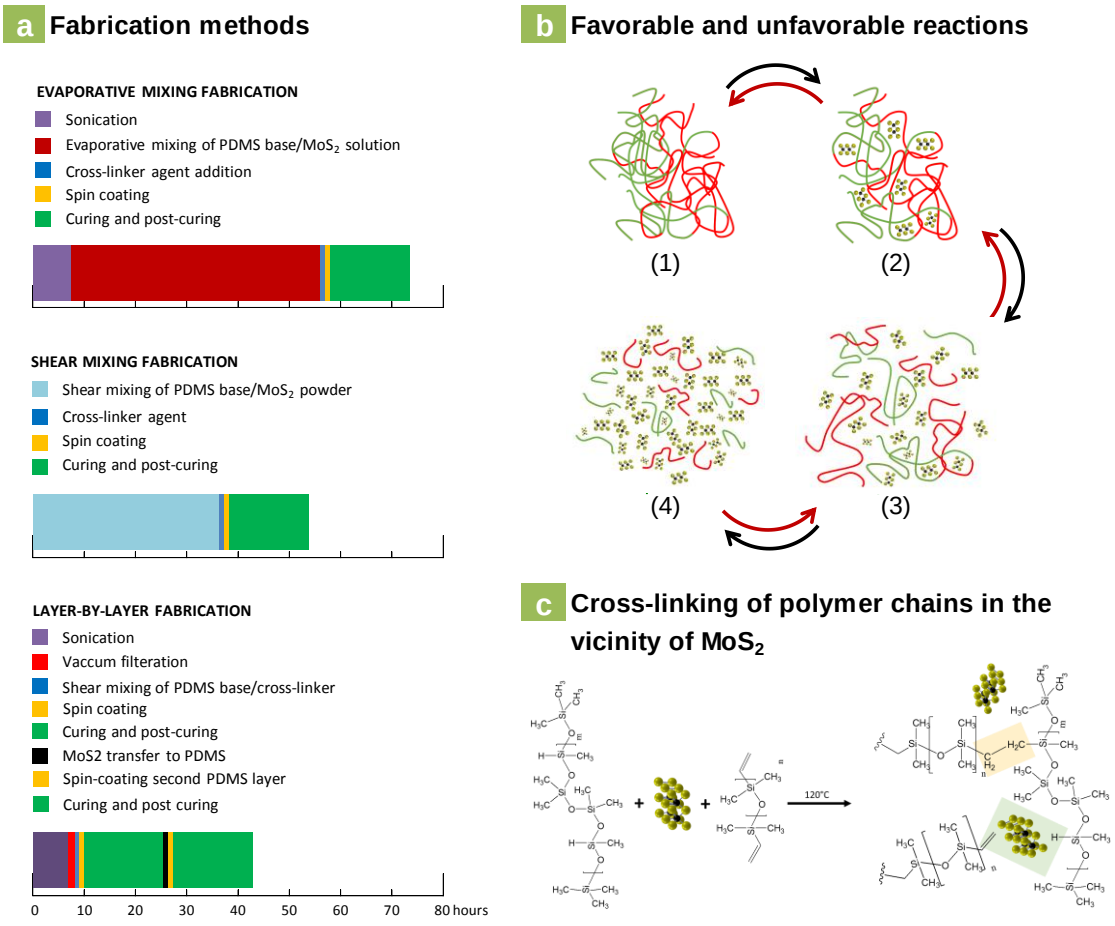

Figure 13- **(a)** sequences of three fabrication methods: layer-by-layer, shear mixing and evaporative mixing **(b)** Schematic of favorable and unfavorable reactions in these methods **(c)** Cross-linking of PDMS polymers

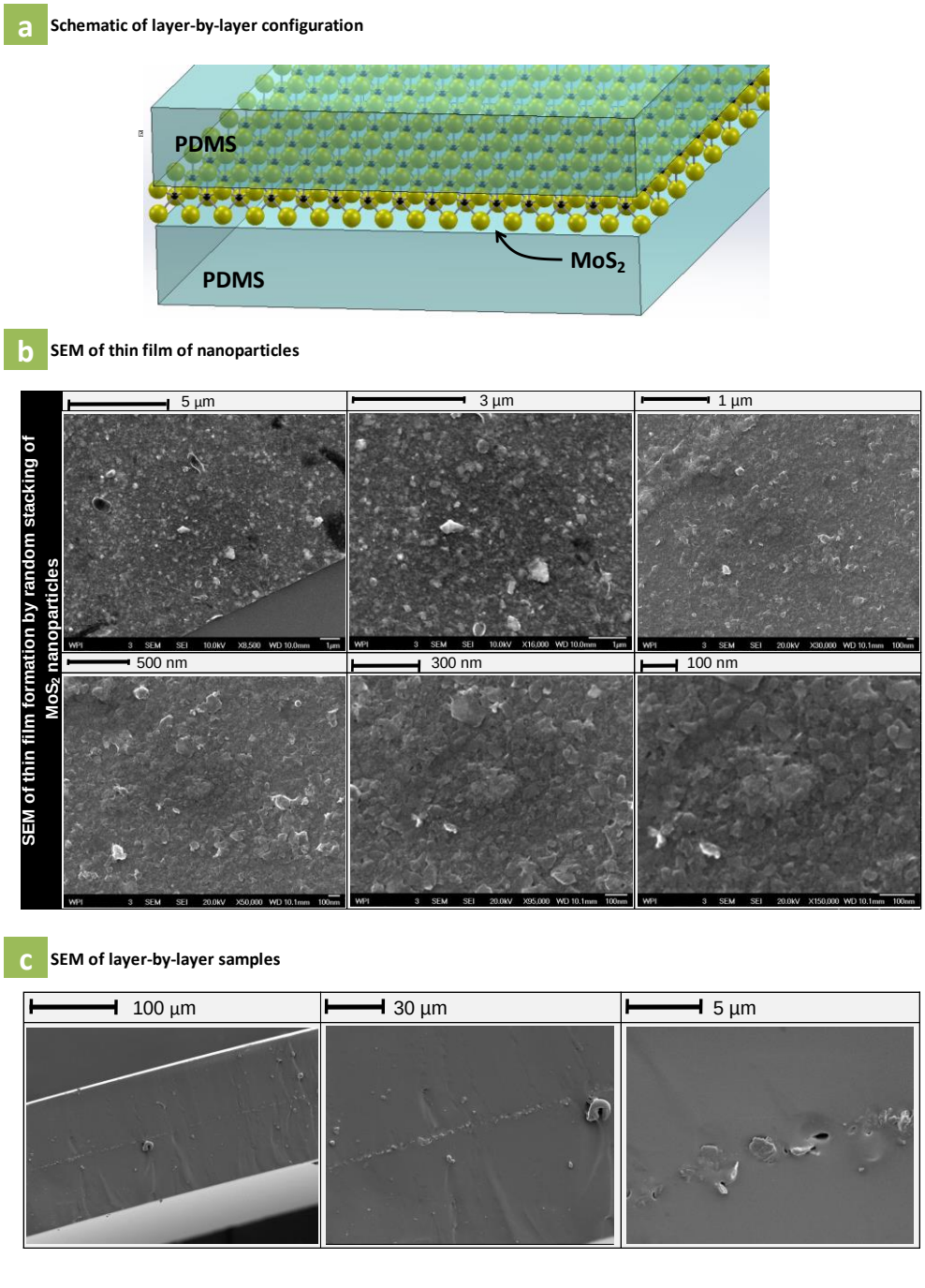

Figure 14- (a) LBL Samples schematic, (b) SEM of thin film of nanoparticles, and (c) cross section of a LBL samples.

Figure 15- Optical view of 80µm thin films of MoS_2/PDMS composites on glass slides (from pristine PDMS on left, to 0.1wt.% MoS_2/PDMS on right).

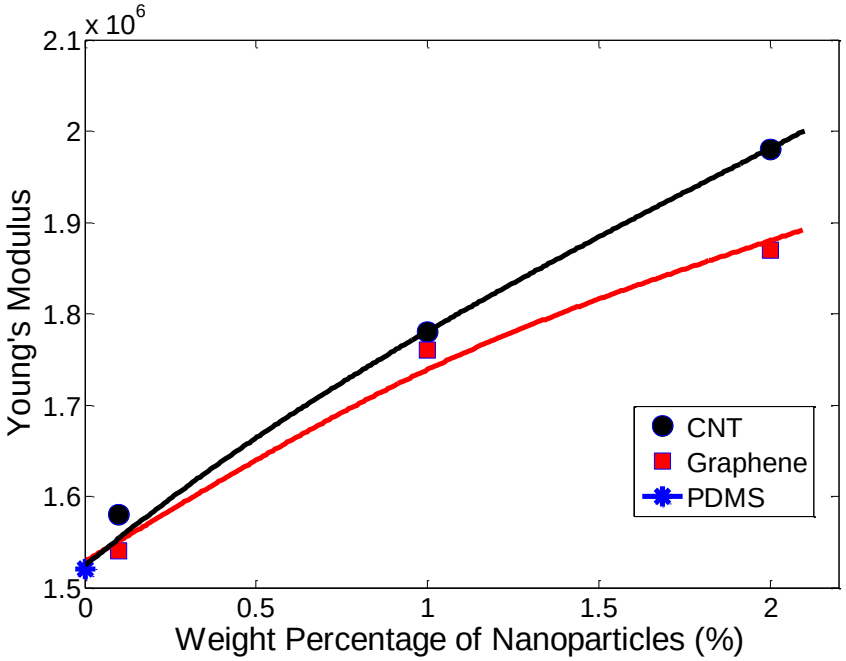

Figure 16- Young's modulus for different types of nanoparticles added to the PDMS host matrix.

The photoactuation mechanism is schematically depicted in Figure 17. Unstretched nanocomposite has random polymeric chain entanglement. When subjected to a pre-strain value, the entanglements become more oriented, thus lowering the entropy of the system. When subjected to illumination, MoS_2 nanoflakes inside the nanocomposites absorb optical energy and transduce it to heat, and consequently, mechanical work as expansion or contraction, based on the applied pre-strain. Photoactuation in these nanocomposites is a purely thermal mechanism and can correspond to a heat-induced actuation [22].

Figure 18a-d shows the photo-actuation results for a LBL sample at different weight percentage of MoS_2 nanoparticles, ranging from 0.1 to 5.0 wt.%. The test apparatus used in these experiments was previously reported by Rahneshin *et al.* and can be found there [22]. The applied pre-strain values to the nanocomposite ranges from zero to 70%. The results show that the photoactuation reaches a value of 44 kPa at 2wt% of MoS_2 nanoparticles and saturate for higher concentrations. The 2wt% threshold is the point where almost all of the incident optical energy is absorbed by nanoparticles, thus increasing the nanoparticle concentration further will not increase the photoactuation [90]. The change of actuation from expansion to contraction happens around pre-strain values of around 7%. At low level of pre-strains (0-7%), the MoS_2 actuators show reversible expansion, while at higher levels of pre-strain (9-70%), they exhibited reversible contraction. These results are in line with previous reports [22, 90].

Figure 18e shows the steady-state temperature profile along these samples at low and high pre-strain values. It is observed that increasing the strain value will decrease the temperature of the sample. This is because at higher pre-strain values, the amount of nanoparticles exposed to incident light is less as the length increases, thus resulting in lower light absorption and smaller temperature profile. Similar results were also observed for GNP-based actuators in the past [69]. Figure 19 shows the stability and reversibility of MoS_2 based actuators in long term.

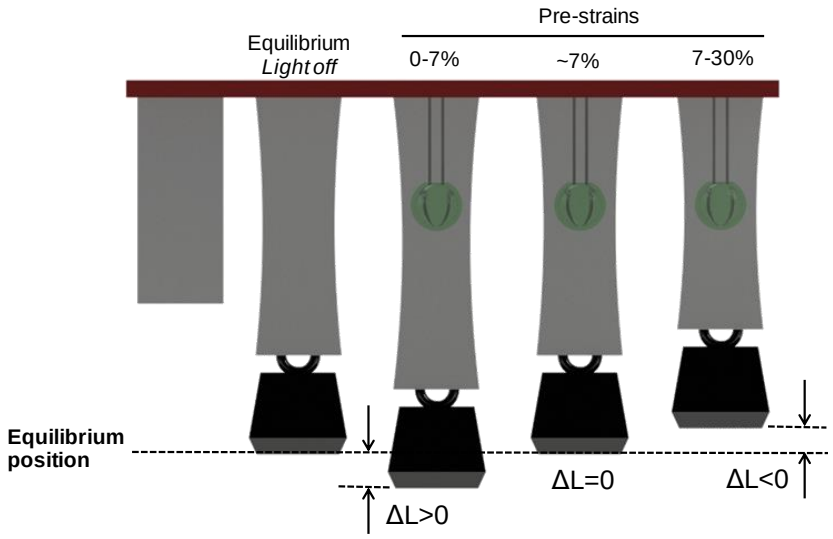

Figure 17- Schematic of photo-induced actuation of PDMS-based nanocomposites

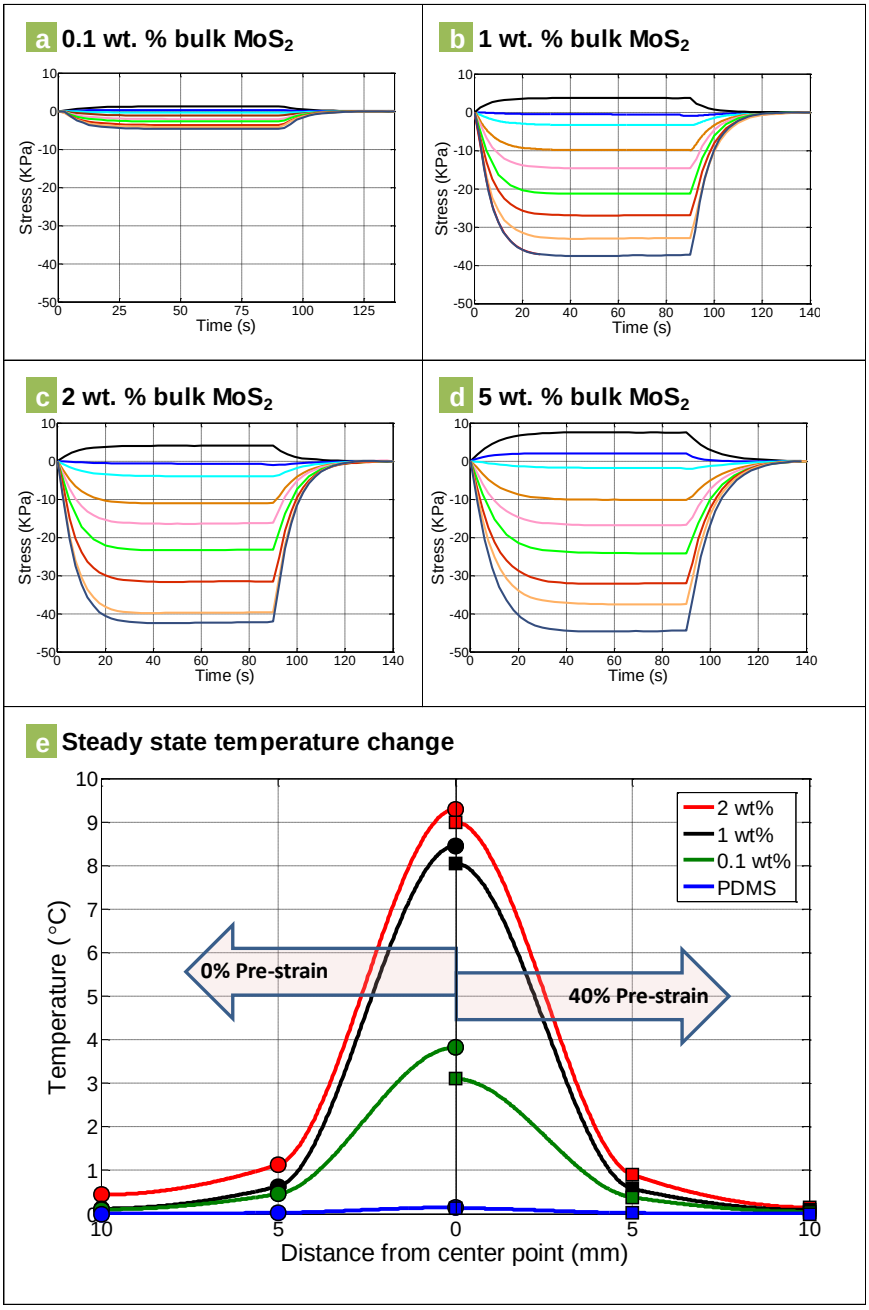

Figure 18- Photo response of bulk MoS_2 layer-by-layer actuators with change in pre-strain for different weight percentages: (a) 0.1 wt% (b) 1 wt% (c) 2 wt% (d) 5 wt%. From the top curve to the bottom, the pre-strain is changing in the sequence of 0, 5, 9, 20, 30, 40, 50, 60, and 70% respectively. (e) Steady state temperature along the samples due to light illumination; left side is when the sample is unstretched and right side is a 40% stretched sample.

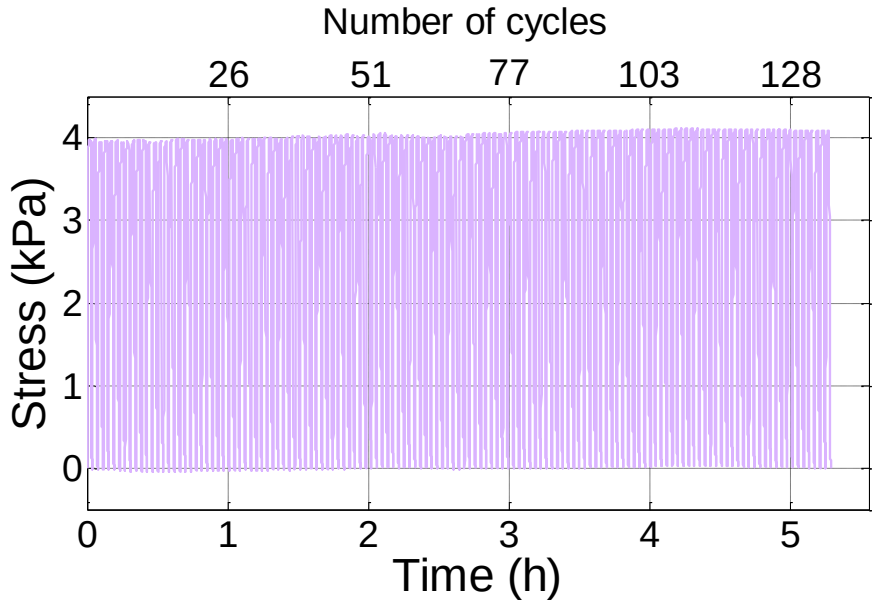

Figure 19- Long-term response of a bulk photo-actuator (the response is for a 1wt% LBL sample)

Unlike LBL samples, the photo-actuation in EM and SM samples does not saturate after a certain weight percentage of additives (Figure 20). Here the trend of photo-actuation is increasing at lower weight percentages of nanoparticles, and decreasing after reaching a certain threshold (around 1 wt.%). To better understand this, we should elaborate on the main factors affecting the value of photo-induced stress. The photo-actuation stress in nanoparticle-based polymeric actuators are mainly dependent on the amount of light absorption (MoS_2 part) and mechanical properties of the polymer host itself, especially its modulus of elasticity. In shear and evaporative mixed samples, as more MoS_2 nanoparticles are added to the host polymer, the former increases, while the latter decreases. The resultant effect of the two factors is an increase in photo-actuation in low weight percentage regimes, where the

photoabsorptions dominates the elasticity effects, and a decrease in the photo-induced stress for high weight percentages of MoS_2 additives, when the elasticity decrease outweighs the photoabsorption increase. Figure 20 depicts these effects. From the results of this figure, whilst the optical absorbance for LBL and EM samples are very close to each other, with LBL having a slightly higher value, SM samples show significantly lower optical absorbance. This is probably due to lower level of exfoliation of nanoparticles as well as lower dispersion in polymer host compared to the other two fabrication methods, as a result of directly mixing as-received nanopowder to the PDMS melt in SM method. This is in line with previous reports on the effects of exfoliation of nanoparticles on light absorption [22]. A slightly higher optical absorption observed in LBL samples compared to their EM counterparts shows the higher efficacy of surface distribution of additives compared to volumetric distribution. The deterioration of mechanical properties in EM and SM samples by increasing MoS_2 additives can be remedied by increasing the ratio of cross-linker to the polymer melt.

Figure 21 shows the effects of coss-linking ratio on the photo-induced stress in the fabricated samples at 40% pre-strain. By increasing the cross-linking ratio in EM and SM samples, the maximum amount of additives that can be added to the polymer host increases. This means higher weight percentages of nanoparticles can be achieved in nanocomposites before their mechanical properties start to deteriorate. This implies a higher photo-actuation can be reached with the same amount of MoS_2 additives,

especially for the higher weight percentage regimes. This is depicted in Figure 21a and b, as a shift in maxima of the curves to the right, due to increase in cross-linker.

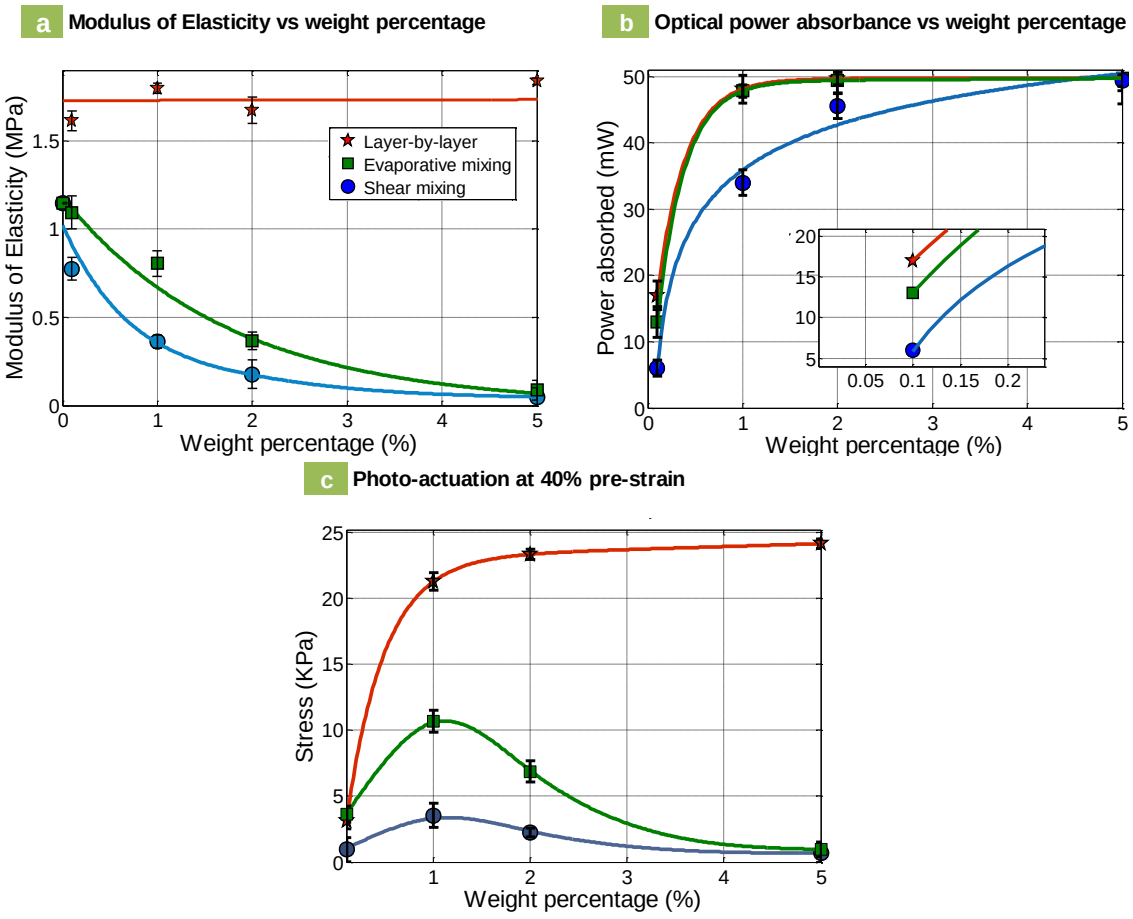

Figure 20- Optical to mechanical energy conversion and its determinative factors for different methods of fabrication: (a) Amount of optical power absorbed by photo-actuators with different fabrication methods (b) modulus of elasticity versus weight percentage for different fabrication methods (c) Photo-actuation for different fabrication methods (all data at 40% pre-strain)

In LBL samples, increasing the cross-linker leads to a decrease in the photo-actuation. Contrary to EM and SM samples, the polymer matrix in their LBL counterparts does not contain any MoS_2 additives, thus increasing the cross-linker ratio will only increase the stiffness (and modulus of elasticity) of the samples. As a result, the same amount of excitation energy results in a lower photo-induced stress due to higher stiffness of the sample.

The peak actuation versus cross-linking ratio for different fabrication methods is plotted in Figure 21d. From the results of this figure, in lower cross-linking ratios, LBL process is the most efficient fabrication method as it gives the highest optical to mechanical conversion rate. In higher cross-linking ratio, SM and EM methods gives better transduction ratio compared to LBL samples. These results imply that energy transduction in MoS_2 nanocomposites are not only a function of weight percentage of nanoparticles embedded in the polymer host matrix, but also a function of fabrication methods as well as cross-linking ratio. This extends the tunability properties of nanoparticle-based actuators beyond nanoparticles as the only tuning agents; meaning the mechanical response of these type of actuators can be engineered by both nanoparticles and the host polymer matrix itself.

3.4. DISCUSSION AND CONCLUSION

In this chapter, we investigated the effects of fabrication method and cross-linking ratio on the effectiveness of optical to mechanical energy transduction in bulk MoS_2 nanocomposite photo actuators. It was concluded that energy transduction in

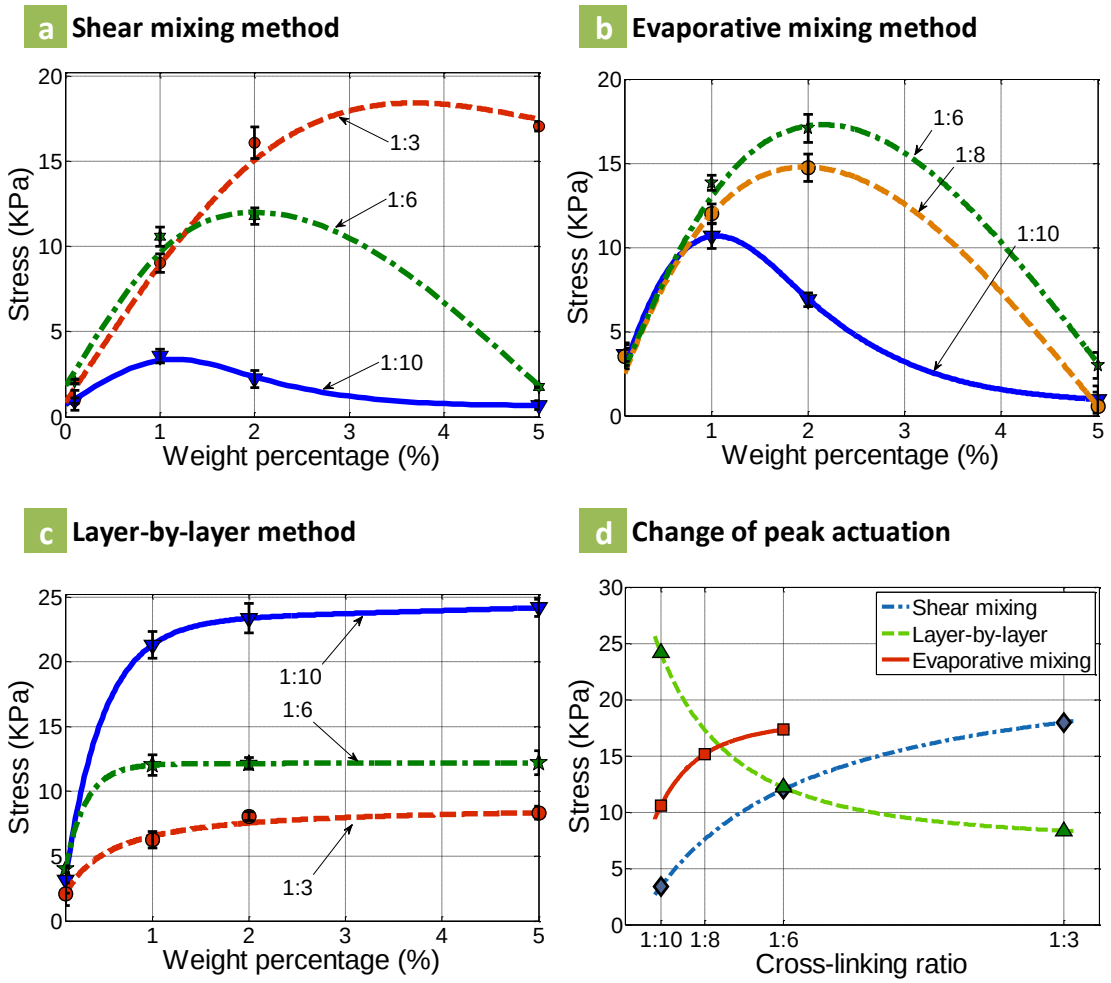

Figure 21- stress versus weight percentage for different cross-linking ratios in (a) shear-mixed (b) evaporative-mixed and (c) layer-by-layer samples. (d) Change of peak actuation as the cross-linking ratio changes in different fabrication methods

MoS_2-based nanocomposite actuators are not just function of weight percentage, but also function of fabrication method and cross-linking ratio of the base polymer. The presented results showed that at lower cross-linking ratios, layer by layer fabrication method gives the best energy conversion, whereas in higher cross-linking ratios shear and evaporative mixing offers higher optical to mechanical energy transduction. Higher

effectiveness of LBL method at lower cross-linking ratios compared to EM method is due to higher efficacy of surface distribution of additives compared to volumetric distribution. Amongst EM and SM fabrication methods, EM give better actuation in all cross-linking ratios, which is due to better dispersion achieved in EM fabricated samples compared to SM counterparts.

3.5. MATERIALS AND METHODS

3.5.1. NANOCOMPOSITE FABRICATION

MoS_2/PDMS actuators were fabricated based on three methods, namely layer-by-leyer (LBL), evaporative mixing (EM), and shear mixing (SM) fabrication. PDMS silicone elastomer obtained from Dow Corning (Sylgard 184) was used as the host matrix. PDMS is a two part solvent-free flexible silicone organic polymer in the form of a base compound with a separate hydrosilane curing agent that acts as a cross-linker. The term cross-linking ratio (CLR) used throughout the paper refers to the ratio of PDMS cross-linker to the base compound. In LBL method, the PDMS base is mixed in 1:10 ratio (or other ratios as referred in the text) to the cross-linker and then deposited on a glass slide. A standard spin coating process at 750 rpm for 90 seconds produces 80 μm thick film of PDMS on the glass slides. The films are then cured at 120°C for 20 minutes. A uniformly distributed layer of MoS_2 nanoparticles deposited on Whatman Anodic inorganic membrane is then transformed into this layer of PDMS. Another layer of PDMS is then spun coated and cured on top of the MoS_2 layer resulting in a layer-by-layer structure of about 160 μm thick. In EM method, MoS_2 nanoparticles are

added to ethanol solvent and then exfoliated using bath sonicator and centrifugation procedures. The exfoliated solution is then added to the PDMS based and stir mixed at 80C to evaporate the solvent while mixing the nanoparticles into the PDMS base. The resulted PDMS/ MoS_2 mixture is then spun coated on a glass slide at 700 rpm for 30 seconds resulting in 160 μm thick film of PDMS/ MoS_2 composite. The films are then cured at 120°C for 20 minutes. In SM method, MoS_2 nanoparticles in form of ultrafine powder is directly mixed with the PDMS base using a shear mixing process at 1000 rpm for 100 hours at room temperature. The resulted PDMS/ MoS_2 mixture is then spun coated on a glass slide at 700 rpm for 30 seconds resulting in 160 μm thick films. The films are then cured at 120°C for 20 minutes. The samples are then cut in 50 mm × 5 mm strips (30 mm of active test area with 10 mm on each side for fixture mounting).

3.5.2. STRESS TEST EXPERIMENTATION

The MoS_2/PDMS nanocomposite samples were mounted vertically between two clamps, with the bottom clamp attached to a weighted assembly (203 g), which in turn was placed on a high precision balance (A&D HR-250AZ), and the upper clamp attached to a linear actuator. The setup is shown in Chapter 4, as well as in [22]. The laser diode was placed ~80 mm away from the middle of the test sample in a way that the illumination is normal to the PDMS/MoS_2 surface. Photo-induced stress due to laser illumination and optical absorbance by MoS_2 agents resulted in a change in weight readings on the precision balance. Stress tests on each nanocomposite sample were directed with pre-strain values ranging from 0% to 70%. The test sequence in the developed LabVIEW program was 50 seconds of irradiation and 30 seconds of

relaxation repeated for five cycles. Engineering stress calculations were done by dividing the change in force due to light irradiation by the cross-sectional area of the composite samples.

CHAPTER 4
CHROMATIC MECHANICAL RESPONSE IN 2D LAYERED TRANSITION METAL DICHALCOGENIDE BASED NANOCOMPOSITES

In this chapter, using few layer 2H-MoS_2 nanosheets, layer by layer process of nanocomposite fabrication, and strain engineering, we demonstrate a reversible and chromatic mechanical response in MoS_2-nanocomposites between 405 nm to 808 nm with large stress release. The chromatic mechanical response originates from the *d* orbitals and is related to the strength of the direct exciton resonance A and B of the few layer 2H-MoS_2 affecting optical absorption and subsequent mechanical response of the nanocomposite. Applying uniaxial tensile strains to the semiconducting few-layer 2H-MoS_2 crystals in the nanocomposite resulted in spatially varying energy levels inside the nanocomposite that enhanced the broadband optical absorption up to 2.3 eV and subsequent mechanical response. The unique photomechanical response in 2H-MoS_2 based nanocomposites is a result of the rich *d* electron physics not available to nanocomposites based on *sp* bonded graphene and carbon nanotubes, as well as nanocomposite based on gold nanoparticles. The reversible strain dependent optical absorption and its rapid reversal suggest applications in broad range of energy conversion technologies that is not achievable using conventional thin film semiconductors.

4.1. INTRODUCTION

Establishing an optical-mechanical interface has been attempted since 1881 when A.G. Bell used the optoacoustic effect (photophone) to produce sound in a gas

with chopped beam of sun light [1]. However, only few materials exist that can convert photons of different wavelengths into mechanical motion that is large enough for practical import. Examples of materials that can directly convert light of different wavelengths into mechanical motion include range of organic photochromic compounds [4, 5], lead-lanthanum-zirconate-titanate (PLZT) ceramics [6], carbon nanotube polymer composites with selective chirality distributions [7] and more recently gold nanoparticle-polymer composites [8, 9]. Photomechanical actuators, motors, and micro-walking devices based on these materials have also been developed [4-8]. In general, most photomechanical actuators based on *sp* bonded carbon namely nanotube/graphene [10, 12, 14-16] are triggered mainly using near infra-red light and they do not exhibit wavelength selectivity. The mechanism in these nanocomposites is non-radiative decay of photons resulting in localized thermal effect [10, 12, 14-16]. While this field is growing rapidly with many applications reported from cantilever based photomechanical actuators [17], photo-mechanical micro-grippers with milli-second (ms) time constants [18], photo-thermal micro-pillar actuators [8], micro-mirrors with large rotational angles [19], nanopositioners [20], and plastic motors [7, 21], there is still need for a material design that is simple, versatile, reversible, wavelength selective, scalable and encompasses large optical to mechanical stress response that is based on their unique structure based tunability in optical absorption at different wavelengths. Phase separated nanocomposites based on TMDs prepared using a layer by layer processing may offer a new material design and approach for chromatic photomechanical actuation with large stress release owing to the van Hove singularities

in the joint density of states in the visible region of the electromagnetic spectrum that could be useful in designing future wavelength selective reconfigurable technologies [23].

Layered transition metal di chalcogenide (TMDs) provide intriguing opportunities to develop low cost, light and wavelength tunable stimuli responsive systems that are not possible with their conventional macroscopic counterparts. Due to the large optical absorption (~$10^7 m^{-1}$ [23]) in these materials, they are already being exploited for photocatalytic [24], photoluminescence [25], photo-transistors [26] and solar cell [27] applications. Bulk form of MoS_2 has an indirect band gap of ~1.29 eV [28] and single layer has a band gap of 1.9 eV [28]. The in-plane structure of MoS_2 is determined by strong covalent bonds resulting from the overlap between the *4d* and *3p* electron orbitals of Mo and S respectively [29]. The elastic modulus and the breaking strength of an ideal defect-free single-layer MoS_2 is expected to be $E^{2D}/9$, where E^{2D} is the in-plane stiffness as per the theory of rupture and flow in solids [29, 30]. The ultra-high strength is generated from the *p* orbitals of the chalcogen atoms which generate the σ bonds[23]. The large breaking strength (potentially capable of withstanding 25% strains) [31] together with large band gap and strong light-matter interaction in these materials has resulted in plethora of investigation on electronic, optical and magnetic properties of such layered ultra-thin semiconductors [31-37].

Utilizing exfoliated MoS_2, unique layer by layer process of nanocomposite fabrication, and strain engineering, here we present direct chromatic mechanical response in MoS_2-polymer nanocomposites between 405 nm-808 nm. The advantage of

our fabrication methods are as follows: 1) liquid phase exfoliation process resulting in high quality few layers with distinctive direct electron transition peaks, 2) phase separated nanocomposite due to the layer by layer processing, 3) access to the unique layer dependent optical absorption properties of MoS_2 layers inside the nanocomposite, 4) the reported architectures enables the creation of spatially varying bandgap profiles of 2-D nanomaterials and study of resonance Raman scattering as a function of number of layers and 5) the design enables scalable and flexible process for developing stimuli responsive and energy conversion devices at macro, micro and nanoscopic length scales utilizing different polymeric systems. Further, the layer-by-layer process as reported here enables preservation of the intrinsic properties and eliminates environmental degradation effects such as oxidation. The reported photomechanical actuators based on this process not only showed strong and wavelength dependent light matter interaction in the visible region of the electromagnetic spectrum, but also showed unexpected deviations. Not only, we found that the photo-thermal energy transduction from the MoS_2 crystals to the polymer chains is high resulting in high amplitudes of photomechanical actuation, it is also dependent on the wavelength of light and the photo-thermal actuation is better than graphene [20] and carbon nanotubes [10], which is unexpected given the low thermal conductivity of the MoS_2 additives (52 W/m-K for few-layer MoS_2 [234] versus 313W/m-K for graphene thin films [235]).

4.2. RESULTS

Figure 22 (a) presents the lattice schematic and Figure 22 (b) honeycomb structure of the semiconducting phase of 2H-MoS_2. In the 2H-MoS_2 lattice, each Mo

atom is located at the center of a trigonal prism created by six S atoms. The lattice constant of 2H-MoS_2 was reported to be: a=b=3.14 Å [236] and c=12.3 Å [237]. A single layer of 2H-MoS_2 is ~0.65 nm thick and can be exfoliated using scotch tape [61] and liquid phase exfoliation techniques [238].

The High Resolution Transmission Electron Micrograph (HRTEM) of the MoS_2 structure is presented in Figure 22 (c) with atoms of S and Mo indicated also showing the honey comb structure in (Figure 22b). The distances a_1, a_2 and a_3 measured from this image are close to the 2.8 Å value of the Mo–Mo interatomic distances in 2H-MoS_2 [239]. The insert in Figure 22 (c) presents the Fast Fourier Transform (FFT) of the HRTEM image indexing the crystallographic planes of the single layer 2H-MoS_2. Small distortions and apparent non-uniform intensity distribution of the spots in FFT are due to a slight tilt of the flake with respect to the electron beam. The bulk form of MoS_2 with an indirect band gap of ~1.29 eV [28] (Figure 22d), the photon absorption process is mainly dominated by electronic polarization and as a result, no wavelength selective optical absorption is observed, since no significant electronic transition happens from the valance to the conduction band. However, as the layers decrease in MoS_2, the indirect band gap becomes so large that the material changes into a direct band gap semiconductor with E_g~1.9 eV (Figure 22e) [28] with intrinsic photoluminescence [25]. The low energy electronic states are dominated by $4d_{z^2-r^2}$, $4d_{xy}$, and $4d_{x^2-y^2}$ orbitals of Mo atoms [240]. MoS_2 few layers are also known to have significant quantum yield (10,000 folds increase in luminescence) compared to bulk [28]. MoS_2 show strong peak and enhanced light-matter interaction in the visible region

of the electromagnetic spectrum due to the van Hove singularities in the density of states [23].

The starting point for our photomechanical actuators is the liquid phase exfoliation of MoS_2 [238] powders in ethanol followed by centrifugation and separation of the layers as presented in Figure 23(a). Three types of samples were prepared namely (a) bulk: sonicated for 7 hours and no centrifugation (b) intermediate: sonicated for 50 hours and centrifuged for 45-120 minutes and layers separated (c) few layers: well characterized commercially available few layers in ethanol was purchased.

The samples were characterized for number of layers using an SEM (Figure 23 (b-d)) and an AFM (Figure 24). It is observed that bulk samples had morphology of flakes (Figure 23b), while the intermediate was well separated crystals. The crystals were also large measuring almost 1 μm in size (Figure 23c) and the few layers were small in size measuring 100 nm in diameter (Figure 23d).

Further characterization for number of layers was done using an AFM (Figure 24). Three different regions were identified based on the Z-axis height measurements of the flakes using an AFM. Based on the number of layers, the suspensions were classified as bulk (100-500 layers), intermediate (10-30 layers) and few layers (1-6 layers) and henceforth the films and the nanocomposites made using these suspensions will be addressed as such throughout the paper. These suspensions were then filtered using vacuum filtration using an Anodisc membrane to yield MoS_2 thin films (Figure 23a, bottom row), with the same mass per area of the membrane (please see materials

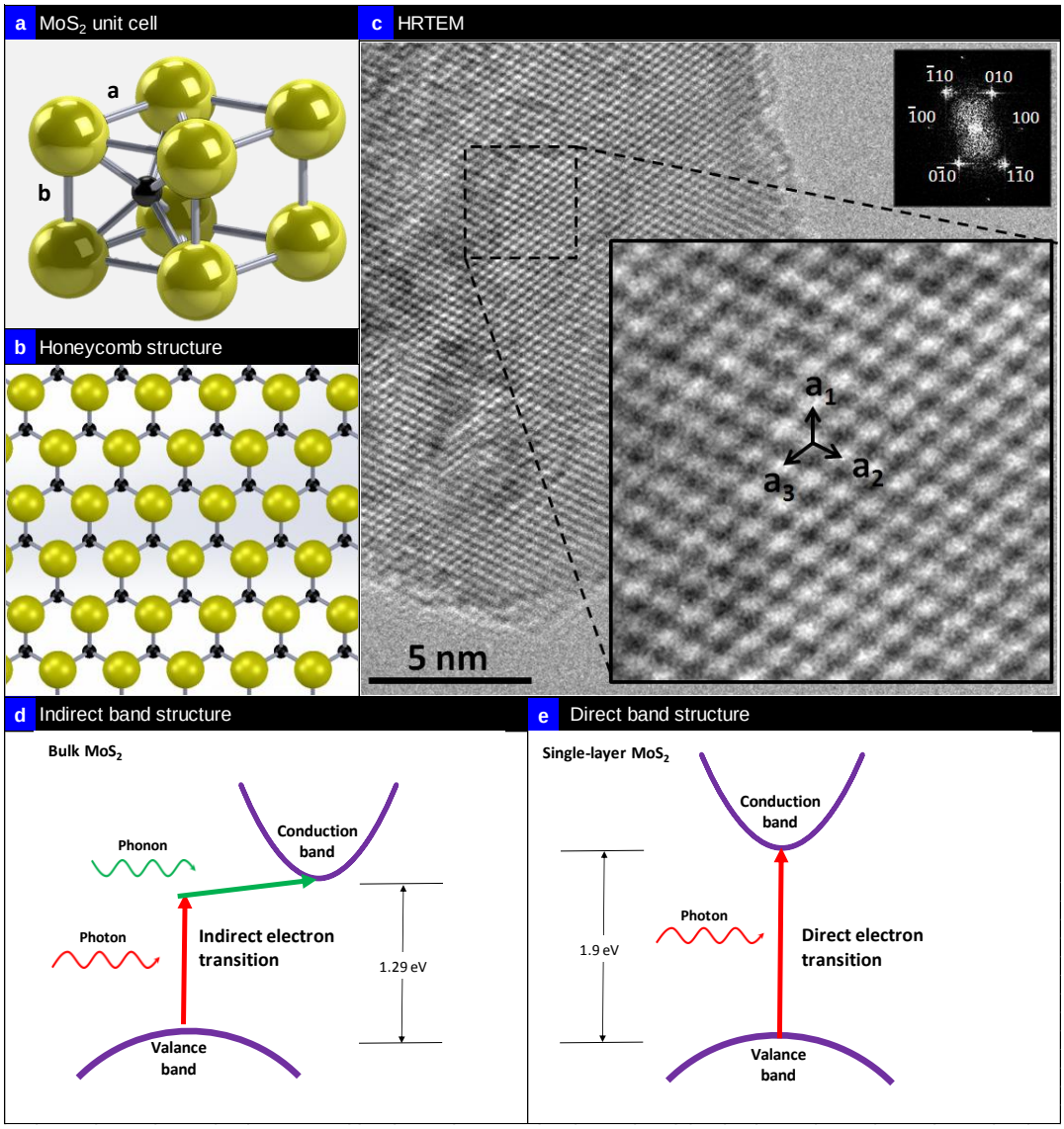

Figure 22- Crystal Structure: (a) Crystal structure of MoS_2: S atoms in gold and Mo in black with unit cell parameter a and b, (b) top view of a single-layer MoS_2 structure in honeycomb shape; (c) HRTEM of 2H-MoS_2 (top insert is the Fast Fourier Transform (FFT) image showing the planes; slight distortion is due to the tilting of the flake in the TEM; a_1, a_2 and a_3 presented HRTEM image is the Mo-Mo interatomic distance of 2.8 Å for 2H-MoS_2 (d-e) schematic of the indirect electron transition in bulk MoS_2 and direct electron transition in single layer MoS_2 respectively.

and methods for sample preparation). It can be observed the thin film samples on membrane have characteristic colors namely few layer films were deep green (1-6 layers), intermediate films were light green (10-30 layers) and bulk samples were grey (100-500 layers) as presented (Figure 23a, bottom row). This suggests that the films themselves are capable of acting as optical filters at these low weight fractions.

Figure 23 (e) presents the optical absorption spectroscopy of bulk, intermediate and few layer solutions using Lambert-Beer's law characterized by $A/l = \alpha C$, where A/l is the absorbance per length, α is the extinction coefficient, and C is the concentration. The A/l scaled linearly with C provided the values for the three types of solution. The calculated extinction coefficient for bulk $\alpha_{bulk} = 890.2$ $(mg/ml)^{-1}$ m^{-1}; for intermediate layer $\alpha_{intermediate\text{-}layer} = 1133.8$ $(mg/ml)^{-1}$ m^{-1}; and $\alpha_{few\text{-}layer} = 2230$ $(mg/ml)^{-1}$ m^{-1}. The extinction coefficient increases with decrease in number of layers. Since extinction is a measure of absorption and scattering, and since the few layer nanoparticles were small (<100 nm), the large values of extinction is a result of optical absorption in the semiconducting few layers.

Figure 23 (f) presents the absorbance versus the wavelength of the three different solutions. It is seen that absorbance is high (25 times higher than bulk) for the few layer solution. The two peaks marked A (1.9 eV) and B (2.1 eV) correspond to the direct exciton transition at the *K* point [241]. The peaks are assigned to excitons involving the conduction band and the two valence bands (which are split due to spin orbit coupling) near the *K* point [241]. The absorbance of the intermediate and the bulk solution was small. The insert in Figure 23 (e) presents the magnified absorbance of the

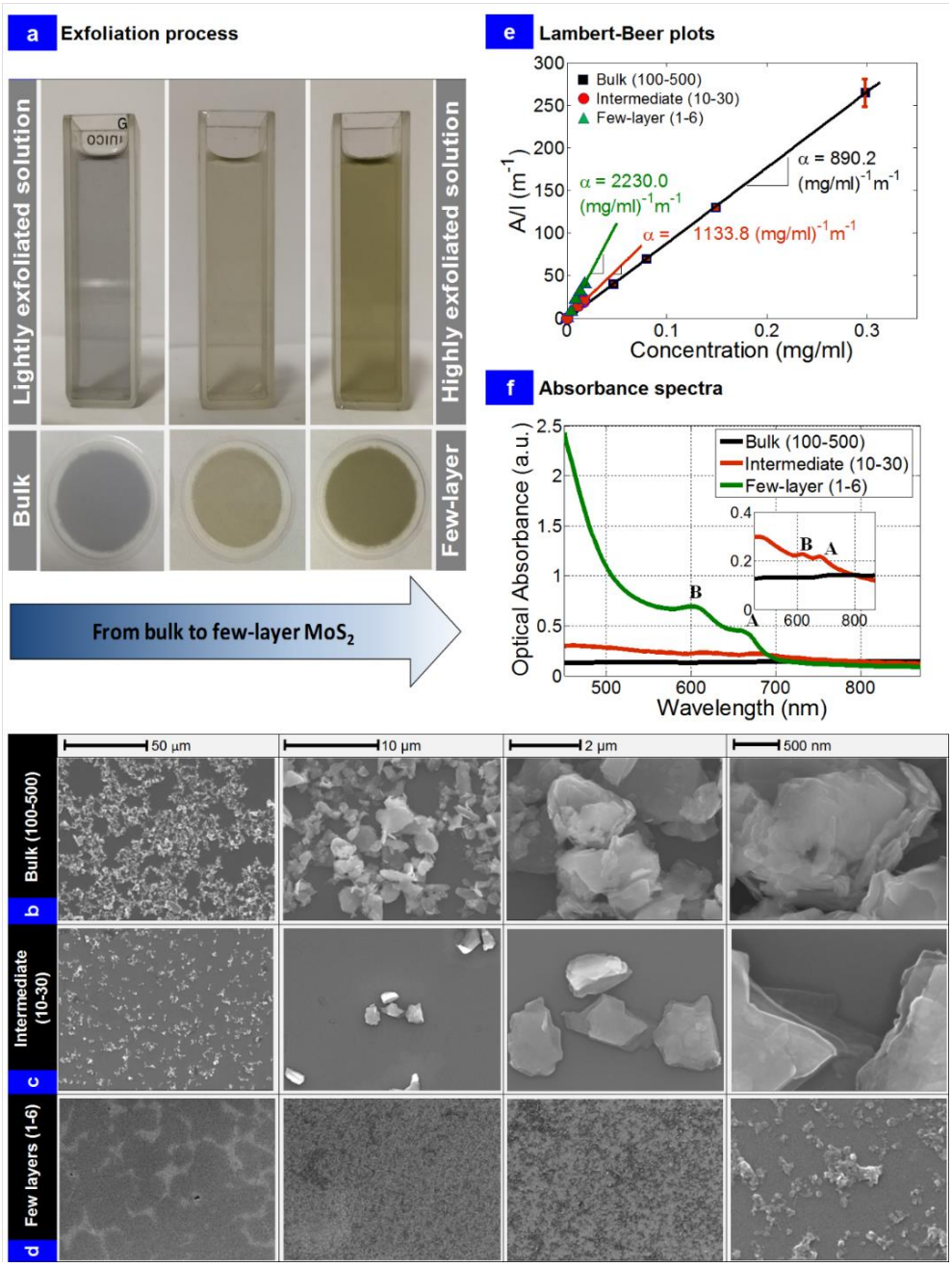

Figure 23- Liquid Phase Exfoliation and Characterization: (a) Suspensions after liquid phase exfoliation in bath sonicator followed by centrifugation and separation of layers into 3 distinct entities namely bulk (left: 100-500 layers), intermediate (middle: 10-30 layers) and few layers (right: 1-6 layers); bottom row corresponds to the bulk, intermediate and few layer films formed on an anodisc membrane from the exfoliated suspensions (b-d) SEM images of the three different suspensions showing the different

morphology of the samples. The bulk were aggregates with particle size greater than 1µm, the intermediate samples were crystals with layered architecture with particle size ~1µm and the few layer samples with layered crystals ~100 nm in particle size; (e) Lambert-Beer plots characterized by $A/l = \alpha C$ provides the extinction coefficient for all the three types of samples; (f) UV-Visible spectroscopy of the bulk, intermediate and few layer samples in solution. The peaks marked A and B correspond to the direct exciton transition peaks at the "*K*" point.

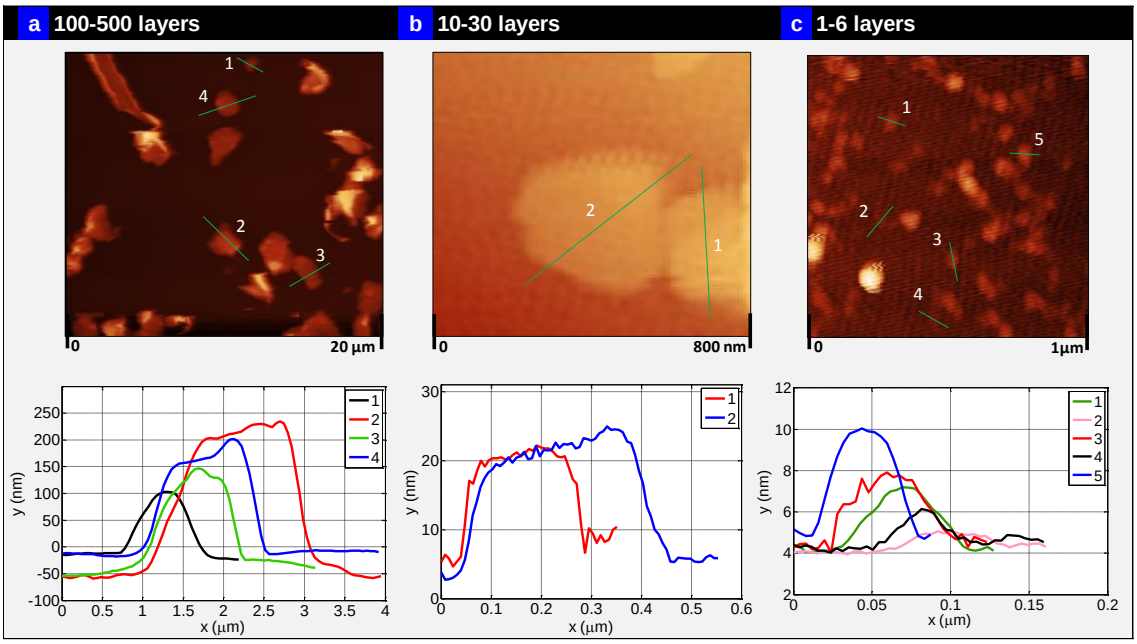

Figure 24- Atomic force microscopy images and *Z* axis height measurements of the flakes for three different levels of liquid phase exfoliation.

intermediate and the bulk solutions. The A and B peaks are also evident in the intermediate solution. The bulk solution showed no peaks with negligible absorption (suggesting no direct electron transition). The negligible absorption is a result of the

high transmittance of light through the sample and geometric scattering of light due to the particle size of the bulk (>1 μm) and intermediate MoS_2 (~1 μm) samples in solution.

Figure 25 (a) presents the nanocomposites prepared using layer by layer (LBL) process consisting of steps namely: sonication, vacuum filtration of exfoliated MoS_2 suspensions, shear mixing of PDMS base with cross-linkers, formation of layer of cross-linked poly dimethyl siloxane (PDMS) on glass substrate using spin coating, curing and post-curing of PDMS, MoS_2 transfer to the PDMS and spin coating another identical second layer of PDMS on to the transferred MoS_2 layer and crosslinking and final step of curing and post-cure relaxation for 12 hours. The MoS_2 concentrations for all the three samples were maintained at 0.1 wt. % and the final nanocomposites are presented in Figure 25 (b). The top and bottom PDMS layer were identical in weight and thickness. All the samples were identical in mass. Following preparation, the samples were cut into 50 mm x 5 mm strips for testing (Figure 25 (b)).

Figure 25 (c) presents the optical absorbance of the three types of nanocomposites measured using UV-Visible spectroscopy. The optical absorbance of the nanocomposites were similar to that of the solution samples as presented in Figure 25 (f) except the normalized absorbance of the Y-axis was lower. The absorbance of neat PDMS was measured and subtracted from the presented data on the nanocomposites. The few-layer based nanocomposites showed the strongest optical absorbance (300 nm to 750 nm) compared to their intermediate and bulk counterparts. The characteristic peak A (~1.9 eV) and B (~2.1 eV) is seen suggesting existence of a

direct bandgap inside the nanocomposite. Again, the absorbance of the intermediate and the bulk nanocomposites was small similar to solution. This suggest high transmittance of light through the sample and geometric scattering due to particle size that caused the lowered optical absorbance in intermediate and bulk nanocomposites at these low weight fractions. It should be noted that the absorbance was exactly the same at higher wavelengths (>800 nm, below the bandgap of the few-layer) for all the three nanocomposite samples suggesting same weight fractions of the MoS_2 additives and similar levels of scattering in all the nanocomposites. The insert in Figure 25 (c) presents the magnified absorbance of the intermediate and the bulk nanocomposites. The A and B peaks are also evident in the intermediate nanocomposite. The bulk nanocomposite showed no characteristic A and B peaks with negligible absorption (suggesting no direct electron transition in bulk). Since the extinction of the few-layer samples was observed to be high, this suggest strong absorption of light in these nanocomposites (300 nm to 750 nm). However, for intermediate and bulk nanocomposites, the absorbance was low due to strong transmission of light through the sample and geometric scattering at these low weight fractions. Photomechanical testing was done in an automated test system (Figure 25d) and the details of the testing is reported elsewhere [16].

In order to better understand the internal lattice dynamics in bulk, intermediate and few layer nanocomposites, we performed resonant Raman scattering studies of our nanocomposites at room temperature as presented in Figure 26. This is the first such measurement performed directly on the nanocomposite, which enables us to non-

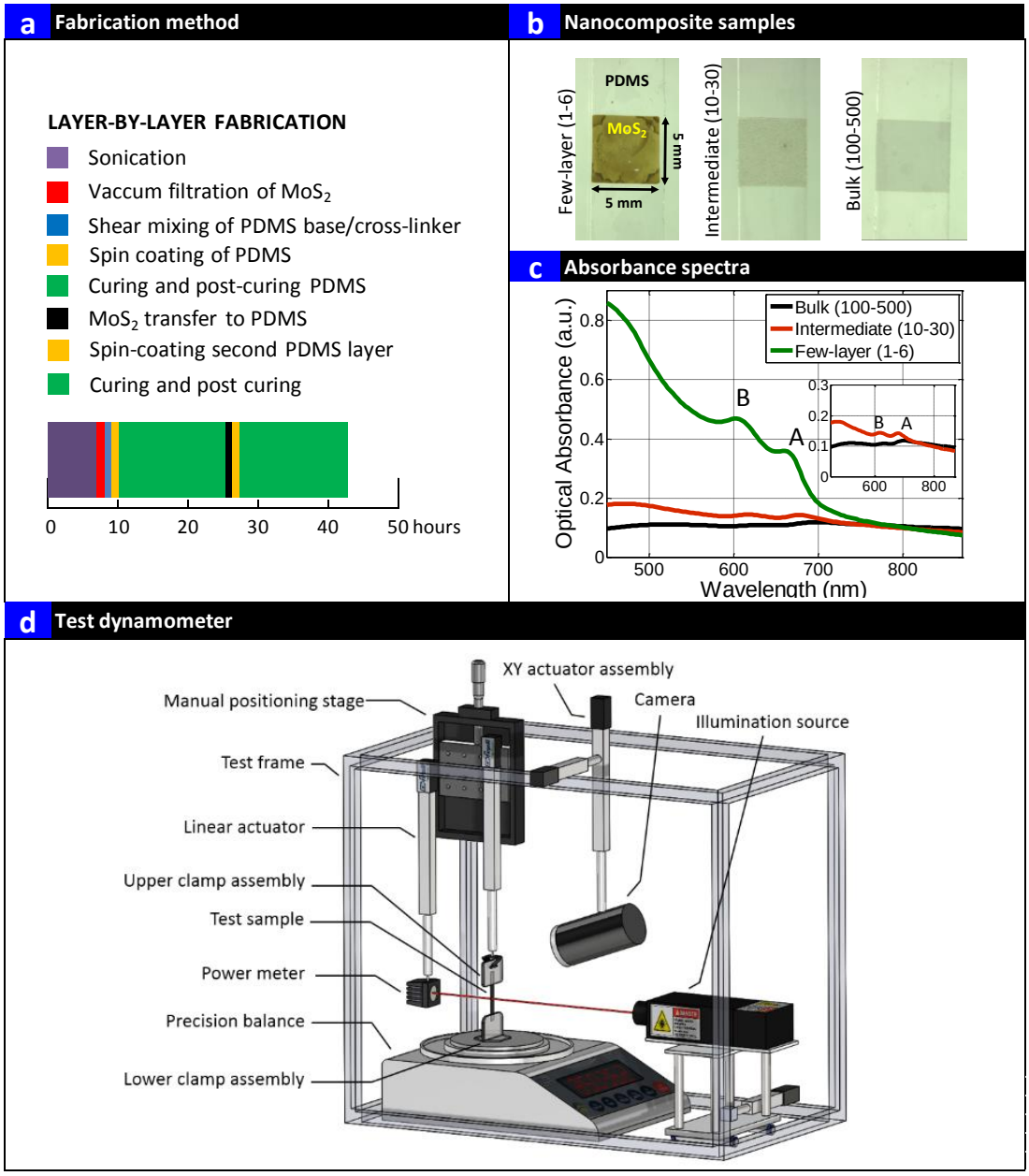

Figure 25- Layer by Layer Assembly of Nanocomposites and Testing: (a) Layer by Layer Fabrication Process; (b) Final nanocomposites formed using layer by layer process; (c) UV-Visible spectroscopy of the bulk, intermediate and few layer nanocomposites; insert is the magnified image of the optical absorbance of bulk and intermediate nanocomposites (d) Schematic of the photomechanical test assembly.

destructively understand the internal dynamics between bulk, intermediate and few layer samples.

Significant changes in the shape of lines are observed between bulk, intermediate and few layer samples in Figure 26 (a) and Figure 26 (b). While the first order E^1_{2g} (~384 cm^{-1}) and A_{1g} (~409 cm^{-1}) peaks, which correspond to the in-plane and out-of-plane vibrational modes of the S atoms with respect to the Mo atoms, are dominant features of the non-resonant Raman spectrum of 2H-MoS_2 [242], these peaks are accompanied by a number of intense second-order Raman scattering process peaks enhanced by strong electron-phonon interactions in the resonant spectrum (Figure 26a).

In the bulk nanocomposite, the strongest spectral feature is a broad line located around 460 cm^{-1} that consists of E_{1g} +XA (~466 cm^{-1}) peak (XA is a transverse phonon from the vicinity of M point of the Brillouin zone) [243, 244] as well as of L_1 (~441 cm^{-1}) peak assigned to a second-order band (possibly $A_{1g}(\Gamma) + E^2_{2g}(\Gamma)$), L_2 (~455 cm^{-1}) peak to a van Hove singularity between K and M and L_3 (~460 cm^{-1}) peak due to LA′ phonon from the vicinity of M point [245]. Thus in bulk, the existence of van Hove singularity is expected to increase optical absorption in the visible region of the electromagnetic spectrum with increase in MoS_2 additives. Other significant lower-frequency lines are the “b” (~420 cm^{-1}) peak due to a two-phonon Raman process involving the emission of a dispersive quasi-acoustic phonon and an optical E^2_{1u} phonon along the c-axis, the $B_{1u}(\Gamma)$ (~404 cm^{-1}) mode, which is the Davydov couple of the A_{1g} (Γ) mode and the “c” (~380 cm^{-1}) peak due to a dispersionless E^2_{1u} (Γ) phonon [246]. In addition, several lines are also observed in the higher-energy region between

550 cm^{-1} and 700 cm^{-1}(Figure 26 (b)), including the E_{1g}(M)+2XA (~644 cm^{-1}) peak [243], the A_{1g}(M)+LA(M) (~466 cm^{-1}) peak, E^1_{2g}(M)+LA(M) (~600 cm^{-1}) peak and $2E_{1g}(\Gamma)$ (~572 cm^{-1}) peak.

Several significant changes of the spectrum are observed with the decrease in the number of layers, especially for the few layer nanocomposite. First, the "b" peak shows higher intensity which is an indicative of the phonon involved that has a wave vector along the c-axis. The "c" and $B_{1u}(\Gamma)$ peaks are also seen to increase in intensity. Both these peaks are Raman-inactive and their appearance suggests symmetry breaking [246]. Since the PDMS spectra were subtracted from the presented measurements, the peaks are indicative of the arrangement and interaction of the MoS_2 atoms between the layers arranged in the few layer sample.

The decrease in the number of layers of the MoS_2 crystal leads also to significant increase of the L_1 and L_2 peaks (Figure 26 a) in the few layer nanocomposites. Furthermore, in the higher-energy region of this sample, broad peaks labeled in Figure 26 (b) as P_1, P_2 and P_3, located at ~566 cm^{-1}, ~592 $cm^{-1}$and ~632 cm^{-1}, respectively, are seen to appear. While there are a number of theoretically-predicted modes in the vicinity of these frequencies [245], the correct identification and assignment will require future detailed studies. All our observations are in line with recently reported studies on resonant Raman scattering in 2H-MoS_2 [242-244]. The change in line shape, intensity and peaks with decrease in number of layers suggest strong electron-phonon coupling and one can access the change in electronic properties with strains of these higher order peaks using this layer-by-layer process. While such

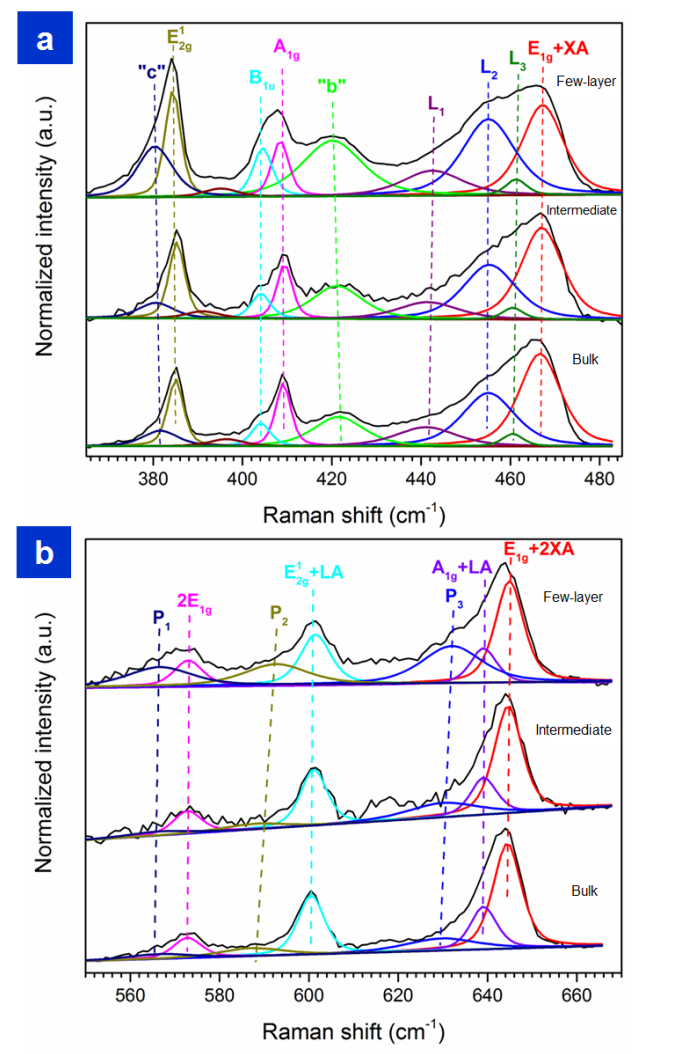

Figure 26- Raman Scattering: Resonant Raman Spectroscopy of bulk, intermediate and few layer nanocomposites.

studies are beyond the scope of the present paper which is the chromatic mechanical response in MoS_2 based nanocomposites, nevertheless, it throws open new investigation into resonant Raman spectroscopy with strains. The resonant Raman scattering experiments confirm the structure is that of 2H-MoS_2, differences in peaks with the

number of layers in the nanocomposites, presence of van Hove singularities, and strong electron-phonon coupling, all of which can affect photomechanical actuation and energy applications.

Photomechanical responsivity testing on the MoS_2 nanocomposites is presented in Figure 27. Figure 27 (a) presents the transmitted power through the bulk nanocomposites and the corresponding photomechanical responsivity (Figure 27b). For bulk nanocomposites, it is seen that power transmitted through the sample is similar irrespective of wavelength (Figure 27a). They also exhibited similar photo-mechanical actuation stress at all wavelengths (Figure 27b). A photomechanical stress value of ~0.6 kPa was measured. The large light transmission and geometric scattering of light resulted in low absorption and wavelength insensitive mechanical response. In these nanocomposites, the photo-mechanical actuation is due to the non-radiative decay of photons resulting in similar thermal response at all wavelengths. Figure 27 (c) presents the power transmitted in the intermediate nanocomposites (10-30 layers) samples that suggest weak but selective absorption of light of different wavelengths. The corresponding photomechanical stress (Figure 27d) is also dependent on the wavelength of light and ~4.5 times larger than bulk nanocomposites (Figure 27 (b)). The selective transmittance of light in these intermediate samples can be traced to the direct exciton peaks A and B indicated in magnified insert in Figure 25(c). These two peaks were observed but weak in the intermediate samples. Correspondingly, the optical absorption and photomechanical response was also wavelength selective but the amplitude of mechanical response was small. Moving on to the few layer

nanocomposites (Figure 27 (e)), the power transmitted through the sample is observed to be highly dependent on the wavelength of light. Again, this can be related to the strength of the direct exciton peak A and B in the nanocomposites in Figure 25 (c). It is seen that the most of the IR is transmitted (~72%) (1.53 eV) through the sample whereas most of the UV (97%) is absorbed (3.0613 eV). The results suggest a direct bandgap dependent absorption in the nanocomposite due to the unique structure of the MoS_2 few layers.

Figure 27 (f) presents the photomechanical actuation of the few layer (1-6 layers) nanocomposites. One can observe not only wavelength dependence but extraordinary increase in mechanical stress as large as 10 times (~5.5 kPa) at 405 nm wavelengths (Figure 27 f). The photomechanical stress of few layer nanocomposites at 808 nm (below the bandgap) was also similar to bulk suggesting no significant optical absorption. The photoactuation stress at 640 nm and 532 nm follow the same trend as the optical absorption. The mechanical response is seen to be strong and follows the light absorption at 640 nm, 532 nm and 405 nm. The mechanical response is also reversible as when the light is switched off irrespective of the wavelength of light, the system comes back to its original state or reversible switching with one type of wavelength. To compare, in Azobenzene chromophores, reversible switching is accomplished with two different wavelengths (420 nm and 365 nm) between an extended *trans* and a shorter *cis* configuration [3].

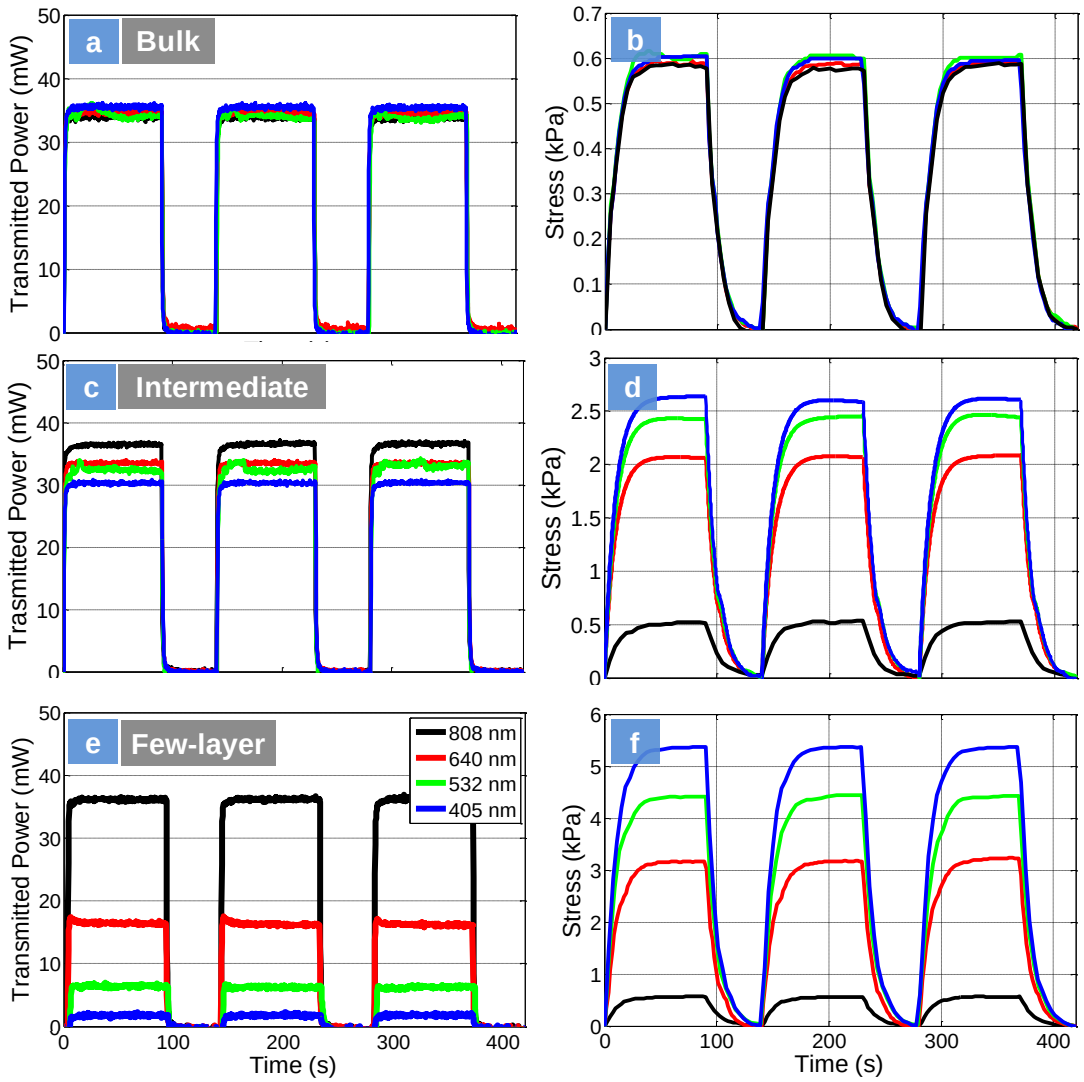

Figure 27- Photomechanical Actuation: Power transmitted through the sample and the corresponding photomechanical actuation of nanocomposites at different wavelength of light respectively: (a-b) bulk consisting of 100-500 layers; (c-d) intermediate consisting of 10-30 layers and (e-f) few layers consisting of 1-6 layers. The samples were all 0.1 wt. % nanocomposites using LBL process. No pre-strains were applied for these experiments.

Scattering of light due to particle size larger than wavelength of light in bulk nanocomposites is a plausible explanation for decreased optical absorbance and wavelength insensitive photomechanical actuation. The lower extinction in bulk coupled with smaller absorption at low weight fractions suggest scattering in these materials affect optical absorbance and subsequent amplitude of photomechanical actuation. However, low weight fractions and strong light transmission suggest scattering may not be dominant even in bulk. Further experiments were conducted to understand how optical absorbance, scattering and photomechanical response change with increase in weight fractions of bulk MoS_2.

Figure 28 presents the photomechanical actuation of bulk nanocomposites with increasing weight percentage of MoS_2 additive. The transmitted power is also plotted on the same graph. An exponential decrease in transmittance is seen between 0.1 wt. % and 1 wt. % at all wavelengths. Above 1 wt. %, the power transmitted is almost zero suggesting strong light absorption. The rise in photomechanical actuation follows the same exact trend as the power absorbed by the sample. If all the power was scattered, this would result in negligible photomechanical stress which is not observed. The insert in this Figure 28 presents the absorbance plot of the bulk nanocomposites with increase in weight fraction of MoS_2 additive. The A/l is seen to follow the photomechanical actuation stress amplitudes. The extinction, absorbance and photomechanical stress amplitudes all increase with increase in MoS_2 additive for bulk. Above 1 wt. % non-linear behavior is noted and saturation of optical absorption and photomechanical response.

Thus we see two regimes in bulk nanocomposites. At low weight percentage of bulk MoS_2 additive (~0.1 wt. %), high light transmission through the sample and geometric scattering cause lower photomechanical response. However, as the weight fractions of bulk MoS_2 additive increases in the nanocomposite, optical absorption becomes dominant resulting in significant increase in photomechanical response. All the bulk samples irrespective of the weight fractions were insensitive to the wavelength of light suggesting the chromatic mechanical response is unique to the few layer semiconducting structure of the 2H-MoS_2 originating in the *d* orbitals. The direct exciton transition peaks A and B is the origin of the chromatic mechanical response and the strength of the A and B peaks determines the power transmitted and the overall mechanical response in few layer and intermediate nanocomposites. Thus, this is a unique photomechanical effect not seen in any other type of actuator. Thus the origin of the photomechanical effect is as a result of optical absorption aided by the unique structure of the additive and its integration with the polymer chains. This is also evident from past reports in this area of carbon nanotube and graphene based photomechanical actuators, where strong sp^2 bonds of nanocarbons resulted in large amplitudes of photomechanical response [20]. In single layer graphene, all bonds are strong sp^2covalent bonds that result in high intrinsic thermal conductivity, while reduced graphene oxide is a mixture of sp^2 and sp^3 bonds that resulted in smaller photomechanical actuation compared to pristine graphene. Finally, amorphous carbon and diamond-like carbon contain a large fraction of sp^3 bonds that lower thermal conductivity and photomechanical actuation [20]. The large IR absorption in nanotubes

is as a result of the van Hove singularity in the density of states. The optical absorption in graphene is dominated by the interband transitions. In MoS_2 chromatic absorption is as a result of the *d* orbitals.

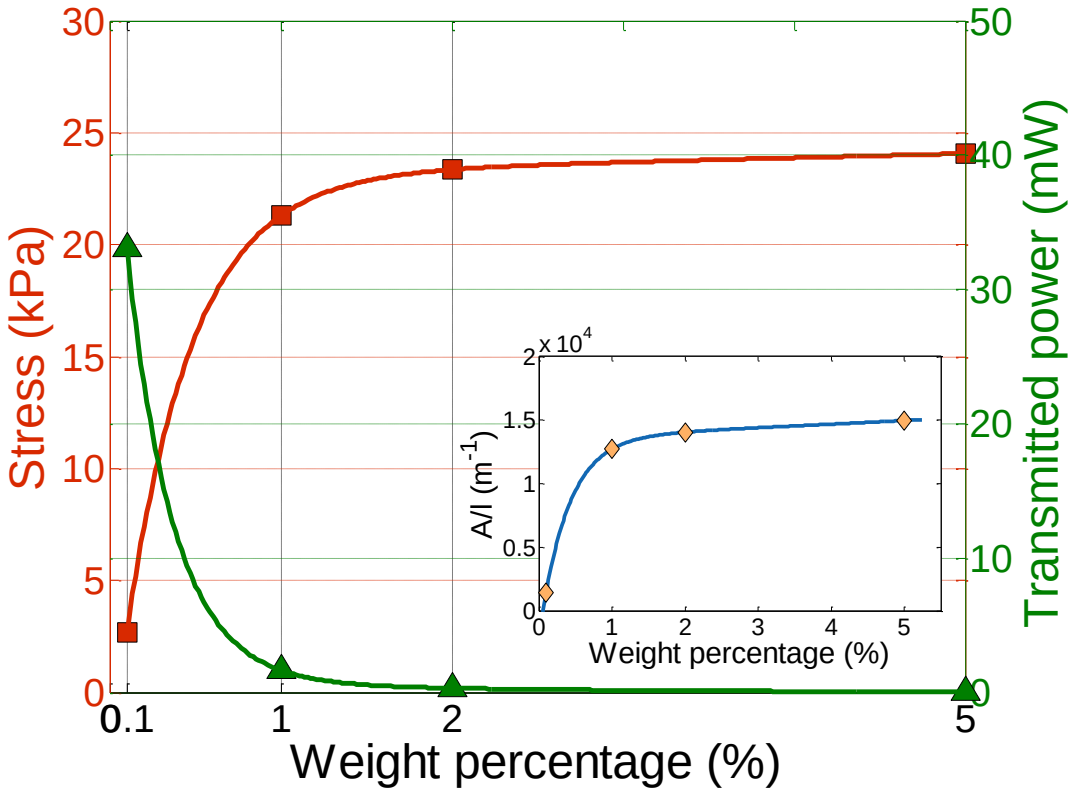

Figure 28- Photo-actuation of bulk nanocomposites with different weight percentage at 40% pre-strain. The transmitted power is also plotted. The input power in all experiments is fixed at 50 mW, 640 nm wavelength. Inset shows the absorbance spectra for different weight percentages of bulk samples at 670 nm.

In MoS_2, Ab initio calculations have suggested strong peaks in the visible region suggesting van Hove singularities in JDOS [23]. This leads to enhanced light absorption in TMDs, which is universal for all TMDs. The valence band consists of *4d* orbitals that are responsible for chromatic absorption, sending electrons from the ground state to the excited state in the conduction band depending on the energy of irradiated light. The strong covalent bonds (σ bonds) of the chalcogen atom couples this absorbed light due to the superposition of the *4d* orbitals of Mo and *3p* orbitals of S in the conduction band into an extraordinary thermal effect thus giving rise to this chromatic photomechanical effect. This is a unique mechanism not available to *sp* bonded materials such as carbon nanotubes and graphene, as well as plasmonic metallic gold nanoparticles.

Figure 29 presents the layer dependent actuation, wavelength selective responsivity, and mechanism of strain engineered optical absorption in these nanocomposites. Figure 29 (a) shows the exerted actuation stress as a function of number of layers. It is observed that the number of layers affect the overall photomechanical response at all pre-strains with few layer nanocomposites showing the greatest change in photomechanical stress.

Figure 29 (b) presents the exerted stress as a function of pre-strains at different wavelengths. A stress of ~25 kPa is observed at 60% pre-strains for 0.1 wt. % few layer nanocomposite sample. This could potentially scale to 250 kPa/1 wt.% and significantly larger than graphene (50 kPa/2 wt.%) [16] and could be useful both in micro and macroscopic actuation technologies based on light. The change in direction

of photomechanical actuation (7-15% strain) is as a result of orientation effects and rubbery/entropic elasticity and has been observed in the past and is in line with previous reports on photomechanical actuators employing similar PDMS based nanocomposite system [10]. Temperature measurements were conducted with thermocouple placed equidistant from the center of the sample to the end of the clamps. The insert in Figure 29 (b) shows the Gaussian profile of the temperature given as:

$$T = a_1 e^{-(\frac{x-b_1}{c_1})^2} + a_2 e^{-(\frac{x-b_2}{c_2})^2} \quad (1)$$

with the fitting parameters a_1, b_1, c_1, a_2, b_2, and c_2 which are dependent on the wavelength (Table 4). The temperature of the sample as a function of wavelength of the light was measured as: 48.1°C (405 nm), 43.7°C (532 nm), 41.1°C (640 nm) and 29.0°C (808 nm). Thus the lower thermal conductivity of TMD's compared to graphene films cannot adequately explain these interesting results.

Table 4- The Gaussian's parameters of wavelength selective temperature along the few-layer samples

	a_1	b_1	c_1	a_2	b_2	c_2
405 nm	24.59	-0.002067	3.176	28.45	2384	5549
532 nm	20.34	-0.001033	3.152	25.61	2593	8925
640 nm	17.59	-0.01081	3.104	2038	1489	7057
808 nm	5.238	-0.00836	3.186	27.49	2203	5776

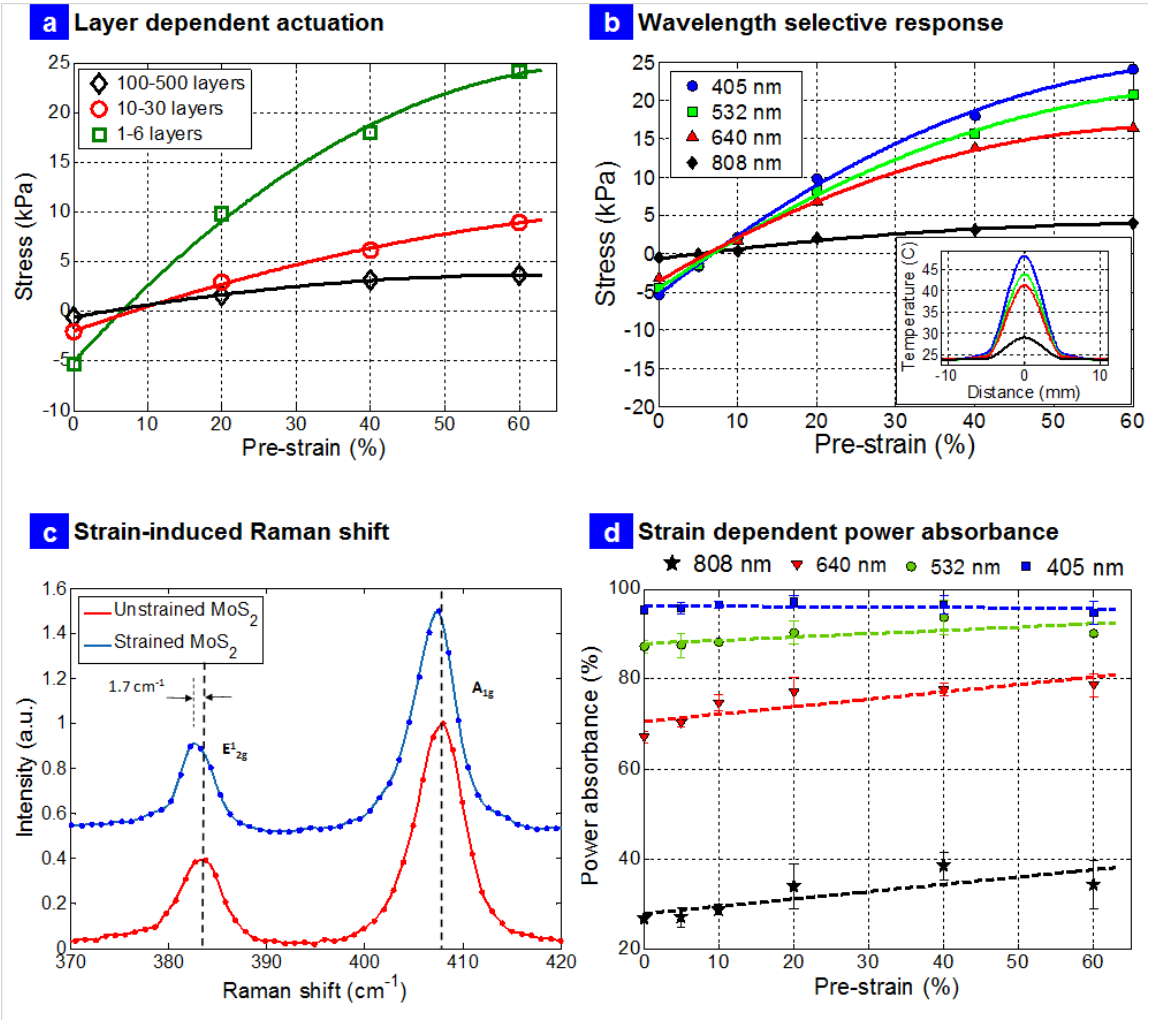

Figure 29- Photomechanical Actuation and Strain Engineering: (a) Magnitude of exerted stress as a function of pre-strains for different layered nanocomposites at 405 nm excitation; (b) Magnitude of exerted stress as a function of pre-strains at different wavelengths for the few-layer nanocomposite; insert is the actual temperature in the sample measured using thermocouples placed equidistant from center of the nanocomposite to the clamps; (c) Shift in the Raman vibrational modes E_{2g}~ 1.7 cm^{-1} for strain of 10% for the few-layer nanocomposite; (d) Strain enhanced optical power absorption in few-layer nanocomposite.

Local strain engineering and bandgap control has been reported in atomically thin samples of MoS_2 [31, 36]. Tuning optical absorption with strains in TMDs seems like an interesting and exciting prospect for energy conversion in MoS_2 due to its high strength and rapid reversal of bandgap. This is not possible using conventional thin film semiconducting materials which will undergo failure before any appreciable change in property can be produced [37]. Recent work has shown computationally that elastic strain is a viable agent for creating a continuously varying bandgap profile in an initially homogeneous, atomically thin layers but not experimentally explored completely [37].

In our few layer nanocomposites, applying global macroscopic uniaxial tensile strain of 10% using a custom-made strain gadget (Figure 30) resulted in the shift of the E_{2g} mode by about -1.7 cm^{-1} and negligible change in A_{1g} as presented in Figure 29 (c). The change in Raman wavenumbers of -1.7 cm^{-1} suggests 1% strain transfer to the MoS_2 from the matrix [31]. It has been suggested that the direct gap transition energy decreases for localized increasing uniaxial strain values for single layers; for a ~2.5 % tensile strain, the reduction in direct bandgap transition energy of 5% for monolayers has been reported [31]. Since our sample is a nanocomposite consisting of layers of PDMS and MoS_2 (Figure 31), lower strain transfer was expected as the strains were applied globally to the composite as a whole and not locally engineered. Further, we also expected to see continuously varying strains in the MoS_2 crystal due to the global application of the strains. These results are exciting in context of strain transfer into a

macroscopic device achieving significant improvement in globalized photomechanical response which has not been reported yet.

Finally, another way to confirm that this is strain induced reduction in bandgap is to measure the power absorption directly at different strains (Figure 29 (d)). The results suggest 1.33 times increase in power absorption of ~808 nm photons at ~40% strains compared to unstrained value, which can only happen if the bandgap is reduced (average bandgap of ~1.71 eV was measured for few layers suspensions based on cutoff of the optical absorption is presented in Figure 23 (f)) and one has a continuously

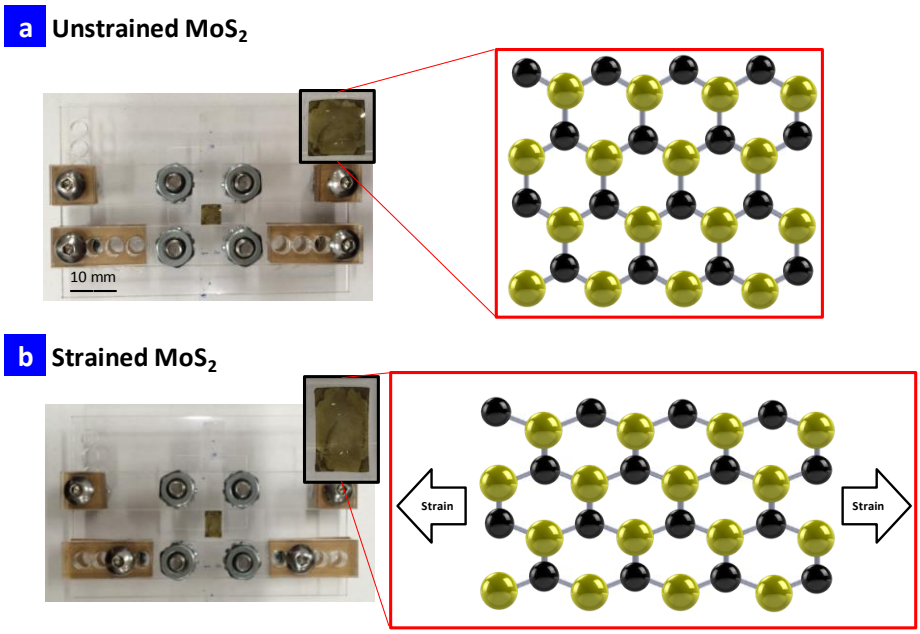

Figure 30- Strain engineering device for applying global strains to few-layer nanoflakes.

varying bandgap in the nanocomposite due to the stacked layers [37]. Similarly, 1.14 times change in power absorbed at 640 nm and 1.05 times change in power absorbed at 532 nm was observed at 40% strains. No significant change was observed in power absorption at 405 nm. These results suggest that as MoS_2 layers in the nanocomposite were strained globally, a continuously varying strains developed inside the material resulting in more power being absorbed by the sample even at energies up to ~2.3 eV (higher than bandgap of single layers) that resulted in significantly better photomechanical response.

It should be noted that although the design enables high strains to be applied to the sample, the strain transfer to the MoS_2 additives inside the sample is between 1-5% for the entire strains applied [31], not enough to cause failure/delamination that can change the optical absorption irreversibly. Since our samples consisted of layers of MoS_2 (1-6 layers) stacked on top of one another, stretching the sample globally must result in strain gradients resulting in spatially varying energy levels of the stacked crystals that led to increase in optical absorption. Our results also suggest one can tune the power absorbed almost all wavelengths in the visible region in a macroscopic device with strains. Thus the strains, optical absorption and photomechanical response can be continuously, rapidly and reversibly tuned in these nanocomposites at different wavelengths and offers room for development of flexible energy harvesting devices in the future with advanced designs of our nanocomposites with scalability of localized strain engineering into macroscopic response. This does not happen in carbon nanotube

[10, 14], graphene [15, 16] and gold nanoparticle based actuators [8] and thus is a unique photomechanical effect due to the rich d electron physics in TMDs.

Figure 32 presents some figures of merit for the few layer nanocomposite actuators. A photo actuation force of 10 to 15 mN at different laser power (405 nm) is observed (Figure 32a). Force as a function of time at different laser power suggests wavelength and intensity dependent actuation similar to Azobenzenes [5]. An important aspect of any actuator is energy efficiency at converting light of different illumination into mechanical movement. Therefore, the efficiency (η) of the MoS_2 composites to a known illumination source was evaluated [20].

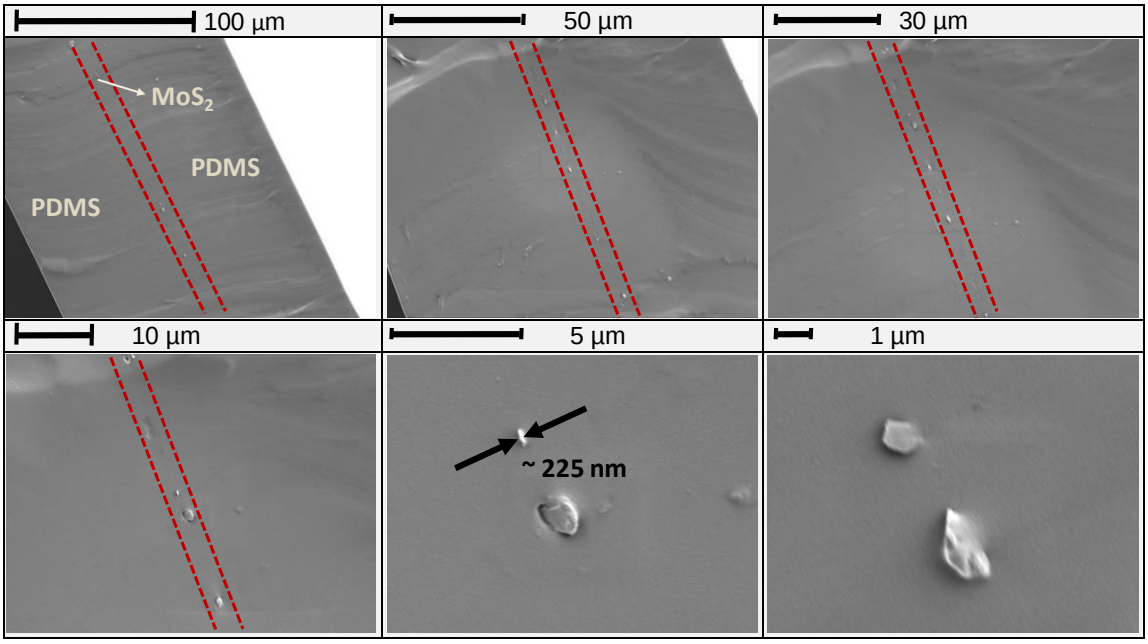

Figure 31- Cross-sectional SEM of 0.1 wt. % nanocomposites

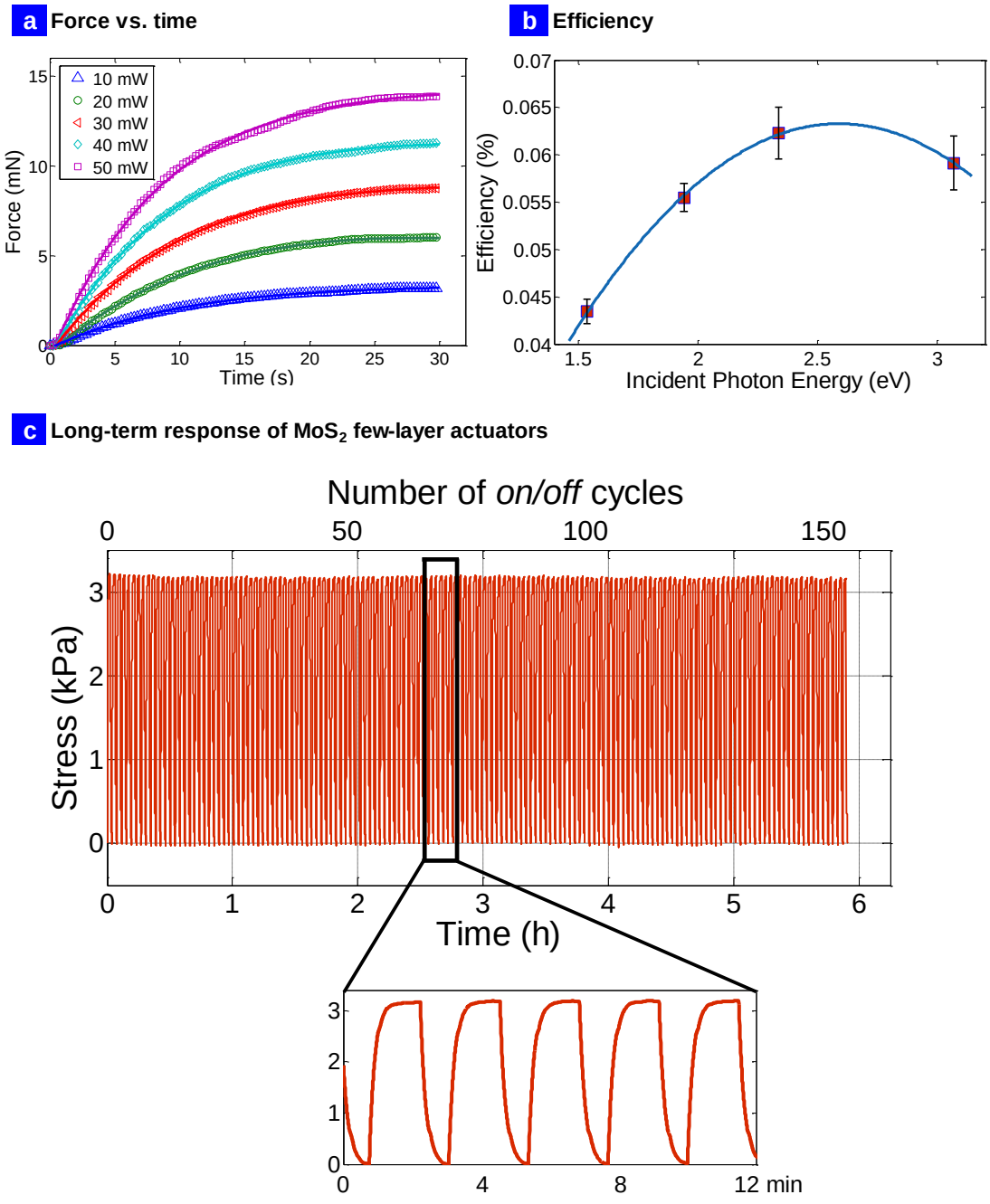

Figure 32- Force and Efficiency: (a) Force versus time at different laser power; (b) Efficiency versus incident photon energy; (c) Long term response of the 2H-MoS_2 few layer actuators operated over ~6 hours (~150 cycles) at 640 nm wavelength suggesting excellent stability.

Figure 32 (b) presents the efficiency relationship as a function of incident photon energy for few layer nanocomposites. A significant increase in efficiency was noted at wavelengths between 808 nm to 405 nm. The highest efficiency achieved was ~0.06% at ~2.5 eV followed by a small drop at higher energies. The efficiencies were calculated exactly as in our previous report [20]. The increased thermal effect at higher energies decreased the efficiency slightly. However, these numbers are still impressive for photo generated work in polymers. In comparison, past–light driven actuators based on polyvinyledene difluoride (PVDF) have demonstrated an efficiency value of ~8.3×10^{-5}% under quasi-static motion, about three orders of magnitude less efficient than our exfoliated MoS_2-elastomer systems (~6×10^{-2}%). Finally, the efficiency was twice as high as recently reported graphene-elastomer photo-mechanical actuators (0.03%) [20] with other excellent features such as wavelength selective response and could find applications in nanopositioning [20], plastic motors [21] and micro-opto-mechanical systems [17] (MOMS).

Figure 32 (c) presents the long term stability of the few-layer photomechanical actuator using 640 nm laser excitation over 150 cycles or 6 hours of continuous operation. No pre-strains were applied to the sample. The slightly greater than ~3 kPa matches exactly the photomechanical actuation experiments presented in Figure 27(f) at 640 nm wavelength (the time delay between these experiments is ~6 months). It should be noted that the long term experiments in Figure 32 (c) were conducted after the strain based optical absorption experiments presented in Figure 29 (d). There are several conclusions that can be deduced from these long term experiments. First, the

photomechanical actuation of the 2H-MoS_2 few-layer nanocomposite is fully reversible and robust actuation mechanism. Second, the strain based optical absorption experiments did not delaminate the interface/sample, which would otherwise cause an irreversible change in the amplitude of photomechanical actuation stress (a significant reduction in stress) due to increased scattering in these long term experiments. Third, the strain gradients on the MoS_2 crystals and the change in bandgap is also completely reversible as the sample exhibits pristine-like behavior (0% strain) with the same amplitude of mechanical response in these long term experiments. The strain transfer to the MoS_2 additive is thus in line with previous reports [31] and should be in between 1-5% in our samples at the highest strain applied to the nanocomposite, not enough to cause failure, delamination and degradation all which will irreversibly change the long term photomechanical response. This also lends credence to the high strength of the few layer MoS_2 additive. Thus the high strength and strong light-matter interactions in 2H-MoS_2 giving rise to this robust chromatic mechanical response is not only a new mechanism but also a new material design for future macroscopic photo mobile polymer networks based on TMDs.

4.3. METHODS

4.3.1. LIQUID PHASE EXFOLIATION, IMAGING AND OPTICAL ABSORBANCE SPECTROSCOPY:

The bulk MoS_2 solution was obtained by 7-hour bath sonication of MoS_2 Ultrafine Powder obtained from Graphene Supermarket. The intermediate solutions were sonicated for 50 hours, and then centrifuged at 1500 rpm for different time durations (45 to 120 minutes). The few layer samples were bought from Graphene Supermarket in ethanol and used as such. The number of layers were characterized for each type of suspension using AFM. The AFM images were taken using a NaioAFM of Nanosurf in tapping mode with a cantilever resonance frequency of ~148 kHz. HRTEM was conducted using an FEI Tecnai transmission microscope (TM) (model G2 F20). FFT was obtained from the HRTEM image. The operating voltage was set at 360 kV and 1 nA emission current connected to a Titan Themis charge-coupled-device camera. The sample was prepared by dropping one drop of exfoliated MoS_2 in ethanol solution on lacey-carbon Cu grids (Ted Pella Inc., CA). The Cu grids were dried in air to make sure there are sufficient isolated flakes to be observed. SEM images were obtained using a JEOL JSM-7000F instrument at 20 kV of power and under an ultra-high vacuum, 10-5 Pa. Secondary electron detector was utilized at 8 mm working distance to capture high-resolution images of MoS2 flakes at magnifications as high as 100,000X. The optical absorbance of the MoS_2 solutions and the nanocomposites were measured using a Hitachi U–5100 ratio beam spectrophotometer in a wavelength range of 190-1100 nm.

4.3.2. SAMPLE PREPARATION:

4.3.2.1. Bulk MoS_2 Actuators

10.0 mg as-received ultrafine nanopowder from Graphene Supermarket is weighed and added to 100 mL of ethanol (200 proof Sigma Aldrich), and sonicated for 7 hours in a bath sonicator. Using this solution, 2 mL of MoS_2 in ethanol is then used (200 µg MoS_2) for vacuum filtration process resulting in a mass per area of MoS_2 nanoparticles of 0.18601 g/m^2 on filter membrane (Whatman Anodisc). Area is calculated based on the diameter of the deposited film. Here 47 mm diameter Anodisc membrane after vacuum filtration resulted in 37 mm diameter of deposited mass. This resulted in 0.18601 g/m^2. This layer is then transferred to an 80 µm thick PDMS layer and then another layer of 80 µm thick PDMS is spun coated on top of this layer. The mass of the two layers of PDMS is then measured by cutting known areas of the neat PDMS (i.e. the clear part without any MoS_2) and calculating the mass/area of PDMS layers. This process is repeated several times for each sample to get averages. The ratio of the mass per area of the MoS_2 to that of the mass per area of the PDMS gives the weight percentage of the MoS_2 in the composite samples (i.e. 0.1 wt. %).

4.3.2.2. Intermediate MoS_2 Actuators

The process for intermediate samples is the same as bulk except that we used 50 hours sonication and then the solution is centrifuged at 1500 rpm. The top and bottom parts of the solution is then separated similar to reported in literature [238]. The concentration of the centrifuged solution is then calculated by weighing the amount of

MoS_2 nanoparticles removed from the top parts of each vial and depositing it on filter membranes. This process is repeated for several samples to ensure repeatability. The concentration of the used centrifuged solution for the intermediate nanocomposites is also verified using the Lambert-Beer law and optical absorbance method [238]. Using 11.628 mL of the centrifuged solution with a concentration of 0.0172 mg/mL resulted in 200 µg of MoS_2 in the solution. This 11.628 ml sample is then vacuum filtered on a filter membrane (deposited material diameter of 37 mm) arriving at a mass per area concentration of 0.18601 g/m^2. The same process as presented above in bulk is accomplished to reach a 0.1 wt. % of intermediate nanocomposites.

4.3.2.3. Few-layer MoS_2 Actuators

As-received MoS_2 solution (Graphene Supermarket) is used in the fabrication process. Because of ultra-small size of few-layer nanoparticles, transferring to PDMS layer cannot be accomplished from Anodisc membrane and is done using an evaporative drop deposition method. The initial concentration of the purchased few-layer solution as per manufacturer specification was 18 mg/L. 258 µL of this solution (4.65 µg of MoS_2) is then deposited directly on the 5 mm ×5 mm sample area of the PDMS to reach the same mass per area as bulk and intermediate samples (i.e. 0.18601 g/m^2). The final weight percentage (0.1 wt.%) calculation is the same as the bulk and intermediate samples after the second PDMS layer is spun coated on top of the PDMS/MoS_2 layers.

4.3.3. STRESS TEST EXPERIMENTS:

MoS_2/PDMS actuators were fabricated based on a layer-by-layer (LBL) method. PDMS silicone elastomer obtained from Dow Corning (Sylgard 184) was used as the host matrix. PDMS is a two part solvent-free flexible silicone organic polymer in the form of a base compound with a separate hydrosilane curing agent that acts as a cross-linker. The term cross-linking ratio (CLR) used throughout the paper refers to the ratio of PDMS cross-linker to the base compound. The PDMS base was mixed in 1:10 ratio to the cross-linker and then deposited on a glass slide. A standard spin coating process at 750 rpm for 90 seconds produces 80 μm thick film of PDMS on the glass slides. The films are then cured at 120°C for 20 minutes and post-cured for 12 hours at room temperature. A uniformly distributed layer of MoS_2 nanoparticles deposited on Whatman Anodisc inorganic membrane using a standard vacuum filtration process is then transferred into the first layer of PDMS. Another layer of PDMS is then spin coated and cured on top of the MoS_2 layer resulting in a layer-by-layer structure of about 160 μm thick. The samples are then cut in 50 mm × 5 mm strips (30 mm of active test area with 10 mm on each side for fixture mounting). All experiments were conducted in a climate-controlled laboratory. The photomechanical testing system, strain application, lasers all form an automated system that is placed inside a black box to avoid stray light from interfering the experiments. The laser sources include wavelengths from ultraviolet to near-infrared regions (405 nm, 564 nm, 640 nm, and 808 nm) all with the same laser power of 50 mW and beam diameters of ~3 mm. The laser diode was placed ~100 mm from the middle of the test strip such that the

illumination impacted normal to the PDMS/MoS_2 surface. More detailed information on photomechanical stress tests are available [69]. Long term stress test experiments for stability and robustness of the actuation mechanism was conducted continuously over 6 hour period.

4.3.4. STRAIN ENGINEERING USING RAMAN SPECTROSCOPY:

A custom strain gadget was developed using design and laser cutting clamps. The stretching fixture was developed with 500 μm resolution and 5 mm initial clamps' spacing. This fixture was used to study the effect of strain on the Raman shifts of polymer/MoS_2 nanocomposite actuators with 10% increments shown in Figure 30. The Raman measurements were performed by the excitation laser line of 532 nm using a Horiba XploRA Raman system in ambient air environment. The power of the excitation laser line was kept at 1 mW. Since there was two 80 micron PDMS layers in between the MoS_2 layer, the incident optical power was significantly less than 1 mW, not enough to induce heating effects in line with previous reports [243]. The laser beam was focused onto the surface of the samples using a 100X objective lens. The measurements were repeated for at least 5 different points on each sample.

4.3.5. RESONANT RAMAN SCATTERING:

Microscopic measurements of the nanocomposite optical spectra were performed in backscattering geometry with a resonant excitation. The 632 nm line of a He-Ne laser was used for these measurements. All measurements were done using an optical filter with an incident power of ~1 mW. Since there was an 80 μm PDMS layer

on top, the incident power is significantly less than 1 mW, not enough to induce local heating effect in line with previous reports on resonant Raman scattering [243]. The size of the laser spot on the sample was ~1 μm. A Leica microscope objective (50 X) was used to excite the sample and collect the emitted light. The collected spectra were dispersed by a Renishaw inVia Raman microscope system, equipped with a multi-channel high resolution Si-CCD device. The spectrum of pure PDMS was measured and subtracted from the measurements taken from bulk, intermediate and few layer nanocomposites. The broadened peaks were deconvoluted to show the overlapping components.

CHAPTER 5
THE COUPLED STRAINTRONIC PHOTOTHERMIC EFFECT

In this chapter, we describe the coupled straintronic-photothermic effect where coupling between bandgap of the 2D layered semiconductor under localized strains, optical absorption and the photo-thermal effect results in a large chromatic mechanical response in hyperelastic nanocomposites. Under the irradiation of visible light (405 nm to 808 nm), such locally strained atomic thin films based on 2H-MoS_2 embedded in a poly (dimethyl) siloxane matrix exhibited a large amplitude of chromatic photo-thermal actuation compared to their unstrained counterparts. Moreover, the locally strain engineered nanocomposites showed tunable chromatic mechanical response giving rise to higher mechanical stress at lower photon energies due to strain induced bandgap lowering.

Scanning photoluminescence spectroscopy revealed a change in bandgap of 20-30 meV between regions encompassing high and low strains compared to the unstrained few layers. For 1.6% change in the bandgap, the photo-thermal response increased by a factor of two. Millimeter scale bending actuators based on the locally strained 2H-MoS_2 additive resulted in significantly enhanced photo-thermal actuation displacements compared to their unstrained counterparts at lower photon energies and operated up to 30 Hz. Two different regions of the photo-thermal response versus wavelength based on film thickness were identified; an almost exponential photo-thermal effect due to strains at ~35 nm and the linear region at film thickness ~70 nm. Almost 1 mN photo-activated force obtained at 30 mW power for the locally strained

actuators and provided excellent long-term stability. This chapter demonstrates a new mechanism of the coupling between localized strains, change in bandgap; optical absorption and photo-thermal actuation in 2D TMD based nanocomposites that would be useful for developing broad range of sensors and transducers.

5.1. INTRODUCTION

Advantages of photo-thermal mechanisms for transducers include remote energy transfer, remote controllability, control of actuation using number of photons (intensity) and photon energies (wavelength), fast actuation (milliseconds), low signal to noise ratio, and scalability at different length scales using batch fabrication and high volume semiconductor manufacturing. However, only few materials exist that can convert light into mechanical work. Azobenzene liquid crystal elastomers were one of the first materials to exhibit photomechanical effect [2].

Recently, various nanomaterials including nanoparticles, nanowires, carbon nanotubes, and graphene were mixed into different polymers from hyperelastic rubbers [10, 11], shape memory polymers [12] and liquid crystal elastomers [13] [8, 9] and triggered using near infra-red light for photo-thermal actuation. In hyperelastic elastomers, based on the pre-strains, the samples when heated, can either expand, exhibit zero stress or contract in volume and can enable high photo-thermal strain energy densities [10, 11]. Large pre-strains result in large volume contraction on photo-thermal heating due to entropic elasticity. The mechanism of photo-thermal actuation in these nanocomposites is the non-radiative decay of photons resulting in localized thermal effect. While, applications of photo-thermal actuators are growing [7, 8, 14, 16-

19, 21, 247], there is need for material design that is simple, enable tunable optical absorption and reversible photo-thermal response. 2D nanomaterials based on TMDs encompassing large optical absorption (10^7 m^{-1}) [22, 23] and strain engineering of such TMDs presents new opportunities in photo-thermal transducers which we have explored in this chapter.

Strain engineering, i.e., the change in electronic properties using mechanical deformation is an important concept in condensed matter physics and material science that is being exploited in 2D materials due to their ultra-large mechanical strength (capable of withstanding 10-20% strains) and possessing a bandgap [31, 36, 38-41]. Strain engineering in 2D layered materials brings potential benefits such as those explored in graphene including; strain induced bandgap opening [42], strain enhanced electron-phonon coupling [43, 44], non-uniform strain induced pseudo-magnetic field [45] and even strain engineered self-assembly of hydrogen on graphene surfaces [46].

The elastic modulus and the breaking strength of an ideal defect-free single-layer MoS_2 is expected to be $E^{2D}/9$, where E^{2D} is the in-plane stiffness as per the theory of rupture and flow in solids [29, 30]. The in-plane stiffness of monolayer MoS_2 is reported as 180±60 Nm^{-1} corresponding to an effective Young's modulus of 270 ±100 GPa, which is comparable to that of steel [29]. Breaking occurs at an effective strain between 6 and 11% with the average breaking strength of 23 GPa [29].

The large breaking strength makes strain engineering an interesting prospect in TMDs, as the bandgaps are highly sensitive to strains. Bulk form of MoS_2 has an indirect band gap of ~1.29 eV [28] and strain engineering has no effect on such bulk

materials and does not produce any significant chromatic mechanical response. On the other hand, single layer MoS_2 has a band gap of 1.8-1.9 eV [28]; bi-layer has a bandgap of 1.5-1.6 eV [36] and strain engineering can modulate electronic and optoelectronic properties. With decreasing thickness, the past experiments have revealed a progressive confinement-induced shift in the indirect gap from the bulk value of 1.29 eV up to 1.90 eV [28]. The in-plane structure of MoS_2 is determined by strong covalent bonds resulting from the overlap between the *4d* and *3p* electron orbitals of Mo and S, respectively [29]. In few layer 2H-MoS_2, the bandgap goes from direct-to-indirect at >1 % strains [36] and undergoes semiconductor-to-metal transition at 10-15% strains [32].

Several techniques are realized for strain engineering of 2D layered materials including bending/elongating a flexible substrate [36], piezoelectric compression [47], exploiting thermal expansion mismatch [48], creating artificial atoms through indentation/capillary forces [49], and controlled wrinkling [31]. However, large area photo-thermal devices based on these mentioned techniques of strain engineering of 2D layered TMDs are yet to be explored.

Utilizing exfoliated nanoparticle MoS_2 suspensions, filtration and layer-by-layer process of nanocomposite fabrication, and strain transfer from polymeric substrate, in this chapter we present the first direct evidence of chromatic optical absorption and reduction in bandgap due to localized strains directly affecting the photo-thermal response of a nanocomposite in macroscopic scale. Our work is also the first locally

strain engineered 2D layered device to perform mechanical work using this coupled straintronic-photo-thermic effect.

5.2. RESULTS

Figure 33 describes the straintronic-photothermal effect. This effect arises due to coupling of electronic properties of semiconductors, thermal properties of polymers and photoexcitation. The mechanism is the coupling between localized strains, change in the bandgap and optical absorption of 2D TMDs transducing into an extraordinary thermal effect that contracts the hyperelastic molecular chains. This effect is chromatic (depends on the wavelength of light), fully reversible, bandgap dependent and produces elastic mechanical response. This nanoscale effect only happens in layered semiconductors and not in bulk materials. The strain induced lowering of the bandgap in 2D layered semiconductor is coupled to the enhanced optical absorption. The thermal energy generated during the process of photoexcitation across the bandgap is coupled to the hyperelastic molecular chains that make them highly mobile internally. In zero strain and strained semiconductor nanocomposites, we observed chromatic mechanical response.

In semiconducting materials, optical absorption and emission processes occurs due to the absorption of a photon exciting an electron and the transfer of that electron to/from the conduction band to the valence band. Since photons have no momentum, only vertical transitions on an E(k) band diagram are allowed in purely optical

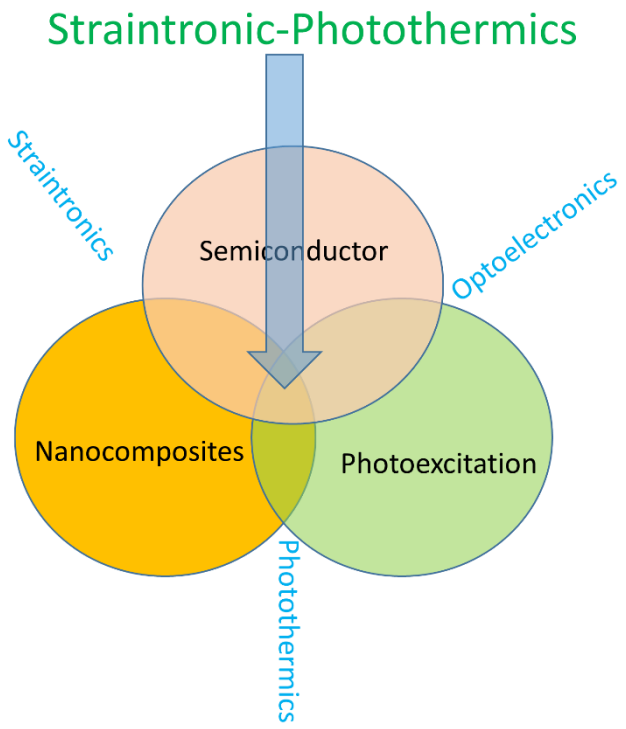

Figure 33- The Straintronic-Photothermic Effect: The straintronic-photothermic effect due to coupling of electronic properties of semiconductors, thermal properties of polymers and photoexcitation. This effect is the coupling of optoelectronics, straintronics, and photothermics all in a single nanocomposite.

processes. On the other hand, phonons have a large momentum. In the band diagram, photons lead to vertical transitions among bands on the E (k) plot while phonons make horizontal transitions. In direct band gap materials, typical electron and hole life time is ~10^{-8} s, and this can be 1000 times larger in indirect band gap semiconductors [248]. In indirect semiconductors, when recombination occurs, most of the energy is emitted in the form of heat rather than light. The heat is converted into mechanical motion by the hyperelastic polymer chains in our samples. In our samples, the optical absorption

follows the direct bandgap A and B in 2H-MoS_2, but the lattice heat is generated due to the indirect horizontal transition by the phonons. Now, one can change the bandgap through various means such as strains and doping, and tune the mechanical response that will be useful in wide variety of transducer applications.

The High-Resolution Transmission Electron Micrograph (HRTEM) of the MoS_2 structure is presented in Figure 34 (a) with atoms of S and Mo indicated. The distances a_1, a_2 and a_3 measured from this image are close to the 2.8 Å value of the Mo–Mo interatomic distances in 2H-MoS_2 [239]. The insert in Figure 34 (a) presents the Fast Fourier Transform (FFT) of the HRTEM image indexing the crystallographic planes of the single layer 2H-MoS_2. Small distortions and apparent non-uniform intensity distribution of the spots in FFT are due to a slight tilt of the flake normal to the electron beam. In the 2H-MoS_2 lattice, each Mo atom is located at the center of a trigonal prism created by six S atoms. The lattice constant of 2H-MoS_2 was reported to be: $a=b$=3.14 Å [236] and c=12.3 Å [237]. In the bulk form of MoS_2 with an indirect band gap of ~1.29 eV [28], the photon absorption process is dominated by electronic polarization, and as a result, no wavelength selective optical absorption is observed since no significant electronic transition happens from the valance to the conduction band. However, as the number of MoS_2 layers decreases, the indirect band gap becomes large and the material changes into a direct band gap semiconductor with E_g~1.9 eV in a single layer [28] with intrinsic photoluminescence [25].

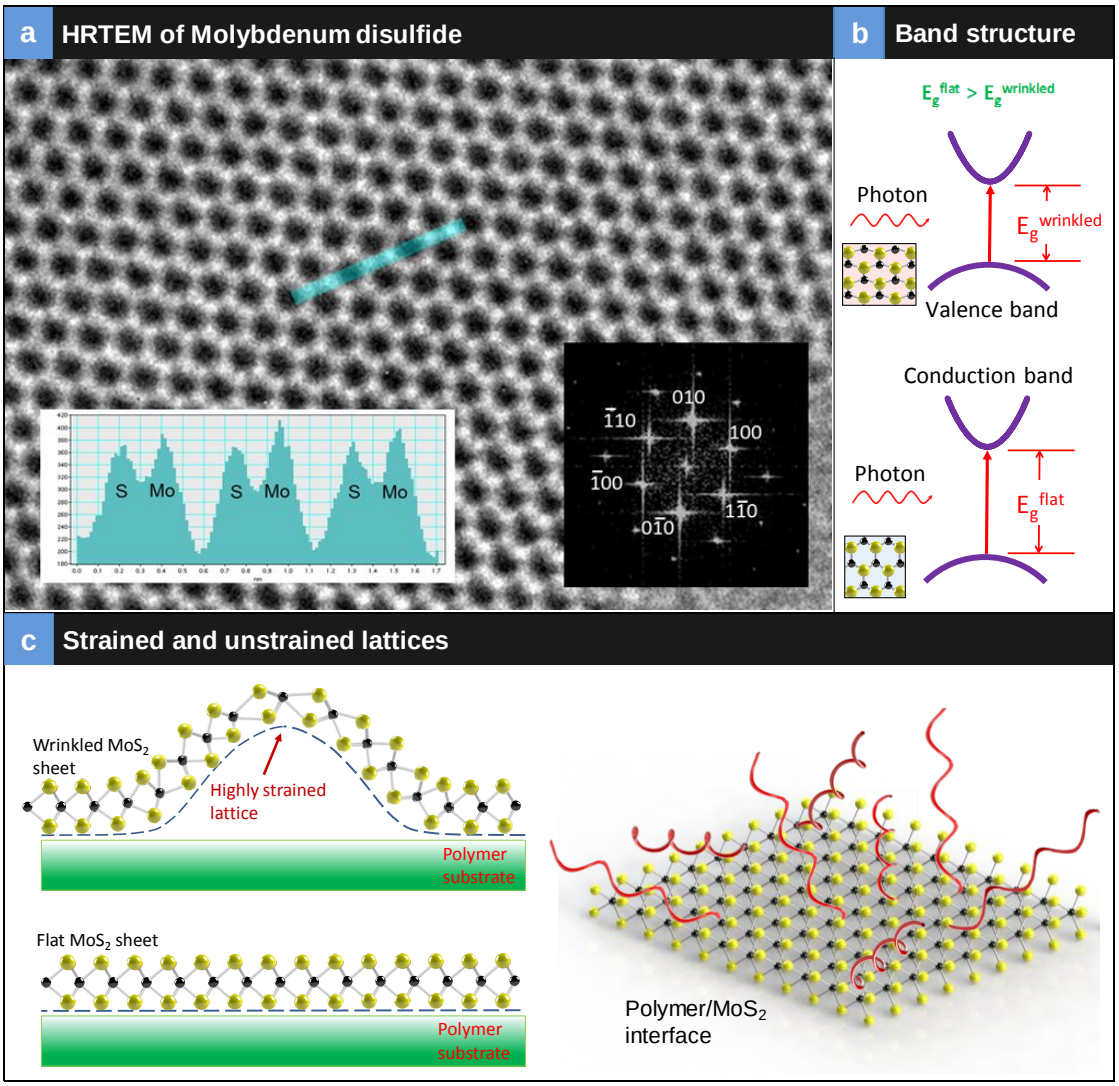

Figure 34- Structure of TMDs: (a) High-Resolution Transmission Electron Microscopy (HRTEM) of single layer TMD. Insert shows the Fourier Transform and the intensity profile measured along the blue line shown in the HRTEM image, The atomic positions of S and Mo atoms is indicated; (b) schematic of the band structure of flat and wrinkled suggesting reduction in bandgap energy with strain; (c) schematic of the highly strained and flat MoS_2 atomic sheets on polymer substrate; the interface suggests that molecular chains are entangled on the sheet that aids in effective heat transfer from the additive into the polymer.

Figure 34 (b) presents the schematic of the band structure of flat versus locally strained architecture for 2H-MoS_2. Inserts next to the band structures show the flat and strained honeycomb structure of the semiconducting phase of 2H-MoS_2. Figure 34 (c) presents the schematic of the strained versus flat actuators. Local strain engineering creates wrinkles. The schematic of a flat sheet with polymer chains in contact is also presented in Figure 34 (d). Since these are layered structures that is transferred from the filter membrane to the polymer, it is expected that the contact between the MoS_2 and polymer is primary adhesion and the molecular chains are just on the surface of the MoS_2 is interacting with them entropically. This contact enables the thermal energy be transferred from the MoS_2 additive to the polymer chains enabling a photo-thermal response due to entropic elasticity.

Figure 35 shows the fabrication schematic, strain transfer and optical images of the samples in PDMS. The starting point of the photo-thermal actuators is the filtration of commercially available 2H-MoS_2 suspensions to form a film [22]. Initial characterization revealed few layered MoS_2 nanoparticle suspensions had a particle size of ~100 nm. AFM measurements suggested from 1-6 layers [22] and were used for preparing the photomechanical actuators. The suspensions were filtered through a membrane using simple filtration (no vacuum is applied). Filtration resulted in optically smooth layers on top of the filter membrane of a specific thickness. A layer of PDMS is then spin coated onto a glass slide, cured and peeled off. The peeled off layer of PDMS is then set up between clamps and strain of 70%, is applied to the PDMS layer by stretching the sample. The filtering membrane consisting of 35 nm or 70 nm 2H-MoS_2

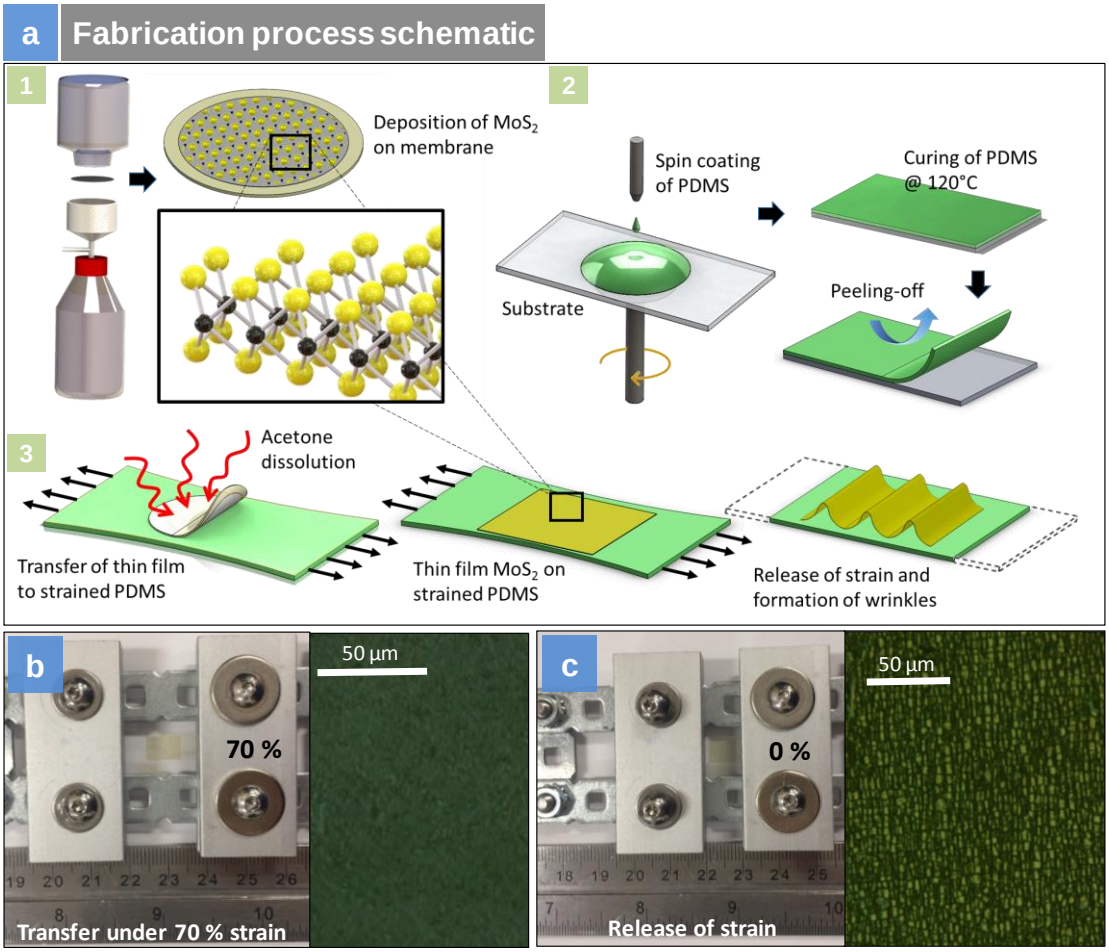

Figure 35- Device Fabrication: (a) Schematic of the fabrication of the actuator and release of strains and formation of wrinkles; (b) gadget used for strain transfer at 70% strains and optical image of the flat sample before the strain is released; (c) gadget at 0% strain and corresponding optical image after the strain is released.

thin film is transferred to the strained layer, and the membrane is dissolved in acetone, leaving behind the thin film of 2H-MoS_2 on the strained PDMS layer. We made two different thickness of film namely 35 nm and 70 nm film to assess the straintronic-

photothermal response. Releasing the strains suddenly results in the formation of *wrinkles*.

Figure 35 (b) and Figure 35 (c) presents the clamps with PDMS thin film before, and after releasing the strain, respectively. Once the strain is released as presented in Figure 35 (c), lamellar structures are seen suggesting the appearance of the "*nanowrinkles*" along the length in an optical microscope.

Figure 36 (a-d) presents the scanning electron micrograph (SEM) of the "*wrinkle*" architecture at different magnification. Strain transfer from an elastomeric substrate such as PDMS resulted in thousands of "*wrinkles*" at a large scale. Here we have used the same strain transfer from a polymer substrate at a large scale. Figure 36 (d) presents the SEM image of a single wrinkle between flat layers, measuring 520 nm in height and 970 nm in width.

Figure 37 presents the AFM image of the wrinkles on the polymer substrate. The lamellar structure is seen from the top extending to several microns. The height image from the AFM is presented for different regions showing ~70-80 nm consistently in height. The height and width of over 100 wrinkles are listed in Table 5, reporting average values of 87 nm and 553 nm for height and width of wrinkles in 35 nm film. Castellanos-Gomez *et al*. showed such wrinkles are generated from a single sheet of of MoS_2 consisting of 3-4 layers using the strain transfer from polymer for studying bandgap engineering in mechanically exfoliated samples [31]. We have used this process to transfer strains into nanoparticles of MoS_2 formed into a thin film. The films,

therefore, are not one continuous sheet, but quasi-continuous sheets consisting of few layer nanoparticles. Such films also create stable wrinkles without disintegrating into the substrate. Releasing the strain from the elastomeric substrate results in delamination induced buckling, of our quasi-continuous sheets [249]. We were able to produce wrinkles that were 12-170 nm in height and 300 to 700 nm in width. Previous work has shown that, the maximum uniaxial tensile strain ε accumulated on top of the winkles is estimated as [249]:

$$\varepsilon \sim \pi^2 h \delta / (1-\sigma^2)\lambda^2 \quad (2)$$

where σ is the Poisson's ratio of MoS_2 (0.125), *h* is the thickness of the flake and δ and λ are the height and width of the wrinkle respectively. However, this model assumes the sheet to be continuous and the strains are often overestimated for thin films of nanoparticles. A modification of this model is thus necessary to accurately predict the strain profile in our quasi-continuous sheets. The analytical strain model for van der Waals packed films was developed based on the original work by Vella *et al.* [249]. The new strain relationship for the nanoparticle films is thus given as:

$$\varepsilon_x(x,z) \cong -\frac{2\pi^2 z\delta}{\lambda^2} cos\frac{2\pi x}{\lambda} \quad (3)$$

where, *x* is the horizontal distance from apex of the wrinkle and *z* the distance from the mid-plane of each individual nanoparticle. The details of this model can be found in Chapter 6.

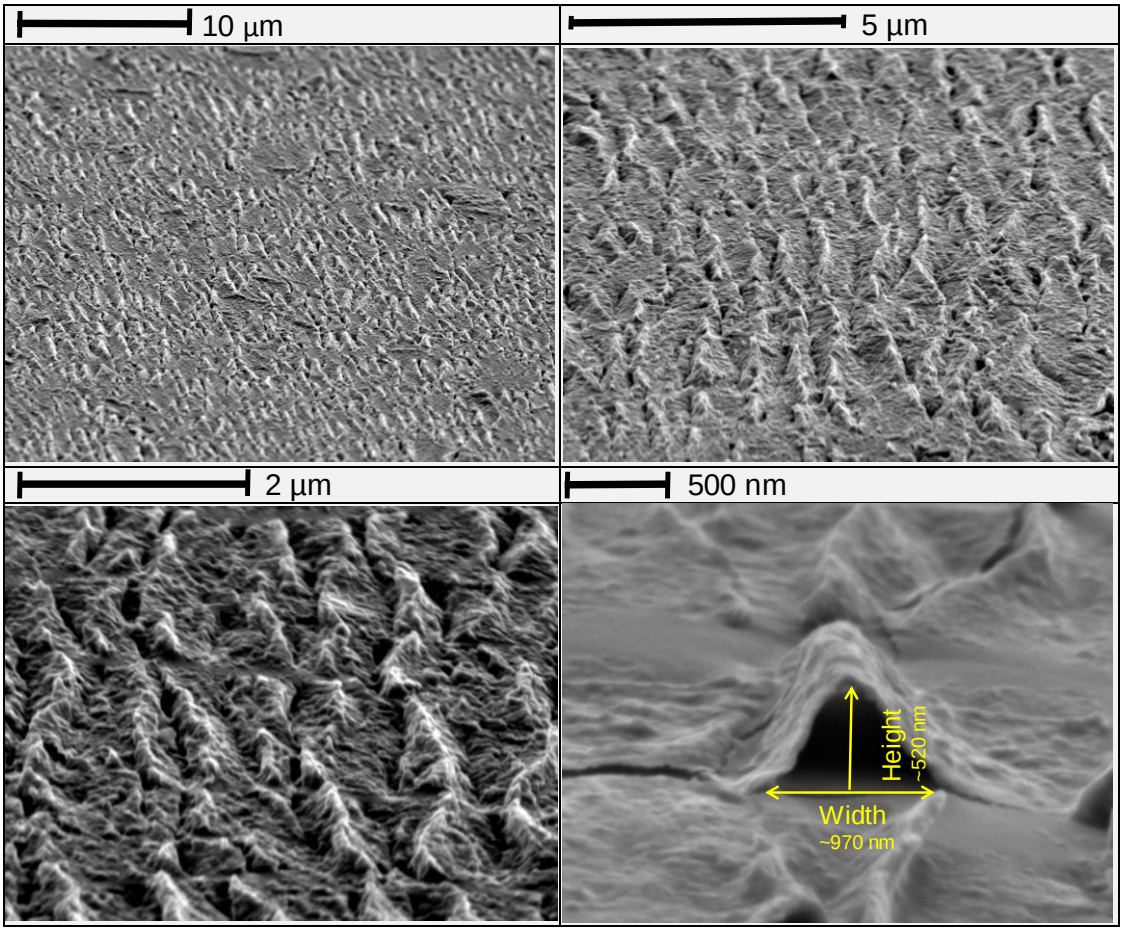

Figure 36- Scanning Electron Microscopy of Wrinkles: High angle SEM image of thousands of wrinkles at different magnification. (a-c) Highly reproducible wrinkles at large scale; (d) A single wrinkle seen between flat layers in the 500 nm image. The image suggests these are highly reproducible structures. A single wrinkle is almost 1 µm in width and 520 nm in height.

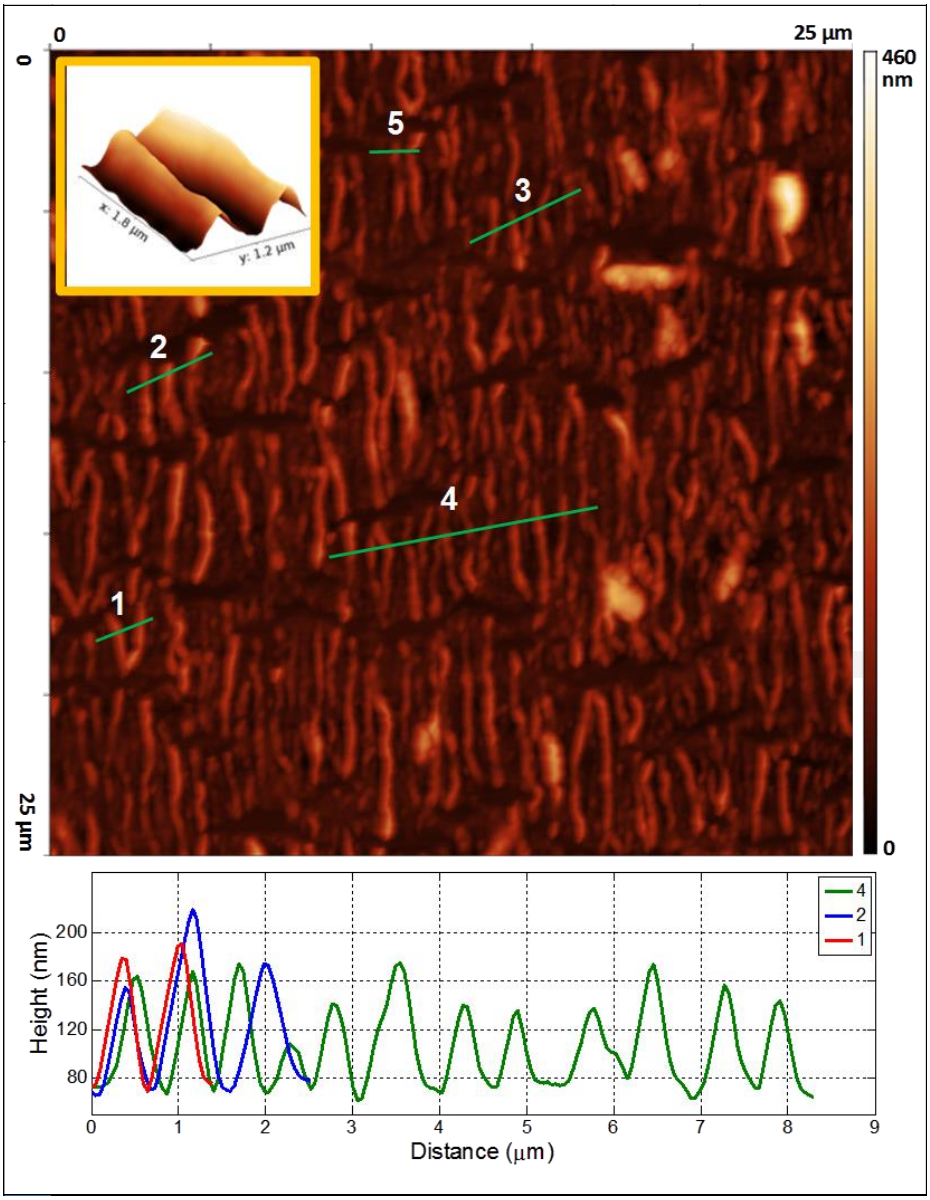

Figure 37- AFM image of large area of wrinkled sample. Insert shows two nanowrinkles right next to each other; AFM height image of three different regions are presented.

Table 5- Statistical information of height, width, strain and percentage strains from 100 different wrinkles for 35 nm film.

height, δ (nm)	135	113	131	168	105	82	147	97	131	115	108	121	82	123	100
width, λ (nm)	488	440	600	645	540	555	578	425	652	441	643	427	448	473	625
strain ε	0.0109	0.0112	0.0070	0.0078	0.0069	0.0051	0.0085	0.0103	0.0059	0.0114	0.0050	0.0128	0.0079	0.0106	0.0049
ε (%)	1.09	1.12	0.70	0.78	0.69	0.51	0.85	1.03	0.59	1.14	0.50	1.28	0.79	1.06	0.49
height, δ (nm)	113	105	97	74	65	106	220	147	55	183	38	27	61	118	73
width, λ (nm)	468	455	562	442	435	551	640	643	719	663	330	365	310	574	495
strain ε	0.0099	0.0098	0.0059	0.0073	0.0066	0.0067	0.0103	0.0068	0.0020	0.0080	0.0067	0.0039	0.0122	0.0069	0.0057
ε (%)	0.99	0.98	0.59	0.73	0.66	0.67	1.03	0.68	0.20	0.80	0.67	0.39	1.22	0.69	0.57
height, δ (nm)	132	76	35	95	83	58	81	125	96	74	104	95	53	37	53
width, λ (nm)	437	570	410	510	525	550	513	700	580	553	580	620	480	650	650
strain ε	0.0133	0.0045	0.0040	0.0070	0.0058	0.0037	0.0059	0.0049	0.0055	0.0047	0.0059	0.0048	0.0044	0.0017	0.0024
ε (%)	1.33	0.45	0.40	0.70	0.58	0.37	0.59	0.49	0.55	0.47	0.59	0.48	0.44	0.17	0.24
height, δ (nm)	68	86	96	51	57	157	34	98	127	92	118	14	73	177	59
width, λ (nm)	630	450	640	340	525	775	435	585	875	623	734	341	402	971	413
strain ε	0.0033	0.0082	0.0045	0.0085	0.0040	0.0050	0.0035	0.0055	0.0032	0.0046	0.0042	0.0023	0.0087	0.0036	0.0067
ε (%)	0.33	0.82	0.45	0.85	0.40	0.50	0.35	0.55	0.32	0.46	0.42	0.23	0.87	0.36	0.67
height, δ (nm)	58	129	82	102	31	14	157	79	78	69	64	118	95	115	106
width, λ (nm)	462	680	560	657	374	360	782	602	588	433	668	717	581	595	573
strain ε	0.0052	0.0054	0.0050	0.0045	0.0043	0.0021	0.0049	0.0042	0.0043	0.0071	0.0028	0.0044	0.0054	0.0063	0.0062
ε (%)	0.52	0.54	0.50	0.45	0.43	0.21	0.49	0.42	0.43	0.71	0.28	0.44	0.54	0.63	0.62
height, δ (nm)	49	98	61	34	104	44	85	99	98	97	97	76	93	56	31
width, λ (nm)	371	706	692	446	743	429	532	546	643	613	522	479	567	461	275
strain ε	0.0069	0.0038	0.0025	0.0033	0.0036	0.0046	0.0058	0.0064	0.0046	0.0050	0.0069	0.0064	0.0056	0.0051	0.0079
ε (%)	0.69	0.38	0.25	0.33	0.36	0.46	0.58	0.64	0.46	0.50	0.69	0.64	0.56	0.51	0.79
height, δ (nm)	69	72	123	134	96	89	78	68	109	113	157	120	94	81	22
width, λ (nm)	523	603	622	738	535	576	522	471	649	635	572	561	655	398	330
strain ε	0.0049	0.0038	0.0061	0.0047	0.0065	0.0052	0.0055	0.0059	0.0050	0.0054	0.0092	0.0073	0.0042	0.0098	0.0039
ε (%)	0.49	0.38	0.61	0.47	0.65	0.52	0.55	0.59	0.50	0.54	0.92	0.73	0.42	0.98	0.39

Average height, δ (nm)	87	(STD=37.6)
Average width, λ (nm)	553	(STD=123)
Average strain ε	0.0060	(STD=0.002)
Average ε (%)	0.60	(STD=0.24)

Table 6- Statistical information of height, width, strain and percentage strains from 100 different wrinkles for 70 nm film.

height, δ (nm)	480	460	510	350	260	270	360	490	310	550	500	650	270	600	290
width, λ (nm)	1700	1700	1700	1300	1200	1300	1500	1400	1100	1800	1700	2050	1500	1900	1400
strain ε	0.0032	0.0031	0.0034	0.0040	0.0035	0.0031	0.0031	0.0048	0.0049	0.0033	0.0033	0.0030	0.0023	0.0032	0.0028
ε (%)	0.32	0.31	0.34	0.40	0.35	0.31	0.31	0.48	0.49	0.33	0.33	0.30	0.23	0.32	0.28

height, δ (nm)	250	450	600	250	430	520	740	560	470	260	370	430	350	345	170
width, λ (nm)	1000	1700	2000	1050	1500	1550	2400	1450	1700	1050	1700	1550	1650	1500	1100
strain ε	0.0048	0.0030	0.0029	0.0044	0.0037	0.0042	0.0025	0.0051	0.0031	0.0045	0.0025	0.0034	0.0025	0.0030	0.0027
ε (%)	0.48	0.30	0.29	0.44	0.37	0.42	0.25	0.51	0.31	0.45	0.25	0.34	0.25	0.30	0.27

height, δ (nm)	430	560	370	260	390	340	600	345	480	580	460	310	390	330	540
width, λ (nm)	1250	1550	1550	1200	1500	1750	1900	1250	1600	1750	1850	1100	1550	1350	2100
strain ε	0.0053	0.0045	0.0030	0.0035	0.0033	0.0021	0.0032	0.0042	0.0036	0.0036	0.0026	0.0049	0.0031	0.0035	0.0024
ε (%)	0.53	0.45	0.30	0.35	0.33	0.21	0.32	0.42	0.36	0.36	0.26	0.49	0.31	0.35	0.24

height, δ (nm)	310	330	270	230	280	540	570	470	610	490	360	300	390	370	210
width, λ (nm)	1450	1700	1500	1450	1400	1850	2000	1900	1900	1800	1500	1300	1400	1400	1250
strain ε	0.0028	0.0022	0.0023	0.0021	0.0027	0.0030	0.0027	0.0025	0.0033	0.0029	0.0031	0.0034	0.0038	0.0036	0.0026
ε (%)	0.28	0.22	0.23	0.21	0.27	0.30	0.27	0.25	0.33	0.29	0.31	0.34	0.38	0.36	0.26

height, δ (nm)	205	140	540	255	330	510	410	380	270	560	470	205	290	270	340
width, λ (nm)	1100	1100	1900	1250	1300	2000	1850	1400	1450	1800	1650	950	1600	1450	1550
strain ε	0.0033	0.0022	0.0029	0.0031	0.0038	0.0025	0.0023	0.0037	0.0025	0.0033	0.0033	0.0044	0.0022	0.0025	0.0027
ε (%)	0.33	0.22	0.29	0.31	0.38	0.25	0.23	0.37	0.25	0.33	0.33	0.44	0.22	0.25	0.27

height, δ (nm)	500	265	270	450	440	220	405	330	380	345	305	440	430	515	500
width, λ (nm)	2150	1650	1450	1300	1600	1600	1600	1700	1750	1650	1200	1550	1700	2200	2000
strain ε	0.0021	0.0019	0.0025	0.0051	0.0033	0.0017	0.0030	0.0022	0.0024	0.0024	0.0041	0.0035	0.0029	0.0020	0.0024
ε (%)	0.21	0.19	0.25	0.51	0.33	0.17	0.30	0.22	0.24	0.24	0.41	0.35	0.29	0.20	0.24

height, δ (nm)	160	590	330	530	330	280	440	280	440	250
width, λ (nm)	1300	2200	1600	1950	1350	1500	1900	1800	2200	1300
strain ε	0.0018	0.0023	0.0025	0.0027	0.0035	0.0024	0.0023	0.0017	0.0017	0.0028
ε (%)	0.18	0.23	0.25	0.27	0.35	0.24	0.23	0.17	0.17	0.28

Average height, δ (nm)	387.18	(STD=124.2)
Average width, λ (nm)	1582	(STD=301.4)
Average strain ε	0.0031	(STD=8E-4)
Average ε (%)	0.31	(STD=0.083)

T**able 7-** Statistical information of the length of the wrinkle and number of wrinkles per area for 35 nm film.

Length (μm)														
2.39	1.59	0.88	0.96	0.75	3.06	0.92	4.62	1.26	1.34	1.38	1.91	2.91	1.33	3.65
1.25	1.87	1.71	1.47	4.78	2.97	1.3	1.51	3.99	3.24	3.41	3.33	3.75	3.88	1.51
2.5	1.33	1.34	0.87	0.74	1.76	1.5	3.27	1.31	2.75	2.99	1.83	1.3	2.52	1.61
1.47	1.55	1.57	1.77	2.21	2.13	3.05	1.06	2.78	1.65	1.99	2.4	2.74	2.35	2.84
2.63	3.65	4.15	3.88	1.35	1.45	0.57	1.11	5.11	5.14	4.12	1.2	1.67	6.47	3.52
3.35	0.88	2.45	2.16	1.5	1.78	3.53	1.44	0.61	1.58	2.16	1.67	0.53	2.29	1.68
2.14	5.61	2.08	2.73	3.08	2.11	2.46	3.01	1.92	1.84	4.59	2.72	3.27	3.32	1.38
3.06	1.39	2.97	1.42	4.15	2.46	3.15	3.58	0.83	1.31	0.76	1.23	2.1	1.92	2.1
2.75	3.64	2.88	5.33	4.31	4.34	3.99	2.02	2.47	1.3	0.4	0.81	3.13	2.01	1.59
1.11	1.1	2.74	1.62	2.46	2.48	2.67	2.47	4.51	4.01	3	0.84	0.85	1.75	0.94
2.28	3.79	3.38	1.64	3.45	1.75	1.6	1.88	2.55	0.86	2.82	2.25	1.93	2.78	5.16
2.32	3.82	2.55	4.21	4.14	1.23	0.91	3.29	4.42	3.32	4.4	3.32	1.26	1.89	5.02
2.61	5.15	5.23	5.06	1.18	1.16	2.02	4.64	4.84	0.7	0.66	1.27	1.86	2.44	1.54
1.75	1.56	1.16	1.85	1.48	1.25	2.9	2.63	1.9	2.43	0.96	0.84	0.82	1.68	1.52
3.32	4.18	4.32	4.04	0.69	1.03	1.4	2.25	2.85	2.29	1.38	1.06	3.11	1.62	1.29
1.92	1.19	1.46	2.63	2.57	3.4	4.06	1.63							

Average length, L (μm)	**2.373**	(STD=1.224)
Average island lengths (μm)	**4.151**	(STD=1.967)
Number of wrinkles*	**247**	
Wrinkles per area (μm^{-2})	**0.395**	

* in an area of 25×25 μm^2

Table 8- Statistical information of the length of the wrinkle and number of wrinkles per area for 70 nm film**.**

Length (μm)														
2.29	2.08	1.63	2.51	1.77	5.98	13.43	6.2	2.34	7.53	10.77	10.05	6.82	2.14	2.44
3.55	9.31	8.49	8.96	9	2.21	2.88	2.66	1.47	1.04	5.72	8.22	8.05	4.89	6.35
9.2	8.28	3.63	9.81	7.6	7.09	1.99	1.95	2.95	3.47	3.54	3.25	2.89	5.39	4.89
4.95	4.93	2.46	2.07	1.48	7.63	6.86	8.86	7.96	5.54	8.63	4.46	3.33	3.21	10.43
5.13	5.18	8.4	9.33	10.3	6.05	6.66	5.65	4.85	6.99	4.23	2.81	1.82	2.67	2.1
1.75	2.74	2.89	3.9	3.93	3.77	0.98	4.14	4.7	5.33	4.86	2.05	4.43	2.62	5.52
2.18	2.89	2.32	1.19	1.14	6.17	5.9	0.82	2.6	5.19	1.96	4.63	9.4	6.83	8.22
2.93	8.08	5.97	2.67	4.47	3.64	6.75	5.24	3.78	8.63	10.24	12.42	13.14	3.16	2.09
2.5	2.31	4.14	1.24	3.79	3.18	3.44	3.93	3.37	9.15	8.77	6.98	4.01	3.6	4.22
5.28	2.81	4.31	4.07	1.53	5.34	3.51	1.61	1.45	2.46	1.96	3.09	2.32	2.59	2.11
1.54	3.08	3.47	5.41	4.99	3.02	5.94								

Average length, L (μm)	**4.755**	(STD=2.770)
Average island lengths (μm)	**5.271**	(STD=2.784)
Number of wrinkles*	**204**	
Wrinkles per area (μm^{-2})	**0.082**	

* in an area of 50×50 μm^2

We calculated strains from >100 different wrinkles based on the height, width and thickness measurements as per equation (3). Table 5 to Table 8 present the statistical information on the width, height and length of each wrinkle measured from the AFM images. The tabulated results show anywhere between 0.2-1.3 % strains were achieved in the wrinkles. For the 35 nm film (Table 5), average strains from >100 different places suggested a 0.6 % and for 70 nm film (Table 6), strains of 0.3% calculated using equation (3).

Figure 38 presents the Raman spectroscopic measurements between flat and wrinkled actuator samples. Raman spectroscopy is a powerful tool to characterize 2D nanomaterials such as graphene and MoS_2 subjected to a uniaxial strain. Initial work by Li et al., showed coupling between electronic transitions and phonons are found to become weaker when the layer number of MoS_2 decreases, attributed to the elongated intralayer atomic bonds in ultrathin MoS_2 [101]. Figure 38 (a) presents the Raman measurements between flat and wrinkle samples measured using 532 nm laser wavelength. Clear changes in the E^1_{2g} and the A_{1g}, modes are seen between the flat and wrinkled actuators. The A_1g mode that corresponds to the sulfur atoms oscillating out-of-plane is less affected than the E^1_{2g} mode which is the sulfur and molybdenum atoms oscillating parallel to the crystal plane. The slight shift of the A_1g peak observed on the wrinkled MoS_2, and the larger Raman shift of the E^1_{2g} peak (~0.75 cm^{-1}) are in good agreement with recent reports on strain engineered MoS_2 [31].

In Chapter 4, in our few layer nanocomposites, applying global macroscopic uniaxial tensile strain of 10% using a custom made strain gadget resulted in the shift of

the E_{2g} mode by about −1.7 cm^{-1} and negligible change in A_{1g} [22]. However, those experiments were performed by measuring the Raman shift versus intensity while the strain was still held by the gadget. In the localized strain engineered sample as reported here, the Raman shift versus intensity was measured after the strain was removed from the samples. The smaller change in Raman wavenumbers may be due to relaxation of the samples after removal of the strain and possibly due to higher thickness of the films compared to few layers.

Raman mapping was conducted over large area to understand the shift in E_{2g}/A_{1g} between strained and unstrained samples. Resonant Raman scattering studies were performed at room temperature as presented in Figure 38 (b). Figure 38 b (b_1-b_2) are the optical images of unstrained (flat) and locally strained actuators showing the visible roughness of the strained sample. Figure 38 b (b_3) is the resonant Raman scattering (measured using 633 nm laser) of the strained few layer 2H-MoS_2 samples.

We have studied resonant Raman scattering of MoS_2 few layers based on number of layers in our past reports [22]. Resonant Raman spectra of the MoS_2 films, both wrinkled as well as flat, showed a complex vibrational modes structure with the same Raman features as the few-layer MoS_2. In addition to the first order E^1_{2g} (~384 cm-1) and A^1_g (~409 cm-1) peaks, the spectra contained a number of intense second-order peaks located between 360 cm^{-1} and 660 cm^{-1} Raman shifts. This includes the “b” (~420 cm^{-1}) peak associated with the emission of a dispersive quasi-acoustic phonon and simultaneously an optical E^2_{1u} phonon along the c-axis, the “c” (~380 cm^{-1}) peak due to the emission of a E^2_{1u} (Γ) phonon, and the B_{1u} (Γ) (~404 cm−1)

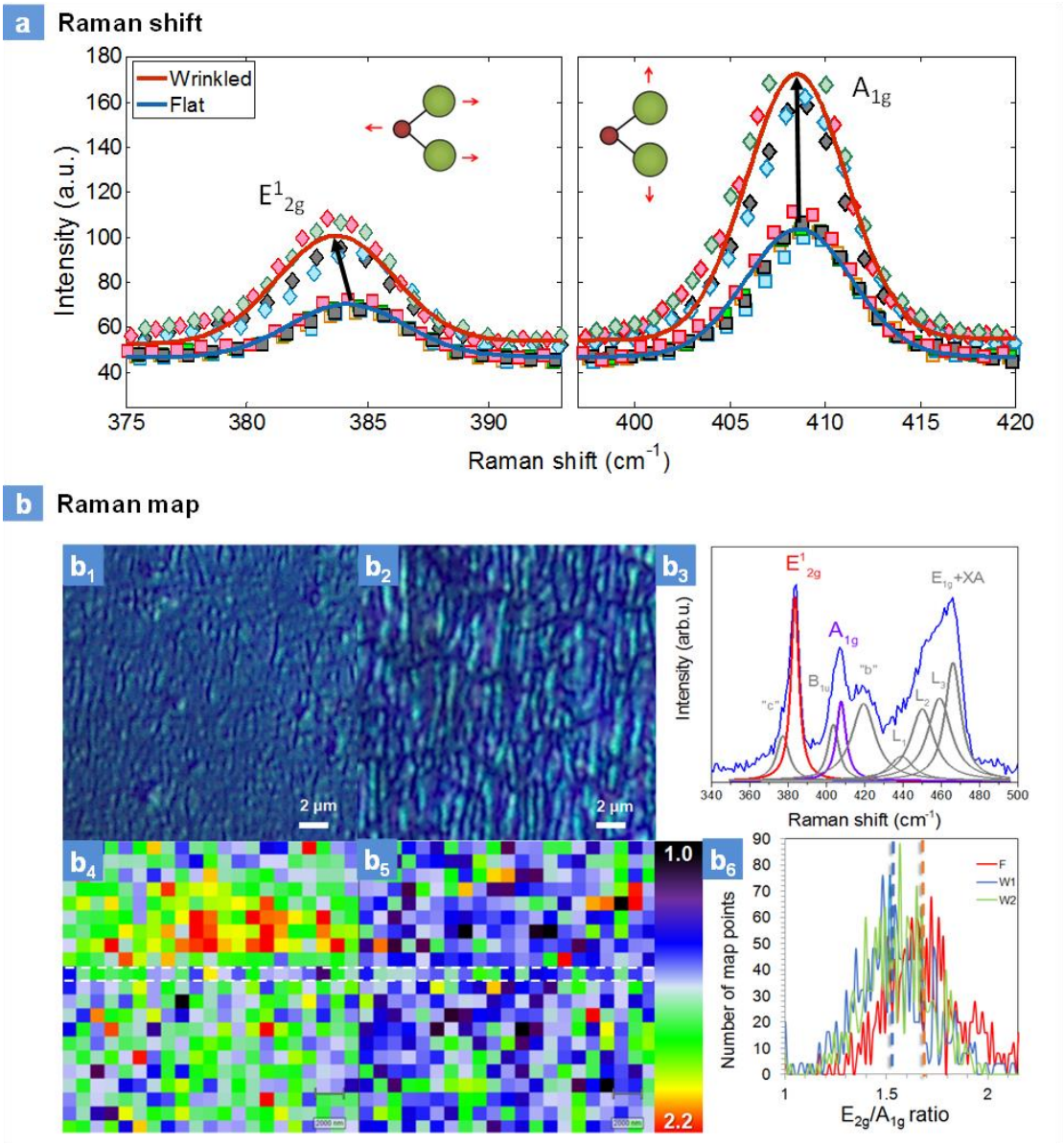

Figure 38- Raman Spectroscopy: (a) Raman shift between flat and wrinkled wrinkle architectures (excitation source: 532 nm); (b) Optical images of flat (b_1) and wrinkled (b_2) samples showing a clear difference of the strained surface; (b_3) resonant Raman scattering spectrum (excitation source: 633 nm) of the wrinkled samples showing a complex vibrational mode structure; (b_4-b_5) Raman maps of E_{2g}/A_{1g} intensity ratio recorded from 400 µm^2 areas of flat and wrinkled samples and (b_6) histograms of E_{2g}/A_{1g} intensity ratio values measured from three Raman maps (F-flat/unstrained, W-wrinkled/strained). Each histogram represents 441 pixel points.

peak, which together with the A_{1g} (Γ) peak form a Davydov couple. Several significant changes of the spectrum are observed with strains for the few layer nanocomposite.

Compared to the flat samples in Figure 38b (b_4), and Figure 39, the A_{1g}, E_{1g} + XA, and "b" peak intensities are partially increased in the strained samples. Figure 39 shows the Raman mapping of flat and wrinkled sample corresponding to the region represented by white lines in Figure 38 (b_4-b_5). For example, the "b" peak shows higher intensity for the locally strained sample compared to the unstrained flat counterparts which is an indicative of the phonon involved that has a wave vector along the c-axis. Similarly, the A_{1g} is the out-of-plane vibrational mode is affected by the strain. The non-uniformity between resonant Raman spectra of the strained samples suggests the non-homogeneity of strain in the wrinkled samples.

Raman mapping was performed, and 21 x 21 spectral maps were collected from 20 μm x 20 μm regions of flat and wrinkled samples over 16 hours as presented in Figure 38 b (b_4-b_5). The mapping of the large area of the sample showed an unambiguous reduction of E_{2g}/A_{1g} intensity ratio in wrinkled samples compared to flat actuators (Figure 38b (b_6)). The histograms of E_{2g} /A_{1g} intensity ratio values measured from three Raman maps: one flat, and two wrinkled ones, showed a good statistical evidence of this change. The average shift in E_{2g} /A_{1g} intensity ratio is about 0.2 (a change of ~11%). The decrease in E_{2g}/A_{1g} intensity ratio is indicative of strain transfer to the additives across a large area of the substrate, suggesting that this process is highly scalable for future device applications.

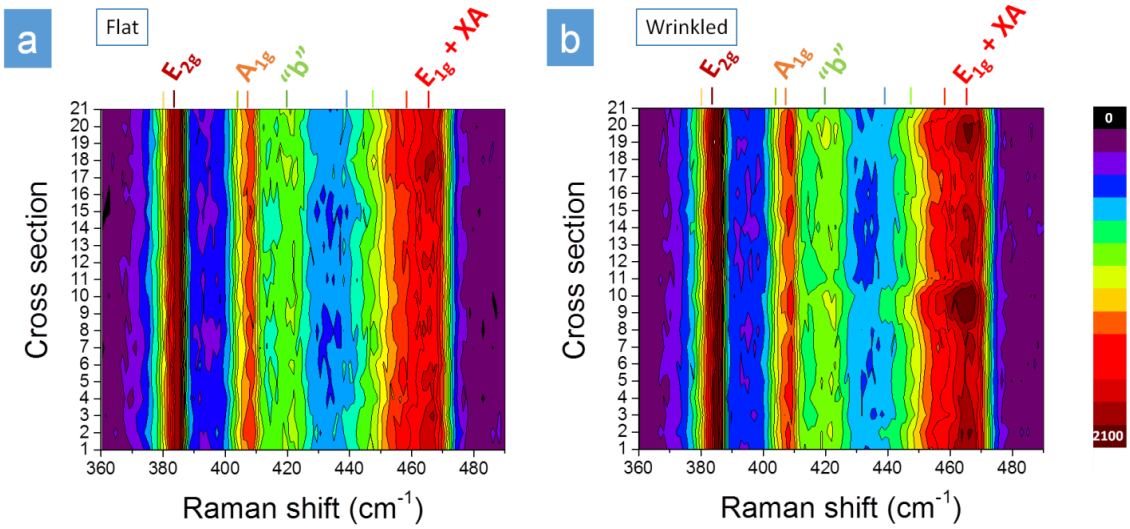

Figure 39- Raman Spectroscopy Map of Flat/Unstrained and Strained Samples: Raman profile maps from (a) flat and (b) wrinkled samples. The profiles sampling is indicated by white dashed lines in Figure 38 of the manuscript. Resonant Raman scattering was measured using 633 nm excitation source. Each profile represents 21 spectra collected each micron. The changes of A_{1g}, E_{1g} +XA and "b" peak intensities between flat and wrinkled samples are easily observable.

Photoluminescence spectroscopy is a powerful technique to unambiguously show the reduction in bandgap in TMDs with strains. Here, we see that those nanoparticle sheets does exhibit distinct PL spectrum with and without strains. Figure 41 (a) presents the schematic of the funnel effects due to exciton drift due to the strains. The top of the wrinkle is the point of the highest strain and the bottom of the wrinkle, where the strain is lowest. Thus, the wrinkle is a geometric structure where strain gradients are established from top to bottom and thus can enable exciton funneling.

Figure 40 (b) presents the photoluminescence spectra of the flat and wrinkled nanoparticle sheets. Both the samples were prepared identically, and the only difference was, application of strain for the sample exhibiting the *wrinkle* architecture. Since these sheets were 35 nm thick, we expected the photoluminescence to be small compared to single layers, to begin with even for flat sheets. However, they do exhibit distinct photoluminescence as seen in the spectra in Figure 40 (b). The flat sheets had small PL intensity. However, there was an increase in intensity and red shifting of the direct electron bandgap for the wrinkle samples. Bulk MoS_2 exhibits negligible photoluminescence as there is no direct electron transition and thus, the first thing we can observe is these sheets; they do not act like bulk materials. The photoluminescence intensity was three times stronger for the strained *wrinkle* architecture for the same thickness suggesting direct electron transition increased due to the application of mechanical deformation. Although few-layer MoS_2 is an indirect bandgap semiconductor, its photoluminescence spectrum is dominated by the direct gap transitions, at the K point of the Brillouin zone, between the valence band and the conduction band.

Here, we see that the A peak is red shifted in the photoluminescence spectra of the flat and the wrinkled samples in line with previous reports on strain engineered few layer MoS_2. Figure 40 (c) presents the bandgap shifts measured using scanning photoluminescence spectroscopy in three regions namely: top of the wrinkle, the bottom of the wrinkle and in a flat film. The insert in this figure presents a wrinkle with regions of low and high strains identified.

The strain values for over 100 wrinkles were studied and listed in Table 5, reporting strains from 0.2% to 1.3% in our wrinkles. These suggest unambiguously that the bandgap decrease of 30 meV is due to the localized strain engineering and our results agree with the literature reports [31]. The calculated values of local strain based on Equation (3) and the bandgap change in Figure 40 (a) are in good agreement with previous studies; according to the experimental data and tight binding (TB) model presented earlier by Castellanos-Gomez et al., [31], a change of −30 meV in the bandgap (A exciton) corresponds to a strain of ~1.0%. The flat samples showed a bandgap of ~1.82 eV suggesting few layers and the strain-induced bandgap was measured as ~1.79 eV, suggesting ~1.6% change in the bandgap due to mechanical deformation.

Figure 41 presents the PL measurements for both plain PDMS and MoS_2/PDMS. One can clearly see the A and B peaks in MoS_2/PDMS sample and not seen in plain PDMS sample.

Having characterized the actuators with and without strains, we investigated photo-thermal effects of flat (unstrained) and *wrinkle* (strained) actuators as presented in Figure 45. Photo-thermal stress measurements were investigated both for flat and wrinkled architectures which are presented in Figure 42. The power transmitted through the sample at different wavelengths is also presented in Figure 43. Both flat and *wrinkle* based actuators gave rise to chromatic mechanical response, i.e. a differential mechanical response at different wavelengths of light arising due to the optoelectronic

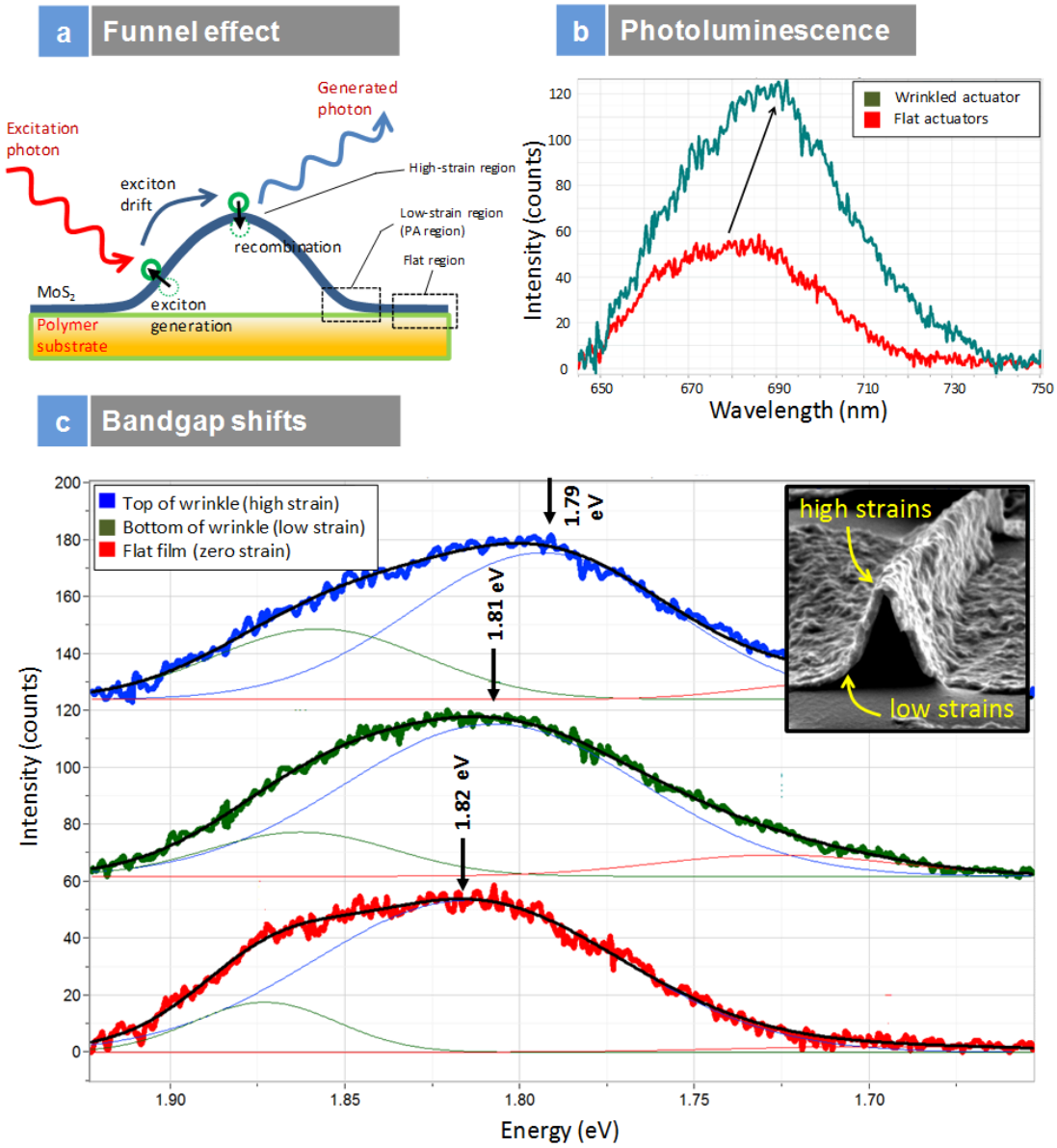

Figure 40- Scanning Photoluminescence Spectroscopy: (a) Schematic of funnel effects suggesting exciton drift; (b) PL intensity of flat and wrinkle actuators at 35 nm film thickness; (c) bandgap shifts with strains; graphs compare top of wrinkle to bottom of wrinkle and flat film; insert is SEM image of the different regions mapped using scanning PL spectroscopy.

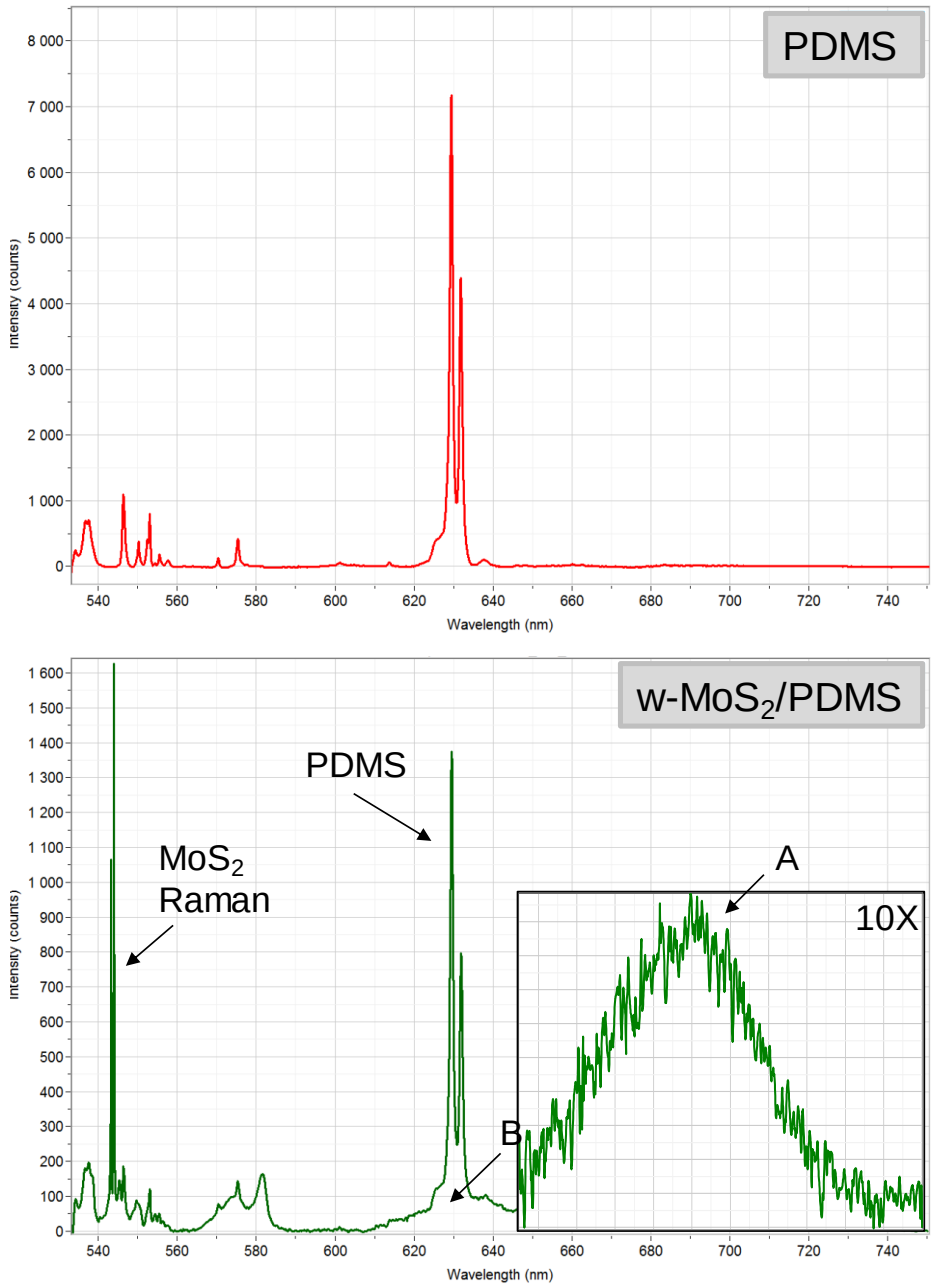

Figure 41- Photoluminescence spectroscopy of plain PDMS and MoS_2/PDMS samples.

transitions across the bandgap. This does not happen in bulk MoS_2 photomechanical actuators, where the mechanical response is insensitive to the wavelength of light [250]

suggesting that these actuators made from nanoparticle sheets do not act like bulk materials.

The chromatic absorption and subsequent mechanical response are first evidence that the semiconductor bandgap is intimately connected to the mechanical response, thus an optoelectronic-photo thermal effect. This effect also does not happen

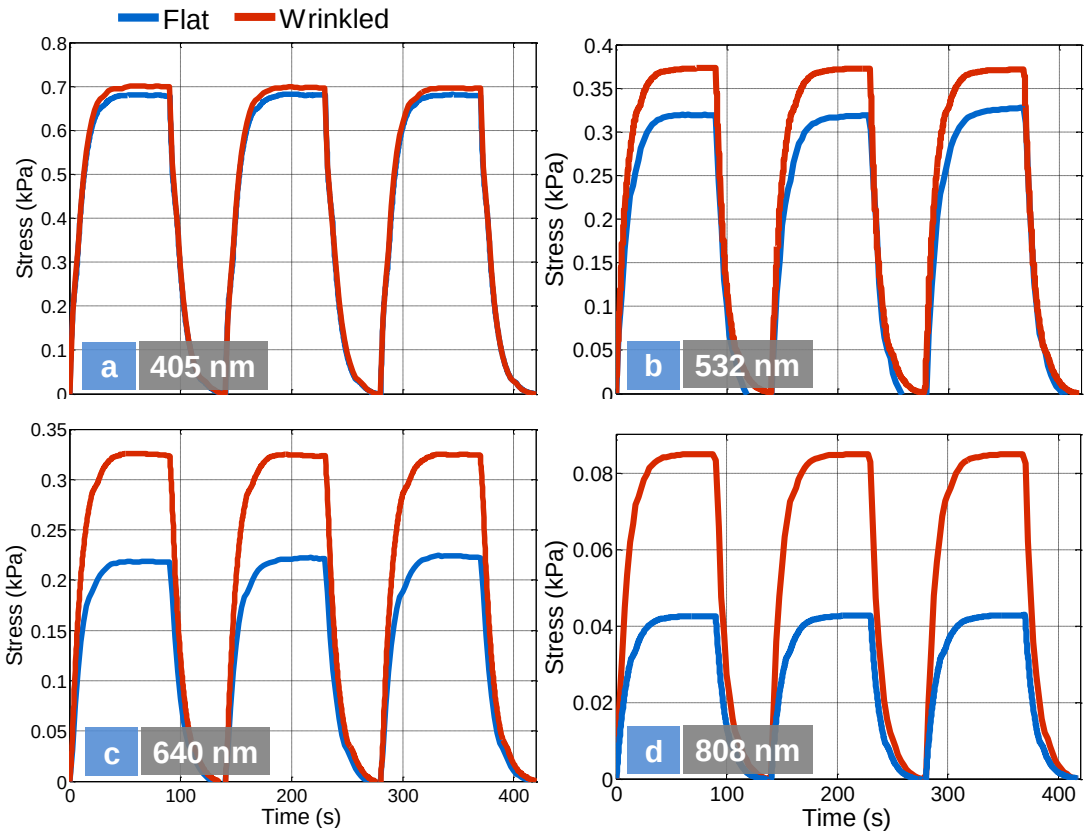

Figure 42- Tunable straintronic photothermal actuation of unstrained and strained actuators between 405 nm-808 nm photon wavelengths

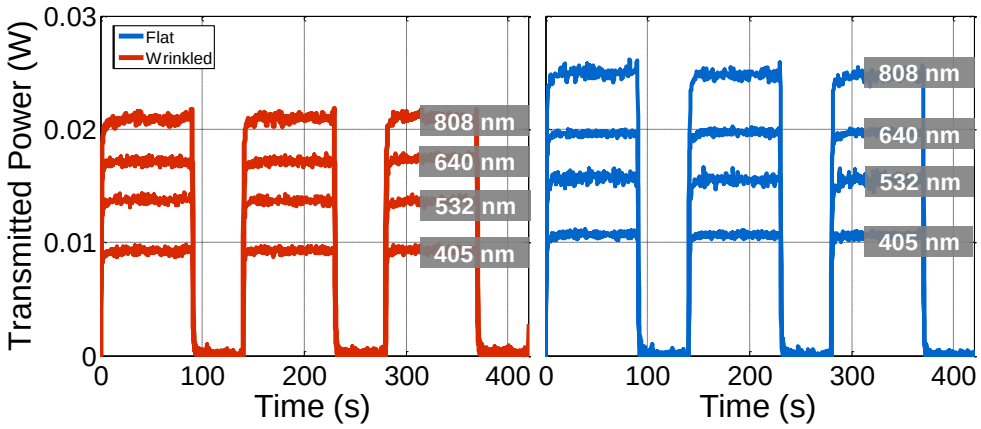

Figure 43- Transmitted power by the unstrained and strained samples at 405 nm to 808 nm wavelengths.

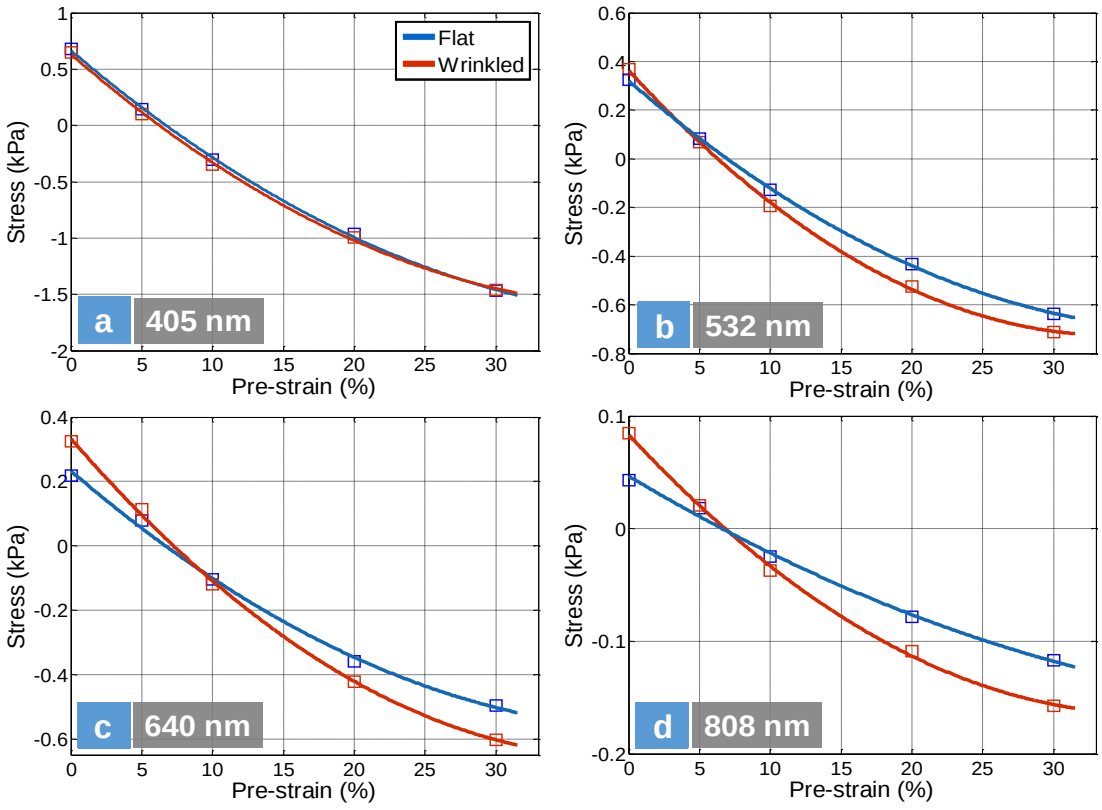

Figure 44- Photo-induced stress versus pre-strain at different illumination wavelengths for flat and wrinkled samples.

in thin film semiconductors. For these measurements, no pre-strains was applied to the sample. At 405 nm, we see that the stress was identical for both unstrained (flat) and strained (wrinkle) architectures. However, for the *wrinkle* samples, the stress was enhanced at lower photon energies between 532 nm to 808 nm. This enhancement in stress at lower photon energies can only arise from the reduction in bandgap due to strains. The thermal and mechanical effect also follows the reduction in the bandgap. The power transmitted through the samples were higher for the unstrained (Figure 43) samples suggesting more light is absorbed by the highly strained samples at all wavelengths. What is striking is the large values of mechanical stress that can be achieved through harnessing internal heat. The pre-strain tests for flat (unstrained) and wrinkled (strained) samples are shown in Figure 44.

The straintronics-photothermal effect is highly useful for millimeter scale and micro-optomechanical systems (MOMS). Figure 45 presents the photomechanical response of a millimeter scale bending actuator. Figure 45 (a) presents the schematic of the bending actuator. A laser displacement sensor was used to monitor the change in deflection of the cantilever. The actuators consisted of a layer of PDMS and thin layer of MoS_2. The thickness of the layers was 80 μm for PDMS, and 35 nm for the 2H-MoS_2 and the length of the actuator was 12 mm. The SEM image presents the cross-section of the PDMS and MoS_2 layers. The insert in the tilted SEM image presents the thousands of *wrinkles.*

Figure 45 (b) presents the displacement of the actuator between 405 nm to 808 nm of the flat nanosheet actuators and Figure 45 (c) presents the displacement of the

wrinkle actuators respectively. Remarkably, both the actuators gave rise to the same displacement at 405 nm (energy above the bandgap). Since 405 nm is much larger than the bandgap, this was expected. As we go down the photon energy, the 532 nm, 640 nm and 808 nm excitation resulted in smaller displacement for the flat actuators. The displacements between the 405 nm and 808 nm excitation are almost ten times for the flat actuators. Now coming to the *wrinkle* actuator sample as presented in Figure 45 (c), we see the same chromatic mechanical response. For the wrinkle architecture, the mechanical response was enhanced at 532 nm, 640 nm, and 808 nm excitations. The mechanical response enhancement was twice at 532 nm, 640 nm, and 808 nm. As the photoluminescence spectroscopy suggested a decrease in bandgap of 20 to 30 meV, this resulted in improved optical absorption at lower wavelengths resulting in enhanced photo-thermal response. For 1.6% change in the bandgap, the mechanical response enhancement factor is almost two. The results suggest that for lower laser energy input; we get a significantly improved mechanical output compared to the flat actuators. This type of photo-tunability of mechanical response at lower light energies has not been achieved in other photomechanical materials namely azobenzene liquid crystal elastomers, carbon nanotubes and nanoparticle based LCEs and this effect opens a new window in the design of photo-thermal systems based on coupled straintronic-photothermic effects. A practical application of this effect would be in tunable photo-thermal nanopositioning [20].

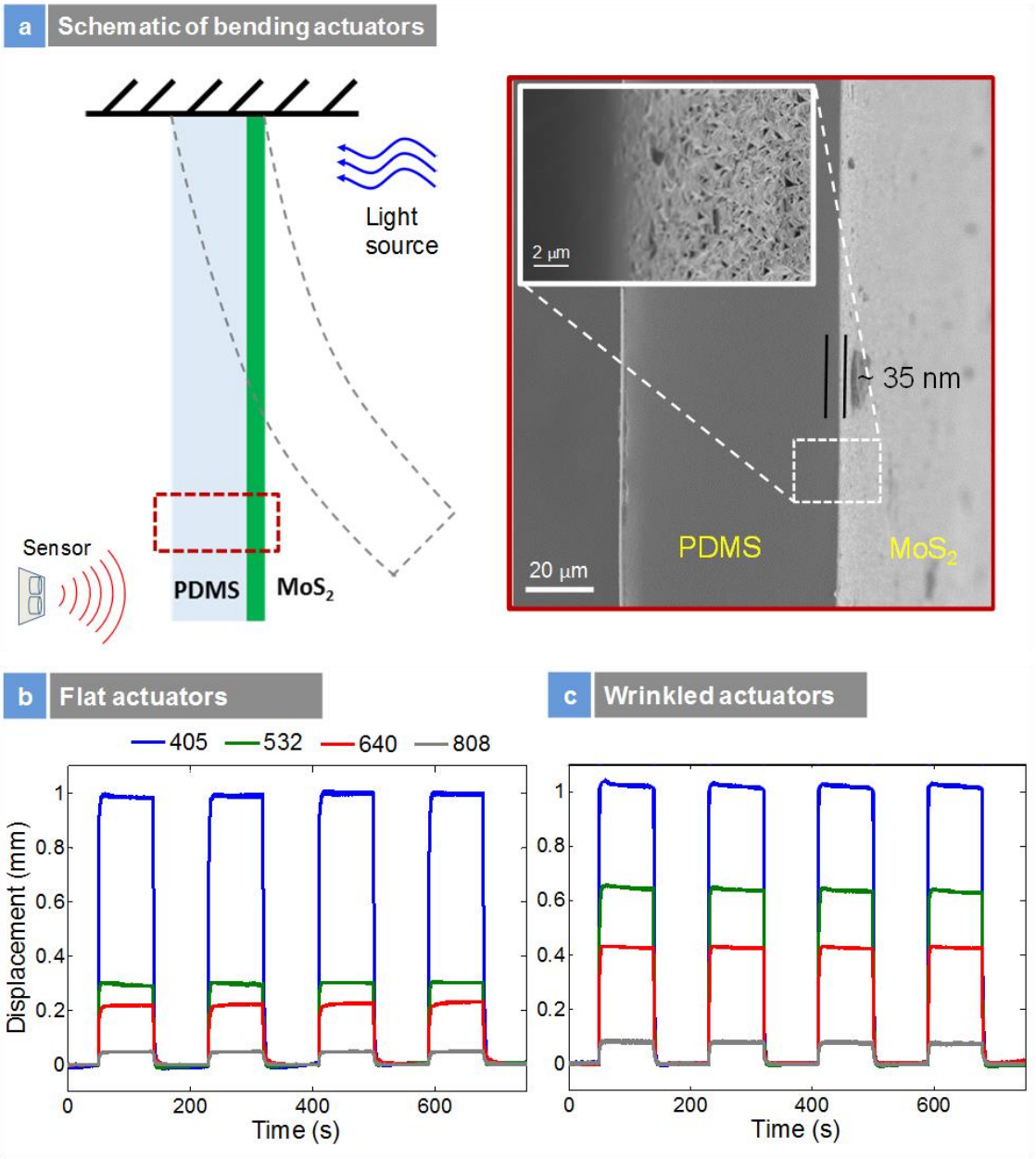

Figure 45- Straintronic Photothermal Actuation: (a) Schematic of bending actuators and corresponding SEM image; Insert show the wrinkles on polymer substrate; (b) photothermal bending of unstrained actuators between 405 nm to 808 nm; (c) photo-thermal bending of strained/wrinkle actuators.

Figure 46 presents the frequency response of the millimeter scale actuators. These actuators were 12 mm in length. The thickness of the PDMS layer was 80 μm. Figure 46 (a) presents the mechanical response amplitude versus excitation frequency for both strained and unstrained samples. An exponential decrease was observed in frequency versus mechanical response for both samples. The locally strained samples showed larger response compared to their unstrained flat counterparts at low frequencies. These actuators could be operated up to 30 Hz quite easily (Figure 47) which is a record by itself for photo-thermal actuators. While these are first demonstrations, with scaling down the actuators to microscopic scales and depending on the thermal mass, one can improve the operability of these actuators to >100 Hz. The relationship between vibrational amplitude (δ) and excitation frequency (ν) for both flat and wrinkled actuators is interpolated as:

$$\delta_F = 233e^{-0.375\nu} + 11.5\, e^{-0.02\nu} \quad (4)$$

$$\delta_W = 589e^{-0.497\nu} + 23.9\, e^{-0.04\nu} \quad (5)$$

Figure 46 (b) presents the photothermal vibration response of unstrained actuators at 0 and 5 Hz. Insert is the magnified image of the laser input and the mechanical output. The amplitude of the photothermal response is smaller for the 5 Hz actuation. The results also suggest that one can pulse the photo-thermal actuators that would be useful for programmed sensing applications using optical methods. The >100 Hz operability could enable these actuators as nanogenerators by combining piezoelectric materials for energy harvesting in low-frequency domains.

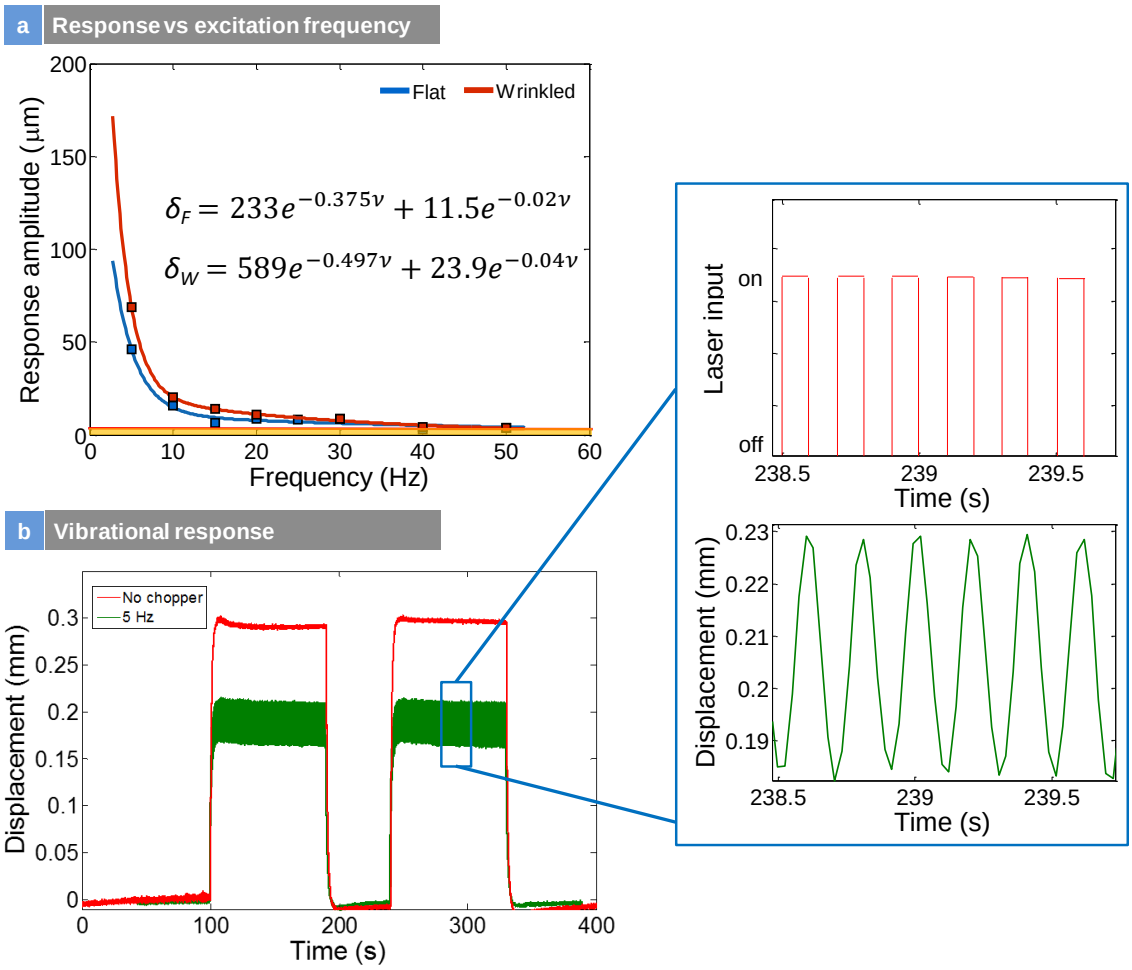

Figure 46- Frequency Response: (a) mechanical response versus excitation frequency; (b) photothermal vibration response actuation of unstrained actuators at 0 and 5 Hz; Insert is the magnified image of the laser input and mechanical output.

Figure 49 (a) and (b) are the photomechanical stress response of the flat and wrinkled actuators at various wavelengths. The average ratio of $\sigma_{UV/NIR}$ (i.e. $\sigma_{405/808}$) in Figure 49 (a) and (b) is an indication of the amplitude of the chromatic mechanical response. For a 35-nm thick film, a value of 12.09 indicates higher chromatic

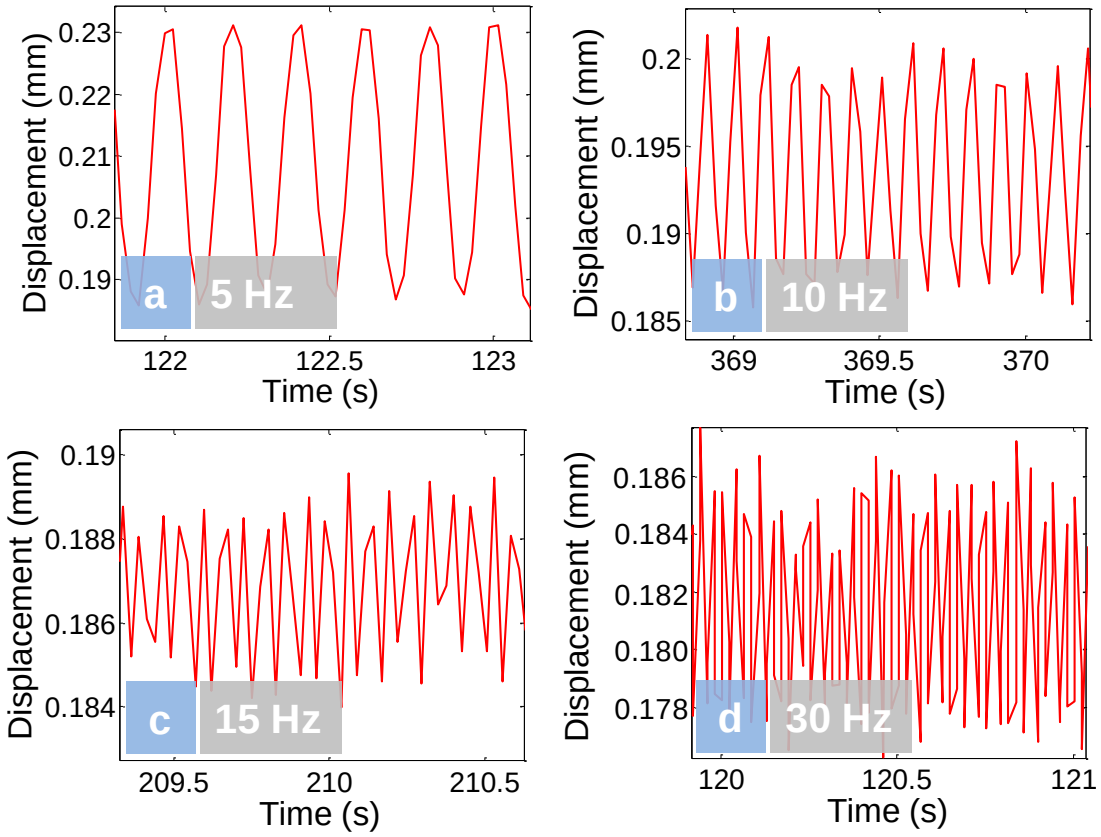

Figure 47- Straintronic photo-thermal displacement of bending actuators as a function of frequency between 5 Hz to 30 Hz.

response compared to 70-nm film with a value of 6.42, also suggesting a higher yield of few layer regions in the 35-nm sample. From these figures, different behaviors of flat versus wrinkle samples are noted; while in 35-nm film, there is a merging point between flat and wrinkle samples at higher wavelengths, there is not such a point in 70-nm film. This suggests as the thickness increases; the direct-bandgap regions are gradually losing their dominance over the indirect bandgap of bulk regions. As a result, the mechanism is gradually changing from direct bandgap absorption to electronic

polarization when increasing the thickness, resulting in disappearance of the merging point (which only occurs in locally strained regions in direct bandgap).

The inset in Figure 49 (a) and (b) is the ratio of the mechanical stress response of wrinkled versus flat samples. Both the flat and wrinkled architecture has the same pattern of the stress response versus wavelength of light. However, the increase in the ratio of mechanical stress response between wrinkled and flat samples by a factor of two in 35 nm film suggests that the wrinkle architecture samples were unambiguously effective in converting light into thermal energy and mechanical work. We also see that the ratio of the mechanical stress response between wrinkled and flat samples depends on the thickness. For the 35 nm film, a near exponential increase in stress ratio with a decrease in photon energies is seen. However, for the 70 nm film, the increase in stress ratio is approaching a linear behavior. If we plot the ratio of wrinkled to flat actuators with respect to incident wavelength and interpolate the experimental data with the following equation:

$$r=ae^{bx} \tag{6}$$

The coefficient *b* for the 35 nm and 70 nm films is 0.00178 and 0.00084, respectively. A decrease in the coefficient with the increase in thickness of thin film is observed. This shows diminishing effect of wrinkling as the thickness of nanoparticle film increases. The exponent coefficient should approach zero for adequately thick film of nanoparticles (>100 nm), where there would not be any increased photoactuation due to bandgap changes as a result of wrinkling, suggesting the thickness limits for the

straintronic-photothermal effect <100 nm. It is expected that below 35 nm thickness, this effect will be highly dominant with large amplitudes of stress and exponential mechanical response between UV and NIR wavelengths. Figure 49 (c) represents the internal force in different intensity of 640 nm light for both wrinkled and flat samples.

To determine the robustness of this actuator, we did long term experiments in line with previous reports. Figure 49 (d) presents the photomechanical stress versus time over 4 hours of continuous operation of the actuators. No drift observed, and we observe that the large-scale wrinkle actuators were stable over long periods. There are conclusions that are deduced from these long-term experiments. First, the photomechanical actuation of the locally strain engineered 2H-MoS_2 nanocomposite is fully reversible and exhibits a robust actuation mechanism. Second, the photomechanical experiments over long periods of time did not alter the structure of the wrinkles, which would otherwise cause an irreversible change in the amplitude of photomechanical actuation stress (a significant reduction in stress). This also means that the wrinkles are highly stable on the surface of the polymer substrate. Figure 48 presents the high angle SEM image of before and after applying cycles of external strains of 60% to a wrinkled sample. The resulting morphology looks the same suggesting no slip, collapse, or permanent changes to the wrinkles. We believe that as long the external strain does not exceed the initial fabrication strains of the wrinkles, they should be stable.

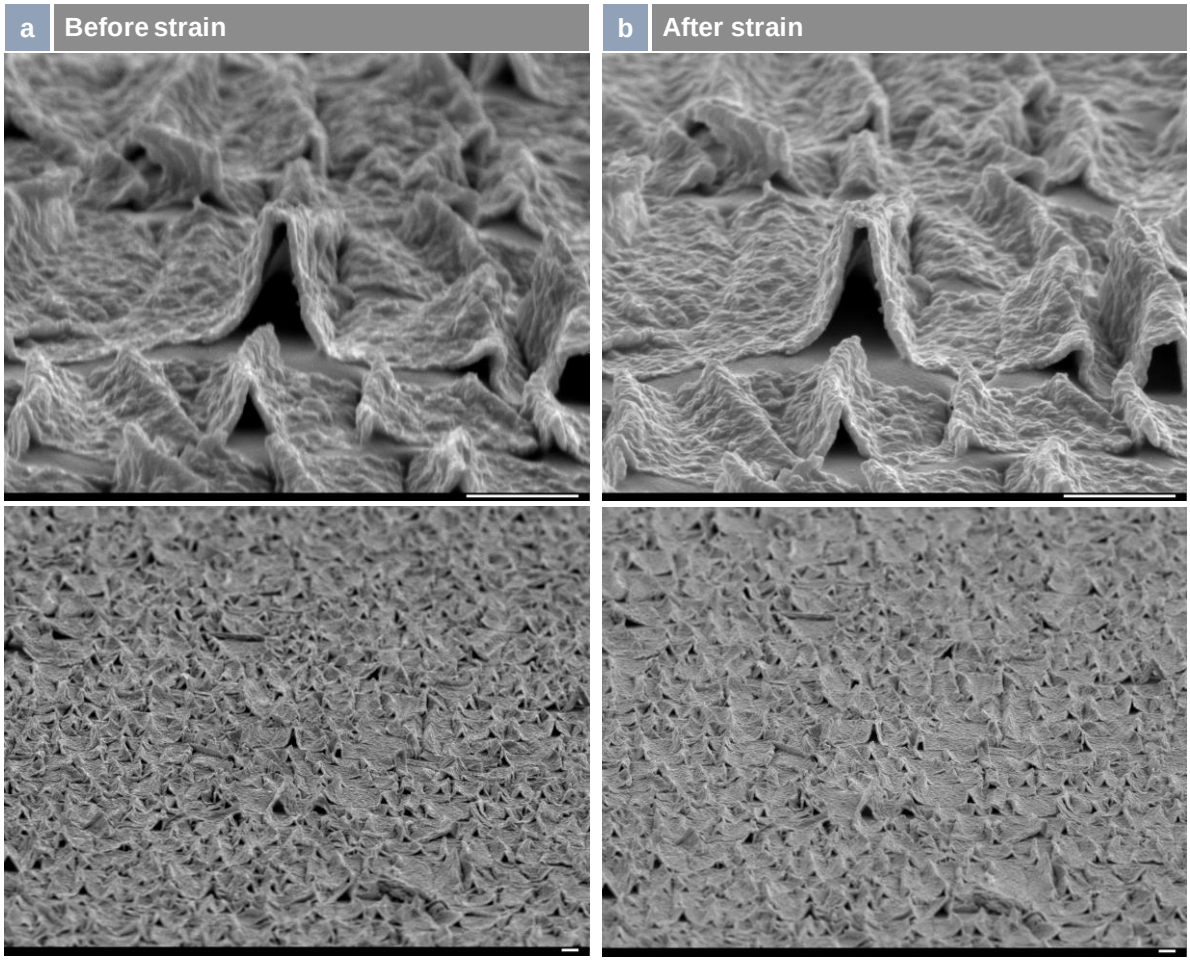

Figure 48- High angle scanning electron microscopy of wrinkles before and after applying an external strain suggesting stability of wrinkles. Scale bars show 1 µm.

5.3. DISCUSSION

In this chapter, we presented the straintronic-photothermic effect, which was the intimate coupling of strains, band gaps, optical absorption and photo thermal response in 2H-MoS_2 hyperelastic nanocomposites. Compared to applying globalized strains

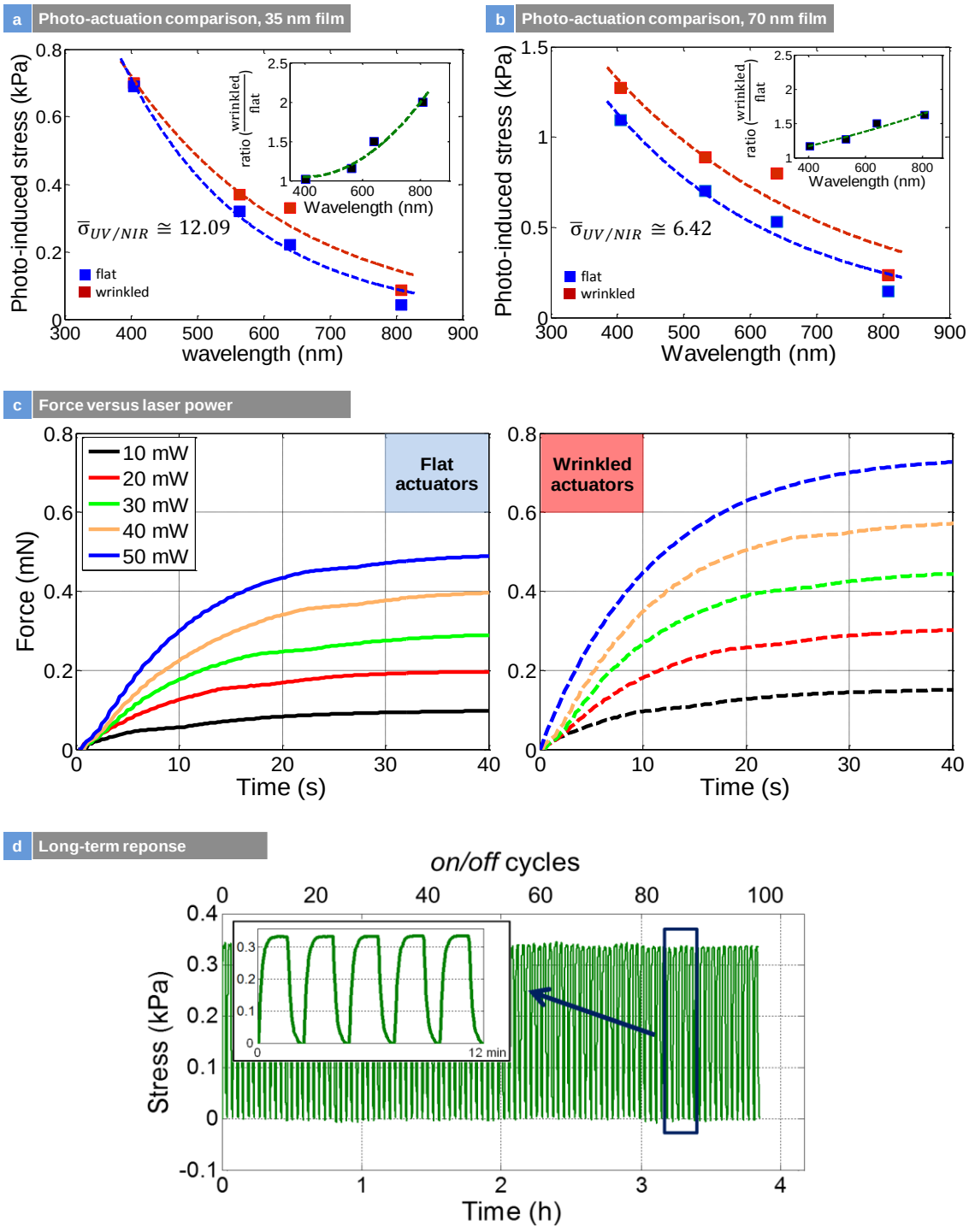

Figure 49- Photoinduced Stress, Force and Long Term Response: (a) comparison of photo-activated stress release between unstrained and strained wrinkle macroscopic hyperelastic actuators for 35 nm film; insert is the ratio of the stress between strained

and unstrained actuators as a function of photon energy; (b) same for 70 nm film; (c) Force versus laser power comparison for unstrained and locally strained actuators; (d) long term response.

with a mechanical gadget, localized nanoscale strain engineering through strain transfer from a polymer or other means is highly desirable. While change in band gaps has been used to modulate electronic properties of devices, our results are the first application of band gap effects and straintronic effects in MoS_2 for mechanical actuation. As the bandgap of 2H-MoS_2 is decreased due to localized strains, the optical absorption and the thermal and mechanical response is enhanced. The localized strains were estimated in the wrinkles accurately through an analytical strain model for van der Waals packed films based on the original work by Vella et al. [249]. The strains from 100 wrinkles showed anywhere between 0.2-1.3% strains. This model is useful for quasi-continuous films based on liquid exfoliated nanoparticles.

The photoluminescence study showed that the direct electron transition is still dominant in local strain engineered few layer additives. The shift in the A exciton resonance peak by 30 meV was clear evidence of the mechanism that the strength of the A-exciton resonance was responsible for the overall chromatic mechanical effect. Straining the layers also increased the PL intensity suggesting strains have a direct effect on the band structure in 2H-MoS_2. A new model that relates the purely thermal effect versus Gaussian photomechanical effect suggests that photomechanical actuation in TMD based nanocomposites is a chromatic thermal effect coupled to the optical

absorption of the semiconductor under strains. The straintronic-photothermal effect only occurs at thickness below 100 nm, and therefore access to nanoscale property is necessary to see this effect. Above 100 nm, bulk behavior dominates, and thus this effect vanishes completely, and strain engineering has no effect on subsequent photo-thermal response.

Combining 2D nanomaterials with hyperelastic materials provides new opportunities in photo-thermal transducers due to the high strain energy densities, high elastic modulus, and enhanced light matter interactions in these materials. We believe that 2D TMD based nanocomposites are one of the few materials to show intrinsic chromatic mechanical response as well as well as a straintronic photomechanical response with tunability of stress due to change in band gap effects, all of which can be exploited for light driven transducers on the macroscopic, millimeter and microscopic scales. In the past, graphene based hyperelastic nanocomposites have shown tunable photo-thermal response [16, 251]. However, they do not exhibit chromatic mechanical response. Compared to that, TMDs are exciting materials as they possess an intrinsic band gap at 1.8-1.9 eV, which is tunable with strains. While the wrinkles are not periodic in our study and the strain distribution is non-uniform, making the wrinkles periodic using chemical vapor deposition (CVD) of TMDs with precise control of number of layers and strain transfer can enable more repeatable wrinkled architectures for tunable photo-thermal actuation. Further, the thermal gradients between the apex and base of the wrinkles enables heat transfer into the polymer. One can also tune the thermal and mechanical response to larger wavelengths through traditional plasmonic

architectures by coating the wrinkles with 10-30 nm noble metals, resulting in exciton-plasmon interactions that can also tune optical absorption and mechanical response. This new straintronic-photothermic effect will be useful for the future development of microscopic transducers based on light, flexible straintronic devices, optoelectronics, substrates for surface enhanced Raman spectroscopy (SERS), biosensing and energy harvesting.

5.4. MATERIAL AND METHODS

5.4.1. SAMPLE PREPARATION:

Few-layer MoS_2 nanoflakes dispersed in ethanol solution was purchased from Graphene Supermarket. The lateral size of flakes was 100-400 nm, according to the manufacturer. Standard vacuum filtration process was used to deposit thin films of MoS_2 nanoflakes with different thicknesses of 25-35 nm and 60-70 nm on mixed cellulose membranes with 25 nm pore size (EMD Millipore VSWP04700). The vacuum filtration process self-regulates the deposition rate of nanoflakes on the filter membrane to produce an evenly distributed thin film of MoS_2. The thin film of MoS_2 was subsequently transferred to strained and non-strained Polydimethylsiloxane (PDMS) substrate using an acetone bath that dissolved the overlaying filter membrane.

PDMS silicone elastomer was obtained from Dow Corning (Sylgard 184). PDMS is a two part solvent-free flexible silicone organic polymer in the form of a base compound with a separate hydrosilane curing agent that acts as a cross-linker. The term cross-linking ratio refers to the ratio of PDMS cross-linker to the base compound. The

PDMS base was mixed in 1:10 ratio to the cross-linker and then deposited on a glass slide. A standard spin coating process at 600 rpm for 30 seconds produces ~140 μm thick film of PDMS on the glass slides. The PDMS films are then cured at 120 °C for 20 minutes and post-cured for an additional 12 hours at room temperature before they were cut into 50mm×8mm strips and installed in a hand-made setup for the transfer process under strain. After successfully transferring a thin and continuous film of MoS_2 to the PDMS substrate, the strain is released, resulting in a wrinkled film of 2D material on top of elastomeric substrate.

5.4.2. MICROSCOPY IMAGING:

HRTEM was conducted using an FEI Titan transmission microscope operating at 300kV. The sample was prepared by dropping one drop of exfoliated MoS_2 in ethanol solution on lacey-carbon Cu grids (Ted Pella Inc., CA). The Cu grids were dried in air to make sure there are sufficient isolated flakes to be observed. SEM images were obtained using a JEOL JSM-7000F instrument at 4 kV of power and under an ultra-high vacuum, 10^{-5} Pa. Secondary electron detector was utilized at 10 mm working distance to capture high-resolution images of MoS_2 features at magnifications as high as 100,000X. The AFM images were taken using a NaioAFM of Nanosurf in intermittent mode with a cantilever resonance frequency of ~148 kHz.

5.4.3. RAMAN AND PHOTOLUMINESCENCE SPECTROSCOPY:

The Raman measurements were performed by the excitation laser line of 532 nm using a Horiba XploRA Raman system in ambient air environment. The power of

the excitation laser line was kept below 1 mW to avoid inducing any heating effects. The laser beam was focused onto the surface of the samples using a 100X objective lens. The photoluminescence measurements were conducted by a Horiba Multiline Raman Spectrometer LabRAM HR Evolution with a 100x objective lens, 600 gr/mm, and 1% ND filter with a 532 nm excitation laser and laser power of 0.2 mW to avoid any damages to the samples.

5.4.4. RESONANT RAMAN SCATTERING AND RAMAN MAPS:

Raman analysis and mapping was performed using a Renishaw inVia Raman microscope system, equipped with a multi-channel high resolution Si-CCD camera. The measurements were performed in backscattering geometry, with a 632 nm He-Ne laser as the excitation source, and an optical filter with an incident power of ~1 mW. Raman mapping was carried out in a point-by- point mode, i.e. a full Raman spectrum was collected from each position in the selected area. The Raman maps were collected using an Leica microscope objective (50 X), and the laser spot focused on the sample to a diameter of ~1 µm. While a motorized stage moved the sample under the laser beam, spectra were successively acquired from the defined region of interest. The maps, acquired with the 1 µm step, from regions of 20 µm x 20 µm, consisted of 441 (= 21 x 21) pixels. A full Raman spectrum was collected at each pixel and the data acquisition time for a typical map was ~16 hours. Such maps were then analyzed, and the desired spectral maps were generated. First, the curve fit parameters method based on a theoretical curve fitting was simultaneously employed to all 441 Raman spectra, and a full set of spectra parameters (peak intensities, peak widths, etc.) was calculated. Then,

specific maps were generated by plotting the specific fitting parameters or their combinations, such as peak intensity ratios.

5.4.5. STRESS AND BENDING TEST EXPERIMENTS:

The stress test experiments were done using a self-made automatic photomechanical test assembly, as was reported earlier on [47]. The bending test samples consist of nanocomposites made of one 80-μm-thick PDMS layer and one 35-nm-MoS_2 layer in wrinkled and flat structures. The nanocomposites were cut in 12mm×4mm strip, and have been clamped in one end, as shown in Fig. 9. The clamping end was illuminated with different wavelengths of lasers with the same laser power of 30 mW. The displacement at the free end of the samples was measured using a high speed MicroTrak II laser displacement sensor (LTC-025-02). A custom LabVIEW program was developed to control the test equipment and collect/monitor the experimental data acquisition. All experiments were conducted in a climate-controlled laboratory.

CHAPTER 6
PHOTO- AND THERMAL- ACTUATIONS: MODELING AND ANALOGY

6.1. INTRODUCTION

To further understand the mechanism of photo-actuation of MoS_2/PDMS nanocomposites, iso-strain tests have been done in Dynamic Mechanical Analyzer (DMA-Q800 TA Instruments). A pristine PDMS sample of ~140μm thick was cut into 8 mm × 30 mm strip and placed in between DMA tension clamps. The sample was stretched to different strain levels. At each of these strain levels, a temperature ramp from room temperature to 60°C was applied to uniformly heat up the polymer sample and measure the change in the internal force of the sample because of the thermal actuation of PDMS at a fixed length.

In Figure 50, the trend in thermal actuation of pristine PDMS is very similar to photo-actuation of MoS_2/PDMS nanocomposites. This suggests that MoS_2 wrinkles act as photo-thermal energy transducing agents that absorb the light energy depending on the bandgap and convert it to thermal energy. The thermal energy is transferred to polymer chains of PDMS, making them expand or contract due to entropic elasticity. Similar to photo-actuation behavior [16], there are three different regimes in the thermal actuation process: expansion, contraction, and zero-actuation regions. In small pre-strains (0-5%), heating of the sample leads to increase in length, i.e. decrease in the internal stress of the PDMS strip. At medium pre-strains (5-10%), heating does not have a significant effect due to the balance between entropic forces and thermal energy keeping the stress level at zero. At high pre-strain values (10-60%), heating results in

significant contraction of the sample, i.e. an increase in the internal stress of the polymer strip. PDMS is a hyperelastic polymer where the stress is derived from the strain energy function. Combining such hyperelastic material with ultra-large strength materials can enable a significant amount of stored strain energy that is released on photo-excitation.

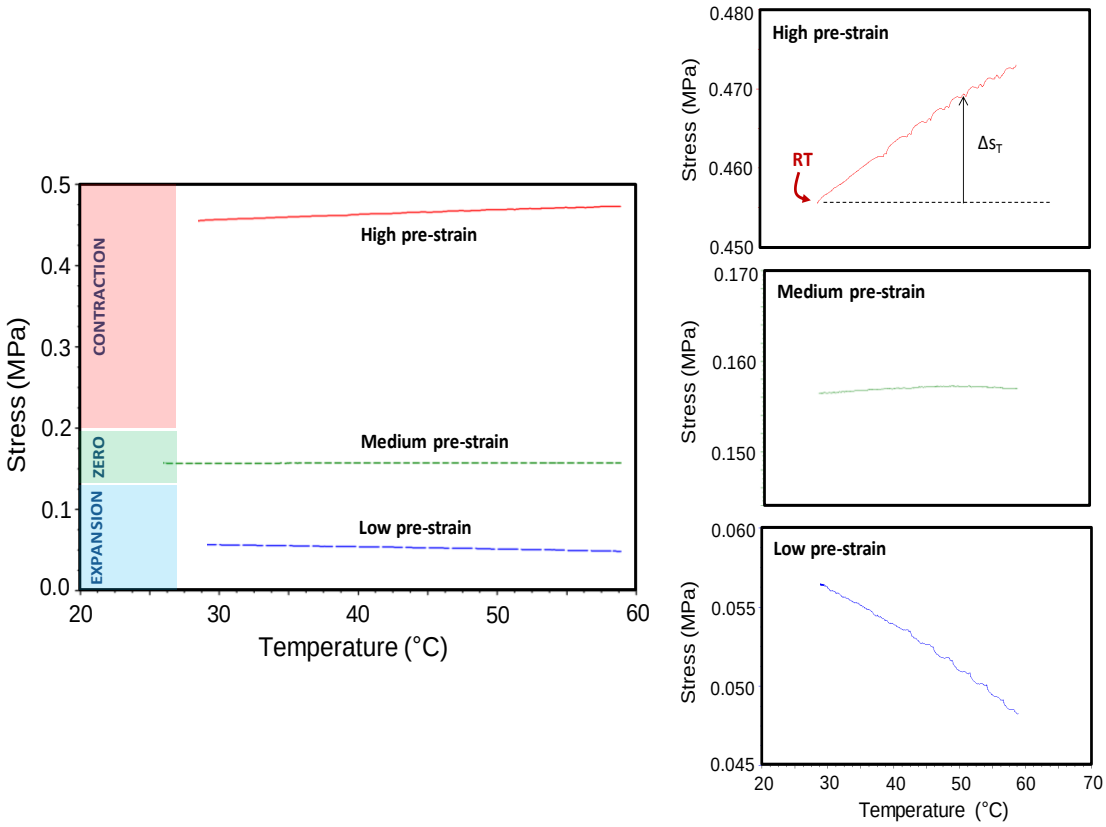

Figure 50- Stress versus temperature profile of plain PDMS using DMA. Three different regions namely contraction, zero stress and expansion are presented.

6.2. PHOTO- AND THERMAL- ACTUATION ANAOLOGY: A MATHEMATICAL MODEL

We developed a new mathematical model for the thermal and photo-thermal actuation by modeling it as uniform and Gaussian response to predict the temperature profile of unstrained and strained actuators. If we consider a specific actuation stress (Δs) resulted from photo-actuation of MoS_2/PDMS nanocomposites, and assuming the same amount of actuation Δs happens in pristine PDMS by heating up the sample, an equivalent temperature rise in the photo-actuation process is found by heat-induced temperature rise in DMA. Although the mechanism in both heat induced and photo induced actuation is purely thermal, the heat-induced stress resulting from thermal experiments in DMA is due to a uniform distribution of temperature (ΔT_u) around the polymer sample. As a result, the uniformly distributed temperature rise corresponded to this thermally induced Δs must be equalized to a Gaussian-distribution temperature profile (ΔT_n), which is the case for a pointed laser photo-actuation of MoS_2-based nanocomposites.

$$\Delta s^H = \Delta s^P = \Delta s \tag{7}$$

$$\Delta s \propto \Delta T_u \propto \Delta T_n \tag{8}$$

where *H* denotes heat-induced actuation, *P* photo-induced actuation, *u* uniform distribution, and *n* Gaussian distribution. Figure 51 shows a common experimental diagram for thermally induced actuation of pristine PDMS. The amount of heat

transferred to the polymer chains because of temperature rise in the actuators is stated by the following equation:

$$Q = mC_p\Delta T \tag{9}$$

where C_p is the specific heat capacity of the polymer. If we consider the steady state part of the thermal actuation and assume a uniform temperature profile along the thickness for thin samples, then we can dual integrate the heat profile along the length and width of the samples and find the relationship between ΔT_n in photo-actuation setup and heat-induced ΔT_u in DMA. Assuming, that the transduced Q for both mechanisms is the same, the change in the temperature has an inverse relationship with the mass of the exposed part of the actuator. If we integrate the temperature profile along the exposed surface of the actuators in the two mechanisms, then:

$$m_u\Delta T_u = m_G\Delta T_n \tag{10}$$

$$\int_{-w/2}^{w/2}\int_{-L/2}^{L/2}\rho_u t_u\Delta T_u dx\,dy = \int_{-w/2}^{w/2}\int_{-L/2}^{L/2}\rho_G t_G\Delta T_n dx\,dy \tag{11}$$

where *dx* and *dy* are the differential length and width elements, ρ the density, and *t* the thickness. From experimental data on MoS_2 based nanocomposites, the distribution of temperature change along the sample in photo-actuation is represented as a Gaussian distribution. The two-dimensional temperature relationship in photo-actuation is expressed by the following equation.

$$\Delta T_n(x,y) = ce^{-\frac{(x-\mu_x)^2}{2\sigma_x^2}}\ e^{-\frac{(y-\mu_y)^2}{2\sigma_y^2}} \tag{12}$$

where μ is the mean, σ the standard deviation and c a constant. In our photo-actuation system, μ is equal to zero for both x and y directions since the coordinate origin is placed at the center of the sample where the laser hits the nanocomposite. Experimental results for MoS_2/PDMS nanocomposites show that the square root of variance value ($2\sigma^2$) is approximately equal to the diameter of laser beam hitting the sample and is around 3.15, as reported in Rahneshin *et al.* [22]. Constant c is directly dependent on the value of photo-induced stress, which itself is a function of different parameters such as laser power, laser wavelength, the thickness of TMD layer, and geometrical pattern of the thin film. Substituting Equation 12 into Equation 11 and integrating over the volume of the sample yields the equivalent temperature relationships.

$$LW\Delta T_u = -2\pi c\sigma_x\sigma_y \left(erf\left(\frac{2\mu_x - L}{2\sqrt{2}\sigma_x}\right) - erf\left(\frac{\mu_x}{\sqrt{2}\sigma_x}\right)\right)\left(erf\left(\frac{2\mu_y - w}{2\sqrt{2}\sigma_y}\right) - erf\left(\frac{\mu_y}{\sqrt{2}\sigma_y}\right)\right) \tag{13}$$

$$c = \frac{-LW}{2\pi\sigma_x\sigma_y \left(erf\left(\frac{2\mu_x - L}{2\sqrt{2}\sigma_x}\right) - erf\left(\frac{\mu_x}{\sqrt{2}\sigma_x}\right)\right)\left(erf\left(\frac{2\mu_y - w}{2\sqrt{2}\sigma_y}\right) - erf\left(\frac{\mu_y}{\sqrt{2}\sigma_y}\right)\right)} \Delta T_u \tag{14}$$

Substituting Equation 14 into Equation 12 gives the equivalent temperature rise in the photo-actuation mechanism.

$$\Delta T_n(x,y) = \frac{-LW\, e^{-\frac{(x-\mu_x)^2}{2\sigma_x^2}}\, e^{-\frac{(y-\mu_y)^2}{2\sigma_y^2}}}{2\pi\sigma_x\sigma_y\left(erf\left(\frac{2\mu_x-L}{2\sqrt{2}\sigma_x}\right)-erf\left(\frac{\mu_x}{\sqrt{2}\sigma_x}\right)\right)\left(erf\left(\frac{2\mu_y-w}{2\sqrt{2}\sigma_y}\right)-erf\left(\frac{\mu_y}{\sqrt{2}\sigma_y}\right)\right)}\ \Delta T_u \quad (15)$$

Thus, this equation for the first time describes the relationship between purely thermal actuation and photo thermal actuation. However, it should be noted that the thermal actuation takes almost 20 minutes for uniform temperature equilibration in DMA compared to photo-actuation which takes about 5-10 s for stress to saturate.

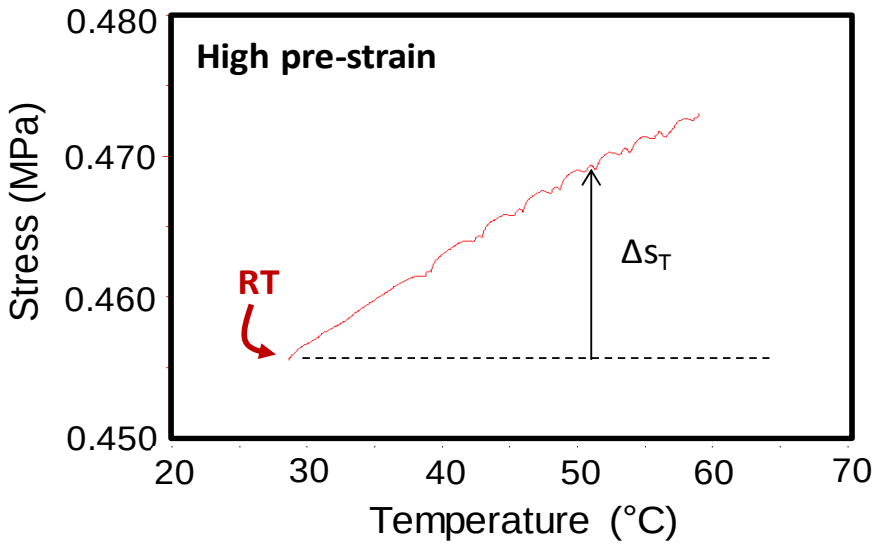

Figure 51- Stress versus temperature profile of plain PDMS using DMA. High strain region.

6.2.1. APPLICATION OF THE MODEL TO EXPERIMENTAL DATA

To verify the presented mathematical model, this model has been applied to the experimental data obtained earlier in chapter 5. Few-layer MoS_2 composite sample was placed between DMA clamps in tension mode. Iso-strain tests were conducted at zero percent pre-strain value. At this pre strain, a temperature ramp from room temperature to 60°C was applied to uniformly heat up the polymer sample and measure the change in the internal force of the sample because of the thermal actuation of PDMS at a fixed length. To corroborate the model, both *wrinkle* and flat MoS_2/PDMS nano composites were tested for heat-induced actuation in DMA TA-Q800 as presented in Figure 52. Obviously, both samples show similar thermal actuation, as in heat-induced actuation the polymer chains are responsible for induced stress, which is the same in both samples. From these results, a corresponding ΔT_n for each of photoinduced stress values of wrinkle and flat samples is obtained.

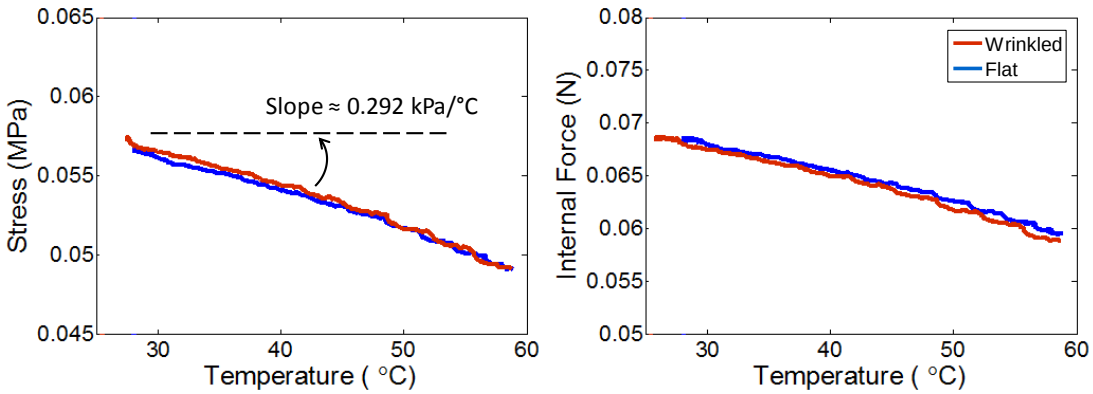

Figure 52- Stress versus temperature profile of unstrained and strained MOS_2/PDMS samples using DMA.

Figure 53 presents the predicted temperature profiles based on our mathematical model for the unstrained and strained actuators at different wavelengths. The temperature of the sample as a function of the wavelength of the light for unstrained actuators was predicted as 35 °C (405 nm), 29 °C (532 nm), 27 °C (640 nm) and 23.9 °C (808 nm). The room temperature is 23 °C as a reference. For the strained actuators, the temperature of the sample as a function of the wavelength of the light was measured as 35 °C (405 nm), 29.9 °C (532 nm), 29 °C (640 nm) and 24.6 °C (808 nm). At 405 nm both give rise to the same temperature profile according to equation 13. However, between 532 nm to 808 nm, the locally strain engineered wrinkle samples gave rise to a higher temperature profile compared to the unstrained actuators. At the nanoscale, it is expected that the apex region of the wrinkle may enable higher temperature compared to flat surface. It is expected that thermal gradients exist between apex and base and heat is flowing from the apex to the base. The wrinkles have MoS_2 layers partially directed with an angle to the surface of the polymer, which directs the generated heat of highly strained regions of the apex to the flat region, and to the polymer underneath.

Looking into the stress data further in Figure 42, for instance, a photo-actuation of around 0.65 kPa for both flat and wrinkle actuators at 405 nm excitation wavelength will lead to a 2.6°C temperature rise for ΔT_u. This temperature rise is the uniformly distributed temperature, which is needed to generate an actuation of 0.65 kPa in heat-induced actuation. Using Equation 15 and the corresponding μ and σ values for these experiments, the equivalent temperature profile along the sample can be easily obtained. Table 9 lists the change in temperature values for wrinkle and flat samples at

different excitation wavelengths at the center of samples (*x=y=0*). The temperature profiles along the length of the samples are also depicted and compared for both wrinkle and flat photo-actuator. The wrinkled sample is predicted to give rise to a significantly increased temperature compared to their flat counterparts on photoactivation, resulting in significantly improved mechanical response.

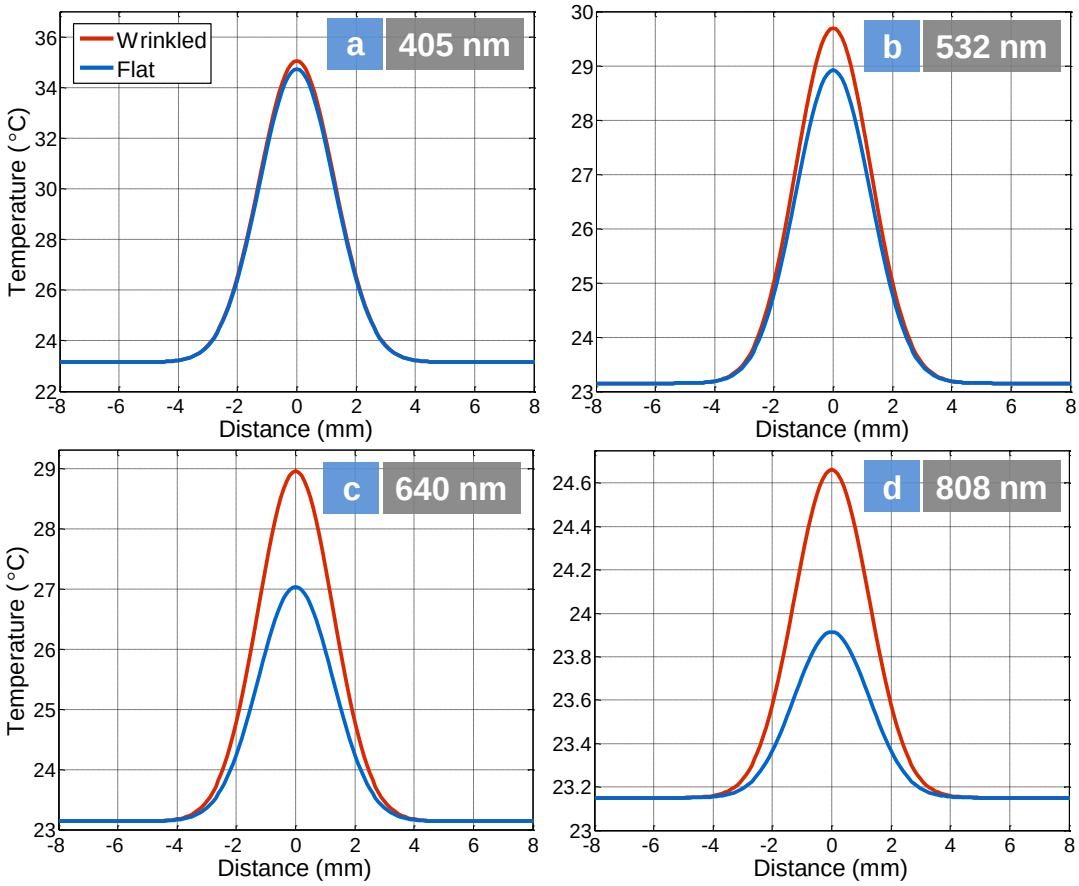

Figure 53- Simulated Temperature Profile: Gaussian temperature profile of wrinkle and unstrained actuators at different wavelengths: (a) 405 nm; (b) 532 nm; (c) 640 nm and (d) 808 nm.

Table 9- Change in temperature comparison in heat-induced and photo-induced actuation for unstrained and strained wrinkle samples

	Δs (kPa)		**ΔT_u (°C)**		**ΔT_n (°C)**	
	wrinkled	***flat***	***wrinkled***	***flat***	***wrinkled***	***flat***
405 nm	0.67	0.65	2.29	2.22	11.93	11.58
532 nm	0.3675	0.3239	1.26	1.11	6.55	5.76
640 nm	0.3259	0.2185	1.12	0.75	5.8	3.89
808 nm	0.0849	0.0429	0.29	0.15	1.51	0.76

6.3. ANALYTICAL STRAIN MODEL FOR VAN DER WAALS PACKED FILMS OF NANOPARTICLES

Wrinkling and delamination of thin films adhered to a polymer substrate was studied earlier by Vella et al [109]. The wrinkle profile for such films can be approximated by a cosine function in the form of the following equation [109]:

$$w = f(x) = \frac{\delta}{2}\left[1 + cos\frac{2\pi x}{\lambda}\right] \quad (16)$$

where δ and λ are the height and width of the wrinkle. According to the classical theory of elasticity of plates developed by Lagrange, the stress and strain in an incremental element with an arbitrary small deflection w(x, y) can be stated as [252]:

$$\varepsilon_x = \frac{\partial u}{\partial x} \quad , \quad \varepsilon_y = \frac{\partial v}{\partial y} \quad (17)$$

$$\sigma_x = \frac{-Ez}{(1-\nu^2)}\left(\frac{\partial^2 w}{\partial x^2} + \nu\frac{\partial^2 w}{\partial y^2}\right) \quad (18)$$

$$\sigma_y = \frac{-Ez}{(1-\nu^2)}\left(\frac{\partial^2 w}{\partial y^2} + \nu\frac{\partial^2 w}{\partial x^2}\right) \quad (19)$$

where:

$$u = -z\frac{\partial w}{\partial x} \quad , \qquad v = -z\frac{\partial w}{\partial y} \quad (20)$$

with z the distance from the mid-plane of the plate. For a curved plate, the radius of curvature κ_x at an arbitrary point can be calculated based on the following equation:

$$\frac{1}{\kappa_x} = \frac{-\frac{\partial^2 w}{\partial x^2}}{\left\{1+\left(\frac{\partial w}{\partial x}\right)^2\right\}^{3/2}} \quad (21)$$

In composite films of nanoparticle, the radius of curvature of individual components, especially those inside the film, can be assumed equal to that of the film. As a result, based on the radius of curvature κ_x, the strain in each individual nanoparticle can be estimated as:

$$\varepsilon_x = \frac{z}{\kappa_x} \quad (22)$$

Introducing Equation 16 into Equations 21 and 22, the radius of curvature and strain in each individual nanoparticles at an arbitrary part of the wrinkle can be found as:

$$1/\kappa_x \cong -\frac{2\pi^2\delta}{\lambda^2} cos\frac{2\pi x}{\lambda} \quad (23)$$

$$\varepsilon_x(x,z) \cong -\frac{2\pi^2 z\delta}{\lambda^2} cos\frac{2\pi x}{\lambda} \quad (24)$$

with *x* being the horizontal distance from apex of the wrinkle and z the distance from the mid-plane of the individual nanoparticle (Figure 54).

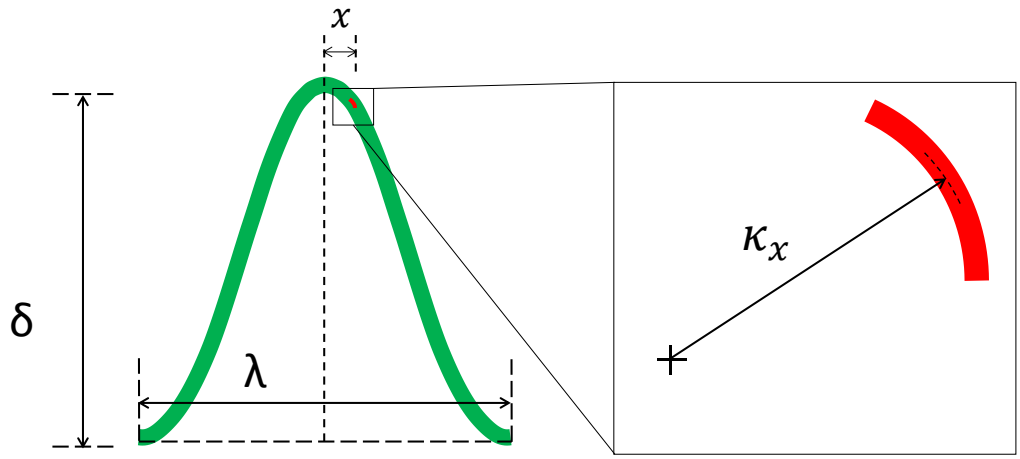

Figure 54- Schematic of wrinkle geometry and an individual nanoparticle at an arbitrary location x with a radius of curvature κ_x

CHAPTER 7
INKJET PRINTING OF 2D NANOMATERIALS: DEVELOPMENT OF VERSATILE HIGH PERFORMANCE PAPER-BASED PHOTO-ACTUATORS

7.1. WATER-BASED INKJET PRINTING OF 2D MATERIALS

The need for simple, versatile, and low-cost manufacturing techniques for the fabrication of functional devices is crucial in new and flexible electronic and optoelectronic industries. The ever-increasing advances in the area of 2D materials urge a need for such techniques. Although the technology in the area of microfabrication and photolithography are fully mature, it is both time-consuming and expensive when it comes to fast advancing new technologies. Inkjet printing of 2D materials is a new and rapidly growing field to overcome such challenges in order to manufacture functional devices [253-255]. Since the discovery of Graphene [54] and the emergence of methods for separation of layers of 2D materials in large quantities, such as liquid phase exfoliation [73], the inkjet printing seems like an attractive field to low-cost and large-scale fabrication of devices based on 2D materials. Current state of the art in inkjet printing still suffers from practical challenges as they are either based on toxic solvents, needs substrate functionalization, need high drying temperatures, or require laborious formulation processing [256, 257]. A new practical inkjet formulation which is both non-toxic and biocompatible and capable of printing multilayer stacks of heterostructures, along with the access to a mass production method of high-quality few and mono layers of nanosheets, would benefit the fields of electronics and optoelectronics in the applications such as large area arrays of photosensors, programmable logic memory devices, transparent, flexible and wearable technologies,

and biomedical applications [73, 143]. In addition, unlike traditional methods such as vacuum filtration or spin or spray coating, the inkjet-printed heterostructures do not suffer from poor control of thickness or limited design flexibility [143, 258]. In this chapter, we use a water-based and biocompatible ink formulation based on McManus *et al.* [143] and Yang *et al.* [259], along with inkjet printing technology with a Dimatix Inkjet Printer, to fabricate inkjet-printed paper actuators, which transduce light into mechanical motion.

7.2. WATER-BASED EXFOLIATION AND INK FORMULATION

The inks developed for inkjet printing in this chapter are fully biocompatible and based on non-toxic materials with the applicability of use in bio applications. The inks formulation is based on McManus *et al.* [143]. Water is used as a biocompatible exfoliating agent as well as the ink solvent. Since water is not a good exfoliating agent, nor a proper inkjet printable solvent, its properties must be modified through addition of surfactants and additives.

The starting point for ink development is the liquid phase exfoliation of nanoparticles of different 2D materials. MoS_2 nanopowder was purchased from Graphene Supermarket, and Graphite Flakes from Alfa Aesar. Deionized water is used as the exfoliating agent, and 1-pyrenesulfonic acid sodium salt (Sigma-Aldrich) is added to it as a surfactant to lower the surface tension and increase the stability of exfoliated nanosheets [126, 259, 260]. We observed at least eight months stability in our exfoliated solutions without any sedimentation. The exfoliation process takes 72

hours of ultrasonication in a bath sonicator (Cole-Parmer 08895-75), followed by 20 minutes of centrifugation at ~900g centrifugal force. The top part of each vial is then collected for further process. To increase the concentration of the inks, a high-speed centrifugation at a Sorval RC-5 Refrigerated Superspeed Centrifuge at ~16,000g centrifugal force is done, and the precipitate is collected for further processing. If need be, a washing step similar to Yang's method [259] can be done using a ~16,000g centrifugal force, to remove extra surfactants or change the solvent. This high concentration precipitate is then added to the printing solvent. The printing solvent consists of 0.1 gram of propylene glycol (Sigma Aldrich) for each gram of deionized water, 0.06 mg ml^{-1} Triton X-100 (Sigma Aldrich), and 0.1 mg ml^{-1} Xanthan Gum (Sigma Aldrich). This combination of additives makes the 2D nanosheets printable. Propylene glycol acts as a co-solvent to increase the viscosity of the inks [143]. Triton X-100 acts as a surface tension modifier, which decreases the surface tension of deionized water.

Although the generation of droplets in inkjet printers are a complex process and precise physics and fluid mechanics of this process are still under research [261], the behavior of drops can be characterized by a dimensionless parameter, i.e. the inverse of Ohnesorge number (*Oh*) [262]. Ohnesorge number is a dimensionless ratio between viscous force to inertial and surface tension forces, and is expressed in terms of Reynolds (*Re*) and Weber (*We*) numbers [262, 263].

$$Re = \frac{\nu \rho a}{\eta} \tag{25}$$

$$We = \frac{v^2 \rho a}{\gamma} \tag{26}$$

$$Oh = \frac{\sqrt{We}}{Re} = \frac{\eta}{(\gamma \rho a)^{1/2}} \tag{27}$$

where γ is the surface tension, η dynamic viscosity, ρ density, v velocity, and a a characteristic length. Reis and Derby initially proposed that in order to achieve stable droplets, the inverse of Ohnesorge number (expressed as Z number) should be in the range $1 < Z < 10$ [264]. The Z number for pure deionized water is ~40, and the overall effect of propylene glycol and triton X-100 lowers the Z number to a value of around 20 for an orifice size of 21.5 µm (i.e. the case for our Dimatix material printer nozzles). McManus *et al*. has shown that despite $Z > 10$, the droplets are still stable and no satellite effects or nozzle blockage are observed [143]. Similar reports for stable inks with Z values higher than 10 have been reported in the literature for N-methyl-2-pyrrolidone- and ethylene glycol- based inks [256, 257].

The use of propylene glycol in the inks also causes the disruption of Marangoni flows and reduction of Coffee Ring depositions [265]. Coffee ring effect is a common phenomenon happening when a droplet of a liquid, such as coffee, dries and leaves ring shape structures of the solute deposits instead of a uniform spot [266]. For a wide range of solvents, solutes, and surfaces, particles dispersed in a drying droplet flows toward the edges of the droplet and leave ring-like stains there [267]. The thermal and concentration gradients, which are caused by the evaporation process, are responsible for a circulating flow driven by surface tension gradients (Marangoni flow) inside the droplet [266]. For some other cases, the coffee ring deposition happens at the center of

droplet rather than the edges [265]. The Marangoni flow transports particles which are close to the free surface of the liquid toward the top, and then downward toward the center of the droplet, where they can adsorb to the surface at that point or continue moving toward the edges of the droplet before adsorbing to the surface (Figure 55) [265]. Xanthan Gum is added to the inks as a binder, to minimize re-dispersion of printed flakes, which allows for printing hetero structures. This also makes the ink a non-Newtonian fluid with shear-thinning properties [143].

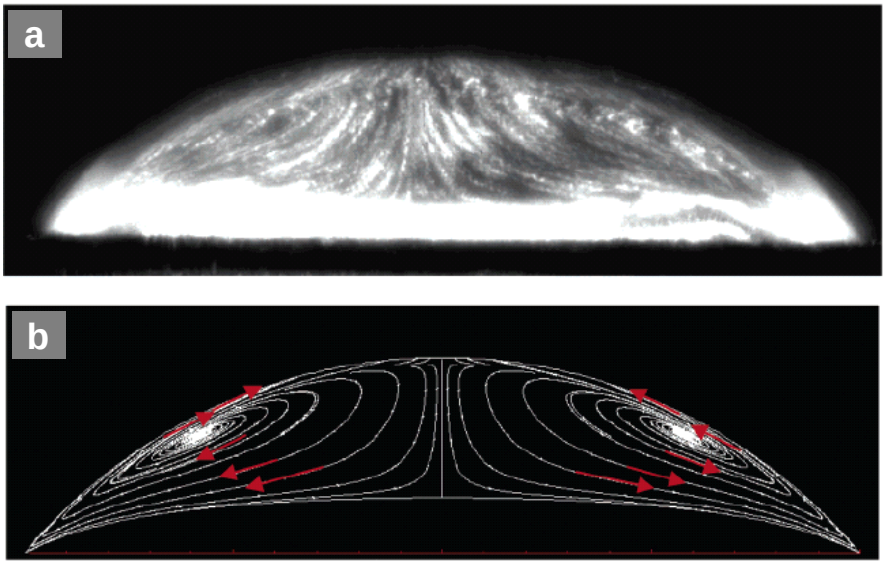

Figure 55- Flow field (Marangoni flow) in a drying droplet, (a) experimentally obtained, and (b) simulated [265].

7.3. INKJET PRINTING TECHNOLOGY

After developing the printable inks as discussed in previous section, we have used a Dimatix Material Printer DMP-2800 to print various patterns on a number of different substrates (Figure 56a). Inkjet printing have been used in many applications in recent years, including displays, flexible electronics, solder dispensing, rapid prototyping, ceramic components, enzyme-based sensors, and tissue engineering [262]. When talking about inkjet printing technology, a number of physical operations define and constrain it. These include generation of droplets, interaction of droplets on a substrate, and drying mechanisms [262].

The technology used in Dimatix printer is based on a drop-on-demand (DOD) inkjet printing, which is based on the generation of individual drops wherever required. Pattern printing is through positioning of inkjet head above the desired position of the substrate. In this technology, drops are formed by applying a pressure wave in the fluid channel just before the individual nozzles. The drops are ejected after a threshold pressure is exceeded. Without applying such pressure, the liquids are held in place due to the surface tension forces and a negative pressure at the exit of nozzles. A jetting frequency between 0.7-10 kHz can be used while jetting. Nozzels are array of 16 squares and around 21.5 μm, and the drops are approximately in the same size. It is also possible to control the droplets size by changing the input waveform and ejection velocity. In our DMP-2800, the drop formation is possible by a pressure pulse through a piezoelectric transducer, which is placed before the exit of nozzles, and mechanical actuation using MEMS technology.

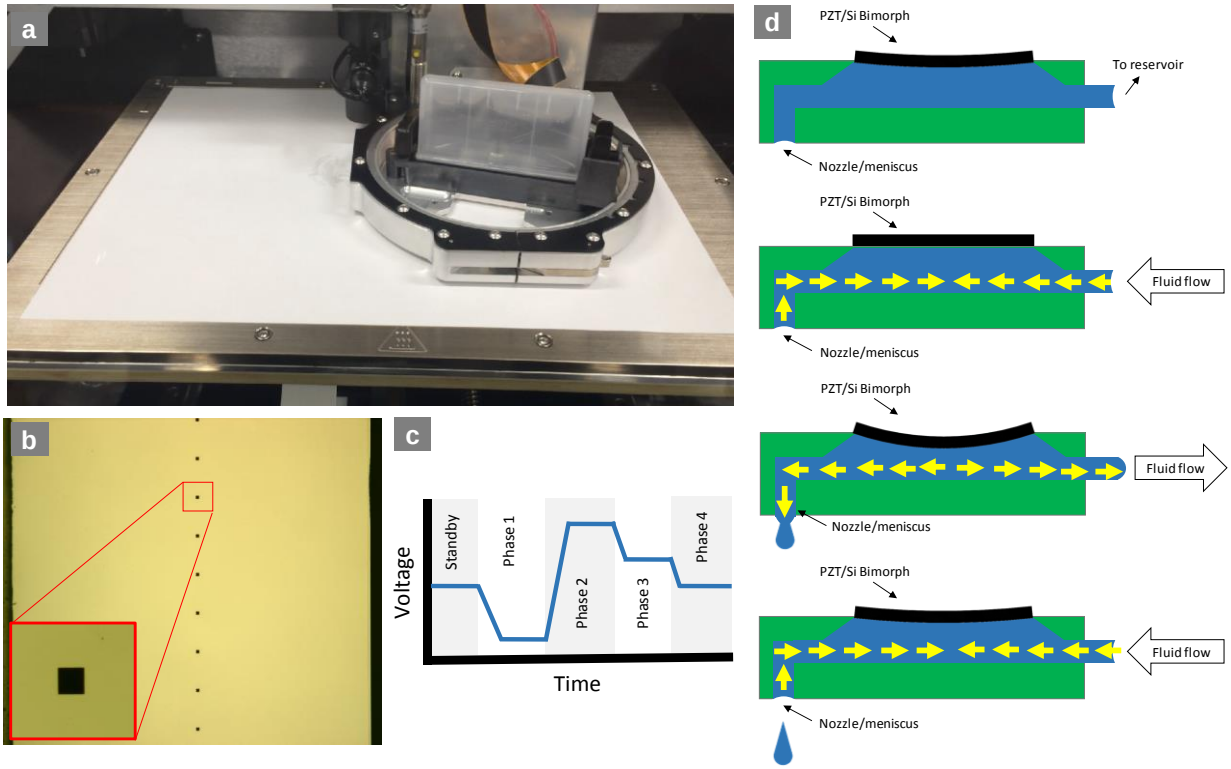

Figure 56- Inkjet printing technology: (a) A Dimatix DMP-2800 material printer with graphene ink cartridge installed, printing a pattern on a paper substrate. (b) Optical microscopy image of array of silicon nozzles; inset shows zoomed view of an individual nozzle with an orifice size of ~21.5 µm and capable of jetting 10-pL drops of inks. (c) A typical waveform applied to the piezoelectric actuators during inkjet printing. (d) The mechanism of drop formation in inkjet printing [268].

The mechanism for drop ejection is shown in Figure 56c: Initially, the piezoelectric actuators are at standby phase, where the PZT bimorph is slightly deflected by a bias voltage. At the beginning of jetting pulse (i.e. phase 1), the voltage is decreased to zero and the piezo membrane is back to the neutral position where the fluid chamber is at its maximum volume. At this phase, the inks are pulled into the

chamber from the reservoir. This also affects the meniscus at the nozzles exit pulling inward slightly. The increase in voltage, then, makes the chamber compressed and generates a positive pressure to initiate the drop formation and finally eject a drop (phase 2). Next phases include reversing the piezo voltage to its bias level where the chamber decompresses and ready for the next cycle of drop generation. There is also a slight pull back at the exit of nozzles at this stage (Figure 56c). [268]

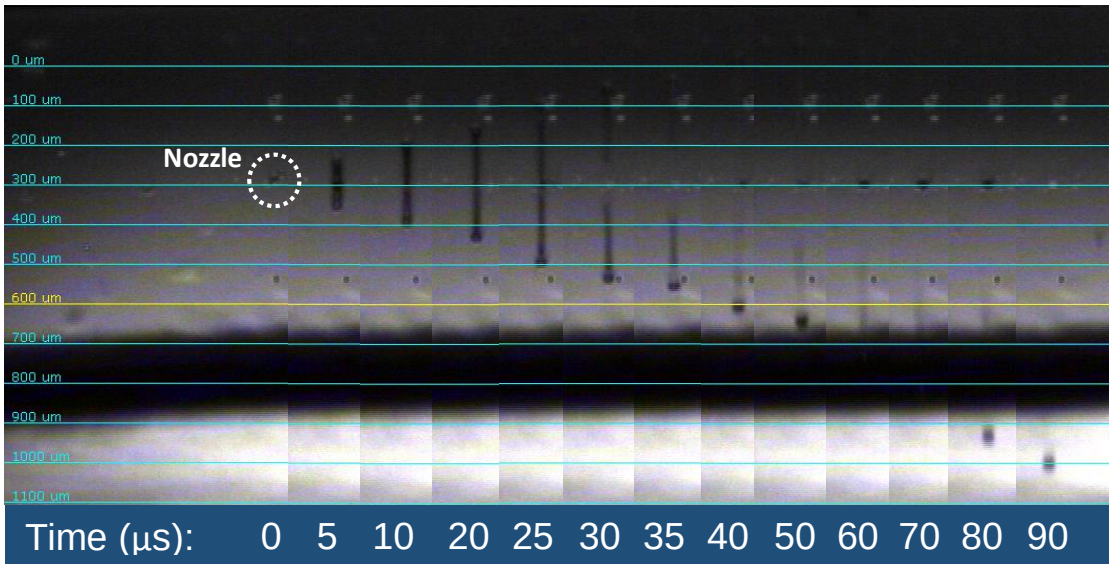

Figure 57 - Drop formation: Formation of 10-pL drops of graphene ink at microsecond snapshots. Nozzles are located at 300-µm horizontal line. An stable drop forms after around 40 µs. No satellite drops or nozzle blockage was observed. An average drop velocity of ~7 m s^{-1} is calculated.

Using the graphene inks that we developed previously as explained in Section 7.2, we captured the drop formation at different time intervals after the drops are ejected from the nozzles. The drops are formed from an initial column of liquids, which thins and constitutes a leading droplet and an elongated tail as the liquid propagates [262]. To successfully print a pattern using inkjet printing, the tail or the satellite drops must merge with the leading drop during the flight and prior to reach the substrate. If this fails and the satellite drops do not merge with the big leading droplet during the flight, the printing quality and resolution will be deteriorated. To give the inks enough time to form a successful single and stable droplet, a stand-off distance between the printer head and the substrate must be employed (we did this by applying a 1 mm distance). As seen in Figure 57, our inks successfully form a single and stable droplet in ~40 μs and after travelling about 300 μm distance from the nozzle exit. We did not observe any satellite formation during printing with our inks. From Figure 57, a drop speed of around 7 m s^{-1} is estimated.

We have printed different patterns/sketches on various surfaces to show the printability of our inks. The exfoliated 2D materials are shown in Figure 58a. As was explained earlier, these are water-based exfoliated nanosheets and they show high stability over the time (more than eight months without aggregation/sedimentation). Figure 58b shows the inks obtained from these exfoliated solutions. Graphene ink is in

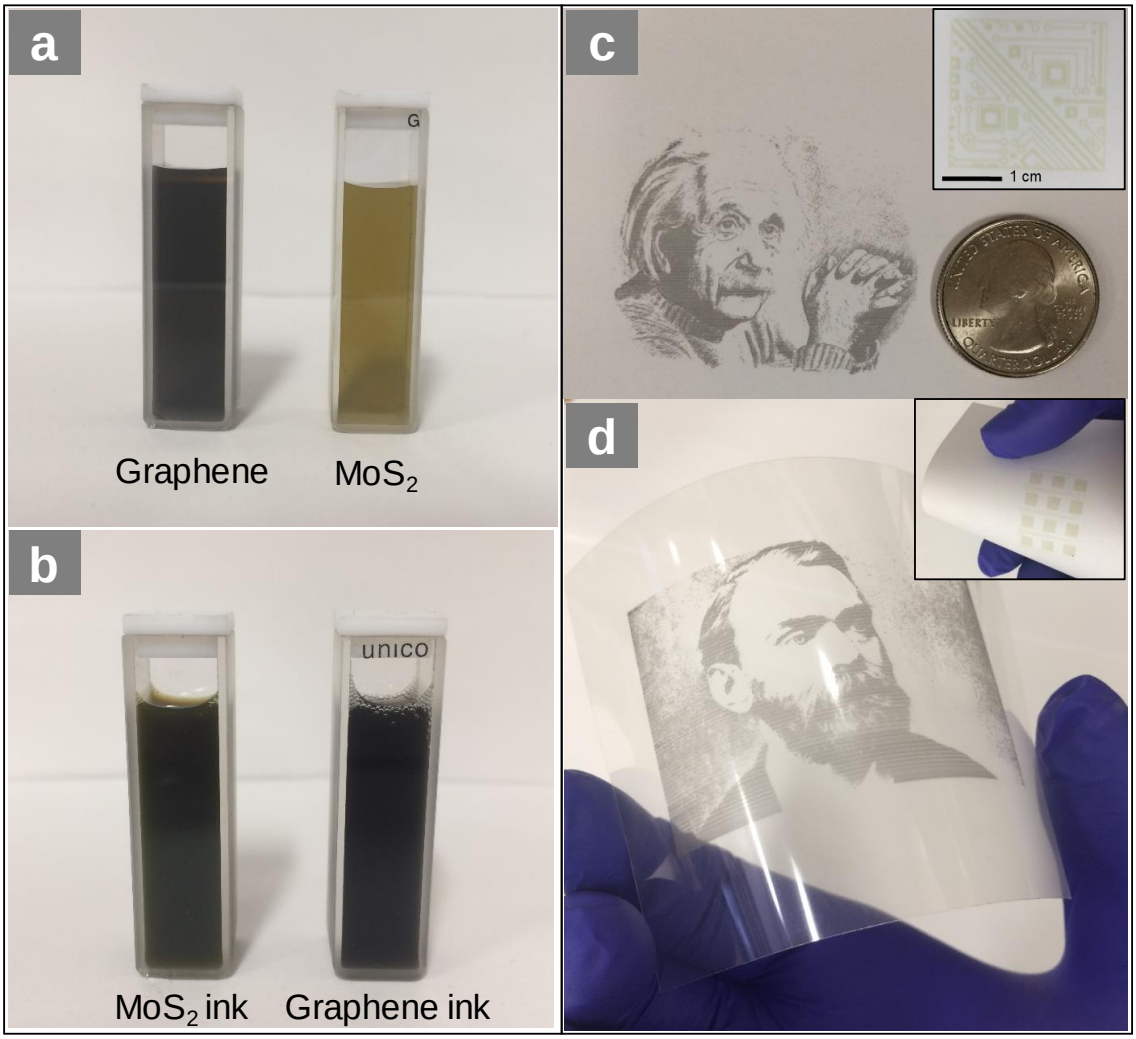

Figure 58- Ink development and printed 2D materials: (a) Exfoliated nanoflakes of MoS_2 and graphene in deionized water, showing high stability in long term without sedimentation or aggregation. (b) Water-based biocompatible inks developed out of exfoliated nanoflakes. (c) An inkjet-printed sketch of Albert Einstein on a regular copy paper. Inset shows an electrical pattern printed using MoS_2 inks. (d) Printed sketch of Alfred Nobel on a flexible cellulose-acetate plastic; inset shows a pattern of squares printed on a paper by MoS_2 inks.

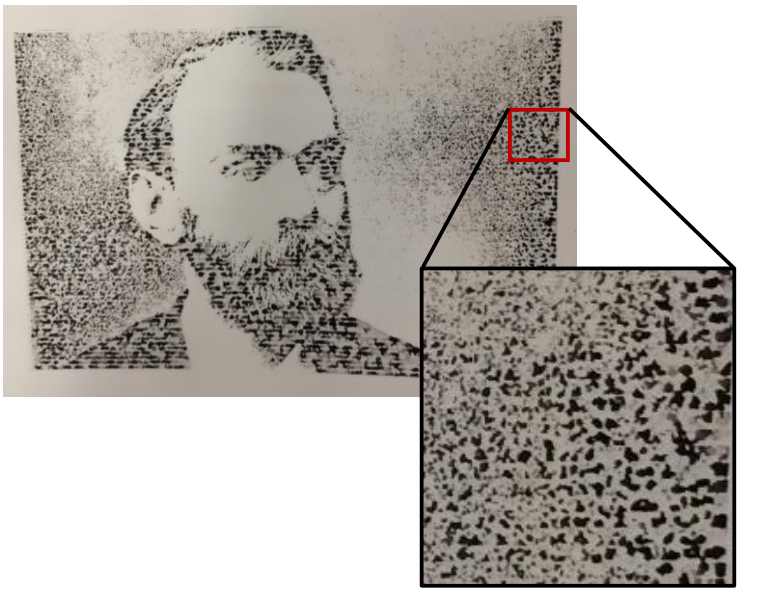

Figure 59- Coffee ring effects observed while printing the similar sketch of Alfred Nobel with a commercially available ink.

grey and MoS_2 ink in dark green. Figure 58c shows Einstein's sketch[1] printed on a regular paper using the water-based graphene ink. The inset shows a printed pattern on a paper using the MoS_2 ink. An sketch of Alfred B. Nobel is printed on a transparent and flexible plastic sheet using graphene ink. We observed high accuracy and resolution in printing different patterns or pictures on various surfaces using our water-based 2D crystal inks, without any major coffee ring or Marangoni effects. The printability of our inks are compared to a commercial ink provided by the Fujifilm Inc. as the default model ink for Dimatix Material Printer, where the sketch of Alfred Nobel

[1] The original sketch accessed from web https://www.pinterest.com/pin/83879611780332870/ on December 15, 2017.

is printed on the same substrate and using the same printing conditions as our graphene inks (Figure 59). The formation of aggregated macro-scale droplets and coffee ring effects are easily observed for this ink.

7.4. INKJET-PRINTED PAPER-BASED PHOTO-ACTUATORS

Due to their importance in areas such as soft robotics, biomimetic devices, and artificial muscles, soft actuators are of great interest with plethora of research being focused on them in recent years [269-273]. Despite the tremendous amount of research in this area over the past decade, there is still the need for improving these actuators and their related applications. Developing programmable soft actuators with easy and diverse shape changing capabilities, versatility, large actuation release, and remote controllability still remains a challenge in the soft actuation technology [274-276].

In this section, we introduce an ultra-fast approach by use of inkjet printing technology to fabricate paper-based photo actuators with large photo-response release. Paper is a hydrophilic and porous network of cellulose fibers, which has been used for centuries in applications such as printing and packaging. It comes in various forms with its fibers made from a range of different materials, such as cellulose, glass, polymer, or even metals [277]. Each type of paper brings different functionalities when used in paper-based technologies. Its excellent mechanical properties are pronounced by its lightweight, flexibility, and foldability. In the past decade, paper has been used in new and novel applications such as microfluidic and low cost diagnostics devices [277,

278], electroanalytical devices [279], cell growth [280, 281], printed electronics [282, 283], microelectromechanical systems [284], and more recently, electrically driven actuators [285, 286].

Here, we develop bilayer paper-based photo-actuators made of simple copy paper and adhesive tape, with the incorporation of graphene nanoplatelets. Figure 60a shows the fabrication process for our actuators; as depicted in this figure, a case-specific graphene pattern is printed on a regular copy paper using a Dimatix inkjet printer (Fujifilm Dimatix, Inc.), and our developed graphene inks. The use of inkjet printing technology eliminates the requirements for pre and post preparation of the substrate or the printed materials before the actuators are ready to fabricate or use, which are necessary steps in some traditional methods. The samples are instantly ready after printing the pattern, and can be cut to any specific shape. An adhesive tape is then assembled to the graphene-patterned paper to make the bilayer actuator.

Figure 60b depicts the mechanism in these actuators, which is based on the hydrophilic properties of the paper and the change in its relative water content upon irradiation by an external light source. Due to these hygroscopic properties, the paper undergoes a large contraction if the photons are absorbed by an external agent, and as a result, the internal temperature of its porous structure is increased. At the same time, the second layer of these actuators undergoes an expansion due to this temperature increase (Figure 60b). The combination of these two active layers with the contraction of the paper and the expansion of the polymer layer results in ultra large bending of these actuators upon an external stimuli. Unlike some previous works where there is

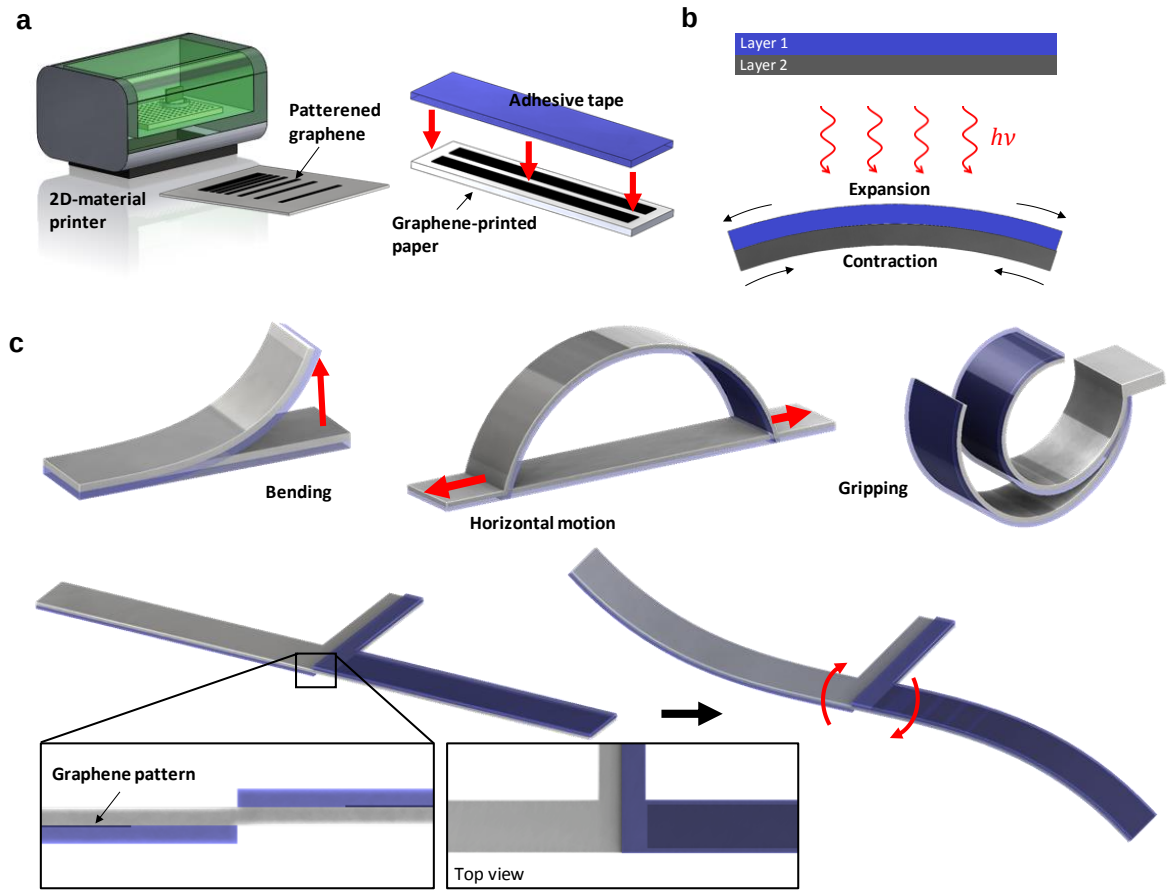

Figure 60- Fabrication method and mechanism of inkjet-printed paper-based actuators: (a) Inkjet printing of desired patterns on a regular paper using the developed graphene inks, and assembling of adhesive tape as the second layer of paper-based actuators. (b) Mechanism of bi-layer paper actuators; the structure undergoes bending upon irradiation of light of a specific wavelength, as a result of expansion in polymer layer and contraction in paper layer. (c) Different designs based on bi-layer paper actuators; bending, curling, uncurling, horizontal movement, and twisting can be achieved depending on the design of bi-layers.

only one active layer along with a passive layer in the actuation mechanism (for instance, the soft actuators developed by Taccola *et al.* [269]), both layers in our actuators are active layers. Therefore, the substantial actuation in our actuators is not only attributed to the mismatch in the coefficients of thermal expansion between paper and plastic layers, but also to the hygroscopic (humidity responsive) properties of the paper and the change in its mechanical properties upon irradiation, along with the humidity inertness of adhesive tape layer.

Depending on the pattern of the printed graphene, structure of the bi-layer, and the overall folding/orientation of the actuators, different mechanical motions can be achieved, which are useful for various programmable and case-specific shape-changing applications. Figure 60c schematically depicts four different mechanical motions for these actuators, including pure bending for a straight and uniform bi-layer design when one end is clamped, horizontal motion for a concave structure of uniform bi-layer with its ends being free to move along horizontal directions, twisting for a convex and one-end-clamped bi-layer structure, and torsional motion for a reversing bilayer structure.

Scanning electron micrographs of a regular copy paper and graphene nanoflakes are shown in Figure 61. Our exfoliated graphene flakes are in an average lateral range of 100-500 nm. Figure 62 depicts a simple design for a graphene/paper actuator; using only a single point light source (a 640 nm laser with a beam of around 3 mm diameter, 30 mW power), the actuator undergoes a noticeable deflection, around 6 mm,

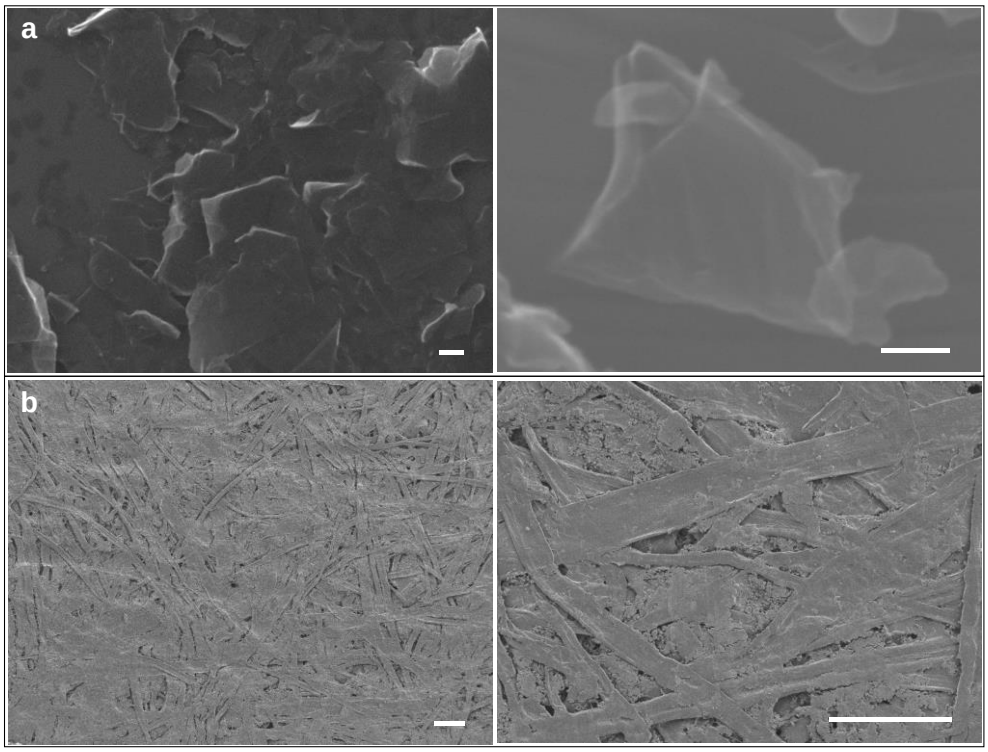

Figure 61- Scanning electron microscopy images of (a) graphene nanoplatelets, and (b) regular copy paper. Scale bars are 100 nm for graphene and 100 μm for paper images.

when illuminated with light (Figure 62a & b). Figure 62 c shows the amplitude of vibrations of the actuator at different *on-off* frequency of light source. The inset in this figure is a typical response of the actuator at 10 Hz *on-off* frequency. An exponential curve with the following equation is fitted to the experimental frequency data:

$$\delta = 172.9\, e^{-0.254\, \nu} \qquad (28)$$

where δ is the amplitude of vibrations and ν is the frequency in Hz.

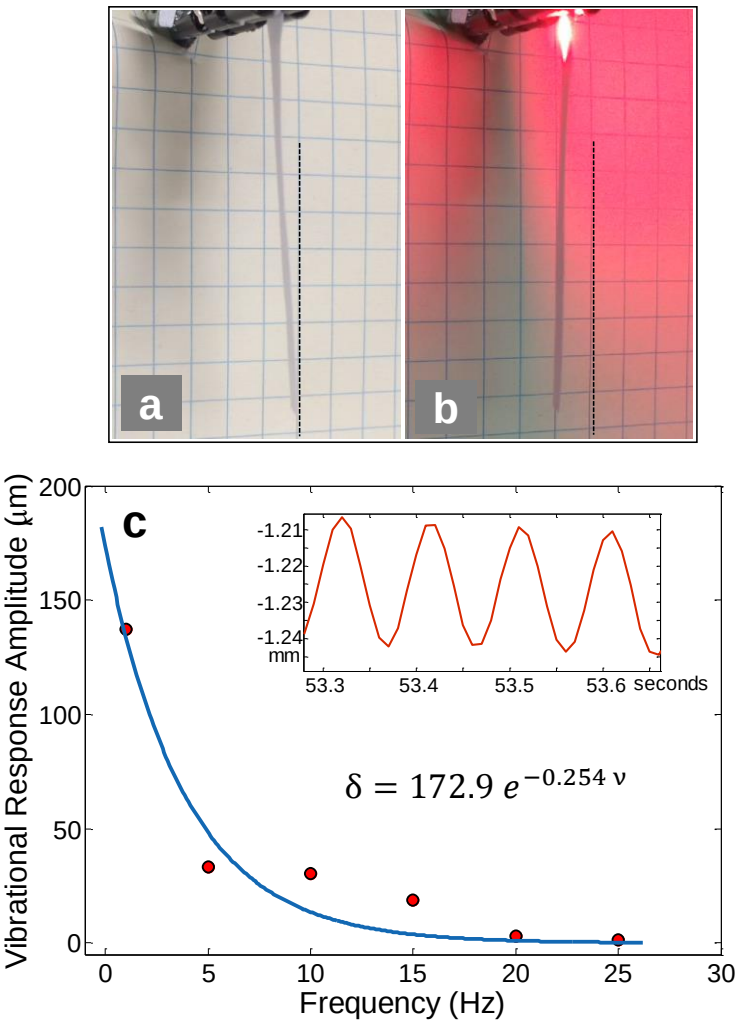

Figure 62- (a, b) A simple design single point actuator illuminated with a laser of 640 nm wavelength; a tip displacement of ~6 mm is observed. (c) Vibrational amplitude versus *on-off* frequencies for a graphene-based paper actuator. Inset shows the vibrational response for an *on-off* frequency of 10 Hz.

Figure 63a depicts a bending paper actuator when illuminated with a NIR light source (860 nm wavelength). The bending actuator undergoes a maximum tip deflection of 33 mm in the vertical direction in 15 seconds. Figure 63b shows the time

history of actuation and relaxation at two different power (185 and 370 mW). The maximum actuations are achieved in 12 s and 20 s for 185 and 370 mW powers, respectively. Relaxation speed is slower compared to the actuation speed, due to the slower rate of moisture adsorption by paper fibers.

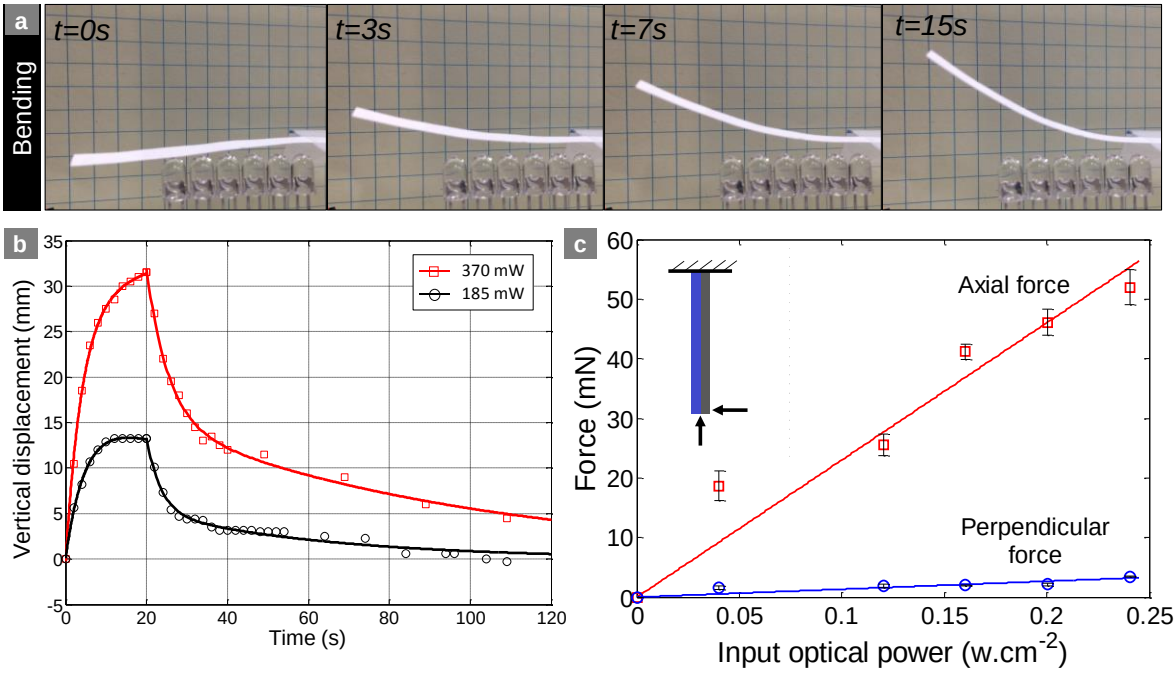

Figure 63- Bending actuation and photo generated forces: (a) snapshots of bending of a graphene-paper actuator when illuminated by near infrared LEDs (860 nm wavelength). Large displacement over 3 cm is achieved in ~15 second. (b) Vertical displacement versus time for different total powers. Maximum actuations are achieved in 12 s and 20 s for lower and higher powers, respectively. Relaxation speed is slower compared to the actuation speed, due to the slower rate of moisture adsorption by paper fibers. (c) Axial and perpendicular blocking forces generated in the paper actuator; a huge photo-induced 50 mN axial force is achieved with 0.24 W.cm^{-2} optical power, enough for lifting a weight of ~166 times the weight of the actuator itself.

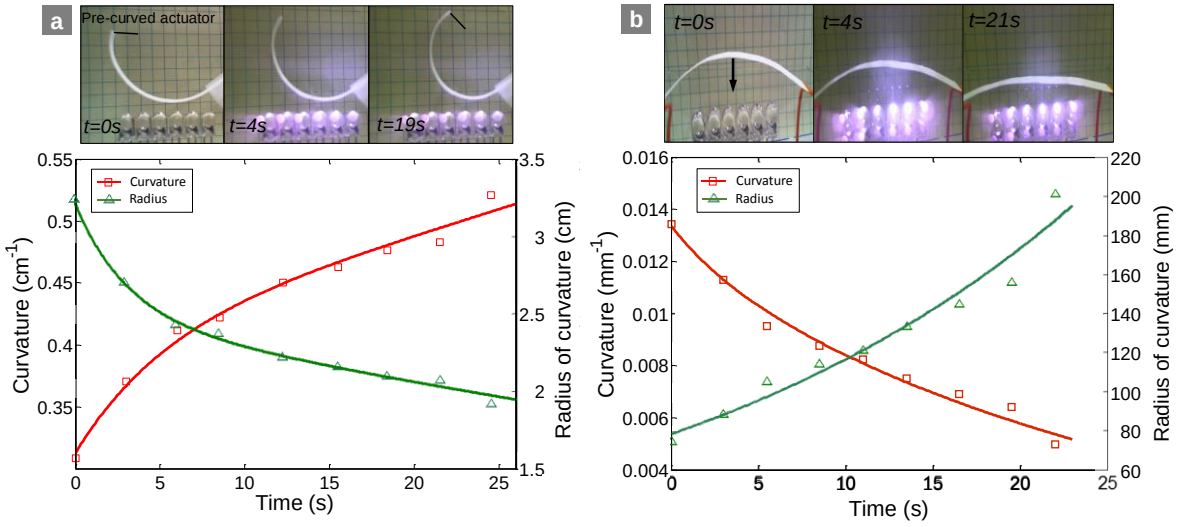

Figure 64- (a) Curling and (b) uncurling mechanism and radius of curvature versus time for graphene paper-based actuators.

Figure 63 (c) shows the axial and perpendicular blocking forces generated in the paper actuator; a huge photo-induced 50 mN axial force is generated in the paper actuator due to 0.24 W.cm^{-2} optical power, enough for lifting a weight of ~166 times the weight of the actuator itself (the weight of paper actuator is ~30 mg).

Curling and uncurling applications are shown in Figure 64. A pre-curved paper actuator increases its radius of curvature from 1.9 to 3.3 cm (change in curvature from 0.30 cm^{-1} to 0.52 cm^{-1}) when illuminated with near infrared LEDs of 860 nm wavelength. Uncurling, or horizontal motion, can be achieved in paper actuators when the actuator is in a concave structure, as shown in Figure 64b.

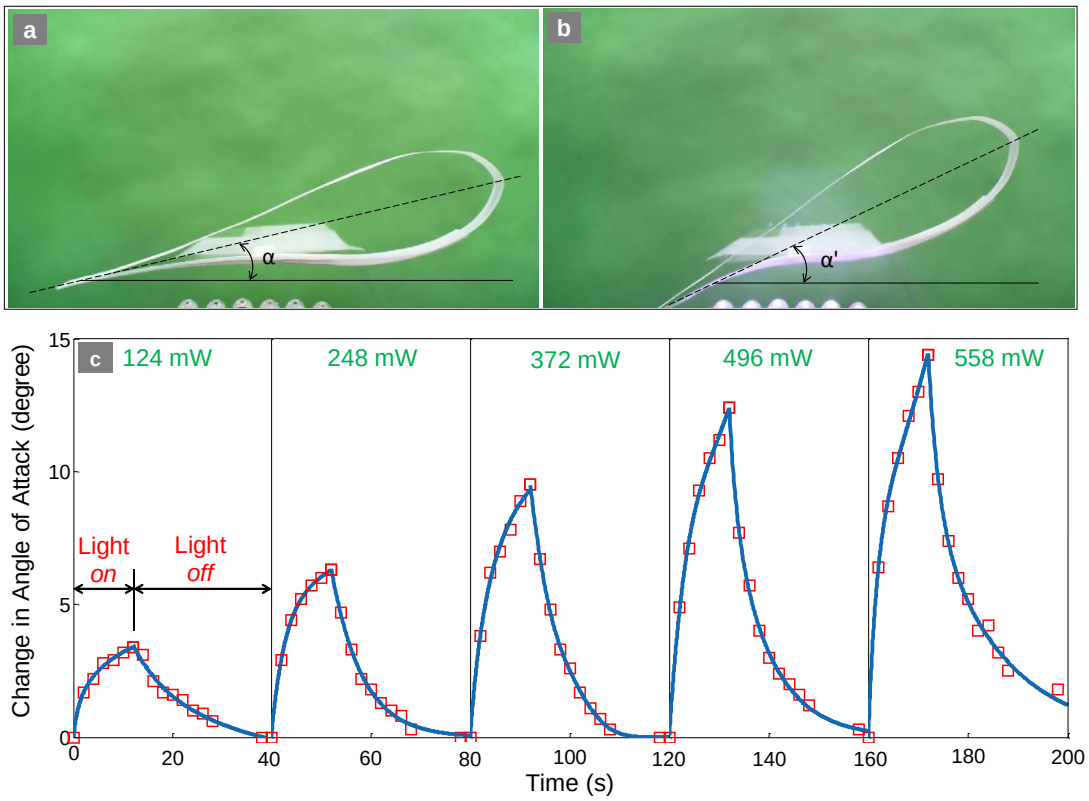

Figure 65- Twisting mechanism: (a, b) an airfoil design based on bilayer actuators undergoing an increase in the angle of attack, i.e. α, when illuminated by photons of 860 nm wavelength. (b) Reversible change in the angle of attack versus time for different optical power, with a huge 14 degree change for 558 mW power. An actuation and relaxation time of 12 and 28 seconds are observed.

Figure 65 shows the twisting mechanism for a paper actuator in form of cross section of an airfoil. The design was presented earlier in Figure 60c. The airfoil undergoes a substantial change in the angle of attack (α) of around 13 degree, when the actuating arms are illuminated with a near infrared light source. Figure 65b is the reversible change in the angle of attack versus time for different optical power, with a

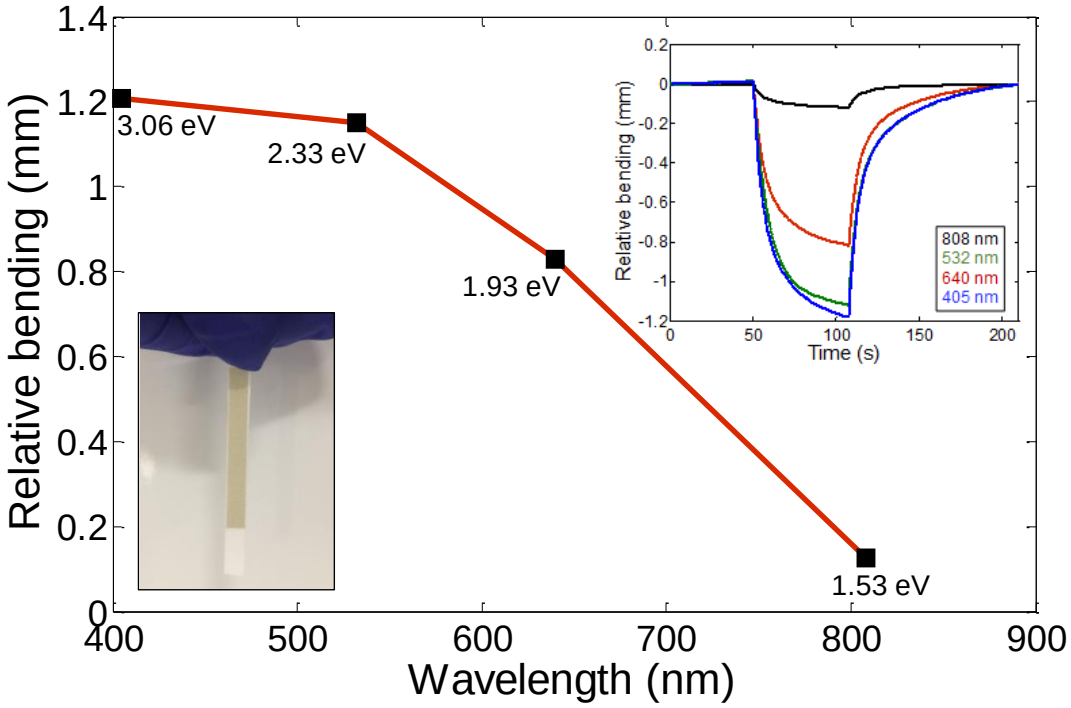

Figure 66- Chromatic mechanical response in water-based-exfoliated MoS_2-paper actuators: relative bending of actuators when illuminated with different wavelengths of light and their associated photon energy (shown in eV), suggesting a wavelength selective nature. Insert shows the time response of actuators to an *on-off* cycle; a photograph of the paper actuator is also depicted in the bottom left of the figure.

huge 14 degree change for 558 mW power. An actuation and relaxation time of 12 and 28 seconds are observed. A paper actuator using the water-based exfoliated MoS_2 (developed in Section 7.2 and Figure 58) is depicted in Figure 66. The relative bending of this actuator in response to different wavelengths of light with different photon energy is plotted, suggesting wavelength selective behavior for energies below and above the bandgap of MoS_2, similar to LBL MoS_2/PDMS actuators developed earlier in

Chapter 5, which is an evidence of existence of individual few/mono-layer nanoflakes on the paper structure. Inset shows the time response of the actuator to 405, 532, 640, and 808 nm wavelengths for an *on/off* cycle.

CHAPTER 8
CONCLUSIONS AND FUTURE DIRECTIONS

8.1. CONCLUSIONS

This dissertation was undertaken to investigate and understand different characteristics of 2D materials, with a focus on transition metal dichacogenides and MoS_2, when used in energy conversion applications such as soft photo-driven actuators and nanocomposites. Compared to graphene, which is just a layer of carbon atoms and has no bandgap, layered transition metal dichalcogenides provide intriguing opportunities to develop low cost, light and wavelength tunable stimuli responsive systems that are not possible with their conventional macroscopic counterparts. MoS_2 nanoparticles were dispersed into a polydimethyl siloxane matrix, and the mechanical and opto-mechanical properties of these nanocomposites were studied in Chapter 3. Three different nanofabrication methods, namely shear mixing, evaporative mixing, and layer-by-layer, were used and the characteristics and opto-mechanical energy conversion of these nanocomposites were compared. It was shown that the proper selection of a method over the other not only depends on the type of nanoparticle used, but also on various factors such as fabrication methods and/or cross-linking ratio of the host polymer matrix. At lower cross-linking ratios of polydimethyl siloxane, such as 1:10, layer-by-layer method presented the best photon-to-mechanical energy conversion, whereas in higher cross-linking ratios, shear and evaporative mixing offered higher photo actuations compared to their layer-by-layer counterparts. The results of this chapter proposed that energy transduction in nanocomposite actuators are

not only a function of weight percentage or exfoliation level of nanoparticles as was reported earlier in [75] and [22], but also functions of fabrication method and cross-linking ratio of the base polymer.

The dimensional dependency of properties of MoS_2 nanoparticles and TMD-based nanocomposites were studied in Chapter 4. As a layered and semiconductive two-dimensional material in the family of transition metal dichalcogenides, and due to the weak van der Waals interlayer forces, MoS_2 nanopartciles were exfoliated based on Liquid Phase Exfoliation method. Three types of samples were prepared namely bulk, intermediate, and few-layers. These samples were characterized for number of layers using Scanning Electron Microscopy and Atomic Force Microscopy, and their number of layers were identified, where three different regions were recognized as 100–500 layers for bulk, 10-30 layers for intermediate, and 1-6 layers for few-layer nanoflakes. Using the layer-by-layer process of nanocomposite fabrication, a chromatic mechanical response was observed for MoS_2-polymer nanocomposites when the nanoflakes are highly exfoliated and less than 4 nm in thickness.

The advantages of the proposed fabrication method for TMD-based nanocomposites were reported as: (1) liquid phase exfoliation process resulting in high quality few layers with distinctive direct electron transition peaks; (2) phase separated nanocomposites due to the layer-by-layer processing, which enables preservation of the intrinsic properties and eliminates environmental degradation effects such as oxidation; (3) access to the unique layer-dependent optical absorption properties of MoS_2 layers inside the nanocomposite; (4) the reported architectures enabled the creation of

spatially varying bandgap profiles of 2-D nanomaterials and study of resonance Raman scattering as a function of number of layers and; (5) the proposed design enables scalable and flexible process for developing stimuli responsive and energy conversion devices at macro, micro and nanoscopic length scales utilizing different polymeric systems.

Photomechanical actuators, fabricated with a layer-by-layer method with the incorporation of highly exfoliated MoS_2 nanoflakes, showed strong and wavelength dependent light matter interaction in the visible region of the electromagnetic spectrum. It was found that the photo-thermal energy transduction from the MoS_2 crystals to the polymer chains is significant resulting in high amplitudes of photomechanical actuation, higher than those reported for graphene [20] and carbon nanotubes [10].

Long term photo-actuation experiments performed in this dissertation showed that (1) the photomechanical actuation of the 2H-MoS_2 few-layer nanocomposites was fully reversible and a robust actuation mechanism; (2) the strain based optical absorption experiments did not delaminate the interface/sample, which would otherwise cause an irreversible change in the amplitude of photomechanical actuation stress (a significant reduction in stress); (3) the strain gradients on the MoS_2 crystals and the change in bandgap were also completely reversible as the sample exhibited pristine-like behavior (0% strain) with the same amplitude of mechanical response in the long term experiments. It was concluded that the strain transfer to the MoS_2 additive should be less than 5% in our samples at the highest strain applied to these nanocomposite, not enough to cause any failure, delamination or degradation all which would irreversibly

change the long term photomechanical response. The high strength and strong light-matter interactions in 2H-MoS_2 gave rise to the reported chromatic mechanical response, which is not only a new mechanism but also a new material design for future macroscopic photo mobile polymer networks based on TMDs.

In transition metal dichalcogenides such as MoS_2, strain engineering, i.e., the change in electronic properties using mechanical deformation, is an important concept and has brought benefits such as bandgap engineering of single and bi-layers, exciton funneling effects, and selective chemical adsorption of gas molecules on strained surfaces due to their ultra-large mechanical strength (capable of withstanding 10–20% strains) and possessing an intrinsic bandgap. Strain engineering was used in Chapter 5 to present the straintronic-phototheric effect, which was the intimate coupling of strains, band gaps, optical absorption and photo-thermal response in 2H-MoS_2 hyperelastic nanocomposites. As the first application of bandgap effects for mechanical actuation in nanocomposites, the presented results showed that as the bandgap of 2H-MoS_2 was decreased due to localized strains, the optical absorption and the thermal and mechanical response was enhanced. An analytical strain model for van der Waals packed films of nanoparticles was developed and presented in Chapter 6, and the strains from over 100 wrinkles were calculated based on this model. The model estimated localized strains of 0.2–1.3% for a 35 nm thick film of MoS_2 nanoparticles when the film was wrinkled. The photoluminescence measurements verified this model and showed that the direct electron transition was still dominant in local strain engineered few layer nanoflakes. The shift in the A exciton resonance peak by 30 meV was shown

as an evidence of the mechanism, which proved that the strength of the A-exciton resonance was responsible for the overall chromatic mechanical effect. Straining the layers also increased the PL intensity suggesting strains had a direct effect on the band structure in 2H-MoS_2.

Purely-thermal actuation experiments were done on elastomer samples by a Dynamic Mechanical Analyzer in Chapter 6, and a new mathematical model that related the purely thermal versus Gaussian photothermal effect was developed, and suggested that photomechanical actuation in TMD based nanocomposites was a chromatic thermal effect coupled to the optical absorption of the semiconductor under strains. It was also shown that the straintronic-photothermal effect only occurred at thickness below 100 nm, and therefore access to nanoscale property was necessary to see this effect. Above 100 nm, bulk behavior dominated, which resulted in vanishing this effect completely, and as a result, strain engineering had no effect on subsequent photo-thermal response.

Combining 2D nanomaterials with hyperelastic materials in this dissertation provided new opportunities in photo-thermal transducers due to the high strain energy densities, high elastic modulus of 2D materials, and enhanced light matter interactions in these nanocomposites. 2D TMD based nanocomposites was shown as one of the few materials to show intrinsic chromatic mechanical response as well as straintronic photomechanical response with tunability of stress or displacement due to change in the band gap, all of which can be exploited for light driven transducers on the macroscopic, millimeter and microscopic scales.

As an essential need for simple, versatile, and low-cost manufacturing techniques for fast fabrication of functional devices in the fast-moving area of 2D materials, for rapid prototyping of new and flexible electronics and optoelectronics, inkjet printing of 2D materials was accomplished in Chapter 7. 2D materials such as graphene and MoS_2 were exfoliated in deionized water, and water-based inks were developed based on these exfoliated nanosheets. The developed inks were bio-compatible and based on non-toxic materials, and were used to print different patterns on a variety of substrates. Developed inks based on 2D materials showed excellent stability over a long period of time (more than eight months), and formed stable droplets of 10 picoliter while being inkjet printed, without any satellite drops or nozzle blockage. Coffee-ring effects and Marangoni flows were minimized by using propylene glycol in the inks. Paper-based hygroscopic actuators were fabricated using inkjet printing of graphene inks, and were actuated by an 860 nm light source. Significant actuation and photo-induced forces in the forms of bending, curling, uncurling, or twisting were achieved using inkjet-printed paper/graphene based photo-actuators. The scalability, simplicity, biocompatibility, and fast fabrication characteristics of the inkjet printing method along with its applicability to a variety of substrates such as plastics and papers can be implemented to high-performance flexible or wearables electronics, sensors, and actuators with countless applications in soft robotics, electronic, optoelectronic, and biomimetic devices.

The following list summarizes some of the original contributions of this dissertation to the field of nanomaterials and nanotechnology:

(1) Development of MoS_2-based nanocomposites with different fabrication methods, and demonstration of the effects of fabrication process on the performance of photo-thermal actuators.

(2) Demonstration of extraordinary characteristics of bulk, intermediate and few layer elastomeric actuators using a unique Layer-by-Layer (LBL) nanofabrication method, not reported for photomechanical actuators up to this date.

(3) Demonstration on how using different number of layers in layered material makes a huge difference both in mechanical actuation and optical absorption.

(4) Demonstration of Chromatic mechanical response and wavelength-dependent actuation in few-layer 2H-MoS_2-based actuators. This unique chromatic response was shown to originate from exciton resonance peaks A and B of the few-layer semiconductive nanoparticles.

(5) Demonstration of Lambert-Beer plots and extinction coefficients for different levels of exfoliation in MoS_2 nanoparticles and reviewing the plausibility of scattering as a function of particles size.

(6) Demonstration of the effects of global transfer of strain to individual nanoparticles through an elastomeric substrate, and the resulted Raman shifts in vibrational modes of MoS_2 nanoparticles.

(7) Bandgap engineering of semiconductive MoS_2 nanoparticles by fabrication of nanowrinkles. The change in the direct bandgap of the material was attributed to the applied local strains in individual nanoparticles.

(8) Development of an analytical model for calculation of strains in van der Waals packed films of nanoparticles.

(9) Demonstration of temperature profiles in photo-actuation mechanism, and development of a mathematical model for the analogy between purely-thermal and photo-thermal actuations and the associated temperature rise using Dynamic Mechanical Analysis.

(10) Development of the first inkjet-printed paper-based photo actuators with large energy transduction release, in the shape of photo-generated displacement or force.

8.2. FUTURE DIRECTIONS

Future directions in the area of photo-thermal actuation based on two-dimensional materials are discussed in this section. While transition metal dichalcogenides provide chromatic mechanical response when incorporated in hyperelastic elastomers, the relatively low thermal conductivity of these semiconductive materials may be an undesirable characteristic for some applications. The use of other members of 2D materials such as graphene along with TMDs in a layer-by-layer heterostructure can help increasing the overall photo actuation efficiency

as well as photo responsivity of these nanocomposites due to excellent thermal conductivity of graphene. A mathematical model for the temperature profile of TMD-based nanocomposites when illuminated by different energy levels of photons were proposed, which can be further extended to the case of the aforementioned nanocomposites with incorporation of multiple 2D materials to tailor the functionalities of these nanocomposites. Such studies can lead to improving the actuation and relaxation speed, optical-to-mechanical transduction efficiency, and tailoring the wavelength of photon absorption in these nanocomposites. Extending the responsivity of these nanocomposites to lower and higher wavelengths of electromagnetic waves than the ones presented in this dissertation can bring about new functionalities with different applications in areas such as cancer targeting and theranostics. Relatively poor photon-absorption of TMDs in the near-infrared wavelengths can also be improved by the addition of nanomaterials such as graphene with proven responsivity in the NIR region [69].

Different nanofabrication methods of dispersing nanoparticles in the polymer host presented in this dissertation can be extended to other memebers of 2D and 1D materials such as $MoSe_2$, WS_2, WSe_2, graphene, and carbon nanotubes, as well as single and few-layer particles of MoS_2. Since the properties of materials at nano scales is extremely depended on the size and morphology of flakes, further studies can be performed on how nanoparticles of a specific size (i.e. 20 nm, 50 nm, or 100 nm) can change the overall functionalities of shear-mixed and evaporative-mixed nanocomposites. Reinforcing these nanocomposites with the use of a high strength

material along with a chromatic responsive few-layer TMDs can benefit to the overall mechanical as well as optical properties of these nanomaterial systems.

Bandgap engineering of MoS_2 thin film of nanoparticles can be extended by studying other thicknesses of the thin film, lower or higher than 35-nm thickness studied in this dissertation. For bilayer bending actuators made from MoS_2 and polymer, study of smaller samples in the micron scale with a lower thickness ratio of polymer-to-MoS_2 layers can lead to higher bending displacements, higher operational frequencies, as well as more accentuated straintronic effects in the wrinkled actuators. While the wrinkled films of nanoparticles presented in this dissertation are not periodic and the strain distribution is non-uniform, making the wrinkles periodic using thin-film fabrication techniques such as chemical vapor deposition (CVD) of TMDs with precise control of number of layers and strain transfer can enable better control of wrinkled architectures for tunable photo-thermal actuation. Furthermore, the optical absorption and mechanical response can be tuned to larger wavelengths through introduction of traditional plasmonic architectures by coating the wrinkles with 10–30 nm noble metals, resulting in exciton-plasmon interactions.

2D-materials-based inks developed in this dissertation for inkjet printing of nanoparticles can be applied to other functional devices other than the ones presented in this study. Inkjet printing of graphene, as an example, can be performed on elastomeric substrate to fabricate wearable skin-like strain sensors. All-2D-material based devices such as field-effect transistors (FETs) can be printed in a similar manner to what was presented in this dissertation, with incorporation of different types of semiconductive,

conductive, and insulator 2D materials. As viable choices of materials, for instance, MoS_2 nanoparticles can be inkjet printed as the semiconductive material along with graphene and boron nitride (BN) as electrodes and insulators in an FET structure. Inkjet printing of heterostructures on flexible substrates with multiple nanomaterials using the method developed in this dissertation can extend the functions of devices such as actuators and sensors, and open up new applications in the fields such as soft robotics, bio-sensing, photovoltaics, flexible electronics, wearable technologies, structural health monitoring, transparent sensors, artificial skins and muscles, transparent displays and photo-detectors.

REFERENCES

1. Bell, A.G., *Upon the production of sound by radiant energy.* Science, 1881. **2**(48): p. 242-253.
2. Eisenbach, C.D., *Isomerization of Aromatic Azo Chromophores in Poly(Ethyl Acrylate) Networks and Photomechanical Effect.* Polymer, 1980. **21**(10): p. 1175-1179.
3. Hugel, T., et al., *Single-molecule optomechanical cycle.* Science, 2002. **296**(5570): p. 1103-1106.
4. Agolini, F. and F.P. Gay, *Synthesis and Properties of Azoaromatic Polymers.* Macromolecules, 1970. **3**(3): p. 349-351.
5. Yu, Y.N., Makoto; Ikeda, Tomiki, *Photomechanics: Directed bending of a polymer film by light.* Nature, 2003. **425**: p. 145.
6. Poosanaas, P., K. Tonooka, and K. Uchino, *Photostrictive actuators.* Mechatronics, 2000. **10**(4-5): p. 467-487.
7. Zhang, X., et al., *Photoactuators and motors based on carbon nanotubes with selective chirality distributions.* Nature Communications, 2014. **5**.
8. Liu, X.Y., et al., *Reversible and Rapid Laser Actuation of Liquid Crystalline Elastomer Micropillars with Inclusion of Gold Nanoparticles.* Advanced Functional Materials, 2015. **25**(20): p. 3022-3032.
9. Xiao, Z.W., et al., *Shape Matters: A Gold Nanoparticle Enabled Shape Memory Polymer Triggered by Laser Irradiation.* Particle & Particle Systems Characterization, 2013. **30**(4): p. 338-345.
10. Ahir, S.V. and E.M. Terentjev, *Photomechanical actuation in polymer-nanotube composites.* Nature Materials, 2005. **4**(6): p. 491-495.
11. Loomis, J., B. King, and B. Panchapakesan, *Layer dependent mechanical responses of graphene composites to near-infrared light.* Applied Physics Letters, 2012. **100**(7): p. 073108.
12. Koerner, H., et al., *Remotely actuated polymer nanocomposites - stress-recovery of carbon-nanotube-filled thermoplastic elastomers.* Nature Materials, 2004. **3**(2): p. 115-120.
13. Sun, X.M., et al., *Unusual Reversible Photomechanical Actuation in Polymer/Nanotube Composites.* Angewandte Chemie-International Edition, 2012. **51**(34): p. 8520-8524.
14. Lu, S.X. and B. Panchapakesan, *Optically driven nanotube actuators.* Nanotechnology, 2005. **16**(11): p. 2548-2554.
15. Liang, J.J., et al., *Infrared-Triggered Actuators from Graphene-Based Nanocomposites.* Journal of Physical Chemistry C, 2009. **113**(22): p. 9921-9927.
16. Loomis, J., et al., *Graphene-nanoplatelet-based photomechanical actuators.* Nanotechnology, 2012. **23**(4).
17. Lu, S.X. and B. Panchapakesan, *Nanotube micro-optomechanical actuators.* Applied Physics Letters, 2006. **88**(25).

18. Lu, S.X., et al., *Nanotube micro-opto-mechanical systems.* Nanotechnology, 2007. **18**(6).
19. Lu, S. and B. Panchapakesan, *All-optical micromirrors from nanotube MOMS with wavelength selectivity.* Journal of Microelectromechanical Systems, 2007. **16**(6): p. 1515-1523.
20. Loomis, J., et al., *Graphene/elastomer composite-based photo-thermal nanopositioners.* Scientific Reports, 2013. **3**.
21. Yamada, M., et al., *Photomobile polymer materials: Towards light-driven plastic motors.* Angewandte Chemie-International Edition, 2008. **47**(27): p. 4986-4988.
22. Rahneshin, V., et al., *Chromatic Mechanical Response in 2-D Layered Transition Metal Dichalcogenide (TMDs) based Nanocomposites.* Scientific Reports, 2016. **6**.
23. Britnell, L., et al., *Strong Light-Matter Interactions in Heterostructures of Atomically Thin Films.* Science, 2013. **340**(6138): p. 1311-1314.
24. Xu Zong, H.Y., Guopeng Wu, Guijun Ma, Fuyu Wen, Lu Wang and Can Li, *Enhancement of Photocatalytic H2 Evolution on CdS by Loading MoS2 as Cocatalyst under Visible Light Irradiation.* Journal of American Chemical Society, 2008. **130**(23): p. 7176-7177.
25. Splendiani, A., et al., *Emerging Photoluminescence in Monolayer MoS2.* Nano Letters, 2010. **10**(4): p. 1271-1275.
26. Yin, Z.Y., et al., *Single-Layer MoS2 Phototransistors.* Acs Nano, 2012. **6**(1): p. 74-80.
27. Tsai, M.L., et al., *Monolayer MoS2 Heterojunction Solar Cells.* Acs Nano, 2014. **8**(8): p. 8317-8322.
28. Mak, K.F., et al., *Atomically Thin MoS2: A New Direct-Gap Semiconductor.* Physical Review Letters, 2010. **105**(13).
29. Bertolazzi, S., J. Brivio, and A. Kis, *Stretching and Breaking of Ultrathin MoS2.* Acs Nano, 2011. **5**(12): p. 9703-9709.
30. Griffith, A.A., *The phenomenon of rupture and flow in solids.* Philosophical Transactions of the Royal Society of Lonon, Series A 1921. **221**: p. 163-198.
31. Castellanos-Gomez, A., et al., *Local Strain Engineering in Atomically Thin MoS2.* Nano Letters, 2013. **13**(11): p. 5361-5366.
32. Scalise, E., et al., *Strain-induced semiconductor to metal transition in the two-dimensional honeycomb structure of MoS2.* Nano Research, 2012. **5**(1): p. 43-48.
33. Kou, L.Z., et al., *Tuning Magnetism and Electronic Phase Transitions by Strain and Electric Field in Zigzag MoS2 Nanoribbons.* Journal of Physical Chemistry Letters, 2012. **3**(20): p. 2934-2941.
34. Lu, P., et al., *Strain-dependent electronic and magnetic properties of MoS2 monolayer, bilayer, nanoribbons and nanotubes.* Physical Chemistry Chemical Physics, 2012. **14**(37): p. 13035-13040.

35. Miro, P., M. Ghorbani-Asl, and T. Heine, *Spontaneous Ripple Formation in MoS2 Monolayers: Electronic Structure and Transport Effects.* Advanced Materials, 2013. **25**(38): p. 5473-5475.
36. Conley, H.J., et al., *Bandgap Engineering of Strained Monolayer and Bilayer MoS2.* Nano Letters, 2013. **13**(8): p. 3626-3630.
37. Feng, J., et al., *Strain-engineered artificial atom as a broad-spectrum solar energy funnel.* Nature Photonics, 2012. **6**(12): p. 865-871.
38. Johari, P. and V.B. Shenoy, *Tuning the Electronic Properties of Semiconducting Transition Metal Dichalcogenides by Applying Mechanical Strains.* Acs Nano, 2012. **6**(6): p. 5449-5456.
39. He, X., et al., *Strain engineering in monolayer WS2, MoS2, and the WS2/MoS2 heterostructure.* Applied Physics Letters, 2016. **109**(17).
40. Lloyd, D., et al., *Band Gap Engineering with Ultralarge Biaxial Strains in Suspended Monolayer MoS2.* Nano Letters, 2016. **16**(9): p. 5836-5841.
41. Su, X.Y., et al., *Bandgap engineering of MoS2/MX2 (MX2 = WS2, MoSe2 and WSe2) heterobilayers subjected to biaxial strain and normal compressive strain.* Rsc Advances, 2016. **6**(22): p. 18319-18325.
42. Ni, Z.H., et al., *Uniaxial Strain on Graphene: Raman Spectroscopy Study and Band-Gap Opening.* Acs Nano, 2008. **2**(11): p. 2301-2305.
43. Si, C., et al., *First-Principles Calculations on the Effect of Doping and Biaxial Tensile Strain on Electron-Phonon Coupling in Graphene.* Physical Review Letters, 2013. **111**(19).
44. Mohiuddin, T.M.G., et al., *Uniaxial strain in graphene by Raman spectroscopy: G peak splitting, Gruneisen parameters, and sample orientation.* Physical Review B, 2009. **79**(20).
45. Yeh, N.C., et al., *Strain-induced pseudo-magnetic fields and charging effects on CVD-grown graphene.* Surface Science, 2011. **605**(17-18): p. 1649-1656.
46. MacLeod, J.M. and F. Rosei, *Molecular Self-Assembly on Graphene.* Small, 2014. **10**(6): p. 1038-1049.
47. Hui, Y.Y., et al., *Exceptional Tunability of Band Energy in a Compressively Strained Trilayer MoS2 Sheet.* Acs Nano, 2013. **7**(8): p. 7126-7131.
48. Plechinger, G., et al., *Control of biaxial strain in single-layer molybdenite using local thermal expansion of the substrate.* 2d Materials, 2015. **2**(1).
49. Li, H., et al., *Optoelectronic crystal of artificial atoms in strain-textured molybdenum disulphide.* Nature Communications, 2015. **6**.
50. Geim, A.K. and K.S. Novoselov, *The rise of graphene.* Nature materials, 2007. **6**(3): p. 183.
51. Peierls, R., *Quelques proprietes typiques des corpses solides.* Ann. IH Poincare, 1935. **5**: p. 177-222.
52. Landau, L., *Zur Theorie der phasenumwandlungen II.* Phys. Z. Sowjetunion, 1937. **11**(545): p. 26-35.
53. Mermin, N.D., *Crystalline order in two dimensions.* Physical Review, 1968. **176**(1): p. 250.

54. Novoselov, K., et al., *Two-dimensional atomic crystals.* Proceedings of the National Academy of Sciences of the United States of America, 2005. **102**(30): p. 10451-10453.
55. Horiuchi, S., et al., *Single graphene sheet detected in a carbon nanofilm.* Applied physics letters, 2004. **84**(13): p. 2403-2405.
56. Shioyama, H., *Cleavage of graphite to graphene.* Journal of materials science letters, 2001. **20**(6): p. 499-500.
57. Viculis, L.M., J.J. Mack, and R.B. Kaner, *A chemical route to carbon nanoscrolls.* Science, 2003. **299**(5611): p. 1361-1361.
58. Rotkin, S.V. and K. Hess, *Possibility of a metallic field-effect transistor.* Applied physics letters, 2004. **84**(16): p. 3139-3141.
59. Butenko, A., et al., *Hall constant in quantum-sized semimetal Bi films: Electric field effect influence.* Journal of Applied Physics, 2000. **88**(5): p. 2634-2640.
60. RadisavljevicB, et al., *Single-layer MoS2 transistors.* Nat Nano, 2011. **6**(3): p. 147-150.
61. Radisavljevic, B., et al., *Single-layer MoS2 transistors.* Nature Nanotechnology, 2011. **6**(3): p. 147-150.
62. Balandin, A.A., et al., *Superior thermal conductivity of single-layer graphene.* Nano letters, 2008. **8**(3): p. 902-907.
63. Lu, Q., M. Arroyo, and R. Huang, *Elastic bending modulus of monolayer graphene.* Journal of Physics D: Applied Physics, 2009. **42**(10): p. 102002.
64. Gusynin, V. and S. Sharapov, *Unconventional integer quantum Hall effect in graphene.* Physical Review Letters, 2005. **95**(14): p. 146801.
65. Dreyer, D.R., et al., *The chemistry of graphene oxide.* Chemical Society Reviews, 2010. **39**(1): p. 228-240.
66. Gómez-Navarro, C., M. Burghard, and K. Kern, *Elastic properties of chemically derived single graphene sheets.* Nano letters, 2008. **8**(7): p. 2045-2049.
67. Potts, J.R., et al., *Graphene-based polymer nanocomposites.* Polymer, 2011. **52**(1): p. 5-25.
68. Loomis, J., et al., *Graphene/elastomer composite-based photo-thermal nanopositioners.* Scientific reports, 2013. **3**.
69. Loomis, J., et al., *Graphene-nanoplatelet-based photomechanical actuators.* Nanotechnology, 2012. **23**(4): p. 045501.
70. Loomis, J. and B. Panchapakesan, *Dimensional dependence of photomechanical response in carbon nanostructure composites: a case for carbon-based mixed-dimensional systems.* Nanotechnology, 2012. **23**(21): p. 215501.
71. Schwierz, F., *Graphene transistors.* Nature nanotechnology, 2010. **5**(7): p. 487-496.
72. Wang, Q.H., et al., *Electronics and optoelectronics of two-dimensional transition metal dichalcogenides.* Nature nanotechnology, 2012. **7**(11): p. 699-712.
73. Coleman, J.N., et al., *Two-dimensional nanosheets produced by liquid exfoliation of layered materials.* Science, 2011. **331**(6017): p. 568-571.

74. O'Neill, A., U. Khan, and J.N. Coleman, *Preparation of high concentration dispersions of exfoliated MoS2 with increased flake size.* Chemistry of Materials, 2012. **24**(12): p. 2414-2421.
75. Lee, Y.H., et al., *Synthesis of large-area MoS2 atomic layers with chemical vapor deposition.* Advanced Materials, 2012. **24**(17): p. 2320-2325.
76. Liu, K.-K., et al., *Growth of large-area and highly crystalline MoS2 thin layers on insulating substrates.* Nano Lett, 2012. **12**(3): p. 1538-1544.
77. Cao, T., et al., *Valley-selective circular dichroism of monolayer molybdenum disulphide.* Nature communications, 2012. **3**: p. 887.
78. Lee, C., et al., *Anomalous lattice vibrations of single-and few-layer MoS2.* ACS nano, 2010. **4**(5): p. 2695-2700.
79. Lee, H.S., et al., *MoS2 nanosheet phototransistors with thickness-modulated optical energy gap.* Nano letters, 2012. **12**(7): p. 3695-3700.
80. Yin, Z., et al., *Single-layer MoS2 phototransistors.* ACS nano, 2011. **6**(1): p. 74-80.
81. Tsai, M.-L., et al., *Monolayer MoS2 heterojunction solar cells.* ACS nano, 2014. **8**(8): p. 8317-8322.
82. Mak, K.F., et al., *Atomically thin MoS 2: a new direct-gap semiconductor.* Physical review letters, 2010. **105**(13): p. 136805.
83. Splendiani, A., et al., *Emerging photoluminescence in monolayer MoS2.* Nano letters, 2010. **10**(4): p. 1271-1275.
84. Sebenik, R.F., et al., *Molybdenum and molybdenum compounds.* Ullmann's Encyclopedia of Industrial Chemistry.
85. Johnson, V.R. and G.W. Vaughn, *Investigation of the mechanism of MoS2 lubrication in vacuum.* Journal of Applied Physics, 1956. **27**(10): p. 1173-1179.
86. Singer, I., et al., *Hertzian stress contribution to low friction behavior of thin MoS2 coatings.* Applied Physics Letters, 1990. **57**(10): p. 995-997.
87. Fleischauer, P.D. and R. Bauer, *Chemical and structural effects on the lubrication properties of sputtered MoS2 films.* Tribology Transactions, 1988. **31**(2): p. 239-250.
88. Sarkar, D., et al., *MoS2 field-effect transistor for next-generation label-free biosensors.* ACS nano, 2014. **8**(4): p. 3992-4003.
89. Wu, W., et al., *Piezoelectricity of single-atomic-layer MoS^ sub 2^ for energy conversion and piezotronics.* Nature, 2014. **514**(7523): p. 470.
90. Fan, X., et al., *MoS2 actuators: reversible mechanical responses of MoS2-polymer nanocomposites to photons.* Nanotechnology, 2015. **26**(26): p. 261001.
91. Ding, Y., et al., *First principles study of structural, vibrational and electronic properties of graphene-like MX 2 (M= Mo, Nb, W, Ta; X= S, Se, Te) monolayers.* Physica B: Condensed Matter, 2011. **406**(11): p. 2254-2260.
92. Beal, A., H. Hughes, and W. Liang, *The reflectivity spectra of some group VA transition metal dichalcogenides.* Journal of physics C: solid state physics, 1975. **8**(24): p. 4236.

93. Wilson, J., F. Di Salvo, and S. Mahajan, *Charge-density waves and superlattices in the metallic layered transition metal dichalcogenides.* Advances in Physics, 1975. **24**(2): p. 117-201.
94. Kam, K. and B. Parkinson, *Detailed photocurrent spectroscopy of the semiconducting group VIB transition metal dichalcogenides.* The Journal of Physical Chemistry, 1982. **86**(4): p. 463-467.
95. Liu, L., et al., *Performance limits of monolayer transition metal dichalcogenide transistors.* IEEE Transactions on Electron Devices, 2011. **58**(9): p. 3042-3047.
96. Wagner, A.B., *GMELIN Handbook of Inorganic and Organometallic Chemistry: Complete Catalog 1997/98.* 1998.
97. Kuc, A., N. Zibouche, and T. Heine, *Influence of quantum confinement on the electronic structure of the transition metal sulfide T S 2.* Physical Review B, 2011. **83**(24): p. 245213.
98. Kobayashi, K. and J. Yamauchi, *Electronic structure and scanning-tunneling-microscopy image of molybdenum dichalcogenide surfaces.* Physical Review B, 1995. **51**(23): p. 17085.
99. Li, T. and G. Galli, *Electronic properties of MoS2 nanoparticles.* The Journal of Physical Chemistry C, 2007. **111**(44): p. 16192-16196.
100. Eda, G., et al., *Photoluminescence from chemically exfoliated MoS2.* Nano letters, 2011. **11**(12): p. 5111-5116.
101. Li, H., et al., *From bulk to monolayer MoS2: evolution of Raman scattering.* Advanced Functional Materials, 2012. **22**(7): p. 1385-1390.
102. Placidi, M., et al., *Multiwavelength excitation Raman scattering analysis of bulk and two-dimensional MoS2: vibrational properties of atomically thin MoS2 layers.* 2D Materials, 2015. **2**(3): p. 035006.
103. Patil, S., et al., *Development of a novel method to grow mono-/few-layered MoS 2 films and MoS 2–graphene hybrid films for supercapacitor applications.* CrystEngComm, 2014. **16**(47): p. 10845-10855.
104. Li, S.-L., et al., *Quantitative Raman spectrum and reliable thickness identification for atomic layers on insulating substrates.* ACS nano, 2012. **6**(8): p. 7381-7388.
105. Molina-Sanchez, A. and L. Wirtz, *Phonons in single-layer and few-layer MoS 2 and WS 2.* Physical Review B, 2011. **84**(15): p. 155413.
106. Manzeli, S., et al., *Piezoresistivity and strain-induced band gap tuning in atomically thin MoS2.* Nano letters, 2015. **15**(8): p. 5330-5335.
107. Zhu, C., et al., *Strain tuning of optical emission energy and polarization in monolayer and bilayer MoS 2.* Physical Review B, 2013. **88**(12): p. 121301.
108. Rice, C., et al., *Raman-scattering measurements and first-principles calculations of strain-induced phonon shifts in monolayer MoS 2.* Physical Review B, 2013. **87**(8): p. 081307.
109. Vella, D., et al., *The macroscopic delamination of thin films from elastic substrates.* Proceedings of the National Academy of Sciences, 2009. **106**(27): p. 10901-10906.

110. Frindt, R., *Single crystals of MoS2 several molecular layers thick.* Journal of Applied Physics, 1966. **37**(4): p. 1928-1929.
111. Liu, Y., et al., *Layer-by-layer thinning of MoS2 by plasma.* ACS nano, 2013. **7**(5): p. 4202-4209.
112. Joensen, P., R. Frindt, and S.R. Morrison, *Single-layer MoS2.* Materials research bulletin, 1986. **21**(4): p. 457-461.
113. Chianelli, R.R. and M.B. Dines, *Reaction of butyllithium with transition metal trichalcogenides.* Inorganic Chemistry, 1975. **14**(10): p. 2417-2421.
114. Wang, X., et al., *MoS2/Polymer Nanocomposites: Preparation, Properties, and Applications.* Polymer Reviews, 2017. **57**(3): p. 440-466.
115. Zhang, W., et al., *Synthesis and sensor applications of MoS 2-based nanocomposites.* Nanoscale, 2015. **7**(44): p. 18364-18378.
116. Nam, H., et al., *MoS2 transistors fabricated via plasma-assisted nanoprinting of few-layer MoS2 flakes into large-area arrays.* ACS nano, 2013. **7**(7): p. 5870-5881.
117. Novoselov, K.S., et al., *Electric field effect in atomically thin carbon films.* science, 2004. **306**(5696): p. 666-669.
118. Lopez-Sanchez, O., et al., *Ultrasensitive photodetectors based on monolayer MoS2.* Nature nanotechnology, 2013. **8**(7): p. 497-501.
119. Paton, K.R., et al., *Scalable production of large quantities of defect-free few-layer graphene by shear exfoliation in liquids.* Nature materials, 2014. **13**(6): p. 624.
120. Zeng, Z., et al., *Single-Layer Semiconducting Nanosheets: High-yield preparation and device fabrication.* Angewandte Chemie International Edition, 2011. **50**(47): p. 11093-11097.
121. Coleman, J.N., *Liquid-phase exfoliation of nanotubes and graphene.* Advanced Functional Materials, 2009. **19**(23): p. 3680-3695.
122. Khan, U., et al., *High-Concentration Solvent Exfoliation of Graphene.* Small, 2010. **6**(7): p. 864-871.
123. Lee, K., et al., *Electrical characteristics of molybdenum disulfide flakes produced by liquid exfoliation.* Advanced materials, 2011. **23**(36): p. 4178-4182.
124. Nicolosi, V., et al., *Liquid exfoliation of layered materials.* Science, 2013. **340**(6139): p. 1226419.
125. Hernandez, Y., et al., *High-yield production of graphene by liquid-phase exfoliation of graphite.* Nature nanotechnology, 2008. **3**(9): p. 563.
126. Lotya, M., et al., *Liquid phase production of graphene by exfoliation of graphite in surfactant/water solutions.* Journal of the American Chemical Society, 2009. **131**(10): p. 3611-3620.
127. Wang, X., et al., *Controlled synthesis of highly crystalline MoS2 flakes by chemical vapor deposition.* Journal of the American Chemical Society, 2013. **135**(14): p. 5304-5307.
128. Liu, Z., et al., *Strain and structure heterogeneity in MoS 2 atomic layers grown by chemical vapour deposition.* Nature communications, 2014. **5**: p. 5246.

129. Wang, J., et al., *Direct growth of molybdenum disulfide on arbitrary insulating surfaces by chemical vapor deposition.* RSC Advances, 2015. **5**(6): p. 4364-4367.
130. Al-Mamun, M., et al., *Directly hydrothermal growth of ultrathin MoS 2 nanostructured films as high performance counter electrodes for dye-sensitised solar cells.* RSC Advances, 2014. **4**(41): p. 21277-21283.
131. Lin, H., et al., *Hydrothermal synthesis and characterization of MoS 2 nanorods.* Materials letters, 2010. **64**(15): p. 1748-1750.
132. Ma, L., et al., *Synthesis and characterization of flower-like MoS 2 microspheres by a facile hydrothermal route.* Materials Letters, 2009. **63**(23): p. 2022-2024.
133. Peng, Y., et al., *Hydrothermal synthesis and characterization of single-molecular-layer MoS2 and MoSe2.* Chemistry Letters, 2001. **30**(8): p. 772-773.
134. Feldman, Y., et al., *High-rate, gas-phase growth of MoS2 nested inorganic fullerenes and nanotubes.* Science, 1995. **267**(5195): p. 222.
135. Li, X.L. and Y.D. Li, *Formation of MoS2 inorganic fullerenes (IFs) by the reaction of MoO3 nanobelts and S.* Chemistry-A European Journal, 2003. **9**(12): p. 2726-2731.
136. Wu, Y., et al., *State-of-the-art graphene high-frequency electronics.* Nano letters, 2012. **12**(6): p. 3062-3067.
137. Wu, Y., et al., *High-frequency, scaled graphene transistors on diamond-like carbon.* Nature, 2011. **472**(7341): p. 74-78.
138. Lin, Y.-M., et al., *Wafer-scale graphene integrated circuit.* Science, 2011. **332**(6035): p. 1294-1297.
139. Ayari, A., et al., *Realization and electrical characterization of ultrathin crystals of layered transition-metal dichalcogenides.* Journal of applied physics, 2007. **101**(1): p. 014507.
140. Sze, S.M. and K.K. Ng, *Physics of semiconductor devices*. 2006: John wiley & sons.
141. Podzorov, V., et al., *High-mobility field-effect transistors based on transition metal dichalcogenides.* Applied Physics Letters, 2004. **84**(17): p. 3301-3303.
142. Yoon, Y., K. Ganapathi, and S. Salahuddin, *How good can monolayer MoS2 transistors be?* Nano letters, 2011. **11**(9): p. 3768-3773.
143. McManus, D., et al., *Water-based and biocompatible 2D crystal inks for all-inkjet-printed heterostructures.* Nature Nanotechnology, 2017. **12**(4): p. 343-350.
144. Avouris, P., M. Freitag, and V. Perebeinos, *Carbon-nanotube photonics and optoelectronics.* Nature photonics, 2008. **2**(6): p. 341-350.
145. Kamat, P.V., *Quantum dot solar cells. Semiconductor nanocrystals as light harvesters.* The Journal of Physical Chemistry C, 2008. **112**(48): p. 18737-18753.
146. Law, M., J. Goldberger, and P. Yang, *Semiconductor nanowires and nanotubes.* Annu. Rev. Mater. Res., 2004. **34**: p. 83-122.

147. Shanmugam, M., et al., *Molybdenum disulphide/titanium dioxide nanocomposite-poly 3-hexylthiophene bulk heterojunction solar cell.* Applied Physics Letters, 2012. **100**(15): p. 153901.
148. Thomalla, M. and H. Tributsch, *Photosensitization of nanostructured TiO2 with WS2 quantum sheets.* The Journal of Physical Chemistry B, 2006. **110**(24): p. 12167-12171.
149. Ho, W., et al., *Preparation and photocatalytic behavior of MoS2 and WS2 nanocluster sensitized TiO2.* Langmuir, 2004. **20**(14): p. 5865-5869.
150. Gourmelon, E., et al., *MS 2 (M= W, Mo) photosensitive thin films for solar cells.* Solar energy materials and solar cells, 1997. **46**(2): p. 115-121.
151. Choi, W., et al., *High-detectivity multilayer MoS2 phototransistors with spectral response from ultraviolet to infrared.* Advanced materials, 2012. **24**(43): p. 5832-5836.
152. Frey, G.L., et al., *Solution-processed anodes from layer-structure materials for high-efficiency polymer light-emitting diodes.* Journal of the American Chemical Society, 2003. **125**(19): p. 5998-6007.
153. Reynolds, K., et al., *Inorganic solution-processed hole-injecting and electron-blocking layers in polymer light-emitting diodes.* Journal of applied physics, 2002. **92**(12): p. 7556-7563.
154. Jariwala, D., et al., *Emerging device applications for semiconducting two-dimensional transition metal dichalcogenides.* ACS nano, 2014. **8**(2): p. 1102-1120.
155. Jariwala, D., et al., *Carbon nanomaterials for electronics, optoelectronics, photovoltaics, and sensing.* Chemical Society Reviews, 2013. **42**(7): p. 2824-2860.
156. Lee, K., et al., *High-performance sensors based on molybdenum disulfide thin films.* Advanced materials, 2013. **25**(46): p. 6699-6702.
157. He, Q., et al., *Fabrication of Flexible MoS2 Thin-Film Transistor Arrays for Practical Gas-Sensing Applications.* Small, 2012. **8**(19): p. 2994-2999.
158. Cho, B., et al., *Bifunctional sensing characteristics of chemical vapor deposition synthesized atomic-layered MoS2.* ACS applied materials & interfaces, 2015. **7**(4): p. 2952-2959.
159. Cho, B., et al., *Chemical sensing of 2D graphene/MoS2 heterostructure device.* ACS applied materials & interfaces, 2015. **7**(30): p. 16775-16780.
160. Li, H., et al., *Fabrication of single-and multilayer MoS2 film-based field-effect transistors for sensing NO at room temperature.* small, 2012. **8**(1): p. 63-67.
161. Late, D.J., et al., *Sensing behavior of atomically thin-layered MoS2 transistors.* Acs Nano, 2013. **7**(6): p. 4879-4891.
162. Perkins, F.K., et al., *Chemical vapor sensing with monolayer MoS2.* Nano letters, 2013. **13**(2): p. 668-673.
163. Tongay, S., et al., *Broad-range modulation of light emission in two-dimensional semiconductors by molecular physisorption gating.* Nano letters, 2013. **13**(6): p. 2831-2836.

164. Zhu, C., et al., *Single-layer MoS2-based nanoprobes for homogeneous detection of biomolecules.* Journal of the American Chemical Society, 2013. **135**(16): p. 5998-6001.
165. Kalantar-zadeh, K., et al., *Two-Dimensional Transition Metal Dichalcogenides in Biosystems.* Advanced Functional Materials, 2015. **25**(32): p. 5086-5099.
166. Knopf, G.K. and Y. Otani, *Optical nano and micro actuator technology*. 2012: CRC Press.
167. Zelenka, J., *Piezoelectric resonators and their applications*. 1986: Elsevier Science Publishers BV.
168. Uchino, K., *Piezoelectric actuators and ultrasonic motors*. Vol. 1. 1996: Springer Science & Business Media.
169. Pulskamp, J.S., et al., *Piezoelectric PZT MEMS technologies for small-scale robotics and RF applications.* MRS bulletin, 2012. **37**(11): p. 1062-1070.
170. Ekreem, N., et al., *An overview of magnetostriction, its use and methods to measure these properties.* Journal of Materials Processing Technology, 2007. **191**(1): p. 96-101.
171. Srinivasan, A.V. and D.M. McFarland, *Smart structures, analysis and design*. 2001, AAPT.
172. Tabib-Azar, M., *Microactuators: electrical, magnetic, thermal, optical, mechanical, chemical & smart structures*. Vol. 4. 2013: Springer Science & Business Media.
173. Jiang, H., S. Kelch, and A. Lendlein, *Polymers move in response to light.* Advanced Materials, 2006. **18**(11): p. 1471-1475.
174. Ikeda, T. and O. Tsutsumi, *Optical switching and image storage by means of azobenzene liquid-crystal films.* SCIENCE-NEW YORK THEN WASHINGTON-, 1995: p. 1873-1873.
175. Irie, M., *Photoresponsive polymers*, in *New Polymer Materials*. 1990, Springer. p. 27-67.
176. Akabori, S., et al., *The novel syntheses of photoreversible cyclobutanocrown ethers by the intramolecular photoaddition of α, ω-dicinnamoyl polyethylene glycol derivatives.* Bulletin of the Chemical Society of Japan, 1987. **60**(9): p. 3453-3455.
177. Nakayama, Y. and T. Matsuda, *Preparation and characteristics of photocrosslinkable hydrophilic polymer having cinnamate moiety.* Journal of Polymer Science Part A: Polymer Chemistry, 1992. **30**(11): p. 2451-2457.
178. Warner, M. and E.M. Terentjev, *Liquid crystal elastomers*. Vol. 120. 2003: OUP Oxford.
179. Finkelmann, H., et al., *A new opto-mechanical effect in solids.* Physical Review Letters, 2001. **87**(1): p. 015501.
180. van Oosten, C.L., et al., *Bending dynamics and directionality reversal in liquid crystal network photoactuators.* Macromolecules, 2008. **41**(22): p. 8592-8596.
181. Van Oosten, C.L., C.W. Bastiaansen, and D.J. Broer, *Printed artificial cilia from liquid-crystal network actuators modularly driven by light.* Nature materials, 2009. **8**(8): p. 677-682.

182. Eelkema, R., et al., *Molecular machines: nanomotor rotates microscale objects.* Nature, 2006. **440**(7081): p. 163-163.
183. Li, J.J. and W. Tan, *A single DNA molecule nanomotor.* Nano Letters, 2002. **2**(4): p. 315-318.
184. Kang, H., et al., *Single-DNA molecule nanomotor regulated by photons.* Nano letters, 2009. **9**(7): p. 2690-2696.
185. Al-Atar, U., et al., *A photocontrolled molecular switch regulates paralysis in a living organism.* Journal of the American Chemical Society, 2009. **131**(44): p. 15966-15967.
186. Carling, C.-J., J.-C. Boyer, and N.R. Branda, *Remote-control photoswitching using NIR light.* Journal of the American Chemical Society, 2009. **131**(31): p. 10838-10839.
187. Boyer, J.-C., et al., *Two-way photoswitching using one type of near-infrared light, upconverting nanoparticles, and changing only the light intensity.* Journal of the american chemical society, 2010. **132**(44): p. 15766-15772.
188. Uchino, K. and M. Aizawa, *Photostrictive actuator using PLZT ceramics.* Japanese Journal of Applied Physics, 1985. **24**(S3): p. 139.
189. Morikawa, Y. and T. Nakada. *Position control of PLZT bimorph-type optical actuator by on-off control*. in *Industrial Electronics, Control and Instrumentation, 1997. IECON 97. 23rd International Conference on*. 1997. IEEE.
190. Uchino, K. *Photostrictive actuator*. in *Ultrasonics Symposium, 1990. Proceedings., IEEE 1990*. 1990. IEEE.
191. Datskos, P.G., S. Rajic, and I. Datskou, *Photoinduced and thermal stress in silicon microcantilevers.* Applied Physics Letters, 1998. **73**(16): p. 2319-2321.
192. Lagowski, J. and H. Gatos, *Photomechanical Effect in Noncentrosymmetric Semiconductors-CdS.* Applied Physics Letters, 1972. **20**(1): p. 14-16.
193. Lagowski, J., H. Gatos, and E. Sproles Jr, *Surface stress and the normal mode of vibration of thin crystals: GaAs.* Applied physics letters, 1975. **26**(9): p. 493-495.
194. Suski, J., et al., *Optically activated ZnO/SiO2/Si cantilever beams.* Sensors and actuators A: Physical, 1990. **24**(3): p. 221-225.
195. Landi, B.J., et al., *Single wall carbon nanotube− nafion composite actuators.* Nano Letters, 2002. **2**(11): p. 1329-1332.
196. Ahir, S.V. and E.M. Terentjev, *Photomechanical actuation in polymer-nanotube composites.* Nature materials, 2005. **4**(6): p. 491.
197. Nan, C.-W. and Q. Jia, *Obtaining ultimate functionalities in nanocomposites: Design, control, and fabrication.* MRS Bulletin, 2015. **40**(9): p. 719-724.
198. Ahir, S., Y. Huang, and E. Terentjev, *Polymers with aligned carbon nanotubes: Active composite materials.* Polymer, 2008. **49**(18): p. 3841-3854.
199. Ahir, S., et al., *Infrared actuation in aligned polymer-nanotube composites.* Physical review B, 2006. **73**(8): p. 085420.
200. Ahir, S. and E. Terentjev, *Fast relaxation of carbon nanotubes in polymer composite actuators.* Physical review letters, 2006. **96**(13): p. 133902.

201. Lu, S. and B. Panchapakesan, *Nanotube micro-optomechanical actuators.* Applied Physics Letters, 2006. **88**(25): p. 253107.
202. Lu, S. and B. Panchapakesan, *Optically driven nanotube actuators.* Nanotechnology, 2005. **16**(11): p. 2548.
203. Lu, S. and B. Panchapakesan, *Photomechanical responses of carbon nanotube/polymer actuators.* Nanotechnology, 2007. **18**(30): p. 305502.
204. Lu, S., et al., *Alignment dependent mechanical responses of carbon nanotubes to light.* Applied Physics Letters, 2007. **91**(10): p. 103106.
205. Loomis, J. and B. Panchapakesan, *Large photocurrents in single layer graphene thin films: effects of diffusion and drift.* Nanotechnology, 2012. **23**(26): p. 265203.
206. Niu, D., et al., *Reversible Bending Behaviors of Photomechanical Soft Actuators Based on Graphene Nanocomposites.* Scientific reports, 2016. **6**: p. 27366.
207. Acerce, M., E.K. Akdoğan, and M. Chhowalla, *Metallic molybdenum disulfide nanosheet-based electrochemical actuators.* Nature, 2017. **549**(7672): p. 370.
208. Pelrine, R., et al., *High-field deformation of elastomeric dielectrics for actuators.* Materials Science and Engineering: C, 2000. **11**(2): p. 89-100.
209. Zhang, Q., V. Bharti, and X. Zhao, *Giant electrostriction and relaxor ferroelectric behavior in electron-irradiated poly (vinylidene fluoride-trifluoroethylene) copolymer.* Science, 1998. **280**(5372): p. 2101-2104.
210. Brochu, P. and Q. Pei, *Advances in dielectric elastomers for actuators and artificial muscles.* Macromolecular rapid communications, 2010. **31**(1): p. 10-36.
211. Pelrine, R., et al., *High-speed electrically actuated elastomers with strain greater than 100%.* Science, 2000. **287**(5454): p. 836-839.
212. Hunter, I.W., et al. *Fast reversible NiTi fibers for use in microrobotics*. in *Micro Electro Mechanical Systems, 1991, MEMS'91, Proceedings. An Investigation of Micro Structures, Sensors, Actuators, Machines and Robots. IEEE*. 1991. IEEE.
213. Hunter, I.W. and S. Lafontaine. *A comparison of muscle with artificial actuators*. in *Solid-State Sensor and Actuator Workshop, 1992. 5th Technical Digest., IEEE*. 1992. IEEE.
214. Lima, M.D., et al., *Electrically, chemically, and photonically powered torsional and tensile actuation of hybrid carbon nanotube yarn muscles.* Science, 2012. **338**(6109): p. 928-932.
215. Haines, C.S., et al., *Artificial muscles from fishing line and sewing thread.* science, 2014. **343**(6173): p. 868-872.
216. Ma, M., et al., *Bio-inspired polymer composite actuator and generator driven by water gradients.* Science, 2013. **339**(6116): p. 186-189.
217. Hara, S., et al., *Artificial muscles based on polypyrrole actuators with large strain and stress induced electrically.* Polymer journal, 2004. **36**(2): p. 151.
218. Foroughi, J., et al., *Torsional carbon nanotube artificial muscles.* Science, 2011. **334**(6055): p. 494-497.

219. Mirfakhrai, T., et al., *Electrochemical actuation of carbon nanotube yarns.* Smart Materials and Structures, 2007. **16**(2): p. S243.
220. Spinks, G.M., et al., *Carbon-nanotube-reinforced polyaniline fibers for high-strength artificial muscles.* Advanced Materials, 2006. **18**(5): p. 637-640.
221. Xie, X., et al., *Load-tolerant, highly strain-responsive graphene sheets.* Journal of Materials Chemistry, 2011. **21**(7): p. 2057-2059.
222. Jin, H.-J., et al., *Nanoporous Au− Pt alloys as large strain electrochemical actuators.* Nano letters, 2009. **10**(1): p. 187-194.
223. Gu, G., et al., *V 2 O 5 nanofibre sheet actuators.* Nature materials, 2003. **2**(5): p. 316.
224. Koyama, Y., et al., *Harnessing the Actuation Potential of Solid-State Intercalation Compounds.* Advanced Functional Materials, 2006. **16**(4): p. 492-498.
225. Chin, T.E., et al., *Lithium rechargeable batteries as electromechanical actuators.* Electrochemical and solid-state letters, 2006. **9**(3): p. A134-A138.
226. Rahneshin, V., et al., *The Coupled Straintronic-Photothermic Effect.* Scientific reports, 2018. **8**(1): p. 64.
227. Liang, J., et al., *Infrared-triggered actuators from graphene-based nanocomposites.* The Journal of Physical Chemistry C, 2009. **113**(22): p. 9921-9927.
228. Podsiadlo, P., et al., *Ultrastrong and stiff layered polymer nanocomposites.* Science, 2007. **318**(5847): p. 80-83.
229. Kumar, S.K., et al., *Nanocomposites with polymer grafted nanoparticles.* Macromolecules, 2013. **46**(9): p. 3199-3214.
230. Frogley, M.D., D. Ravich, and H.D. Wagner, *Mechanical properties of carbon nanoparticle-reinforced elastomers.* Composites Science and technology, 2003. **63**(11): p. 1647-1654.
231. Breuer, O. and U. Sundararaj, *Big returns from small fibers: a review of polymer/carbon nanotube composites.* Polymer composites, 2004. **25**(6): p. 630-645.
232. Lisensky, G.C., et al., *Replication and compression of surface structures with polydimethylsiloxane elastomer.* J. Chem. Educ, 1999. **76**(4): p. 537.
233. Kalathi, J.T., G.S. Grest, and S.K. Kumar, *Universal viscosity behavior of polymer nanocomposites.* Physical review letters, 2012. **109**(19): p. 198301.
234. Sahoo, S., et al., *Temperature-Dependent Raman Studies and Thermal Conductivity of Few-Layer MoS2.* Journal of Physical Chemistry C, 2013. **117**(17): p. 9042-9047.
235. Wu, H. and L.T. Drzal, *Graphene nanoplatelet paper as a light-weight composite with excellent electrical and thermal conductivity and good gas barrier properties.* Carbon, 2012. **50**(3): p. 1135-1145.
236. Young, P.A., *Lattice parameter measurements on molybdenum disulphide* British Journal of Applied Physics (J.Phys.D), 1968. **1**(2): p. 936-938.
237. Dickinson, R.G. and L. Pauling, *Crystal Structure of Molybdenite.* Journal of American Chemical Society, 1923. **45**(6): p. 1466-1471.

238. Coleman, J.N., et al., *Two-Dimensional Nanosheets Produced by Liquid Exfoliation of Layered Materials.* Science, 2011. **331**(6017): p. 568-571.
239. Qin, X.R., et al., *Real-Space Imaging of Single-Layer Mos2 by Scanning Tunneling Microscopy.* Physical Review B, 1991. **44**(7): p. 3490-3493.
240. Ho, Y.H., W.P. Su, and M.F. Lin, *Hofstadter spectra for d-orbital electrons: a case study on MoS2.* Rsc Advances, 2015. **5**(27): p. 20858-20864.
241. J. P. Wilcoxon, P.P.N., and G. A. Samara, *Synthesis and optical properties of MoS 2 and isomorphous nanoclusters in the quantum confinement regime.* Journal of Applied Physics, 1997. **84**: p. 7934-7944.
242. Lee, C., et al., *Anomalous Lattice Vibrations of Single- and Few-Layer MoS2.* Acs Nano, 2010. **4**(5): p. 2695-2700.
243. Golasa, K., et al., *Multiphonon resonant Raman scattering in MoS2.* Applied Physics Letters, 2014. **104**(9).
244. Golasa, K., et al., *Resonant Raman scattering in MoS2-From bulk to monolayer.* Solid State Communications, 2014. **197**: p. 53-56.
245. Livneh, T. and J.E. Spanier, *A comprehensive multiphonon spectral analysis in MoS2.* 2d Materials, 2015. **2**(3).
246. Livneh, T. and E. Sterer, *Resonant Raman scattering at exciton states tuned by pressure and temperature in 2H-MoS2.* Physical Review B, 2010. **81**(19).
247. Lu, S., et al., *Nanotube micro-opto-mechanical systems (N-MOMS).* Transducers '07 & Eurosensors Xxi, Digest of Technical Papers, Vols 1 and 2, 2007.
248. Rockett, A., *Physics of Solids*, in *Materials Science of Semiconductors*. 2008, Springer: New York. p. 615.
249. Vella, D., et al., *The macroscopic delamination of thin films from elastic substrates.* Proceedings of the National Academy of Sciences of the United States of America, 2009. **106**(27): p. 10901-10906.
250. Fan, X.M., et al., *MoS2 actuators: reversible mechanical responses of MoS2-polymer nanocomposites to photons.* Nanotechnology, 2015. **26**(26).
251. Loomis, J., B. King, and B. Panchapakesan, *Layer dependent mechanical responses of graphene composites to near-infrared light.* Applied Physics Letters, 2012. **100**(7).
252. Mansfield, E.H., *The bending and stretching of plates*. 2005: Cambridge university press.
253. Sirringhaus, H., et al., *High-resolution inkjet printing of all-polymer transistor circuits.* Science, 2000. **290**(5499): p. 2123-2126.
254. Baeg, K.J., M. Caironi, and Y.Y. Noh, *Toward printed integrated circuits based on unipolar or ambipolar polymer semiconductors.* Advanced Materials, 2013. **25**(31): p. 4210-4244.
255. Hutchings, I.M. and G.D. Martin, *Inkjet technology for digital fabrication*. 2012: John Wiley & Sons.
256. Finn, D.J., et al., *Inkjet deposition of liquid-exfoliated graphene and MoS 2 nanosheets for printed device applications.* Journal of Materials Chemistry C, 2014. **2**(5): p. 925-932.

257. Torrisi, F., et al., *Inkjet-printed graphene electronics.* ACS nano, 2012. **6**(4): p. 2992-3006.
258. Withers, F., et al., *Heterostructures produced from nanosheet-based inks.* Nano letters, 2014. **14**(7): p. 3987-3992.
259. Yang, H., et al., *A simple method for graphene production based on exfoliation of graphite in water using 1-pyrenesulfonic acid sodium salt.* Carbon, 2013. **53**: p. 357-365.
260. Yang, H., et al., *Dielectric nanosheets made by liquid-phase exfoliation in water and their use in graphene-based electronics.* 2D Materials, 2014. **1**(1): p. 011012.
261. Martin, G.D., S.D. Hoath, and I.M. Hutchings. *Inkjet printing-the physics of manipulating liquid jets and drops*. in *Journal of Physics: Conference Series*. 2008. IOP Publishing.
262. Derby, B., *Inkjet printing of functional and structural materials: fluid property requirements, feature stability, and resolution.* Annual Review of Materials Research, 2010. **40**: p. 395-414.
263. McKinley, G.H. and M. Renardy, *Wolfgang von ohnesorge.* Physics of Fluids, 2011. **23**(12): p. 127101.
264. Reis, N. and B. Derby, *Ink jet deposition of ceramic suspensions: Modeling and experiments of droplet formation.* MRS Online Proceedings Library Archive, 2000. **625**.
265. Hu, H. and R.G. Larson, *Marangoni effect reverses coffee-ring depositions.* The Journal of Physical Chemistry B, 2006. **110**(14): p. 7090-7094.
266. Deegan, R.D., et al., *Capillary flow as the cause of ring stains from dried liquid drops.* Nature, 1997. **389**(6653): p. 827-829.
267. Deegan, R.D., et al., *Contact line deposits in an evaporating drop.* Physical review E, 2000. **62**(1): p. 756.
268. *Fujifilm dimatix materials printer DMP-2800 series user manual.* FUJIFILM Dimatix, Inc., 2010.
269. Taccola, S., et al., *Toward a new generation of electrically controllable hygromorphic soft actuators.* Advanced Materials, 2015. **27**(10): p. 1668-1675.
270. Chen, L., et al., *Large-Deformation curling actuators based on carbon nanotube composite: advanced-structure design and biomimetic application.* ACS nano, 2015. **9**(12): p. 12189-12196.
271. Chen, P., et al., *Electromechanical actuator ribbons driven by electrically conducting spring-like fibers.* Advanced Materials, 2015. **27**(34): p. 4982-4988.
272. Zhou, Z., et al., *A large-deformation phase transition electrothermal actuator based on carbon nanotube–elastomer composites.* Journal of Materials Chemistry B, 2016. **4**(7): p. 1228-1234.
273. Hines, L., et al., *Soft Actuators for Small-Scale Robotics.* Advanced Materials, 2017. **29**(13).
274. Liu, Q., et al., *Nanostructured carbon materials based electrothermal air pump actuators.* Nanoscale, 2014. **6**(12): p. 6932-6938.

275. Zeng, Z., et al., *Low-voltage and high-performance electrothermal actuator based on multi-walled carbon nanotube/polymer composites.* Carbon, 2015. **84**: p. 327-334.
276. Li, Q., et al., *Large-strain, multiform movements from designable electrothermal actuators based on large highly anisotropic carbon nanotube sheets.* ACS nano, 2015. **9**(1): p. 409-418.
277. Martinez, A.W., S.T. Phillips, and G.M. Whitesides, *Three-dimensional microfluidic devices fabricated in layered paper and tape.* Proceedings of the National Academy of Sciences, 2008. **105**(50): p. 19606-19611.
278. Connelly, J.T., J.P. Rolland, and G.M. Whitesides, *"Paper machine" for molecular diagnostics.* Analytical chemistry, 2015. **87**(15): p. 7595-7601.
279. Nemiroski, A., et al., *Universal mobile electrochemical detector designed for use in resource-limited applications.* Proceedings of the National Academy of Sciences, 2014. **111**(33): p. 11984-11989.
280. Mosadegh, B., et al., *Three-dimensional paper-based model for cardiac ischemia.* Advanced healthcare materials, 2014. **3**(7): p. 1036-1043.
281. Mosadegh, B., et al., *A paper-based invasion assay: Assessing chemotaxis of cancer cells in gradients of oxygen.* Biomaterials, 2015. **52**: p. 262-271.
282. Lessing, J., et al., *Inkjet Printing of conductive inks with high lateral resolution on omniphobic "Rf paper" for paper-based electronics and MEMS.* Advanced Materials, 2014. **26**(27): p. 4677-4682.
283. Mazzeo, A.D., et al., *Paper-Based, Capacitive Touch Pads.* Advanced Materials, 2012. **24**(21): p. 2850-2856.
284. Liu, X., et al., *based piezoresistive MEMS sensors.* Lab on a Chip, 2011. **11**(13): p. 2189-2196.
285. Amjadi, M. and M. Sitti, *High-Performance Multiresponsive Paper Actuators.* Acs Nano, 2016. **10**(11): p. 10202-10210.
286. Hamedi, M.M., et al., *Electrically activated paper actuators.* Advanced Functional Materials, 2016. **26**(15): p. 2446-2453.